

UNIVERSITY OF PALERMO
*Department of Chemical, Management, Informatics
and Mechanical Engineering*

FRIEDRICH-ALEXANDER-UNIVERSITÄT
ERLANGEN-NÜRNBERG
Institute of Manufacturing Technology

COMPUTER AIDED ENGINEERING OF SOLID BONDING PHENOMENA

PhD Thesis:

Davide Campanella

Tutors:

Prof. Dr. Ing. Livan Fratini

Prof. Dr.-Ing. habil. Marion Merklein

ACADEMIC YEAR 2013 / 2014
XXIV Cycle

Cotutelle

The joint supervision of thesis is a mode of carrying out the PhD, which involves the registration of the candidate in two universities, in two different countries, and the issuing of a qualification recognized by both states.

In order to apply for the admission under the joint supervision the candidate must be already registered in a PhD program, and both the involved Countries must have already signed a mutual framework agreement. If these conditions exist, it is necessary to enter into an agreement for each student registered at joint supervision. The agreement must be prepared by the candidate together with the two tutors and approved by the Academic Senate and signed by the Rectors of the involved universities.

During the preparation of the thesis, the student is under the joint supervision of both the two tutors, one for each university. The student must stay alternately in the two institutions, to which the two tutors belong (and usually for equal periods). The oral defense takes place in front of a joint committee of university professors from both countries (at least two per side). The diploma can be unique or double, but in any case it must mention the existence of the joint supervision.

In Italy, the authority responsible for the drafting of agreements for joint supervision is the CRUI (Conference of Italian University Rectors).

This thesis is the result of a research study carried out under the joint supervision operated by the University of Palermo and the University of Erlangen-Nuremberg, and in particular between the departments of the “Chemical Engineering, Management, Computer Science, Mechanical Engineering (DICGIM)” and the “Lehrstuhl für Fertigungstechnologie (LFT)”. Prof. Livan Fratini (for the University of Palermo) and Prof. Marion Merklein (for the University of Erlangen-Nuremberg) were the tutors of this thesis.

Abstract

Joining is a fundamental technological process in manufacturing used to create a single piece from two or more parts. Welding is still today one of the most popular joining techniques used in manufacturing allowing a permanent junction. Traditional welding processes are based on the melting of the materials to be joined. In this way, several defects may arise because of solidification problems, joints deformation due to elevated residual stress and metallurgical integrity of the joints (intermetallic, porosities, etc). As an example, some aluminum alloys present considerable problems the junction is carried out by traditional fusion welding methods. During the melting process, in fact, the liquid material can react with the surrounding atmosphere oxidizing and creating a weak joint.

On the other hand, Solid Bonding based welding processes allow for defect free joints with low residual stress and low distortion. However, these processes are usually characterized by complex mechanics due to peculiar material flow. Hence, the engineering and optimization of solid bonding processes is difficult and requires a large number of time and cost consuming test trials. In this way, proper numerical models are essential tools permitting effective process design.

The aim of this research was the computer aided engineering of two different manufacturing processes taking advantage of the same metallurgical phenomenon, namely solid bonding. Linear Friction Welding (LFW), used to weld non-axisymmetric components and Accumulative Roll Bonding (ARB), used to increase the mechanical properties of sheet metals, were selected. Experiments, both of LFW and ARB, were run with the aim to study the effects of the process input parameters on the final product quality, to define proper process windows and to acquire the data needed for the numerical models set up and validation. In particular, as far as LFW is regarded, a dedicated experimental machine, able to produce LFWed joints with varying pressure, oscillation frequency and amplitude, was designed and built.

Numerical models were set up, validated and used to design the process by studying the complex material behavior during the solid bonding of different aluminum alloys. In particular, as far as ARB is regarded, two different numerical

models were considered, using an explicit and implicit approach, respectively, in order to study the process. An implicit approach was used for the LFW process, leading to the understanding of the main process variables influence on the field variables distribution and the occurrence of actual bonding. The simulation tools used in this work were DEFORM3D and ABAQUS CAE/6.9 (2D and 3D modes). The first prototype of the LFW machine was designed and developed during the first doctorate year. During the second doctorate year, the Accumulative Roll Bonding process was studied at the University of Erlangen-Nuremberg while, during the third year, the Linear Friction Welding process was analyzed at the University of Palermo.

Index

Abstract.....	2
1. Solid State Bonding	6
1.1. Introduction	6
1.2. Friction stir welding.....	8
1.3. Rotary friction welding	12
1.3. Porthole Die Extrusion.....	13
2. Linear Friction Welding	14
2.1. Process description	15
2.2. Machine requirements.....	18
2.3. Current state of the art	19
3. Prototype Machine.....	30
3.1. Machine description	30
3.1.1. Oscillation mechanism.....	30
3.1.2. Machine layout	33
3.1. Kinematic analysis.....	40
3.2. Dynamic analysis	51
3.3. Measurement devices	55
4. Linear Friction Welding Experiments	58
4.1. Experimental set up.....	58
4.1.1. Used materials.....	58
4.1.2. Specimens geometry.....	61
4.1.3. Process parameters	61
4.1.4. Joints analysis	62
4.2. Similar joints: AA2011 and AA6082	65
4.2.1. Process windows	65
4.2.2. Temperature trends analysis	66
4.2.3. Macroscopic analysis	68
4.2.4. Micrographic analyses.....	78
4.2.5. Microhardness analyses.....	83
4.3. Mixed joint.....	86
4.3.1. Process windows	87
4.3.2. Macroscopic analysis	87
4.3.3. Micrographic analysis	93
4.3.1. Temperature trends analysis	99
4.3.2. Microhardness analysis	100
4.3.3. EDAX analysis.....	102
4.4. Numerical Analysis.....	103
5. Accumulative Roll Bonding	121
5.1. Process description.....	121
5.2. Process parameters	124
5.2.1. Temperature	124
5.2.2. Reduction per rolling cycle	124
5.2.3. Rolling cycles number	125
5.2.4. Roll diameter	125
5.2.5. Oxide layer removal.....	126
5.2.6. Friction.....	126
5.3. Current state of the art	126

6. Accumulative Roll Bonding Experiments	132
6.1. Experimental set up.....	132
6.1.1. Used material	132
6.1.2. Fixture and parameters	133
6.2. Experimental Tests.....	134
6.3. Numerical Analyses.....	138
6.3.1. Explicit model	139
6.3.2. Implicit model.....	146
7. Comparison of Thermo-mechanical Implicit models	151
7.1. Comparison between ARB thermo-mechanical models	151
7.2. Comparison between LFW and ARB models	153
8. Conclusion.....	159
9. Future developments	163
10. Bibliography	164

1. Solid State Bonding

1.1. Introduction

Frequently, in the mechanical industry field, the junction of several parts is used to obtain a complex system, whose implementation in block would be difficult or not recommended.

Different manufacturing difficulties may arise:

- It is not possible or economical to produce the product in a single piece.
- It is easier to manufacture the individual parts and subsequently assemble them.
- The product has been cut or disassembled for repair or maintenance.
- Different properties, in different areas, are not achievable using a single material.
- It is better to transport the product divided into parts, and assemble them directly on site.

Two types of connections can be distinguished, such as:

- Removable connection
- Permanent connection

The removable connections are used to disassemble the connected parts, while the permanent connections can be achieved principally by:

- *Fusion Welding*, a process that allows the permanent connection of solid parts between them. This process allows for material continuity where it is applied.
- *Bonding*, where the junction is obtained using a sort of glue between the parts (as in the adhesive bonding technique).
- *Mechanical fixing*, process that involves the junction of several parts by deformation of a third element (nail, rivet).

Further distinction can be made, for the fusion welding process, depending on presence (or not) of the filler material. The two families can be divided in autogenous or heterogeneous welding:

- The first process is characterized by the involvement of the base material. In fact, this material, that is part of the elements to be bonded, participates directly in the formation of the joint.
- In the heterogeneous welding process, however, the junction is usually made with a different material (respect to material of the parts), usually called filler material. This process is more properly identified with the term of “brazing”. The brazing, compared to the traditional welding process, has characteristics more similar to the bonding process.

One of the principal problems related to autogenous welding process regards the mechanical strength of the joint, because reaching the melting point of the base material produces a change in the microstructure of the metal. This microstructural change alters the mechanical properties. It is known that maintaining the metal to the melting temperature causes grain growth, and, consequently, an increase of the grain boundaries, which represents an energetic barrier. Grain growth produces lower hardness, but higher ductility: this characteristic is not positive for a metal junction. The principal problem of fusion welding process is the creation of an HAZ (Heat Affected Zone) in the weld seam, causing relevant problems in strength.

In solid state welding, differently from fusion welding processes, the material never reaches the melting point, as the coalescence of the coupling parts occurs at significantly lower temperatures. The relevant aspect of this phenomenon concerns the atoms involved in the junction. The atoms on the surface of the metals to be welded are spaced a few Angstroms. This means that an atoms cloud of negative charge can result where the potential barrier is eliminated by the interaction between free electrons and ionized atoms, allowing the electrons cloud to become unitary. In the other words, a solid bonding can be reached and called welding or mechanical junction. In this way the negative effects of the HAZ are avoided and the joints show better mechanical properties than those obtained by the fusion welding methods.

The main variables controlling the occurrence of solid bonding are:

- Time
- Contact Pressure
- Temperature

Usually, process times are short, while temperature remains between the 50% and the 90% of the melting point (i.e. a necessary condition to refer to this process as a solid-state bonding) [1-2]. It has to be noticed that the parameters governing the solid bonding phenomena are controlled by the technological and geometrical parameters proper of the considered process.

Solid bonding occurs in several different manufacturing processes. Figure 1 reports a scheme of the main processes whose mechanics is based on the solid bonding phenomenon.

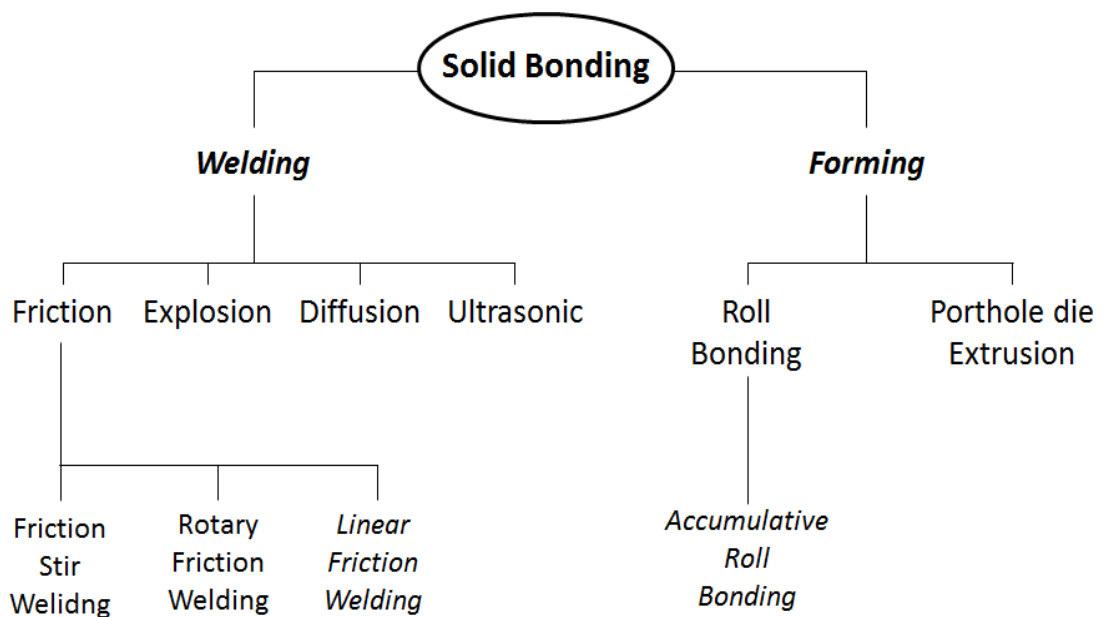


Figure 1. Schematic representation of the solid bonding manufacturing processes

In the following of this chapter, only a few processes will be briefly described. In particular, the Friction Welding processes, namely Friction Stir Welding and Rotary Friction Welding will be introduced due to the similarities with the Linear Friction Welding process. By the same token, the Porthole Die Extrusion process will be described in order to point out similarities and differences in the process mechanics with ARB.

1.2. Friction stir welding

Friction Stir Welding (FSW) is a solid state welding process patented by The Welding Institute in Cambridge (UK) in 1991. This process is becoming increasingly important due to the exceptional results obtained for the mechanical

junction of materials, such as aluminum alloys, referred as "not weldable" with conventional welding technologies.

Through FSW it is possible to obtain sound joints out of several light alloys and to join different materials in terms of both chemical composition and supply state (fused, extrusions, laminates, and foams). These materials, when subjected to conventional welding technologies are problematic, presenting hot cracking, porosity and distortions. The process was originally developed to weld "not weldable" aluminum alloys, as 2xxx, 5xxx, 6xxx, 7xxx and 8xxx alloys and Al-Li-Cu alloys. Due to the high quality of the obtained joints, other alloys have been tested as magnesium, titanium and nickel based superalloys.

As mentioned above, the welding occurs in the solid state. During the execution, keeping temperature away from the melting point avoids the material solidification and, consequently, the problems related to the presence of brittle phases in the weld bead. At the same time, significant improvements in ductility and strength can be obtained.

The potential of FSW process supports a wide range of applications such as in aerospace components, ship, railway or automobile parts: applications can be found also in electric motors development, cooling elements, food industry field and all industries making use of light alloys.

The machine tool used for the process is a milling machine with a vertical axis, providing the possibility to apply a load on the tool. The joining process, for two or more pieces, occurs with the use of a properly designed tool. In its basic shape, the tool is made by two concentric cylinders (Figure 2): the shoulder, whose base surface slides on the upper surface of the joint, and the pin, which is inserted in the sheets to be welded. The tool, once brought into rotation, penetrates into the sheets, adequately positioned on a backplate or over a support, and then is moved along the joint line.

The trajectory of the tool could also assume curvilinear profiles.

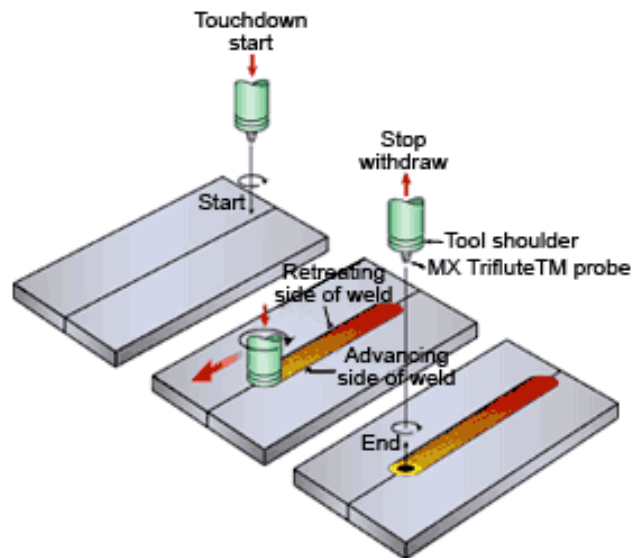


Figure 2. Steps of the FSW process [3]

The choice of the tool material depends on the materials to be welded. The geometrical characteristics of the tool [4] are (Figure 3):

- *A cylindrical body that is inserted into the tool-holder on the welding machine;*
- *The press and strip actions on top of the sheets, called "skin", are carried out by the "Shoulder". This part is in charge of generating the heat and preventing the escape of plasticized material from the area of the joint. It is the part of the tool responsible for the forging.*
- *The stirring action of the material affects one part of the tool named "Pin". This part penetrates into the material and, through the rotary motion around its own axis, stirs the material. It is the part of the tool responsible of the material flow lines [5].*

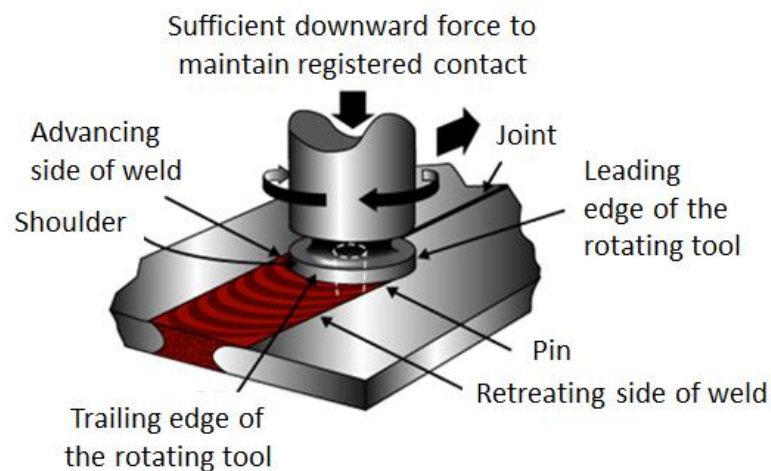


Figure 3. The FSW process [6].

The process parameters are different from the typical ones used for the fusion welding, due to the different nature of actions in the process. Selection and optimization of these parameters are related to several aspects, such as the material to be welded and the joint morphology. Important parameters to be set up are:

- *Tool size (both shoulder and pin);*
- *Tool rotational speed;*
- *Tool feed rate (welding speed);*
- *Tool penetration depth or Force superimposed on the tool;*

A tilt angle is given to the tool, usually ranging between 1° and 3°, opposite to the welding direction. Larger values are not commonly used as the resistant section of the weld bead decreases too much. In turn, small values reduces the forging effect of the shoulder in the trailing edge.

A peculiar material flow is obtained because of the tool action. The material in the leading edge is dragged around the tool many times before being deposited in the trailing edge. In this way a circular flow is obtained in the horizontal plane.

Looking at a transverse section of the joint, two zones can be identified, called advancing side and retreating side. In the advancing side, the rotation speed and feed rate tool are in the same direction; vice versa, in the retreating side, the two speeds are discordant. Due to the rotation of the pin, the material is dragged around the tool before being left at the advancing side, where the actual solid bonding takes place and the weld consolidates once the tool left.

The high temperatures reached and the severe plastic deformations induced on the material near the tool allow producing a zone at the center of the weld bead characterized by equiaxial and very fine grain. This grain refinement results from a process of dynamic recrystallization, and results in an increasing of the mechanical characteristics in the nugget zone.

1.3. Rotary friction welding

Rotary Friction Welding is indicated to join axially symmetric components and, in particular, with a cylindrical shape. In the process, a lathe is used to generate the relative movement between the specimens. One specimen is kept between the jaws of a lathe and then put in rotation around its own axis. The other component is moved along its axis to approach the piece fixed to the chuck.

The process takes place through four different phases:

- One specimen is put in rotation until it reaches the speed selected for the test.
- The heat generated by friction forces work decaying into heat softened the material near the contact interface. Usually this phase is evident since the glow area is present.
- Material extrusion occurs in the contact area due to the increase of the axial forces between the two specimens [7].
- The spindle rotation is suddenly stopped [8], while the contact force remains constant or further increases.

Figure 4 shows the four process phases.

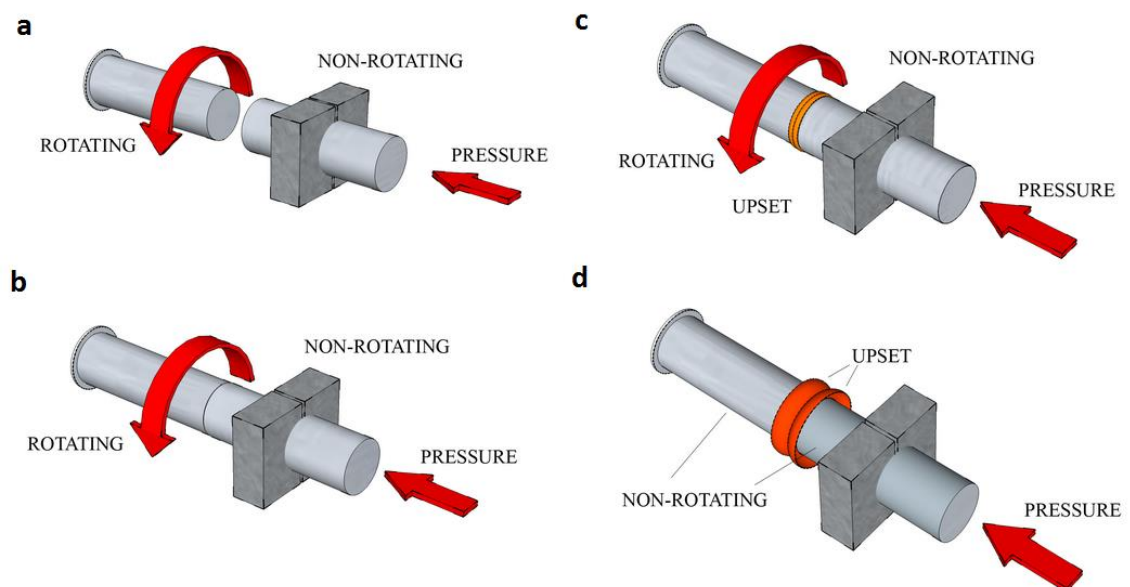


Figure 4. RFW process phases [9]

Elevated joints quality, process speed and reduced equipment cost have determined the success of the process and its large application in different industries for the welding of axle shafts and stems.

1.3. Porthole Die Extrusion

Porthole Die Extrusion (PDE) is the standard production technique for hollow profiles extrusions in the aluminum industry. Tubes and profiles produced by this process are generally limited to a specific number of alloys, as EN AW-6060 and EN AW-6082 [10]. However, PDE of other low-alloyed materials, as S900A and Armco-iron [11], is also possible.

Porthole extrusion is used to produce hollow unsymmetrical shapes in aluminum alloys.

The metal is forced to flow into separate streams around the central bridge, which supports a short mandrel thus creating two or more different material flows. Then, the separated metal fluxes are brought together in the so-called welding chamber (Figure 5), due to its peculiar geometrical characteristics leading to an increase of pressure between the flows. Therefore, solid bonding occurs in the welding chamber due to the simultaneous effect of temperature and pressure applied for a time depending on the material velocity in this area. Since the separate metal streams are jointed within the die, where there is no atmosphere contamination, a sound weld can be obtained [12]. When small dimensions are being extruded, multi-hole die can be used.

Porthole extruded parts often show an excellent ratio between part integrity and manufacturing costs.

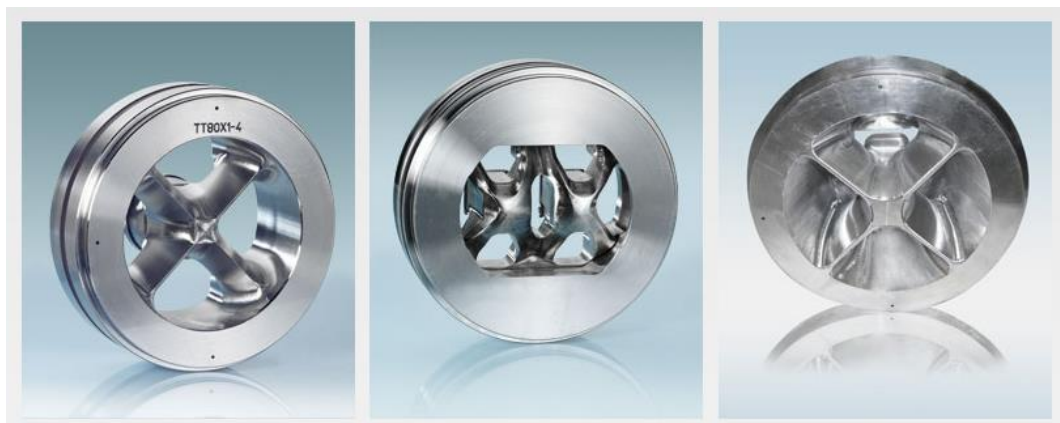


Figure 5. Porthole Dies Extrusion [13]

Moreover, due to the peculiar process mechanics, further advantages can be found with respect to the seamless extrusion method. In fact, the use of porthole extrusion dies also allows the production of tubes with larger diameters.

2. Linear Friction Welding

Linear Friction Welding (LFW) is a solid state welding process in which the joining of the two parts is achieved through the intimate contact of plasticized layers constituting the specimens interface. These layers are plasticized by a combination of applied force and frictional heating, occurring when reciprocating linear motion is generated between the two adjoining parts (Figure 6).

Linear Friction Welding was patented in 1929 [14], but the description of the process was unclear. The revised concept was recorded in 1960, but it was still unclear due to the difficulty in generating the reciprocal linear motion [15]. The Caterpillar Tractor Company [16] spoke of this process in a patent. However, the patent was focused on the machine that generates the linear reciprocating motion and not on the process of welding. In fact, a patent search has shown that there are no currently valid patents that protect the foundations of the LFW process.

The process is currently established as a niche technology for manufacturing bladed disks (blisks, Figure 6), especially using titanium alloys [17] [18] [19] in aircraft engines; furthermore, the same process is under development for assembling nickel-based super-alloys [20]. However, the interest in the process is growing, especially for applications where other alloys or non-metallic materials are used.

Therefore, the aim of the following chapter is to provide an understanding of the process of the LFW.

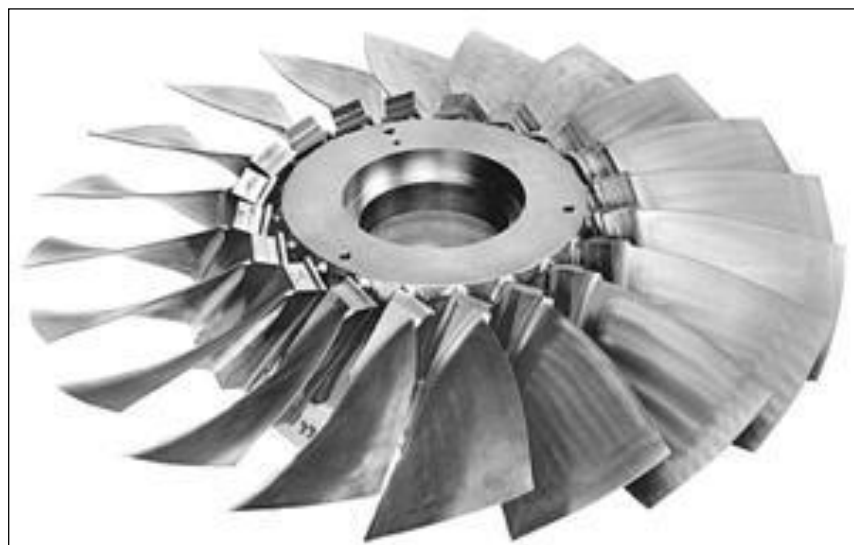


Figure 6. Bladed disk by LFW process [21]

2.1. Process description

When a reciprocating motion occurs under an assigned pressure, a significant amount of heat is produced. Due to the concurrent effect of oscillation and pressure, the material at the interface is forced to flow out of the joint. Part of this plasticized material, called flash, is removed during welding. In this way, any pre oxidized surface and other impurities are removed through the flash, allowing intimate contact between the materials and the creation of the joint.

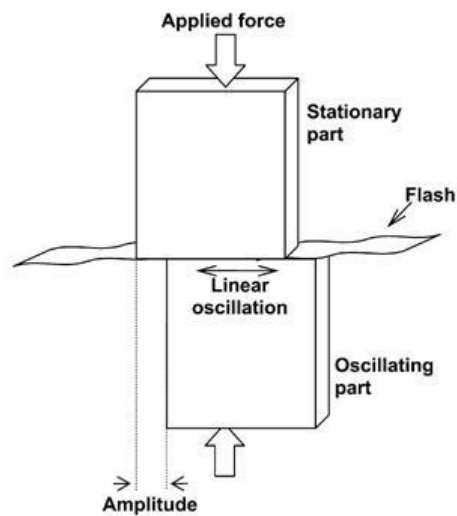


Figure 7. Diagram of Linear Friction Welding process [22]

Different phases can be identified during the process (Figure 8).

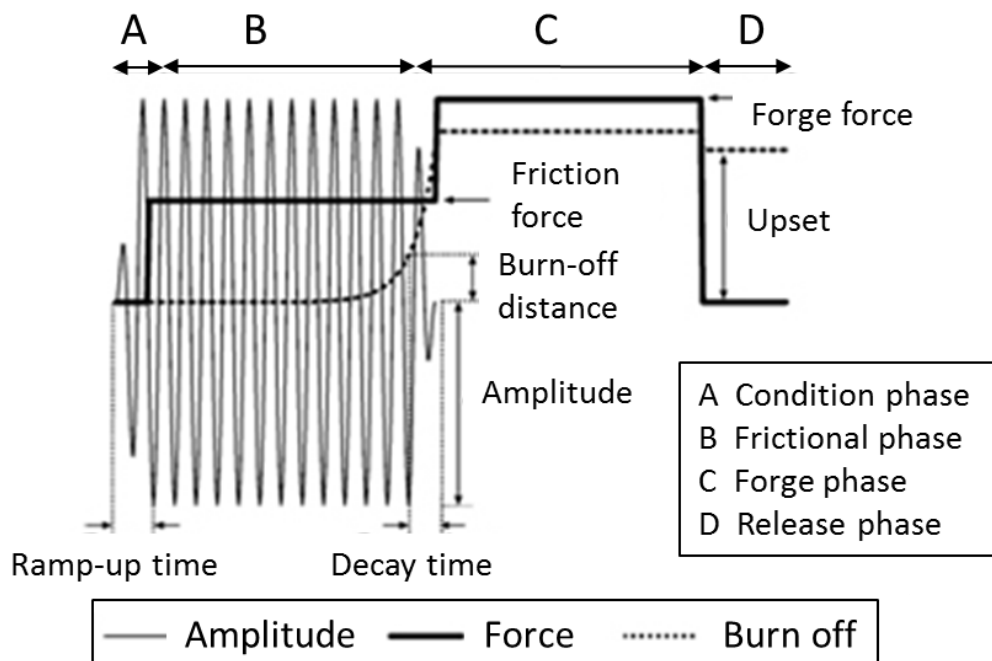


Figure 8. Schematic representation of the LFW parameters [22]

- 1- **Datum and Retract.** The specimens are clamped together under a small compressive force in order to determine the specimen position and set the machine zero (*datum*). The specimens are then retracted in order to leave a small separation distance between the pieces (*retract*).
- 2- **Conditioning Phase:** the oscillatory motion of one specimen begins, and the parts are placed in contact with a small force [18] for an assigned time.
- 3- **Frictional Phase:** the compressive action increases up to a set value generating heat at the interface. The material at the interface softens and flows out from the joint as flash. This loss of material from the welding zone, causes an axial-shortening of the pieces (called *burn-off*). This phase ends when the burn off reaches a predetermined distance. Due to the crucial role played by this phase for the effectiveness of the process, a deeper analysis can be performed. In particular, The *Frictional Phase* can be further divided into three distinct sub-phases, depending on the behavior of the material [22] [23] (Figure 9).

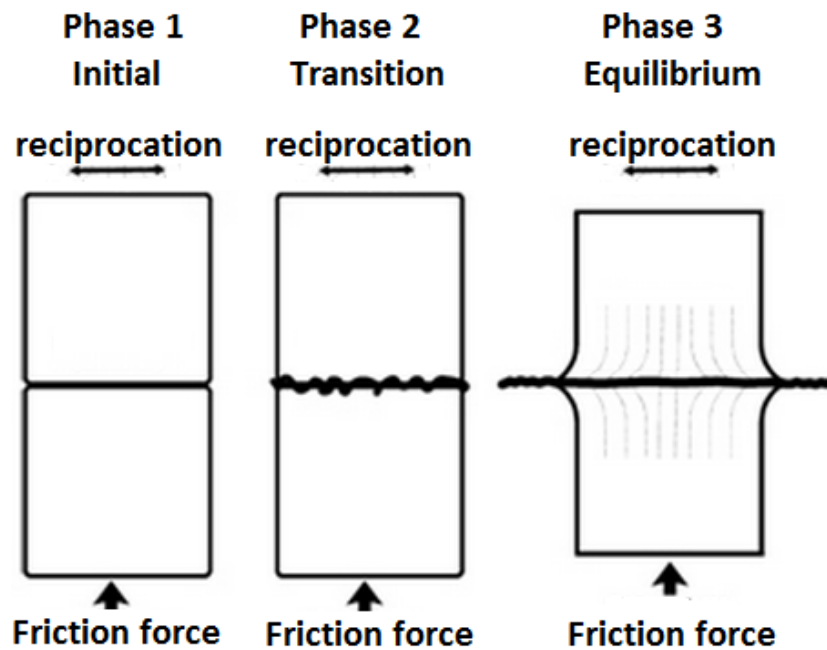


Figure 9. phases of LFW process [22]

- **Initial Phase:** At the beginning, the two materials are put into contact under pressure. During this sub-phase, heat is generated due to the peaks and valleys rubbing. The actual contact area significantly increases due to the wear of the roughness and no axial-shortening of the specimens is present. If the frequency of the alternative motion is too low for a given axial force, the generated heat is insufficient to

compensate the losses for conduction and irradiation. This condition does not allow the material softening, causing the failure of the passage to the next sub-phase.

- *Transition Phase*: if sufficient frictional heat is produced in the previous sub-phase, the temperature at the interface increases and, consequently, the resistance of the material decreases. Some particles begin to be expelled at the interface and the Heat Affected Zone (HAZ) expands. The real contact area is considered to be 100% of the cross section. In these conditions of temperature and pressure, the axial load is overly high for the plasticized material.
 - *Equilibrium Phase*: the plasticized material is ejected from the interface as flash due to the oscillatory motion and the applied pressure. During this sub-phase the axial shortening of the specimens begins as a consequence of the ejected material. In the softened area of the interface a uniform weld bead (i.e. flash) is formed. Instability may appear at this stage, due to an irregular temperature distribution. If temperature increases too much, an excessive extrusion of plastic material is obtained.
- 4- **Forging Phase**: the relative motion is stopped instantly, and the specimens are aligned very quickly. Usually a forging strength is applied to consolidate the welding. The force is maintained for a time set to consolidate the joint. The force value can be equal to or greater than the friction force.

An important feature of the LWF process, as well as for others friction welding processes, is that it does not present any fusion of the parts to be bonded. In this way, the junction takes place in the solid state [15] [24], with several advantages over fusion welding techniques often characterized by well-known solidification problems (e.g. porosity, hot cracking, segregation, etc...). Moreover, for many materials, the strong deformations in the weld region during the welding enable recrystallization phenomena, resulting in a fine microstructure and in enhanced mechanical properties with respect to the base material [17].

Other benefits include the speed of execution of the process itself (e.g. less than 10 seconds for the Ti-6Al-4V4 and about 1.5 seconds for aluminum alloys) and

its good repeatability. Due to the expulsion of oxides during the movement, controlled atmosphere is not required even when welding reactive materials as titanium alloys.

On the other hand, one of the main drawbacks of the process is the high cost of the equipment. In fact, the process is generally limited to niche applications such as the production of bladed disks for aircraft engines. However, the machines used for the process have undergone a significant reduction in costs and this can lead to a wider industrial application of the process. Finally, a further disadvantage of the process is that it can be noisy [25].

2.2. Machine requirements

As it arises from the process description, a number of variables must be taken into account when designing LFW experiments. In the following, the most important process variables are listed and briefly described:

- *Frequency*: number of oscillation cycles per second, usually ranging from 20Hz to 100Hz;
- *Rise time*: used time to increase the welding parameters up to the desired level (Figure 8).
- *Width*: maximum oscillating amplitude of the specimen from its equilibrium position, usually ranging from 1 mm to 5 mm.
- *Friction pressure*: pressure applied during the frictional process phase. This pressure is calculated using the contact nominal area at zero amplitude.
- *Burn-off distance, time or cycles*: specimen axial shortening, or time/cycles during which axial shortening occurs.
- *Deceleration time*: time necessary to reduce to zero the amplitude before the beginning of the forging phase.
- *Forging pressure*: the pressure applied during the forging process.
- *Forging Time*: time for the application of the forging pressure.

Other important parameters, which cannot be directly input but depends on the previously listed process parameters include:

- *Shear force*: parallel force to the oscillatory movement. It depends by friction pressure and friction factor (i.e. the used materials);

- *Burn-off Speed*: shortening velocity, i.e. the gradient of burn-off curve (Figure 8).
- *Welding time*: total welding time of a workpiece

Based on the relevant number of process variables influencing the final results, it appears clear that LFW machine design is quite complex and challenging. Besides allowing for the needed ranges of motion and offering the possibility to set and monitor the listed variables, they must be characterized by proper stiffness in order to assure process repeatability and reliability. Due to the oscillatory motion, significant inertial forces and vibrations occurs during the process, with potential detrimental effects on the final product quality.

Finally, it is worth noticing that a critical aspect of the machine design is the *Tightening of the Parts*: the specimens must be held by an equipment designed to withstand the forces encountered during the process. The preparation of the samples and of the tools is a critical step for the process: generally, the equipment is tailored to suit the particular geometries of the sample.

2.3. Current state of the art

Few information is available in literature about LFW, as only a few pioneering studies can be found. However, a major interest is rising nowadays, especially in the aeronautics field, where the Buy-to-Fly ratio, i.e. the weight ratio between the weight of the raw material used for a component and the weight of the component itself, is a key factor.

Until now, most linear friction welding researches have been focusing on titanium. In this field, the research team of Vairis and Frost (University of Bristol) [18], is one of the most active groups. Additionally, a few papers can be found also on the **machine design**. This is a peculiarity of this process, for which a dedicated machinery is needed.

The first article of Vairis and Frost group (1998) [18] describes an experimental campaign on titanium alloy (Ti 6Al 4V). The article highlights the relations between the technological parameters, such as amplitude, oscillation frequency and the applied pressure (Figure 10).

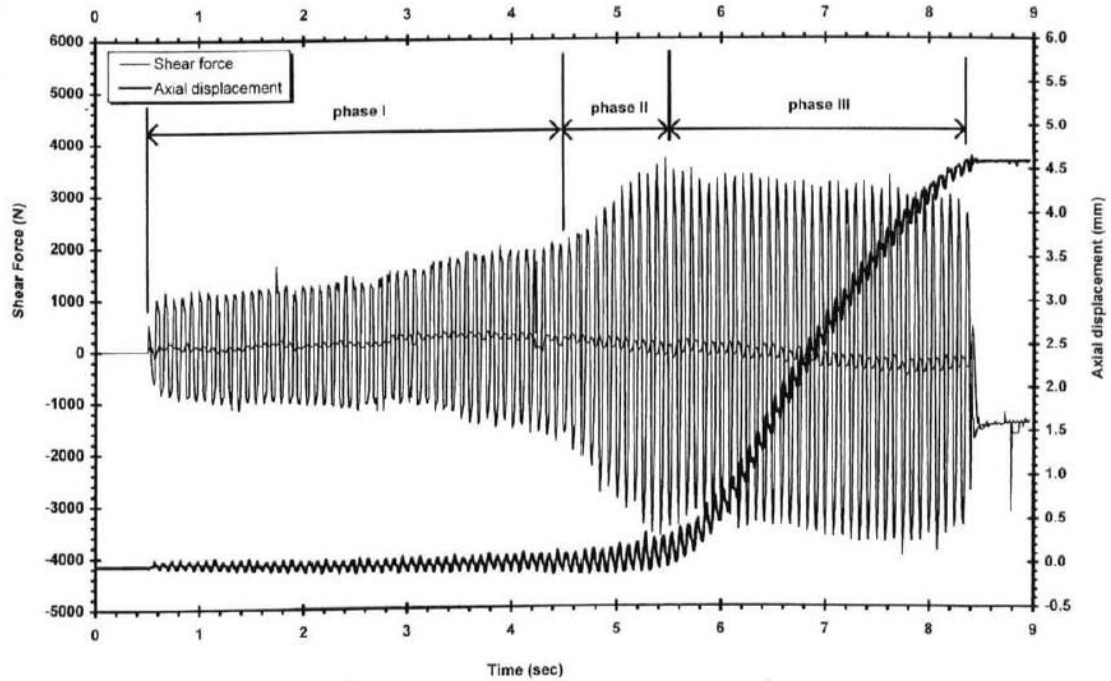


Figure 10. Shear force and axial displacement history (Ti 6Al 4V, amplitude of oscillation: 3mm, frequency of oscillation: 12 Hz, friction pressure: 42.9 MPa) [18]

In addition to the effect of the technological parameters, the paper also investigates the evolution of the material physical condition during the process. Finally the authors focus their attention on the importance of the minimum power required to obtain the weld.

The comparison of three control methods for a friction-welding machine has been carried out by Bayindir and Ates [26]. The conventional automatic control, based on a programmable logic controller, and peripheral interface controller systems were set up to design a friction welding machine. In the study, it has been observed that these systems worked successfully and the peripheral interface controller system showed the best performances.

As the **joints characterization** is regarded, a few papers can be found focusing on different materials. In the study of Mumin [27], an experimental set-up was designed and produced to achieve the friction welding of components having equal dimensions. The set-up was designed as a continuous drive, and the transition from friction to forging stage can be done automatically. In the experiments, high-speed steel (HSS—S 6-5-2) and medium-carbon steel (AISI 1040) were used to produce a mixed joint (Figure 26).

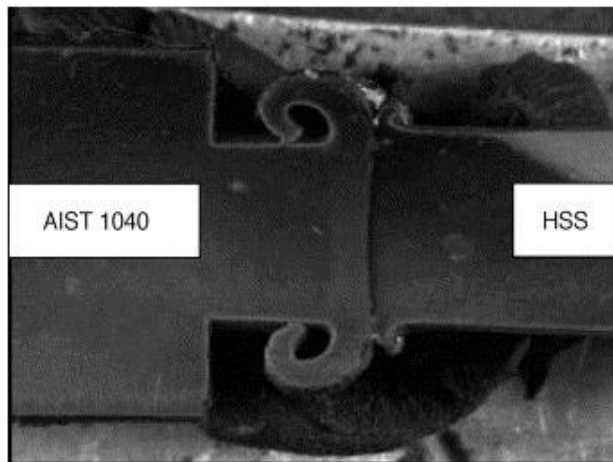


Figure 11. Macrophotograph of joint, as welded [27]

Post-weld annealing was applied to the joints at 650 °C for 4 h. Firstly, the optimum welding parameters for the joints were obtained. Later, the strengths of the joints were determined by tension, fatigue and notch-impact tests, and results were compared with the tensile strengths of materials. Then, hardness variations and microstructures in the post-weld of the joints were obtained and examined. Regarding the LFW process, Wanjara and Jahaz published a study on the morphological analysis, through scanning electron microscope (SEM), of the joints produced with different technological parameters [17] (Figure 12).

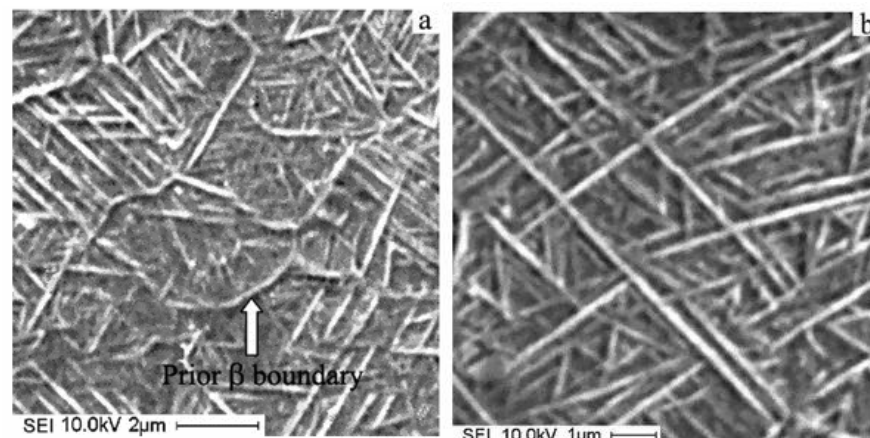


Figure 12. Scanning electron microscope image of the microstructure in the central weld region of Ti-6Al-4V produced by linear friction welding, showing a) the transformed beta grain structure having b) a Widmanstätten morphology [17].

Corzo, Torres, Anglada and Mateo [28] carried out a study of the fracture on the Linear Friction Welding specimens, taking into account of the titanium alloys used in aeronautical field. This research investigated the joint microstructure through a mechanical analysis of the heat affected zone, pointing out high hardness and also recrystallization of morphological structure. When the joint failure is located

on the welding line poor mechanical properties are found. For sound joints, the frail material breaks due to the trigger and diffusion of fatigue crack [29].

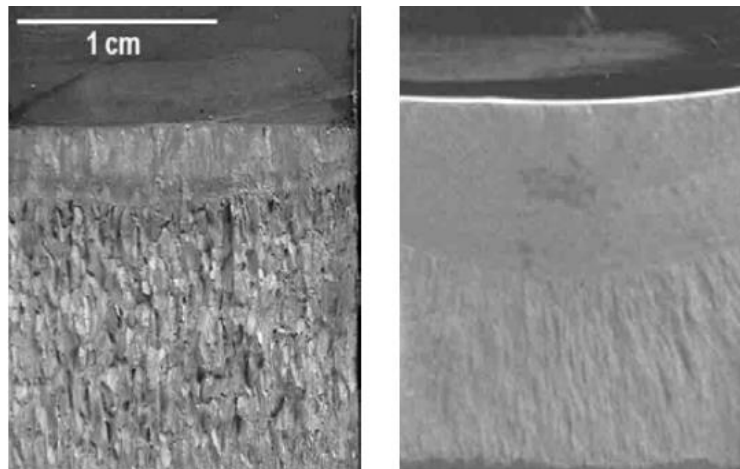


Figure 13. Fracture surfaces of toughness specimens [29]

Li, Ma, Zhang, Xu and Yang [30] studied the microstructure of the LF welded joint. The material used was the titanium alloy (Ti-6Al-4V) (Figure 14). The material extruded in the form of flash was studied, observing the hybrid material phase (composed of the alpha phase plus beta phase).

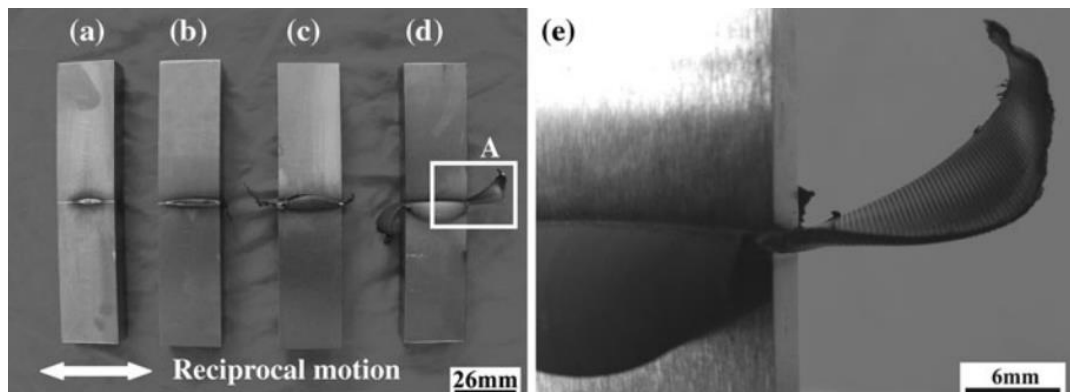


Figure 14. Fracture surfaces of toughness specimens [30]

Finer prior-beta grains were obtained in the flash as compared to the parent material. The authors show in the paper as some defects, namely kiss bonding and porosity, are expected in the joint when relatively low oscillation amplitude is selected. In turn, high oscillation amplitude generates a fully bonded joint.

A similar study was conducted by Tiejun et al. [31]. The authors investigated the location of the failure line during the tensile tests, demonstrating that for sound joints fracture is located in the base material zone, far from where welding takes place (Figure 15).

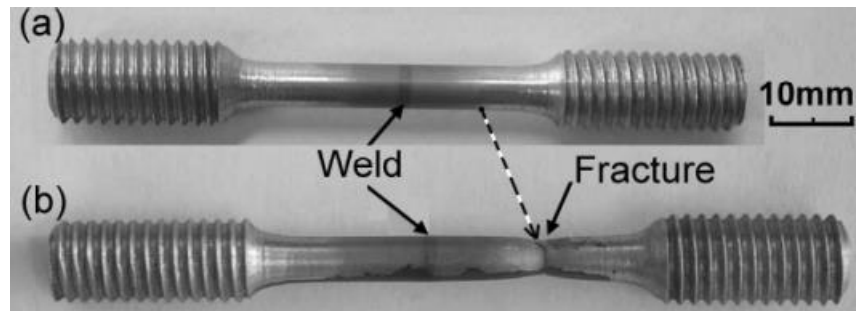


Figure 15. Photos of a tensile specimen before (a) and after (b) tensile test (slightly etched) [31]

The same analysis was conducted by the authors on steel (C45) [32], obtaining similar results to those achieved with the titanium alloy. In particular, also for this material, the existence of a region with a superfine structure in which there was a single material phase, presenting a hybrid phase in the TMAZ region (Figure 31).

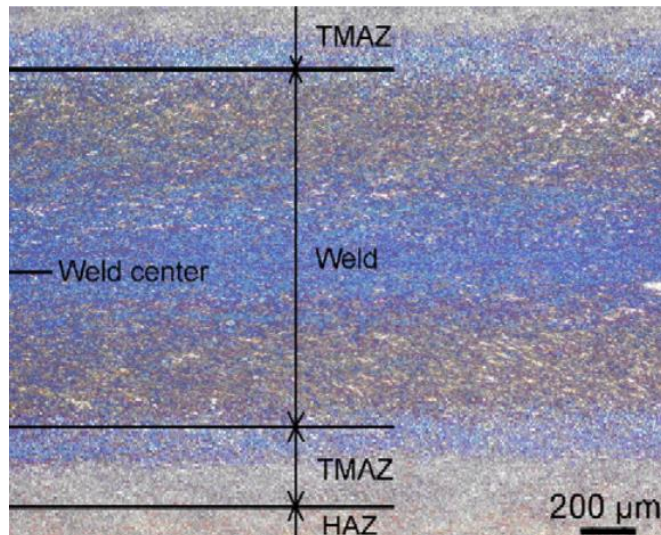


Figure 16. Typical OM micrographs of the cross-sections of linear friction welded 45 steel (etched) [32]

In the research of J. Romero et al. [33] a detailed investigation for the influence of the forging pressure on the microstructural, microhardness, and residual stress development in linear friction welded Ti-6Al-4V has been performed. In this paper, the energy dispersive synchrotron X-ray diffraction scans were performed in the three main directions across the welds to characterise the residual stress development (Figure 17).

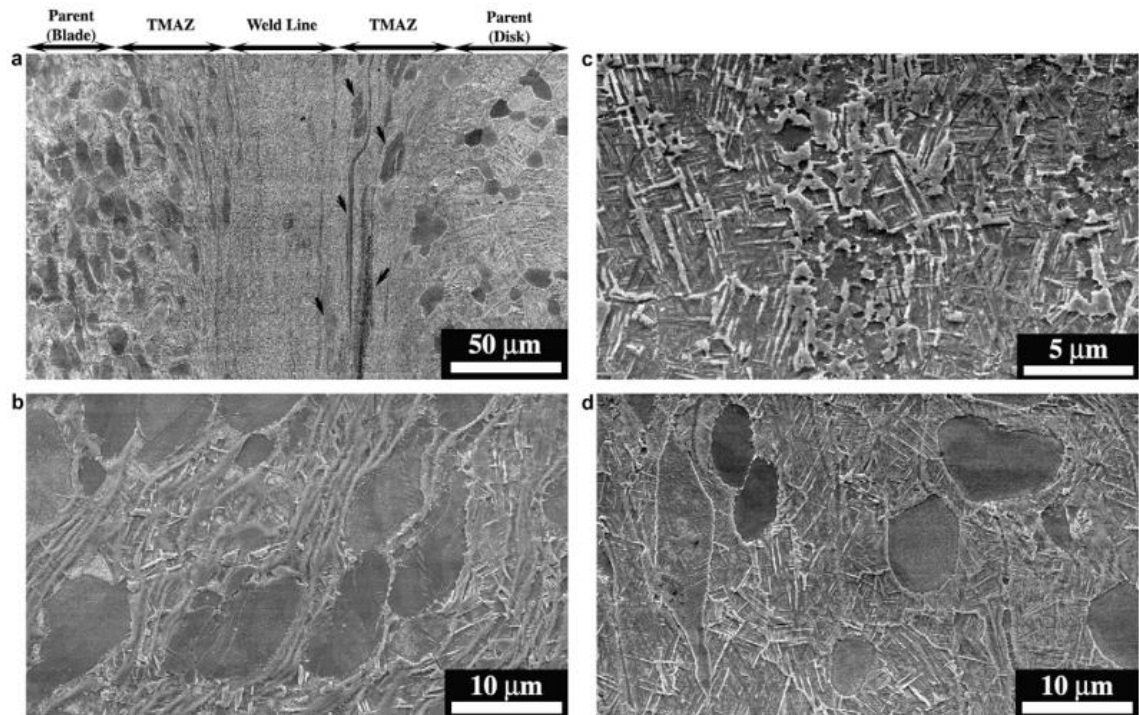


Figure 17. The TMAZ/WL microstructures in the 9P-LFW, showing (a) Typical microstructural zones in a linear friction weld (b) Blade Ti-64 TMAZ (c) WL (d) Disk Ti-64 TMAZ [33]

The experimental results identified a strong relationship between forging pressure, residual stresses and weld microstructure, whereby the residual stresses, the width of the weld region, and the α -Ti texture strength in the weld region generally decreased with the increase in forging pressure.

A study on superalloy was conducted by Chamanfar et al. [34]. Linear friction welding (LFW) was used to join the nickel-base superalloy, WASPALOY. Under the experimental conditions used in their investigation, temperature was recorded by inserting thermocouples at different locations from the weld interface, indicating that the temperature in the weld area reached up to 1280°C, which is at least 50°C below the melting point of the bulk alloy. However, this temperature is well above the liquation temperature of the low melting point components in the alloy (1245°C). As a result, liquation may occur in linear friction welded (LFWed) WASPALOY. Furthermore, according to the SEM and X-ray mapping results, LFW altered the chemical composition, morphology and size of the γ' precipitates at a location of 2mm from the weld interface (Figure 33).

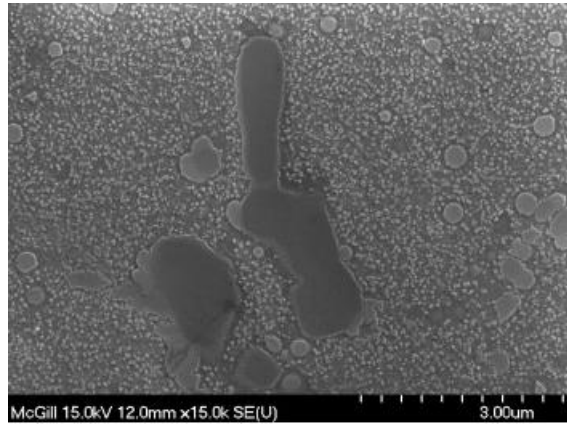


Figure 18. SEM image of the minor precipitates in the base metal [34]

It was determined that γ' coalescence at 2mm from the weld interface played a role in decreasing the microhardness (by 30%) relative to the base metal. A detailed examination of Titanium joint by Helm et al. [35] revealed the very fine microstructure directly in the weld plane that is characteristic of LFW. This fine microstructure evolves from the fact that the temperature during the process exceeds the β -transus in a small volume and that the cooling rate for this small volume is high.

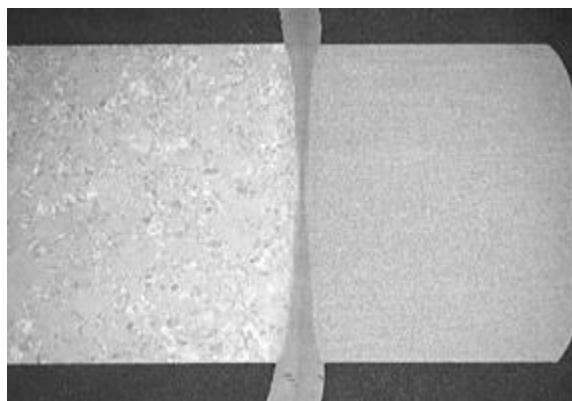


Figure 19. Macrograph of a welded block [35]

The investigation carried out by Mary and Jahazi [36] is focused on Linear Friction Welding of a widely used Ni-based superalloy, namely IN-718. Commercial blocks IN-718 alloy were linear friction welded under optimized processing conditions. In their paper, the evolution of the welded joint microstructure was investigated using optical and scanning electron microscopy (Figure 20).

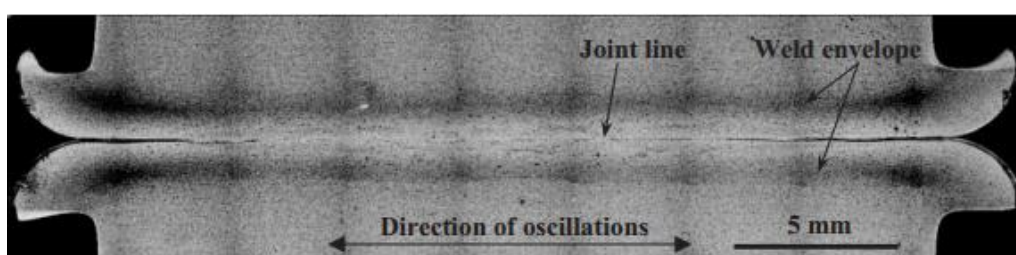


Figure 20. SEM image of the minor precipitates in the base metal [36]

In particular, the visual examinations and macroscopic observations of microstructure evolution in the transverse section revealed a specific shape and a dual nature for the flash due to the presence of oxide layers expelled during the beginning of the equilibrium phase from the parts interface.

Linear friction welded titanium alloy microstructures were investigated by B. Lang et al. [38] to understand the microstructural evolution in the joints. In particular, the material extrusion at the rubbing interface was investigated after complete transformation of alpha to beta phase. In this article the authors show that no dynamic recrystallization was observed in the thermo-mechanically affected zone. The authors conclude that some defects, such as kiss bonding and porosity, occurred in the joint at relatively low amplitude of oscillation (Figure 21).

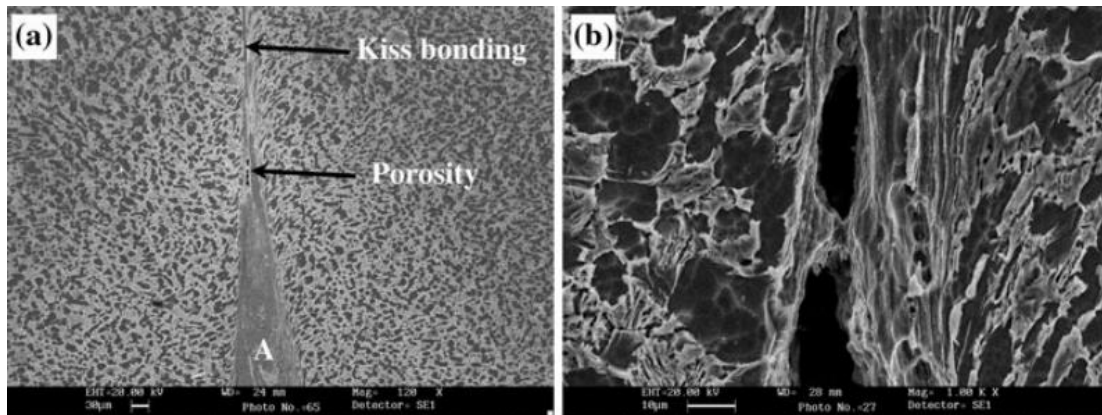


Figure 21. Microstructure of joints at 1.56-mm amplitude of oscillation a at relatively low magnification and b at relatively high magnification [38]

Therefore, relatively high amplitude of oscillation is more preferable for obtaining a fully bonded joint.

Only a limited number of papers were found on the LFW of **aluminum alloys**. In the paper by Tea-Sung Jun et al. [45], the study of residual strains in AA2024/AlSiCp linear friction welds was carried out using a novel approach based on eigenstrain (Figure 22).

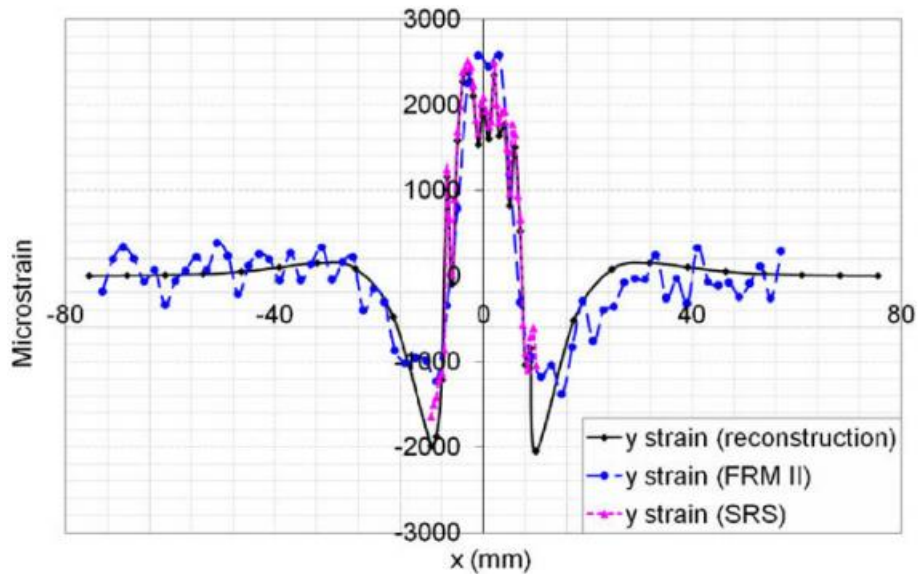


Figure 22. Comparison of the y-strain by experiment (SRS and FRM-II) and reconstruction [45].

Synchrotron X-ray and neutron diffraction were used to measure the interplanar lattice spacing in the welds and to deduce the residual elastic strains as a function of the distance from the bond line. The limited experimental datasets were combined with eigenstrain-based FE modelling in order to reconstruct the complete strain states in the entire components. The article shows that the approach based on eigenstrain is a powerful basis for reconstructing full-field residual strain/stress distributions in engineering structures.

The aim of the study of Rotundo et al. [46] was to evaluate the possibility of using the linear friction welding (LFW) technique to produce sound joints on a 2124Al/25 vol. %SiCp composite. The MMC joints were subjected to microstructural and mechanical characterization, including hardness, tensile and fatigue tests, without any post-weld heat treatment. In the articles it was shown that the joint efficiency was higher than 80%, both in respect to the ultimate tensile strength and fatigue strength (Figure 23) at 107 cycles.

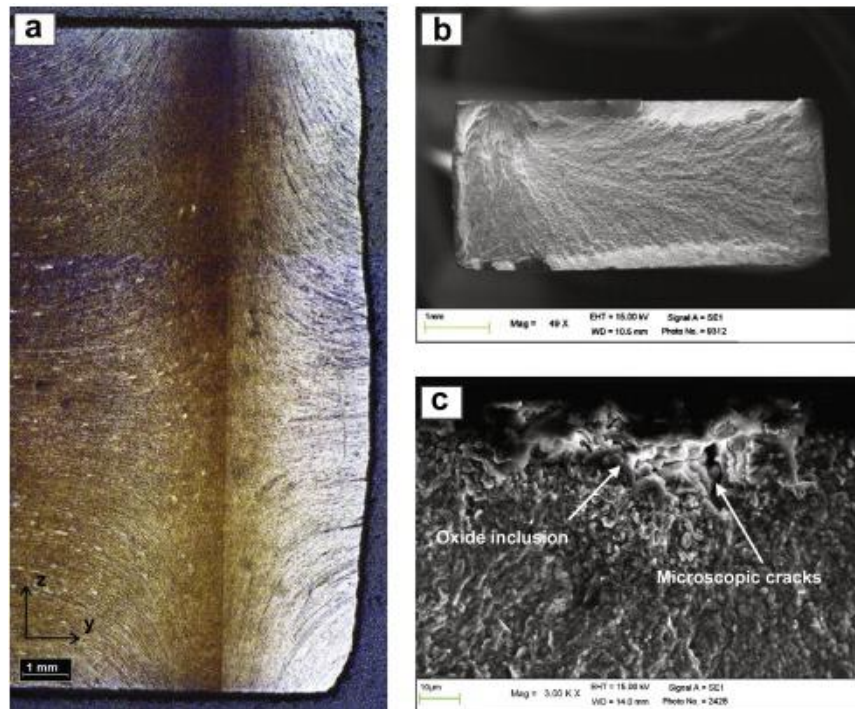


Figure 23. (a) Optical micrograph of a LFW joint showing the fatigue fracture zone; SEM micrographs of (b) low magnification fatigue fracture surface and (c) oxide inclusion and microscopic cracks in the nucleation zone. [46]

Furthermore, the authors have demonstrated that the fracture occurred in the Thermo-Mechanically Affected Zone (TMAZ), with a relevant reduction in the elongation to failure.

Finally, as far as **numerical modeling of LFW** is regarded, again an extremely limited number of papers is found in literature. The most complete article in literature about numerical modeling of linear friction welding is the one by Li and Ma [37]. LFW simulations of TC4 titanium alloy were conducted using ABAQUS/Explicit with a 3D and 2D models (Figure 24)

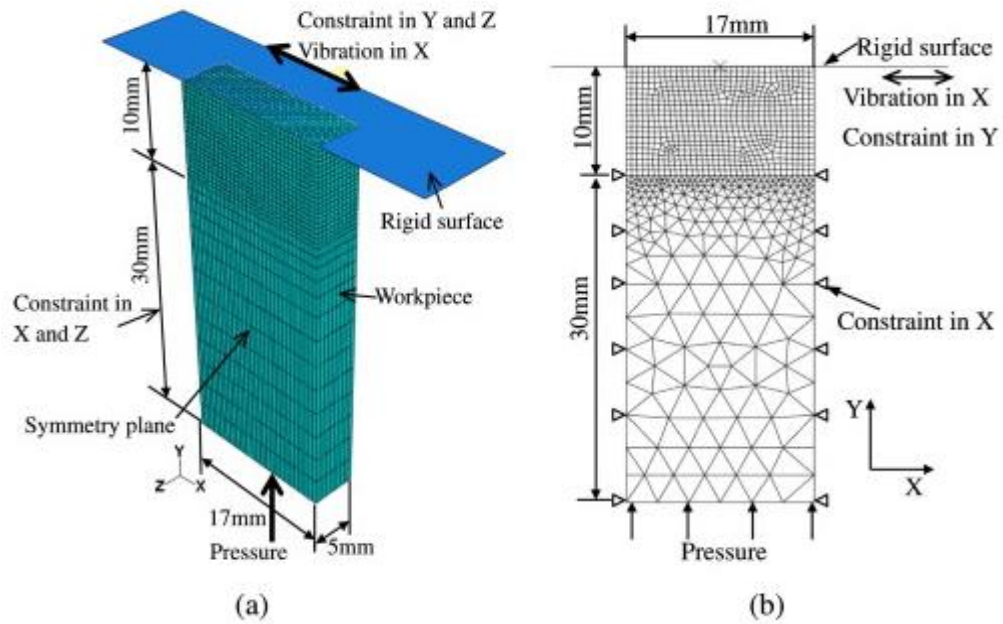


Figure 24. (a) 3D and (b) 2D models with boundary conditions and meshing arrangement [37]

The coupled thermo-mechanical analysis was performed with the Johnson–Cook material model. The effects of processing parameters, on the temperature evolution and axial shortening of LFW joints were numerically investigated. The article, shows that the temperature at the interface can first increase quickly to about 1000 °C within 1 s, then increases slowly, and finally tends to become uniform across the interface under certain processing conditions. Moreover, it is also shown that the axial shortening increases with increasing heat input almost linearly as the heat input exceeds a critical value.

Yamileva et al. carried out an analysis on the LFW numerical model efficiency in terms of CPU time. ANSYS and ABACUS commercial codes were used. A significant decrease of the process time was found when GPU is used as massively-parallel coprocessor. However, the model is developed for the elastic stage of the process (till the flow stress is reached) only. This aspect makes the model unusable for the prediction of the whole process.

From the literature analysis it arises that a lack of knowledge is still present in LFW. In particular, aluminum alloys have been only partially studied and an exhaustive numerical model for the process is still missing.

3. Prototype Machine

During the first doctoral year, a prototype machine for the LFW process was studied, designed and manufactured. The developed prototype has been undergoing several changes and improvements. In the following, the actual machine layout will be illustrated.

3.1. Machine description

3.1.1. Oscillation mechanism

A unique feature of the developed machine is that the reciprocating motion is obtained through a *desmodromic system*. This system consists of two cam-plate mechanisms, placed at the ends of the oscillating parts. The cams must be properly phased so that one cam maximum lift corresponds to a minimum of the other one and vice versa.

The term desmodromic derives from the Greek words "*desmos*" (bond) and "*dromos*" (stroke, course). In Applied Mechanics, this term indicates a kinematic mechanism whose reciprocating motion is controlled by a cam or leverage in both ways (no springs) (Figure 25) [52].

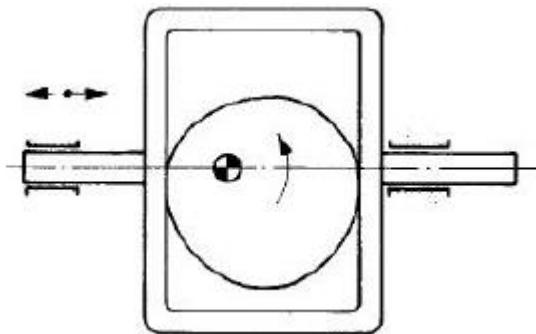


Figure 25. Schematic representation of a simple desmodromic system [52]

The spring absence reduces the contact force between the cams and the dynamic effects of the elastic yielding of the spring. This mechanism is used in some industrial machines, such as sewing machines and in the motorcycle field (Ducati Motor). The cams used in desmodromic mechanisms require a high precision and almost total absence of clearance. However, they have a higher cost and they are more complex to build, having the considerable advantage of allowing high speeds without encountering the gap between the cam and the

follower, i.e. the phenomenon called "*jump*". The system complexity makes the application of this mechanism feasible in niche areas except in rare cases, such as motorcycle field, where the Ducati has made of the desmodromic distribution system one of its strengths. In traditional systems, where the returning force is exerted by a spring, the spring preload has to be added to the resistant forces applied on the follower during the lift. In this phase, it is important that the resistant forces applied are not too high, since such forces must be overcome by the cam. In fact, in order to minimize the preload, the maximum acceleration during the return stroke is limited.

Compared to a traditional sprung-valve actuation, the desmodromic system is more complex to design, but avoids many drawbacks such as the excessive stiffness of the return spring due to the high forces involved. In order to avoid the detachment between the cam and cam follower (called "jump" phenomenon), the spring must be preloaded. In this way, the maximum force exerted by the spring is greater by at least 30-50% of the maximum external force (inertial force). In the case of increased safety factor, the margin can also be higher than 50%. In order to determine the spring stiffness is necessary to know the inertial and drag forces. In LFW, the resisting force is the force caused by the welding process: it is a frictional force, having a direction opposite the motion.

The trend of the resisting welding force, as a function of the cam1 rotation angle θ_1 , is shown in Figure 26. Based on preliminary tests, the maximum tangential force was determined equal to 5000N.

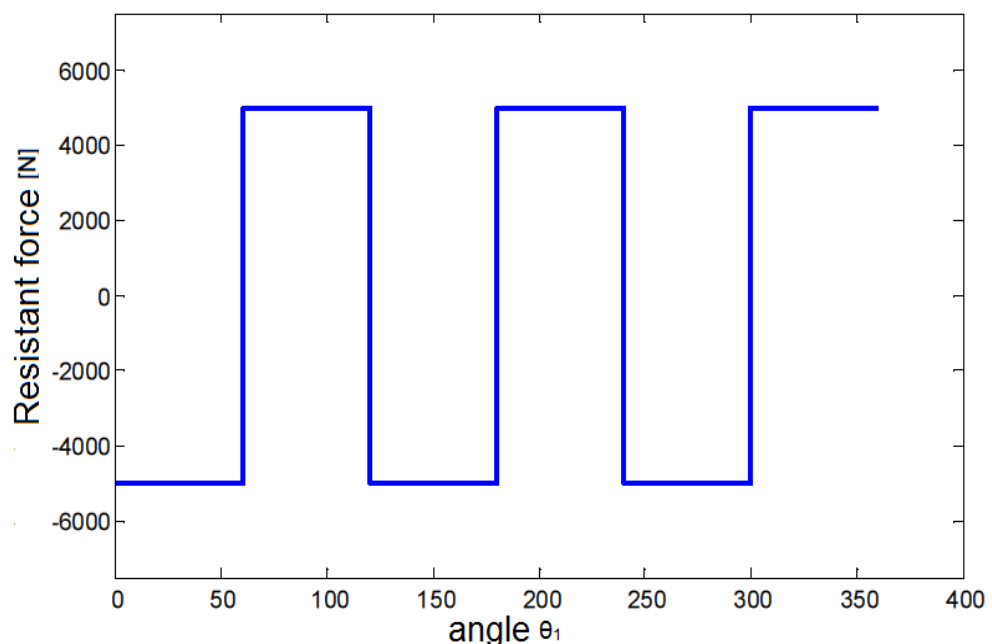


Figure 26. Resistant force as function of the reference angle θ_1

The inertial force was calculated based on the mass of the oscillating parts and the resulting force was determined (Figure 27)

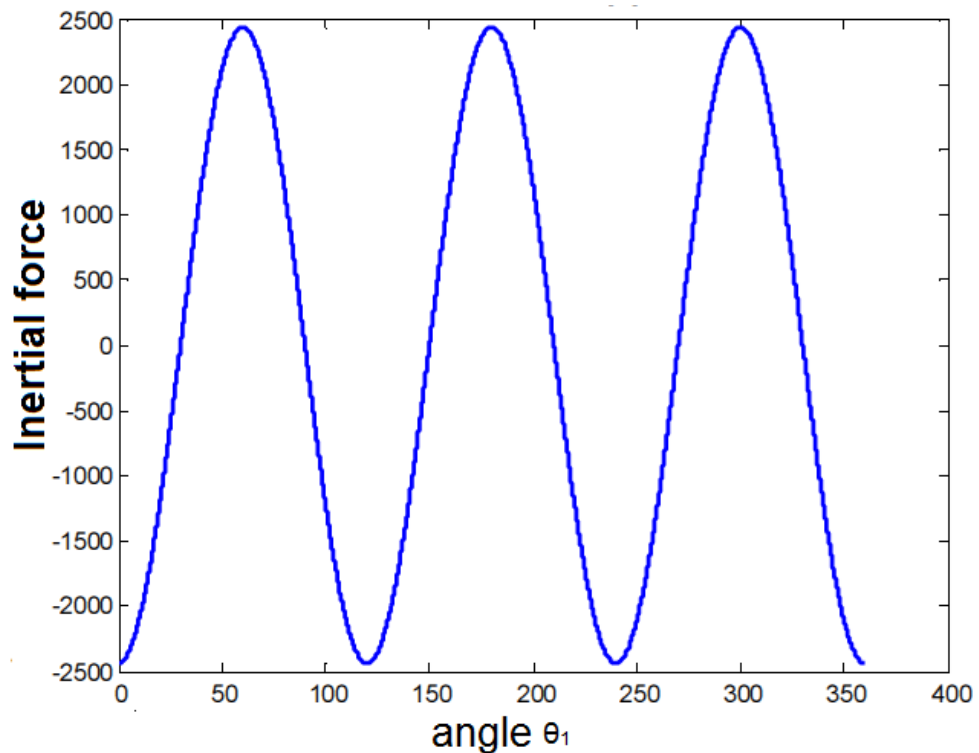


Figure 27. Inertial force as function of the reference angle θ_1

The total force the spring has to overcome can be finally obtained as sum of the two previously show components (Figure 28).

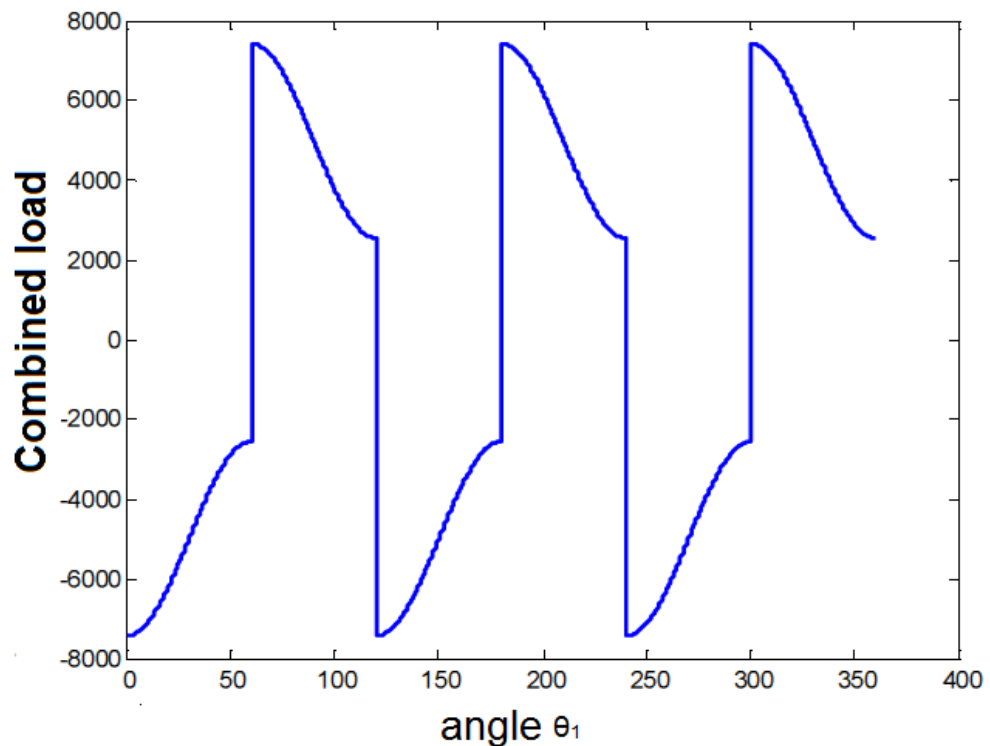


Figure 28. Combined loads on the follower as function of the reference angle θ_1

The maximum value of the total load transmitted to the cam follower is equal to 7438 N. Assuming that the cam is positioned on the left (generating a left to right movement), while the spring generates the right to left stroke, it can be stated that maximum load condition is reached when the cam is in the “dead center” right, corresponding to the maximum lift of the follower. In this configuration, the spring compression is equal to the maximum lift and the load to overcome is equal to the resistant force determined by the process.

The spring stiffness can be calculated as:

$$k = \frac{F_w}{h_{max}} = \frac{5000 \text{ N}}{6 \text{ mm}} = 833 \frac{\text{N}}{\text{mm}} = 8.33 \cdot 10^5 \frac{\text{N}}{\text{m}}$$

It is noted that the stiffness value is very high causing the problems previously mentioned. The value of the spring preload justifies the choice made (relatively to desmodromic mechanism). Adopting a safety margin of 30%, the preload is equal to:

$$\Delta F = 30\% F_{max} = 2231 \text{ N}$$

Where the initial spring compression corresponding is:

$$\Delta x = \frac{\Delta F}{k} = 2.7 \text{ mm}$$

Additionally, the preload value is very high thus entailing a considerable increase of the resistant torque. Hence, the main advantage of desmodromic systems consists in not having to win the spring preload during the lift and also in avoiding the onset of the follower float, typical of the engines valves. In fact, due to the high rotational speeds, the momentum of the valve can overcome the spring ability to close completely before a new cycle begins. In this way, the contact between the eccentric and the follower is no longer guaranteed [20].

3.1.2. Machine layout

Figure 29 shows a sketch of the developed machine.

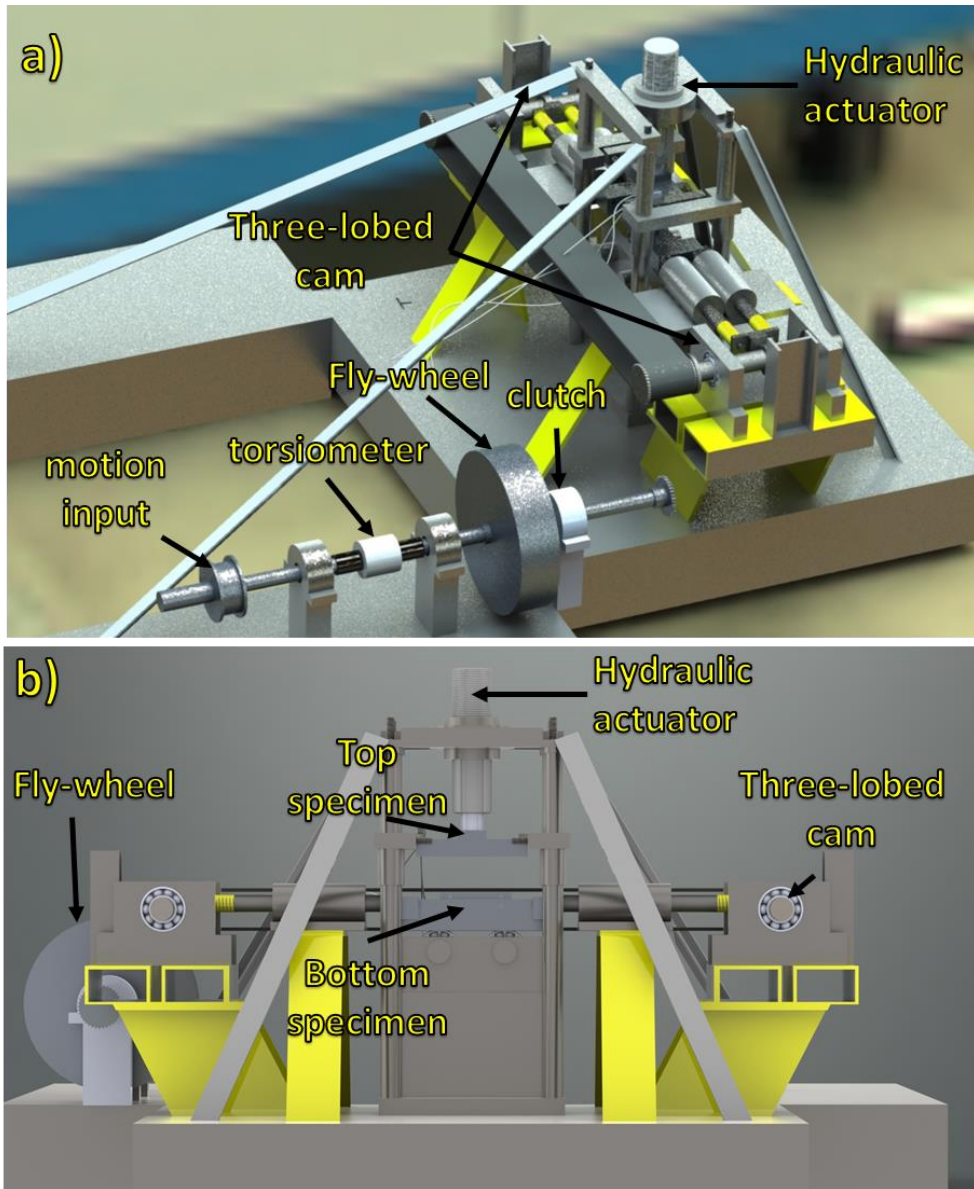


Figure 29. (a) Render of the developed machine and (b) close up of the specimens area

Two toothed pulleys are fixed on the two parallel camshafts (Figure 30) in order to allow the motion transmission and the correct phasing between the two cams.



Figure 30. Toothed transmission belt

Multi-lobe profiles were used for the cams in order to increase the range of oscillation frequencies. In particular, two lobe and tri-lobe cams were used (Figure 31).

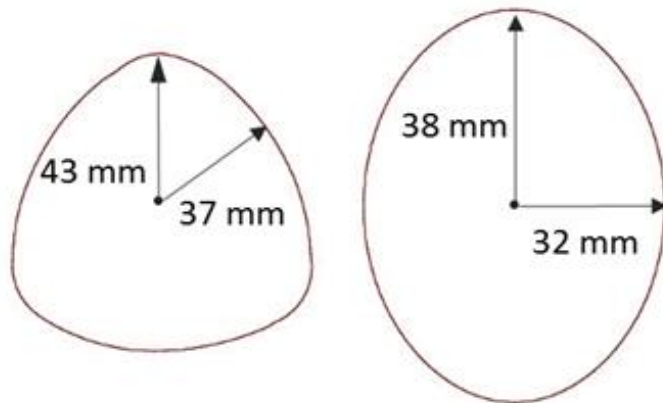


Figure 31. Geometry of three-lobed cam (left) and two-lobed cam (right)

The bottom specimen holder is located between the two followers. Two preloaded springs, preventing sudden machine failure due to the incorrect cam phasing, are interposed between the plates and the bottom specimen holder.

The top specimen is fixed to a hydraulic actuator capable of ensuring loads up to 15000 kN. An appropriate steel frame supports the system. The hydraulic actuator is connected to a hydraulic circuit providing the needed pressure between the specimens. A gear pump, able to ensure a pressure in the circuit ranging from 0 up to 25 bar, is used.

The Figure 32 shows a sketch of the hydraulic circuit.

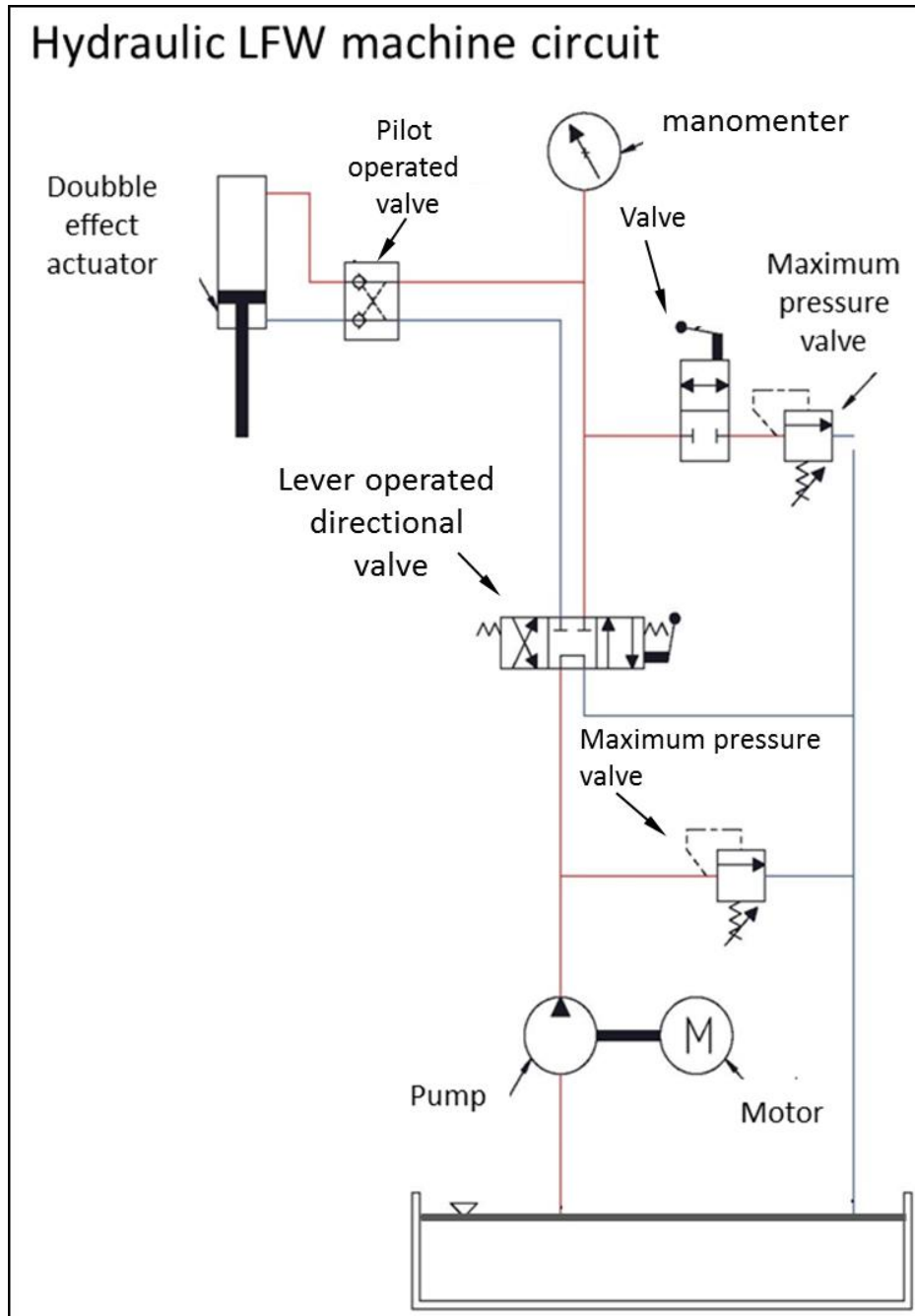


Figure 32. hydraulic circuit

The driving motion is taken from a lathe through a transmission trapezoidal belt. The belt is connected to the lathe by a pulley fixed on the lathe spindle, while it is connected to the LFW machine by another pulley fixed to a camshaft. In order to transmit the desired power, the pulleys have a double groove profile.

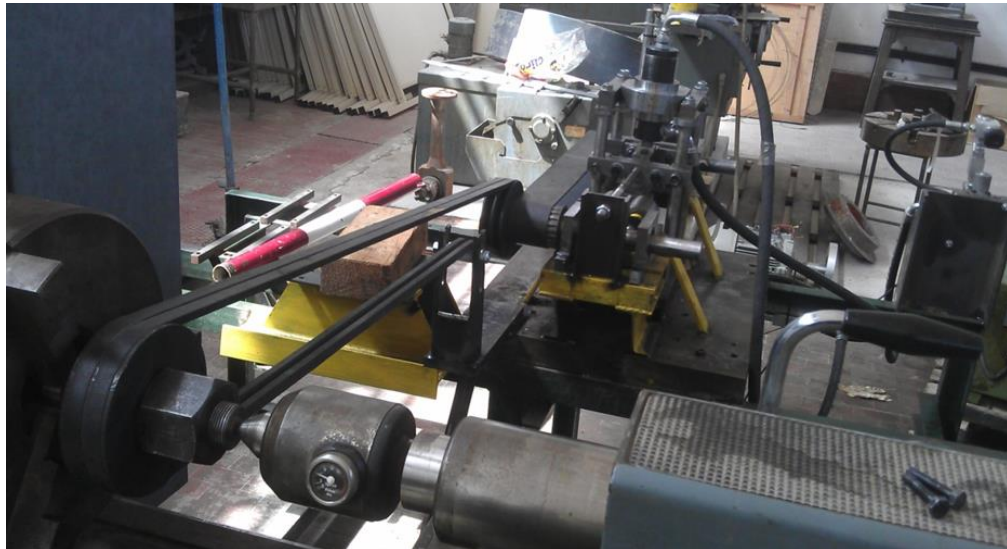


Figure 33. Transmission belt lathe-LFW machine

In order to avoid direct coupling between the lathe and the LFW machine, an intermediate shaft was utilized. In this way, the resistant torque variations coming from the LFW machine are not transmitted directly to the lathe. As a matter of fact, the resistant torque is variable in time and the torque peaks, resulting from a possible malfunction of the machine, are perceived by the lathe causing serious damage.

The additional shaft was connected between the lathe and the LFW machine. On the shaft, the following devices have been fixed:

- *A double groove pulley*, utilized to derive the power from the lathe;
- *A fly-wheel*, used to stabilize the resistant torque perceived by the lathe;
- *A speed-torque meter*, (“before” the fly-wheel in the kinematic chain) to measure the torque and the rotation speed of the intermediate shaft in order to assess the power absorbed by the machine;
- *A pneumatic clutch*, (“after” the flywheel in the kinematic chain) to allow the instantly stop of the reciprocating motion of the LFW machine.

In the following Figure 34 a sketch of the intermediate transmission shaft is shown.

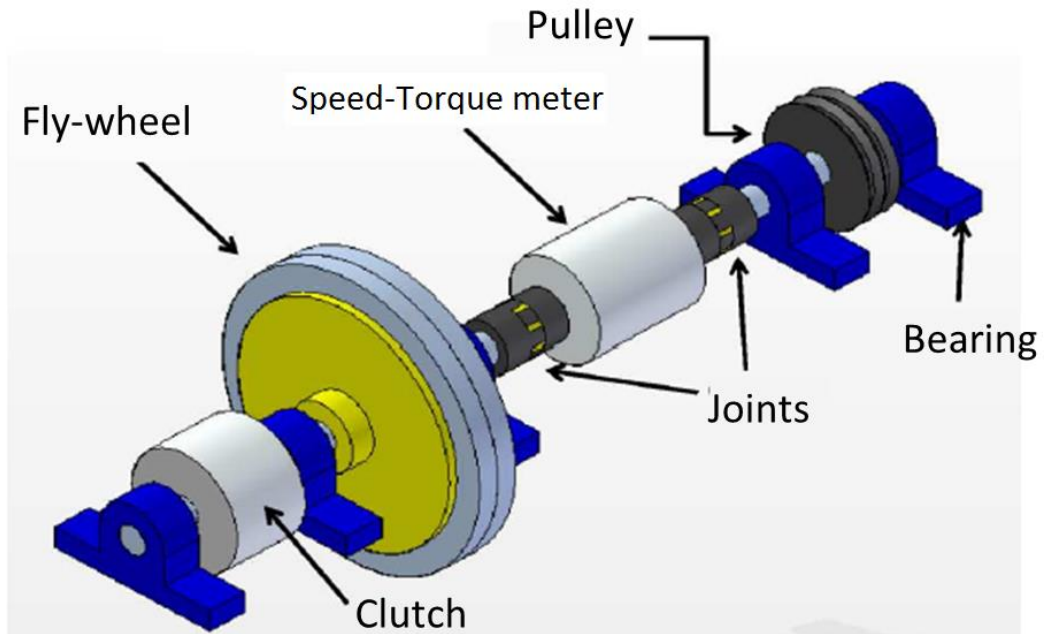


Figure 34. Intermediate transmission shaft



Figure 35. block diagram of the machine kinematic chain

The transmission ratio between the lathe and the intermediate shaft, namely T_1 is equal to 1. The transmission ratio T_2 between the intermediate shaft and the machine is equal to the ratio between the teeth number of the sprockets on the respective shafts. The number of teeth of the sprocket on the machine cam shaft was chosen smaller than the one of the intermediate shaft in order to increase the oscillation frequency range. The rotational speed permitted by lathe for the welding processes are as follows: 560-710-900-1120 rpm. The oscillation frequency of the tests was given by the relation:

$$f = \frac{n_{\text{lathe}}}{60} \cdot n_{\text{lobe}} \quad 1)$$

Since the transmission ratio between the lathe and machine in unitary, after changes, the oscillation frequency is given by the relation:

$$f = \tau_1 \cdot \tau_2 \cdot \frac{n_{\text{lathe}}}{60} \cdot n_{\text{lobe}} \quad 2)$$

In order to increase the oscillation frequency between the specimens and to limit the rotational speed of the lathe the transmission ratio T_2 was chosen so as to allow an oscillation frequency of 45 Hz when the lathe rotates at 710 rpm:

$$\tau_2 = \frac{60 \cdot f}{\tau_1 \cdot n_{\text{lathe}} \cdot n_{\text{lobe}}} = 1.268 \quad 3)$$

Since the chain drive is used, the T_2 will be also equal to:

$$\tau_2 = \frac{Z_{cf}}{Z_{cm}} \quad 4)$$

Although the number of teeth may be only an entire number a sprocket with 35 teeth to achieve the transmission was chosen. The effective transmission ratio is equal to:

$$\tau_2 = \frac{45}{35} = 1.286 \quad 5)$$

Finally a structural verification of the chain was made by calculating the maximum strain to which this is subjected and comparing it with the breaking load provided by the manufacturer. The maximum torque calculated is 64 Nm, and the sprocket diameter mounted on the machine input shaft is equal to 109 mm. The tensile strength provided by the manufacturer is 4900 N. The maximum load on the chain is equal to:

$$T_{max} = \frac{C_{max}}{R_{\text{sprocket}}} = 1174 \text{ N} \quad 6)$$

The maximum stretch of the chain to which it is subjected is quite lower than the tensile strength provided by the manufacturer, therefore the safety conditions are satisfied.

As far as the two coupled flywheels are regarded, they are placed ahead of the clutch, in order to obtain an instantaneous LFW machine motion arrest. It is worth noticing that it has not sense to put the flywheels after the clutch because once the transmission of power is stopped, the flywheel would continue to provide more energy to the machine thus rendering useless the action of the clutch.

Finally, in the next Figure 36 the clutch is shown. The device used is a pneumatic clutch "Comintec DSF / TF / AP 2.90" capable of transmitting a torque from 30 up to 125 Nm. The torque provided is a linear function of the air pressure with which the device is activated. Once the desired torque is selected, the control pressure of the pneumatic circuit is determined [47]. The clutch has also the function of torque limiter against torque peaks, thus securing the lathe and the other components. Air pressure equal to 9 bar was chosen in order to transmit a maximum torque of 114 Nm.



Figure 36. Pneumatic clutch

3.1. Kinematic analysis

Although an ideal desmodromic distribution has a clearance equal to zero, in practical applications a non-zero clearance value is needed. The introduction of the clearance results in a modified oscillation with respect to the expected theoretical one. In this paragraph, a detailed study of the actual motion of the oscillating specimen is illustrated. The study was carried out with a duplex target: the implementation of the actual motion in the developed numerical model (see the end of this chapter) and the quantitative evaluation of the stroke "loss" due to the clearance.

In the developed machine, the oscillation amplitude is controlled by the cams geometry. Once the cam profile is fixed, the stroke of the reciprocating motion is determined. During this study the selected cams allow for a maximum stroke of 6 mm (oscillation amplitude 3 mm).

The stroke diagram is therefore the one reported in Figure 37:

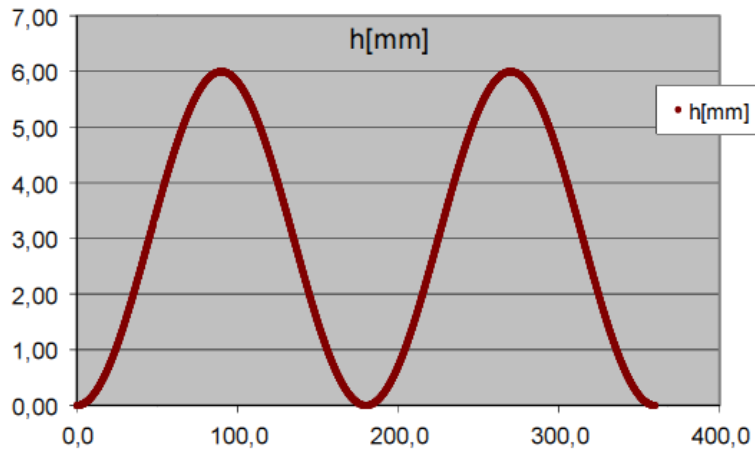


Figure 37. Displacements diagram

The oscillation frequency is determined by the cam rotational speed. The frequencies used in the LFW processes vary between 35 and 70 Hertz approximately. Three-lobed cams allow an oscillation frequency three times larger than the cam rotation frequency. In this way the shaft rotational speed, on which is mounted the cam, is limited thus protecting the spindle lathe used to provide the input motion.

As described in the previous paragraph, the oscillatory motion is given alternately by the two cams, properly phased to ensure that the lift phase on one side corresponds to a return phase on the other side and vice versa.

In the Figure 38, a schematic ideal desmodromic transmission shows the phase just described.

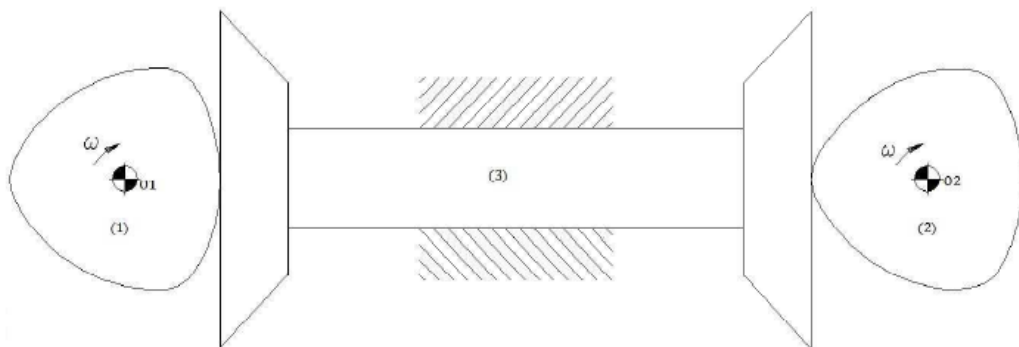


Figure 38. Schematic representation of the ideal desmodromic transmission

The motion equation of the plate-cam (1) respect to the rotational joint O_1 , has the following expression:

$$O_1C = R_b + s(\vartheta) \quad 7)$$

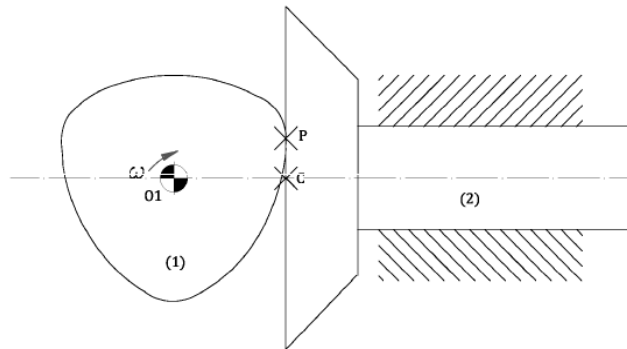


Figure 39. Real contact cam-plate

Where C is the point on the normal at the plate passing through the cam rotation center (Figure 39); R_b is the minimum cam lift and $s(\theta)$ is the plate motion as function of θ angle.

It is worth noticing that eq.7 is valid only if the closure force is guaranteed and in this specific case is alternatively ensured by the two cams.

For the kinematic analysis of the actual machine, two assumptions were introduced:

- The safety preload springs are rigid objects, i.e. no unwanted overload is present;
- Rotational speed and relative cam position are constant.

These last assumptions are met by the real machine. In fact the real welding process starts only when the machine has reached the predetermined rotation regime and not during transients.

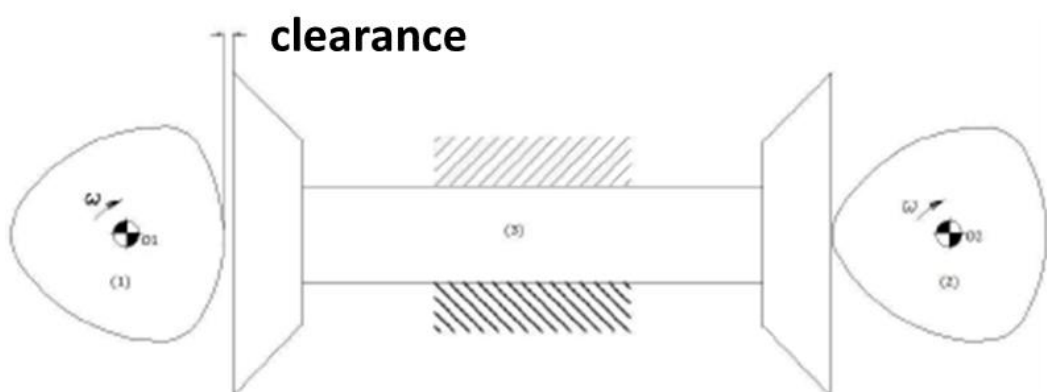


Figure 40. Schematic representation of real desmodromic transmission

A briefly described, in the actual configuration a clearance is needed (Figure 40). When cam (2) reaches the maximum lift, the cam is still in contact with the corresponding plate but is no longer able to move the plate. At the same time, cam (1) is not yet in contact with the respective plate but has the same angular velocity of the cam (2) thus maintaining the correct phase with respect to it.

According to the mechanism scheme, the oscillating object (3) has the potential to continue its motion toward cam (1) due to the inertial forces, and impact with the cam (1).

However, in the LFW process, after cam (2) detaches from the oscillating object (3), the velocity the latter is zero due to the resisting forces at the interface between the specimens to be welded. In other words the oscillation instantly stops once the contact with the cam ceases. In Figure 41, the position of cam (1) before and after the clearance recovery, is reported:

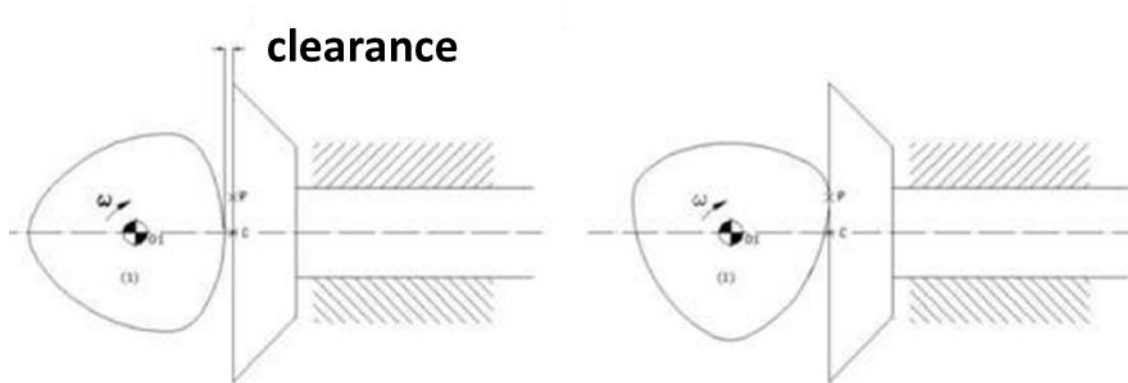


Figure 41. Clearance recovery

Assuming cam (1) as the driving one, the distance between O_1 and P constant (since the plate is stopped) and finally indicating with the subscripts "a" as initial phase and "b" as final phase of the mechanism, it is possible to write

$$O_1P_a = O_1P_b \quad 8)$$

$$R_b + gap = R_b + displ.b \quad 9)$$

but also it is possible to hypothesize that:

$$displ.b = clearance$$

Therefore cam (1) resume contact when the plate displacement required is equal to the initial clearance. From the "b" phase on, cam (1) will cause the displacement as if no clearance was present.

When cam (1) gives the maximum lift, cam (2) will be found at the minimum lift point (Figure 42).

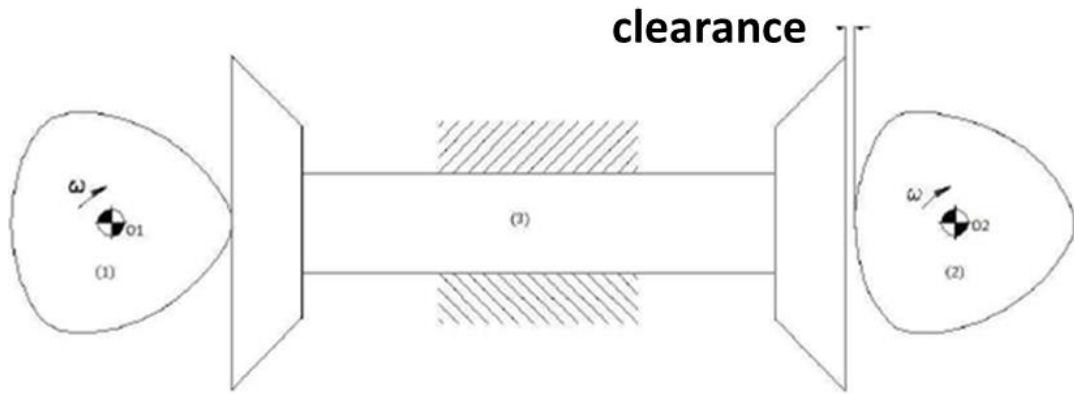


Figure 42. Cam clearance

Based on these considerations, it is possible to perform a numerical analysis studying the kinematic and dynamic mechanism.

The equations used are the ones of the mechanisms without clearance. There is contact between the cam and the plate, while during the recovery phase of the clearance, lift (h), velocity (h') and acceleration (h'') are zero because the plate is stationary. The equations governing the oscillation with no clearance are:

$$\begin{aligned}
 h &= \frac{h_{max}}{2} \cdot [1 - \cos(n\theta)] \\
 h' &= \frac{n}{2} \cdot h_{max} \cdot \sin(n\theta) \\
 h'' &= \frac{n^2}{2} \cdot h_{max} \cdot \cos(n\theta)
 \end{aligned}
 \tag{10}$$

In the equations shown, h_{max} is the maximum lift of the mechanism, n is the number of cam lobes, θ is the rotation angle of the reference cam. h' and h'' are Lagrangian derivatives with respect to the variable θ .

The relationship between the Lagrangian derivative and the time derivative is the following:

$$\begin{aligned}
 \dot{h} &= \omega \cdot h' \\
 \ddot{h} &= \omega^2 \cdot h''
 \end{aligned}
 \tag{11)$$

Where ω is the cam rotational speed expressed in rad/s.

MATLAB was used to carry out the numerical analysis. In the script, the following parameters were varied:

- *Maximum lift*
- *Clearance*
- *Number of lobes*

- Base radius
- Rotational Speed

Imposing clearance equal to zero and cam rotational speed equal to 710 RPM, the following h , h' and h'' are calculated. Additionally, the speed and acceleration of the oscillation object, as function of the rotation angle of the reference cam θ_1 , were calculated.

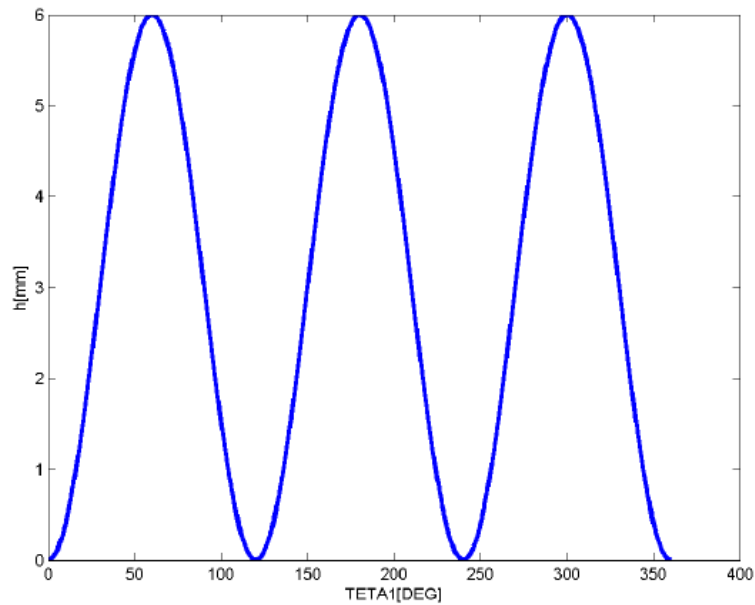


Figure 43. Cam (1) lift VS rotation angle θ_1

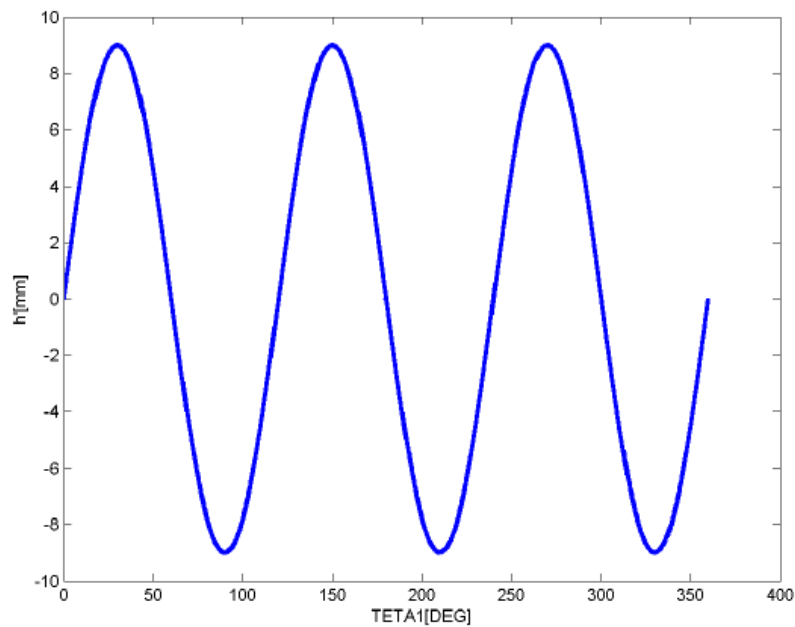


Figure 44. Cam (1) Lagrangian derivative (h') of the lift VS rotation angle θ_1

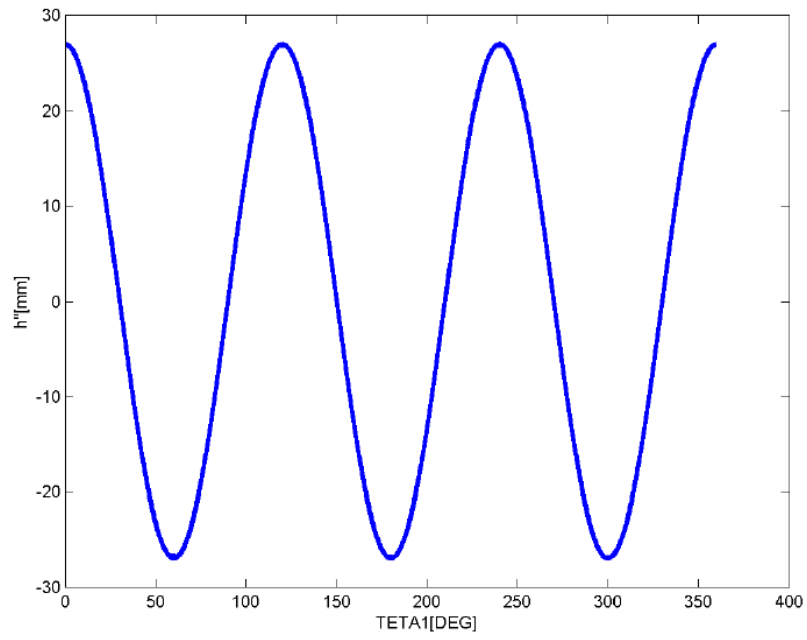


Figure 45. Cam (1) second Lagrangian derivative (h'') of the lift VS rotation angle θ_1

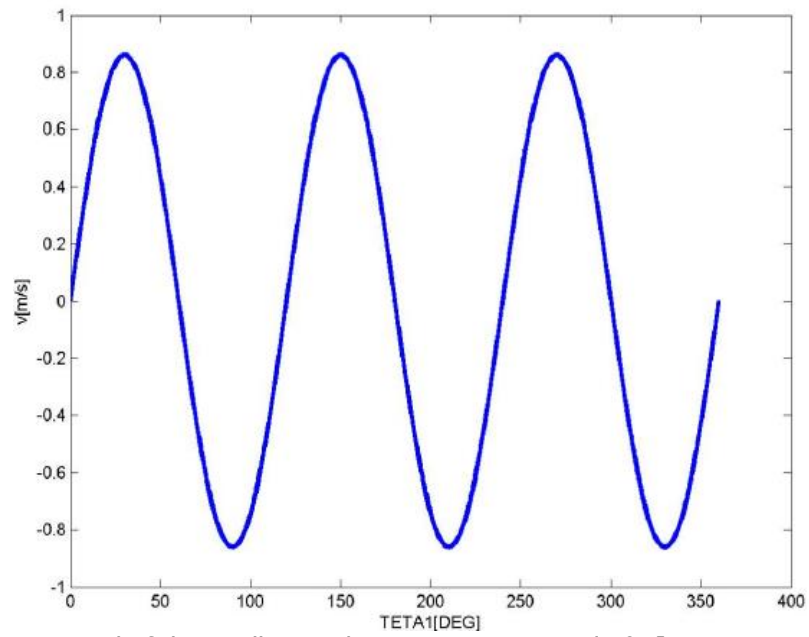


Figure 46. Speed of the oscillating object VS rotation angle θ_1 [cam rotational speed $n = 710$ rpm]

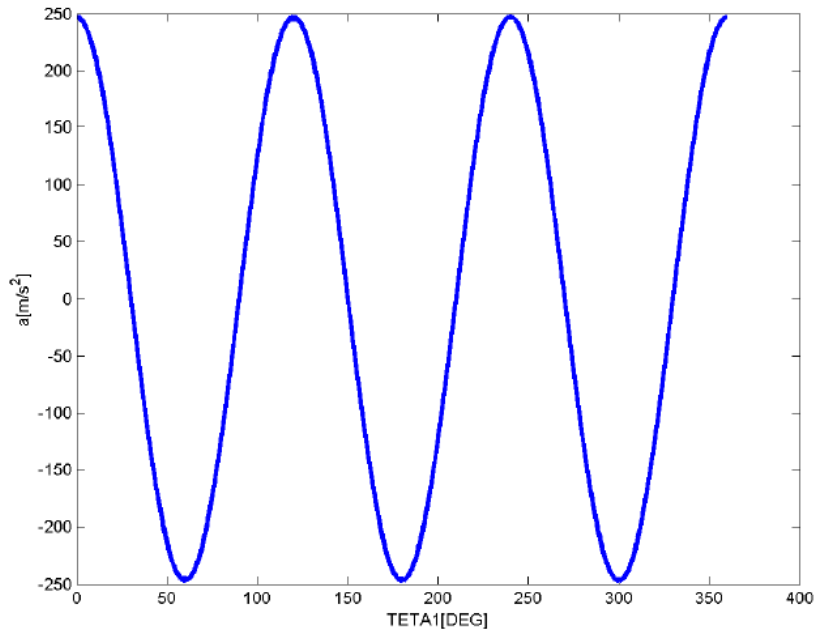


Figure 47. Acceleration of oscillating object VS rotation angle θ_1 [cam rotational speed $n = 710$ rpm]

The trends shown are typical for a harmonic motion. It is worth noticing that the maximum acceleration value is equal to 246.73 m/s^2 , i.e. 25 times the gravity acceleration.

The mechanism kinematics was studied including the effect of the real clearance of the machine, i.e. 2.2 mm. A cam rotational speed equal to 710 rpm was imposed. From Figure 43, through Figure 47 it can be clearly seen that lift, speed and acceleration are quite different from the previous ones.

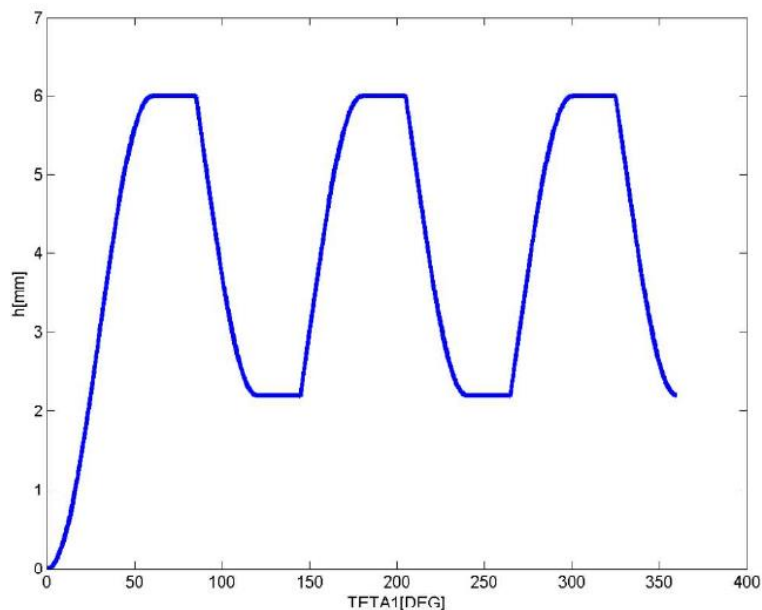


Figure 48. Cam (1) lift Vs rotation angle θ_1 – clearance=2.2mm

The oscillating object remains stationary for a certain period. This period is proportional to the initial clearance value. Therefore, the difference between maximum and minimum lift is decreased by an amount equal to the initial clearance. In this way a break, not present in the ideal diagram (see again Figure 48), is introduced in the lift diagram,

In the following Figure 49 and Figure 50, it is shown how the clearance affects the performance of speed.

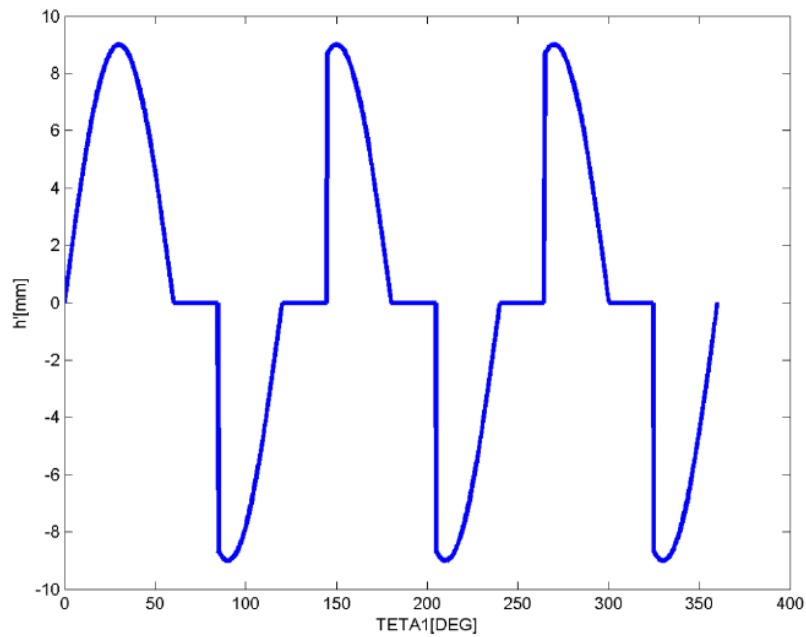


Figure 49. Cam (1) Lagrangian derivative (h') of the lift VS rotation angle θ_1

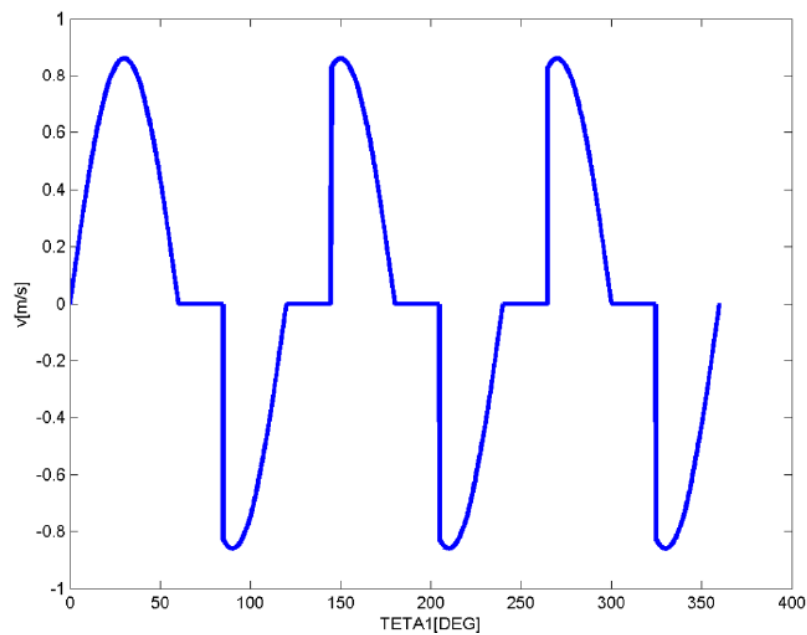


Figure 50. Speed of oscillating object VS rotation angle θ_1 [cam rotational speed $n = 710$ rpm - clearance=2.2mm]

It is noted that maximum speed remains the same with respect to the ideal case. From the graphs, it is clear that the recovery phase of the clearance is particularly delicate. As a matter of fact, the oscillating object velocity changes from zero up to maximum speed in a time theoretically equal to zero. For this reason, a bump between the cam and plate occurs. This impact will not be taken into account for the numerical analysis, while it will be evaluated in the experimental analysis of the machine.

Finally the acceleration performance is shown (Figure 51-Figure 52):

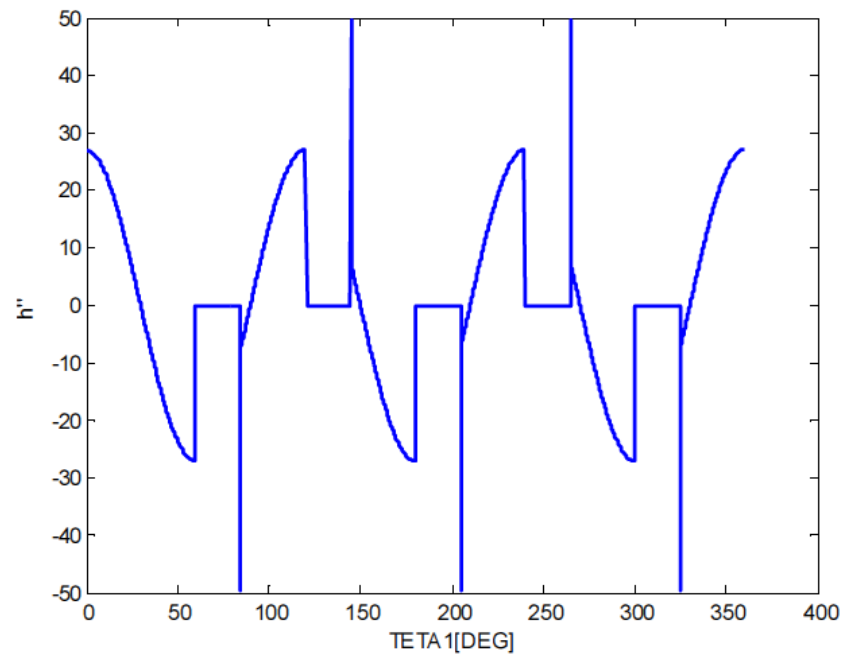


Figure 51. Cam (1) second Lagrangian derivative (h') of the lift VS rotation angle θ_1

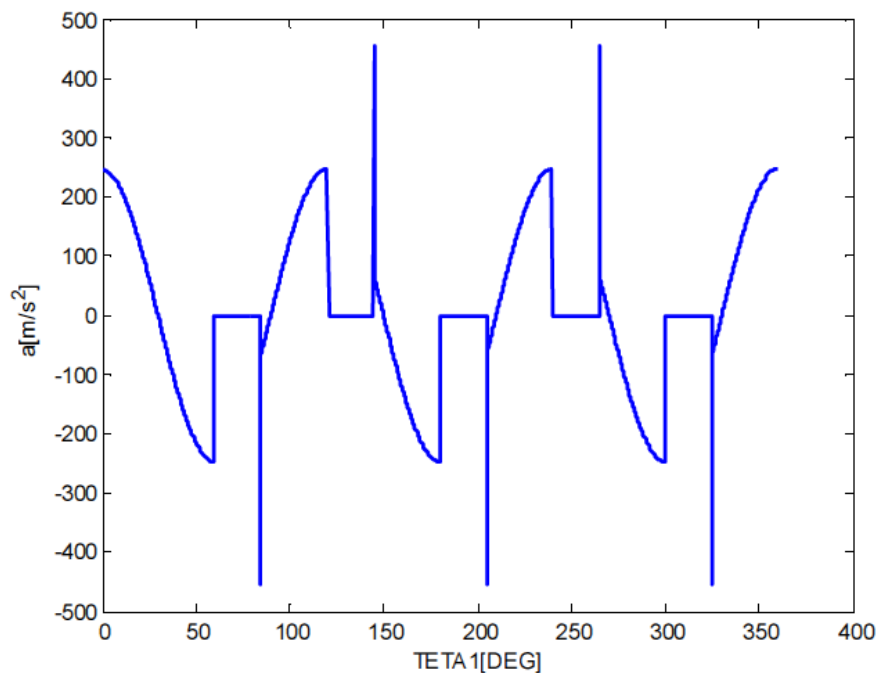


Figure 52. Acceleration of oscillating object VS rotation angle θ_1 [cam rotational speed $n=710rpm$ - clearance=2.2mm]

Similarly to the speed diagram, also the acceleration maximum value is the same as the ideal case. During the contact, the acceleration tends to infinite, as shown in Figure 51 and Figure 52. It is worth pointing out that the irregular and discontinuous acceleration affects the inertial forces.

Although the clearance determines changes in the displacement, velocity and acceleration of the oscillating object, the modified trends remain periodicals and then the mean value is zero. It is possible to evaluate the influence of the clearance through the calculation of effective value of the defined speed, as

$$h'_{rms} = \sqrt{\frac{1}{2\pi} \int_0^{2\pi} [h'(\vartheta)]^2 d\vartheta} \quad 12)$$

Eq.12 calculates the effective value of the Lagrangian velocity of the oscillating object. This value will be affected by the clearance. Figure 53 shows the influence of the clearance on the effective Lagrangian velocity (h'_{rms}).

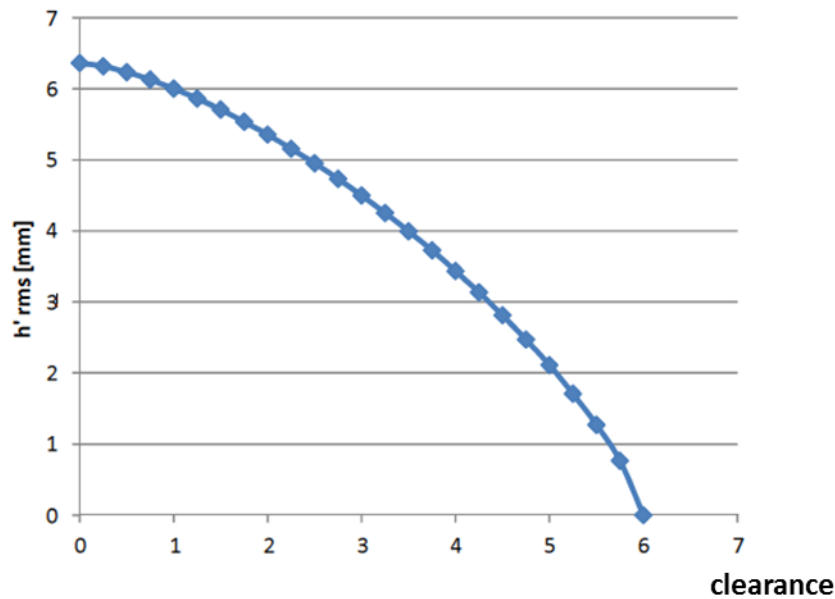


Figure 53. the effective Lagrangian velocity (h'_{rms}) Vs clearance

Form the above figure it is noted that, with increasing clearance, the effective speed value decreases. When the clearance is equal to 6 mm, i.e. the theoretical value of the oscillation amplitude, an effective velocity equal to zero is obtained. This means that no welding can be produced. In turn, when the clearance is equal to 2.2 mm, the effective velocity is about 5.2, corresponding to 84% of the ideal value. In this way, it can be stated that the clearance introduced in the machine results in acceptable loss of effectiveness of the effective lagrangian velocity.

3.2. Dynamic analysis

In order to calculate the forces the machine undergoes to during the process, so to correctly design the machine structure, a dynamic analysis was performed. For the analysis it was assumed that the friction present in the axial guides of the osculating object is negligible. The guide is obtained through a roller contact. This assumption is acceptable as the rolling friction is lower by at least one order of magnitude compared to the friction between the specimens. Additionally, for the preliminary analysis, the clearance effect is not taken into account.

Considering a generic configuration, the Forces highlighted in Figure 54 are exchanged.

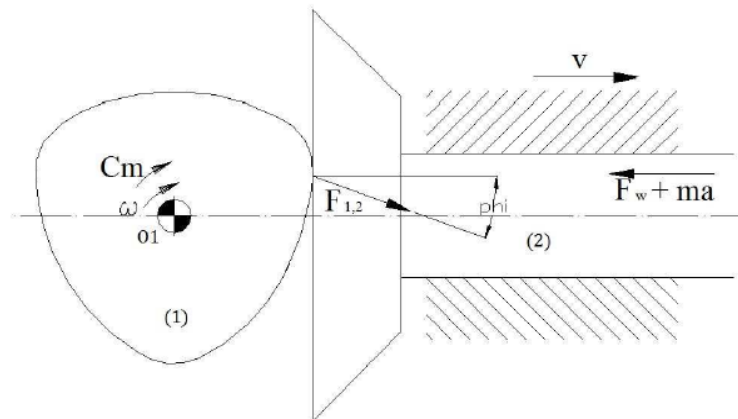


Figure 54. The mechanic equilibrium during the lift phase

In Figure 54 the force exchanged between the cam and plate and the resistant force, exerted by the oscillating object during the lift of the cam, were represented. The cam exerts on the plate a force $F_{1,2}$, inclined of friction angle φ . The equilibrium equation along the horizontal axis is:

$$F_{1,2} = -F_{2,1} = -\frac{F_w + ma}{\cos\varphi} \quad 13)$$

Where F_w is the friction force due to the welding assuming that this is constant. The exchanged force, between the cam and plate, have one component constant and one component as function of F_w and periodically varying in time due to the inertial force $-m \cdot a$. The acceleration varies and changes sign within a stroke. Therefore, the inertial force is added to the resistant force during the half stroke in which the cam pushes the plate, while it is subtracted during the other half stroke. The torque C_m has a value that ensures the mechanism balance.

An energetic approach is imposed and the equation of the powers balance is reported:

$$P_{in} = P_{out} + P_{friction} \quad 14)$$

Where P_{in} is the input power on the mechanism, namely the power provided by the cam, and P_{out} is the power dissipated by the oscillating object.

By developing the relationship, the following equation is obtained:

$$C_m \omega = F_{2,1} \cdot \cos\varphi \cdot h' \cdot \omega + F_{2,1} \cdot \sin\varphi \cdot (R_b + h) \cdot \omega \quad 15)$$

$$C_m \cdot \omega = (F_w + ma) \cdot [h' + f(R_b + h)] \cdot \omega$$

The first term expresses the power absorbed by the welding process and the increase of kinetic energy of the oscillating crew. The second addend is the additional resistant torque due to friction between cam and plate.

Making proper simplifications the equation is:

$$C_m = (F_w + ma) \cdot [h' + f(R_b + h)] \quad 16)$$

Where f is the friction coefficient between the cam and plate and is equal to:

$$f = \frac{\sin\varphi}{\cos\varphi} = \tan\varphi \quad 17)$$

During the return phase, the other cam will be in contact and therefore the above considerations also apply to the right cam. The lift, the speed and the acceleration of the right cam are functions of the rotational torque O_2 . Hence, a change of the reference system is necessary in order to calculate the rotational torque O_1 . With respect to O_1 , the equation of torque required to maintain the balance on the system, during the return phase is:

$$C_m = (F_w - ma) \cdot [-h' + f \cdot (R_b + h_{max} - h)] \quad 18)$$

Eq. 18 takes into account the different reference system by changing the sign of the acceleration and of the speed expressing the lift as the difference between the maximum lift and the stroke of the cam which drives the return. In this way the equations of the torque necessary to ensure the balance of the mechanism for both phases are determined.

In the real case, i.e. when a non-zero clearance is present, the machine torque is null during the clearance recovery, because there is no contact between the cam and the plate. It should be noticed that the real torque is never null due to the friction losses long the kinematic chain. However, these losses are not

evaluated in this discussion because negligible when compared to the forces present during the contact between the cam and plate.

In the expression of the torque, all parameters are known, except for the resistant welding force F_w . This force is a function of the pressure on the two specimens and of the material to be bonded. In the developed LFW machine, the load depends on the pressure of the hydraulic circuit, varying from 9 kg/cm² up to 20 kg/cm² which acts on the actuator, characterized by an area of 23.75 cm². In Table 1 a few F_w values are reported as function of the hydraulic circuit pressures.

P [kg/cm ²]	ActuatorArea[cm ²]	F_n [N]	m	F_w [N]
9	23,75	2096	1	2096
12	23,75	2795	1	2795
15	23,75	3494	1	3494
18	23,75	4193	1	4193
20	23,75	4659	1	4659

Table 1 F_w values as function of the hydraulic pressure

Where: m is the friction coefficient between the specimens, estimated equal to 1 in order to overestimate F_w for safety reasons; F_n is the pressure force between the specimens.

As already done in the kinematic analysis, two cases were considered, one with zero clearance and the other with a clearance equal to the real one (2.2 mm). The cam rotational speed was set equal to 710 rpm. Figure 55 shows the torque obtained assuming a resistant welding force of 5000 N. This value was estimated considering a weld test between two steel specimens having contact area of 100 mm² and interface pressure of 50 MPa:

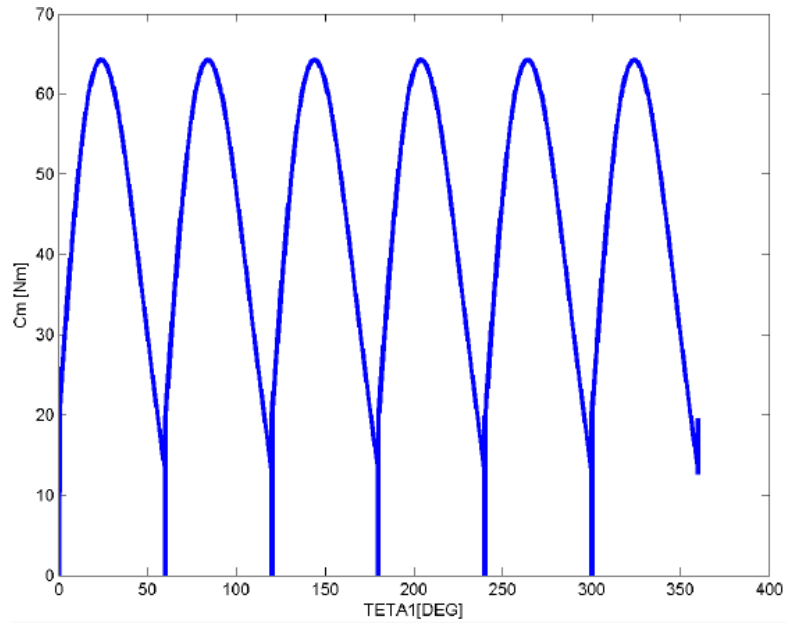


Figure 55. Machine torque as function of the reference angle θ_1 –zero clearance

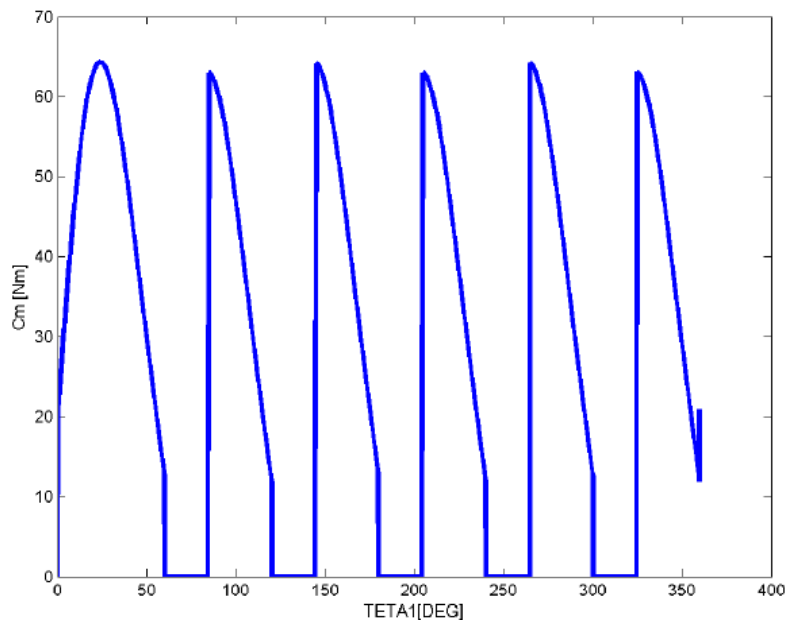


Figure 56. Machine torque as function of the reference angle θ_1 - clearance=2.2.mm

From Figure 55 and Figure 56, it is seen that the torque is irregular. Using the input data previously described the resulting machine torque oscillates periodically between a maximum value of 64 Nm and a minimum value equal to 0 Nm. The torque thus varies rapidly in a very wide range. Based on these results the flywheel was designed and utilized to prevent damages to the driving lathe electric motor.

3.3. Measurement devices

In order to carry out the experimental campaign on LFW, the machine was equipped with a few measurement devices (Figure 57):

- *Piezoelectric accelerometer*: Bruel & Kjaer type 4370 (range 0-6 kHz, 2000 g)
- *Extensometer torsio tachymeter*: Tekkal TT-4000 (range 0-200 Nm, 0-4000 rpm)
- *Charge amplifier*: Bruel & Kjaer (2626), connected to the accelerometer.
- *Digital pressure gauge*
- *National Instruments acquisition card*: DAQ Card 6062 12 bit 500 kSa/s
- *Thermocouple K type*
- *Electrical contactor*

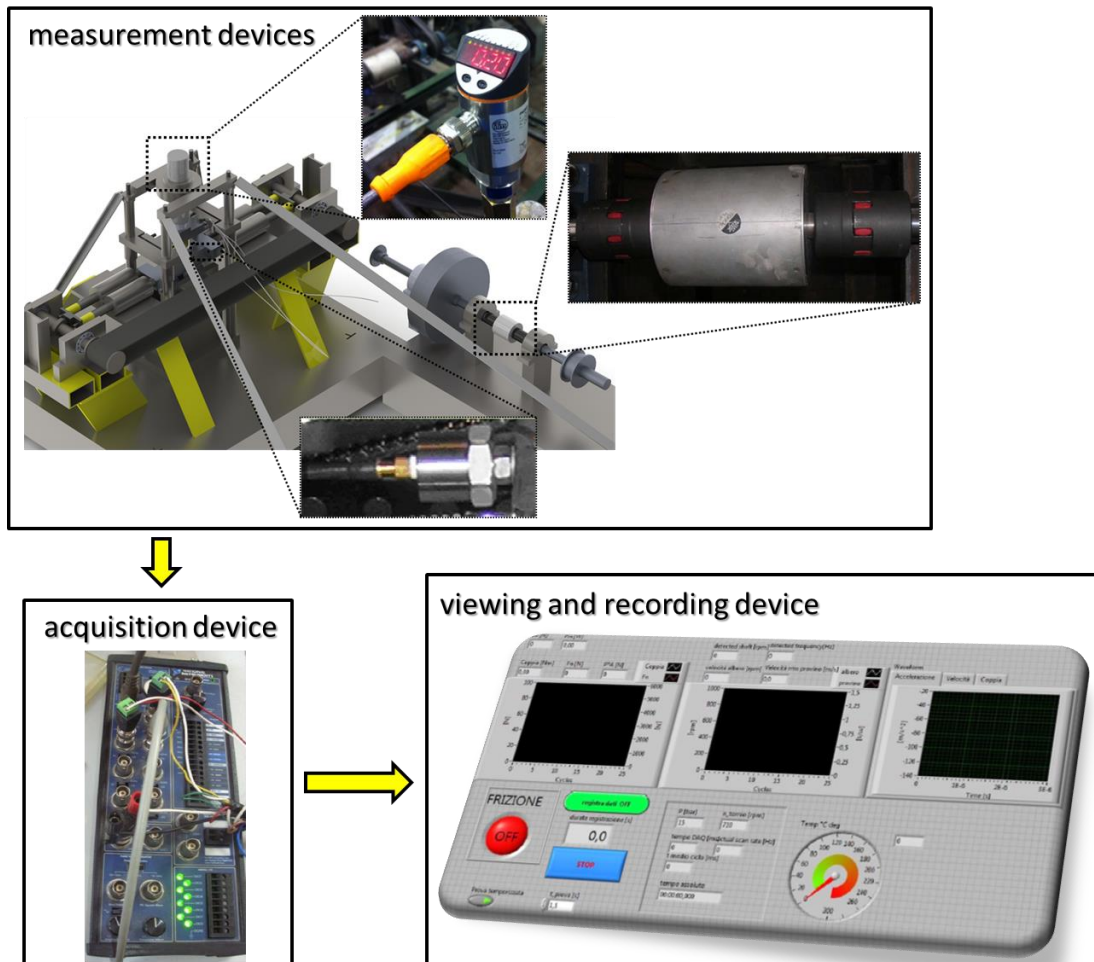


Figure 57. Machine measurement devices

Besides the above cited measuring devices, also the solenoid valve that controls the clutch is connected to the acquisition data board. In this way a unique control

panel has been created allowing the setting an in-process monitoring of the controlled variables by means of a virtual instrument built in LabVIEW (Figure 58).

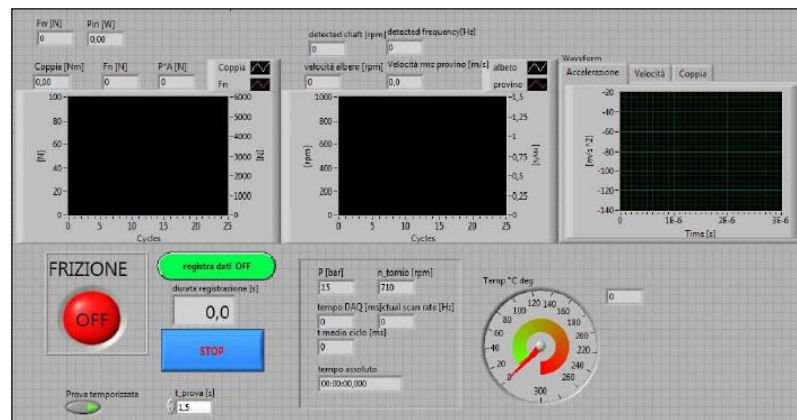


Figure 58. Virtual Instrument Front Panel

In particular, the front panel acquisition allows to set to the nominal rotational speed of the lathe and the pressure of the hydraulic circuit. Data recording starts when the electrical contactor (Figure 59) properly located, sends an input signal once the top specimen begin the vertical stroke.

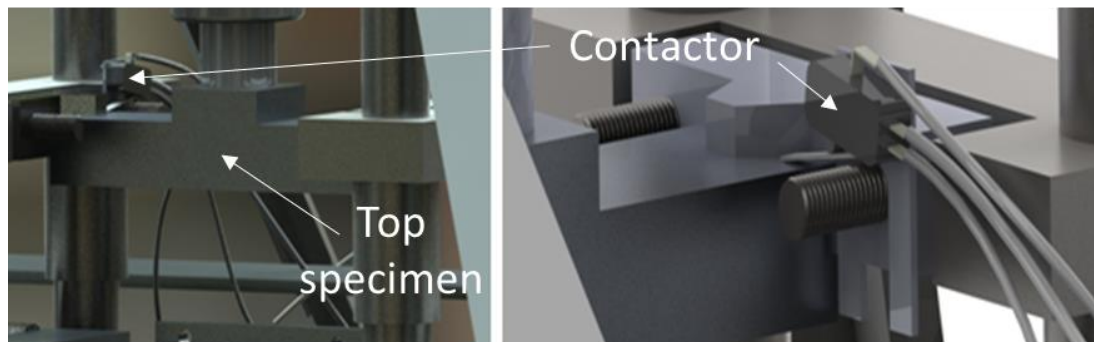


Figure 59. Electrical contactor

When the process time expires, a timer sends to the clutch an opening signal. During the test, the front panel records the input data and stops the records as soon as the clutch is open, i.e. at the end of the test. It is worth noticing that fixing the duration of the process is a crucial step to achieve a good repeatability. Finally, a thermocouple was fixed to the top specimen in order to measure the temperature during the process. The temperature is acquired by the same virtual instrument and is displayed in real time together with the other variables. The torque measurement can be used also to calculate the actual friction factor during the process as a function of time and/or temperature. The relation between the measured torque and the shear force (in the oscillation direction) is:

$$F_w = \frac{C_t - C_{t_0}}{\tau \left[\frac{A}{\sqrt{2}} (3 - f) + f (R_b + a) \right]} \quad 19)$$

Where C_t is torque, C_{t_0} is idle torque and T is the chain (drive).

Assuming a shear model, the shear factor can be obtained dividing the force by the interface area and the shear yield stress of the material in any given temperature condition.

4. Linear Friction Welding Experiments

As far as linear friction welding is regarded, during the third doctoral year, the experimental campaigns were carried out. In particular, experimental activities permitted to draw process windows for two aluminum alloys, namely AA2011 and AA6082. Additionally, a mixed joint with the same aluminum alloys was produced. For the study of the mixed joint, the relative position of the two alloys was varied during the tests.

Table 2 summarizes the different joint configuration analyzed.

	Similar welding		Dissimilar welding	
Top	AA2011	AA6082	AA2011	AA6082
Bottom	AA2011	AA6082	AA6082	AA2011

Table 2 Summary diagram of aluminum tests

For each joint configuration, a dedicated experimental campaign was carried out measuring the temperature trend and energy input. The mechanical characteristics were analyzed in order to identify the proper process parameters ranges for effective solid bonding.

A numerical analysis of the process was carried out in order to set up a robust numerical model and to investigate the evolutions of the most relevant field variables, namely temperature, strain, strain rate.

4.1. Experimental set up

4.1.1. Used materials

The aluminum obtained from electrolytic cells, called primary aluminum, has a titer from 99 up to 99.99% (mean 99.5%). This constitutes the starting material for the production of aluminum alloys. The refined aluminum (or second melting) is instead intended for use in ornamental field, for the production of certain special alloys or for applications in which corrosion is particularly severe. The degree of impurities of different nature tolerated in the various aluminum types depends on the purpose for which the metal is produced.

The fundamental aluminum properties are:

- *excellent electrical and thermal conductivity;*
- *low specific weight;*

- *corrosion resistance.*

Regarding the thermal and electrical conductivity, it is possible to evaluate the influence of the main impurities present in the aluminum taking into account the fact that each element has a different influence. It is worth noticing that thermal conductivity is a key feature to the LFW process as it determines how the heat produced at the interface between the specimens diffuses in the joint going “away” from the welding area:

- *elements with minimal effect: Ni, Si, Zn, Fe;*
- *elements with average effect: Cu, Ag, Mg;*
- *elements with high impact: Ti, V, Mn, Cr.*

An important aspect concerning on the thermal conductivity, is the ratio Fe/Si: in fact, in order to ensure the highest thermal conductivity to the alloy, the ratio must be kept constant and equal to 1.5; otherwise, the conductivity drops dramatically. This behavior is due to the formation of an intermetallic compound, which if present in the alloy in the dispersed phase, subtracts a certain impurities amount thus improving the conductivity.

The specific weight is a second crucial point for aluminum and its alloys, as the impurities can cause a change in the specific weight of pure aluminum. As before, the elements are divided according to their ability to increase or decrease the specific weight:

- *elements increasing the specific weight: Pb, Cu, Ni, Fe, Mn, Zn;*
- *elements decreasing the specific weight: B, Si, Be, Mg, Li.*

In particular, the composition of the two utilized alloys is reported in Table 3:

Alloy	Si	Fe	Cu	Mn	Mg	Cr	Zn	Ti	Al
2011	0.5-1.2	0.7	5.0	0.4-1.2	0.2-0.8	0.1	0.25	0.15	remainder
6082	0.7-1.3	0.5	0.1	0.4-1	0.6-1.2	0.25	0.2	0.1	remainder

Table 3 Composition alloys

Finally, the mechanical properties of the materials are shown in Table 4:

Property	AA2011	AA6082
Density [kg/m^3]	2820	2700
Melting temperature [$^{\circ}C$]	535	555
Thermal expansion coeff. [K^{-1}]	$23 \cdot 10^{-6}$	$24 \cdot 10^{-6}$
Young modulus [GPa]	71	70

Thermal conductivity [$W/m\cdot K$]	138	180
Electrical resistance [$\Omega\cdot m$]	$0.045\cdot 10^{-6}$	$0.038\cdot 10^{-6}$
Yield stress [MPa]	300	310
Tensile strength [MPa]	395	340
Elongation [%]	12	11
Shear strength [MPa]	235	210
Vickers hardness [HV]	115	100

Table 4 Mechanical properties

The variation of the two material flow stress as a function of temperature has been taken into account in order to explain the mechanical behavior of the joint obtained with varying process parameters [62] (Figure 60).

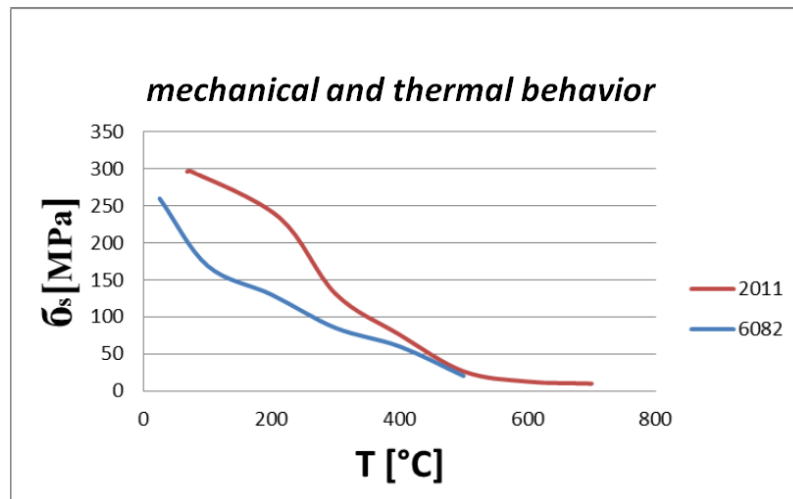


Figure 60. Mechanical and thermal behavior

The elastic modulus of aluminum alloys also depends on the elements content: Ni, Fe, Cu, Si, Mn provide an increase in the Young's modulus of the alloy, proportional to the respective elastic modulus.

It is also to be noted that, in virtue of the crystal lattice type, the material may have a favorable behavior for the low temperature applications. In particular, as temperature decreases, resilience does not vary appreciably while the ductility and mechanical strength grow for almost all materials. Aluminum and its alloys, have remarkable features of drawability, ductility, malleability. In fact, it is suitable for all the plastic operations in cold and hot processing.

The working tool of the aluminum is not difficult, however must be used a high cutting speeds thus requiring a robust machine.

The good castability of the aluminum and its alloys makes them suitable for the classical foundry material. In this technological process, due to the high shrinkage coefficient, pure aluminum is less usable than its alloys.

Finally, one of the most important drawbacks when processing aluminum alloys is the affinity to oxygen. Aluminum oxide (alumina) creates an extremely hard layer on the surface of aluminum sheets or specimens. Its elevated hardness and higher melting point makes some aluminum alloys not weldable by traditional fusion welding processes. For this reason, other joining techniques are usually utilized (e.g. adhesive bonding, nailing, riveting, etc.).

4.1.2. Specimens geometry

The used specimens were CNC machined from bars having 20mm x 20 mm cross section. The specimen geometry can be divided into two parts: a base, intended to be fixed by screws to machine supports (specimen motion is reciprocating and vertical translational for the bottom and top specimen, respectively); the actual element to be welded, whose dimensions are reported in the following:

bottom: height 10 mm, length 10 mm and width 10 mm

top: height 10 mm, length 10 mm and width 7 mm

Figure 61 shows a sketch/picture of the specimens

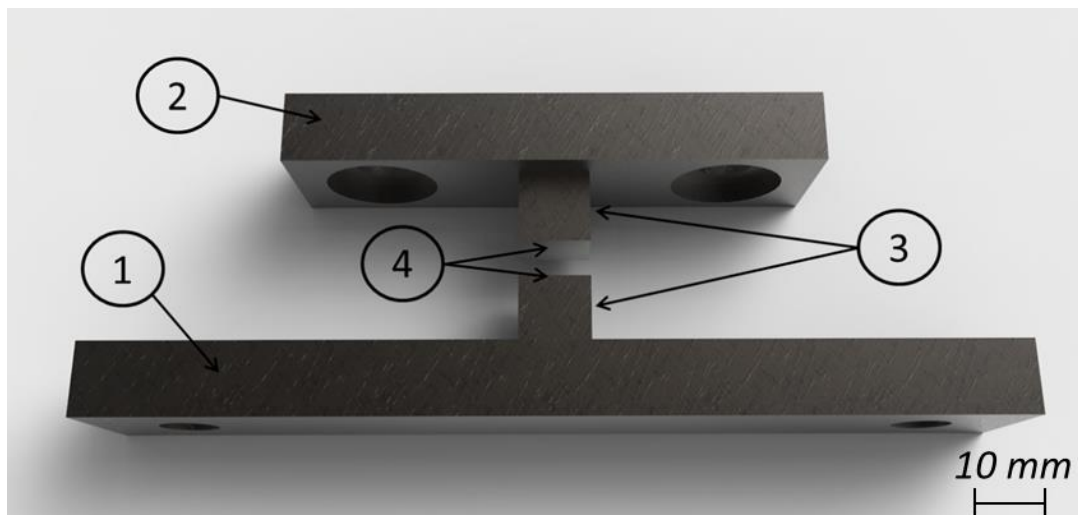


Figure 61. 1-2) base to be fixed to the machine 3) specimens to be welded 4) welding interface.

4.1.3. Process parameters

One of the main goals of the carried out research, was the determination of a process window highlighting the combination of process parameters needed in order to obtain sound joints.

During the experiments campaign, specimen geometry and oscillation amplitude were kept constant. For the latter, a reference value of 3 mm was utilized. Oscillation frequency [f], pressure at the specimen interface [p] and process time [t] were varied according to Table 5

f [Hz]	72, 57.8, 45.6, 36
p [MPa]	20, 30, 40, 50, 60, 70, 80
t [s]	1.25, 2.25

Table 5 Process parameters ranges

Each test was repeated several times. In order to verify the joint performances, different analyses were performed. In particular, tensile strength of the joint, macroscopic and micrographic examination of the welded transverse section and material hardness measurement were carried out.

For all the considered case studies, the proper process time was set through a preliminary campaign. Then a process window was built with varying oscillation frequency and interface pressure. In the obtained graph a different marker was utilized to indicate sound joints, cold joints (low heat input) and instability conditions (excess of heat input).

Eq 19 shows the way W was calculated:

$$W = \frac{2 \pi f A p}{\sqrt{2}} \quad \left[\frac{kW}{mm^2} \right] \quad 19)$$

For a given frequency, the W parameter increases with increasing and frequency.

4.1.4. Joints analysis

For all the considered case studies, the produced welds were properly prepared for micro and macro observations. In particular, the preparation cycle was performed through the following steps:

- *Specimens cutting,*
- *Resin embedding,*
- *Polishing*
- *Chemical etching.*

Cross sections were cut along a plane perpendicular to the welding section, in the specimen centerline, using a vertical band saw. The obtained sample was embedded into a thermosetting resin. This operation makes it manageable during polishing and during observation by optical microscope. For a good result of the sample it is necessary to clean the surfaces in the proximity of the cut in order to

remove waste materials such as shavings and burrs. In order to facilitate the adhesion between resin and sample, degreasing of the outer surface with solvents, e.g. acetone or nitro solvent, is recommended.

A machine for hot embedding, REMET IPA 30 (Figure 62) and an epoxy resin were used. In particular, maximum temperature of 175°C and a pressure of 4.5 bar were selected.



Figure 62. REMET IPA 30 machine

TAKEN MECAPOLp260 (Figure 63) was used for fine grinding and polishing. The operation is performed starting from dishes with progressively smaller abrasive grain (0,20 to 0,10 mm) and ends when no scratches are found in the surface of the specimen.



Figure 63. TAKEN MECAPOLp260 machine

For the grinding step were used the following parameters:

- papers of 400-600-1000-1200 μm ,
- rotational speed of spindle: 60 rpm,
- rotational speed of plate: 300 rpm,
- pressure between the specimen and the plate: 60 N,
- duration for each paper: 5 min,
- Lubrication: water

For the polishing step, a cloth with alumina solution was used. The following parameters were utilized:

- rotational speed of spindle: 60 rpm,
- rotational speed of plate: 150 rpm,
- pressure between the specimen and the plate: 45 N,
- duration for each paper: 10 min,
- Lubrication: alumina solution

If this steps has been done correctly, the specimen appears mirror-polished.

After the polishing step, the sample has a perfectly lapped surface, and therefore it cannot be examined by optical microscopy because light would be reflected. In order to perform the analysis it is necessary to proceed with a chemical etching selectively eroding the most reactive phases and highlighting the structure of the material. In the case of aluminum alloys, the Keller solution (1 cm³ HF, 1.5 cm³ HCl, 2.5 cm³ HNO₃ and 95 cm³ H₂O) was used as reagent. The specimen was immersed into this acid for an assigned time. The immersion time for AA6082 was 90 s while for AA2011 it was equal to 10 s.

As the dissimilar joints are regarded, a selective etching was carried out according to the times previously described. At the end of the assigned time, the specimens were rinsed in water, in order to stop the acid action.

The specimen were observed by an optical microscope; mixed joint, were also observed by a scanning electron microscope in order to highlight chemical mixing of the two alloys. The samples are finally subjected to EDAX analysis. This analysis is a non-destructive investigation and a very fast method allowing the analysis of solid samples that have the following characteristics:

- Stability in the operating conditions with low pressure and electron bombardment. Phases containing volatile substances must be properly pre-treated.

- The sample must be an electrical conductor: wrapping the specimen in aluminum foil or depositing a layer of carbon on its surface, are methods used to increase the conductivity of the specimen.

This technique is used for the qualitative and quantitative characterization of solid substances and elemental analysis, thus allowing detecting the atomic interaction occurred after the junction in the different weld zones.



Figure 64. Scanning electron microscope

4.2. Similar joints: AA2011 and AA6082

4.2.1. Process windows

During the tests, three different conditions were observed using different combinations of the process parameters (Figure 65):

- *Sound bonding between the specimens;*
- *Insufficient heat input to the weld;*
- *Incipient bonding:* this condition is reached when sound bonding is only partially observed in the transverse section of the joint.
- *Instability phenomenon due to excessive softening:* this phase is reached when a large heat input is generated during the process.

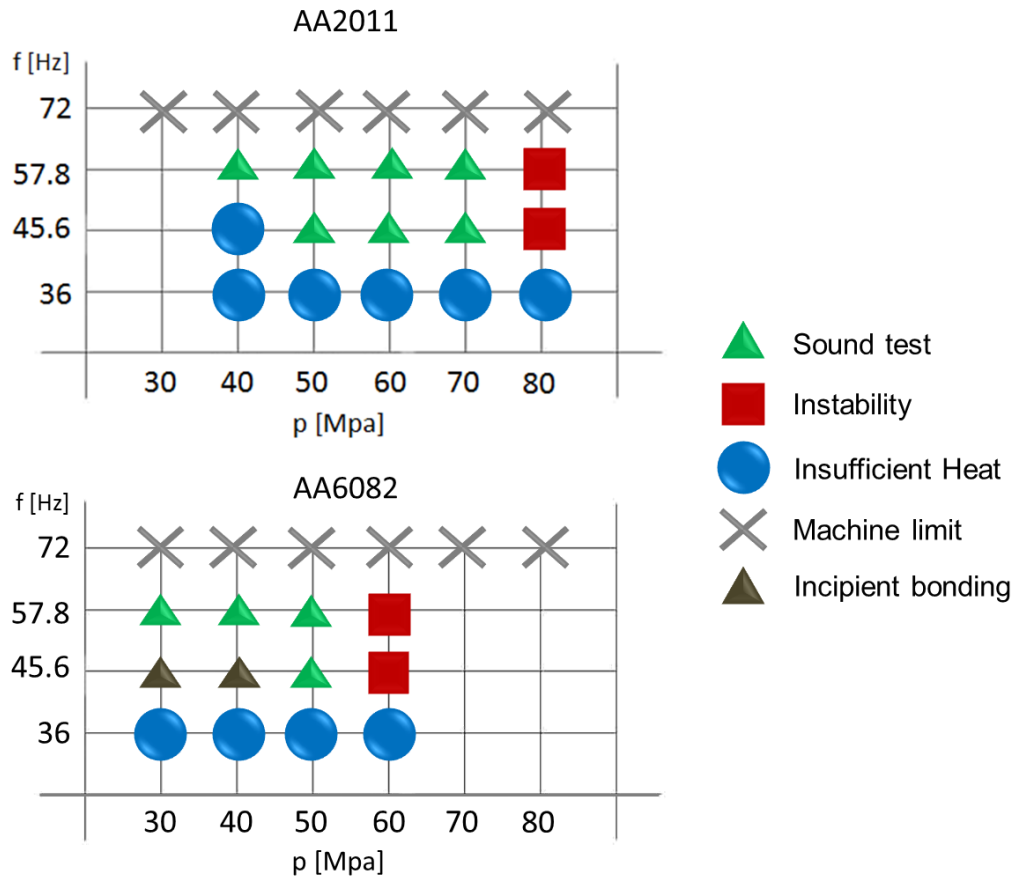


Figure 65. Process Windows for AA2011 and AA6082

For each alloy, it was not possible to perform the welds with the maximum oscillation frequency theoretically available in the machine, namely 72 Hz, due to the vibrations the machine produced. Due to the vibrations of the top specimen, the relative motion between the specimens is significantly reduced or even null, thus drastically reducing the heat input in spite of the increased frequency.

4.2.2. Temperature trends analysis

Temperature in the top specimen was monitored during the process using a thermocouple inserted into a blind hole at a distance of 6 mm from the interface. Thermocouples are temperature sensors formed by connecting two different thermal conductive materials. The thermal contact has been obtained by welding (electric discharge) the two materials. A K-type thermocouple (Chromel (Ni-Cr) (+) / Alumel (Ni-Al) (-)) was used. These thermocouples allow a wide measuring range varying from -200 ° C to 1260 ° C.

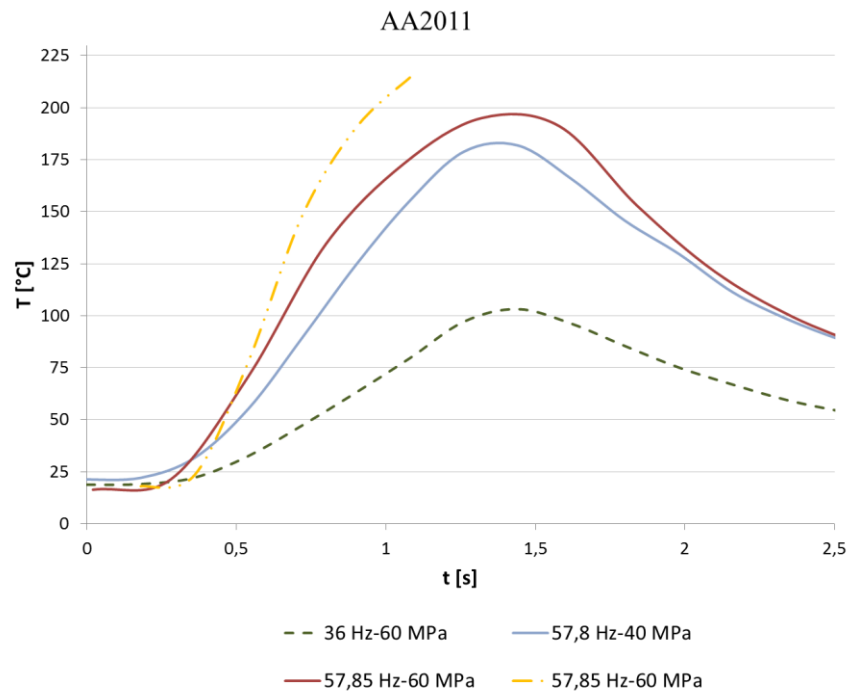


Figure 66. Measured temperatures for the AA2011 alloy

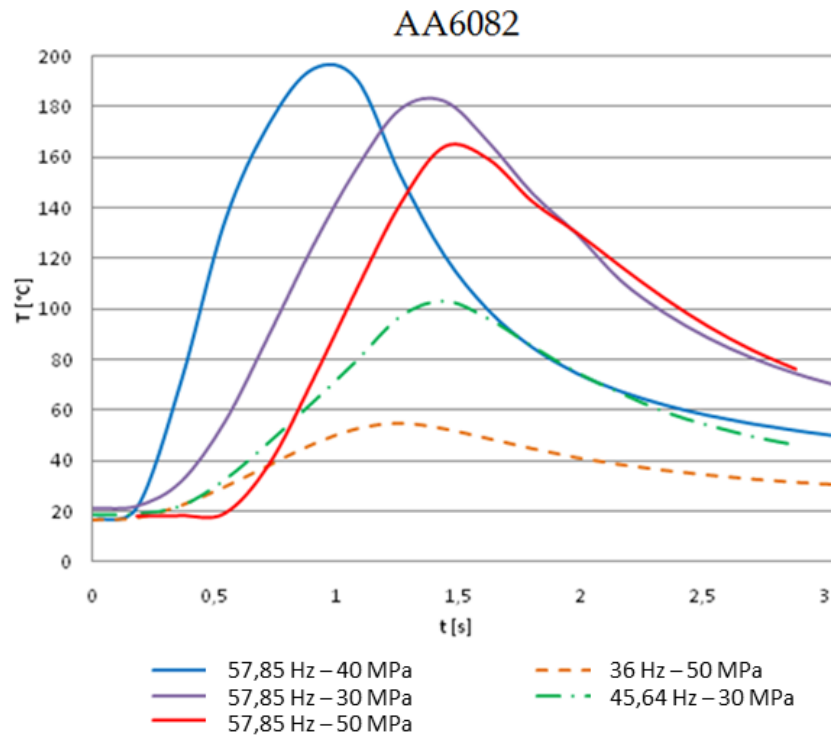


Figure 67. Measured temperatures for the AA6082 alloy

In the Figure 66 and Figure 67 the measured temperatures are reported for the two materials. Solid lines are used for sound tests, while dotted lines are used for tests characterized by insufficient heat and dash-dot lines indicate the limit conditions for bonding (incipient bonding). Maximum peak temperature equal to

195°C was measured using oscillation frequency of 57.85 Hz and an interface pressure of 40 MPa with both alloys.

It is interesting noticing that fixing the frequency at 57.85 Hz, temperature increases with increasing pressure from 30 MPa up to 40 MPa, while decreases when interface pressure increases up to 50 MPa. This effect is due to the large amount of flash expelled at higher pressure, causing significant thermal energy losses. The conclusion that the welding temperature decreases with increasing the pressures, over a certain threshold value, is further supported by J. Romero, M. M. Attallah, M. Preuss, M. Karadge and S. E. Bray [33].

A particular tendency regards the double line section - initially solid line eventually turning into stretch dotted line - used for AA2011, $f=57.85$ Hz and $p=80$ MPa and indicating instability conditions. As it can be seen, a sudden increase of temperature before the thermocouple indicates over load conditions due to the physical destruction of the thermocouple itself. However, the trend curve suggests that the maximum temperature is higher than 200 ° C at 6 mm from the interface. Another aspect regards the time trend, namely the temperature gradient over time, as this curve increases very rapidly causing instability phenomena, i.e. excess of burn off until complete upsetting of the specimen. Analogous considerations can be done for the AA6082 alloy.

4.2.3. Macroscopic analysis

The joints were characterized by the presence of plastically deformed flash. The flash was extruded both in the parallel and normal direction relatively to the oscillation movement. The length of flash was comparable along the two extrusion directions. For some joints, the flash was also expelled from the corners. This is a necessary condition to obtain good joints, even if the amount of material coming from the central area is higher than that coming from the peripheral areas.

AA2011

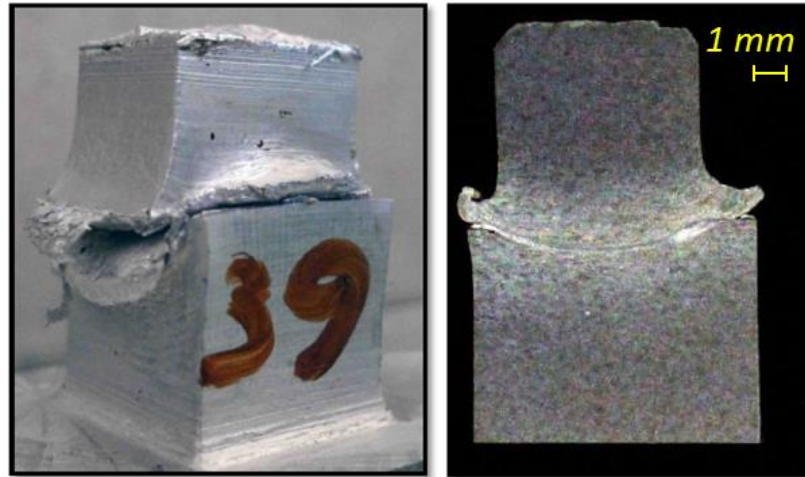


Figure 68. Joint 57.85 Hz, 70 MPa

A sound joint obtained with $f=57.85$ Hz and $p=70$ MPa is shown in Figure 68. A very deformed specimen is observed, due to the technological parameters used, close to the parameters causing the instability phenomenon and machine limit (Figure 65). In the joint micrograph, the deformation of the two samples separated by a thin line of welding is observed. As shown in the process window of the alloy AA2011 (Figure 65), keeping constant the frequency of oscillation and increasing the interface pressure, the instability phenomenon occurs. Figure 69 shows an unstable joint after the process, the operating parameters used are 57.85 Hz and 80 MPa.

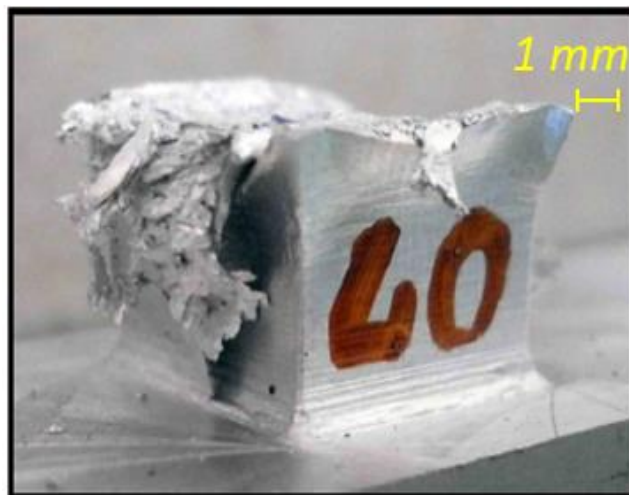


Figure 69. Unstable joint 57.85 Hz, 80 MPa

Maintaining the same oscillation frequency and decreasing the interface pressure, sound joints are obtained as shown in Figure 70, Figure 71 and Figure 72.



Figure 70. Joint 57.85 Hz, 60 MPa

In Figure 70 a joint obtained using an oscillation frequency of 57.85 Hz and an interface pressure of 60 MPa is shown. In the etched section, a very abundant flake-shaped flash is observed. The two samples are characterized by a thick welding line.

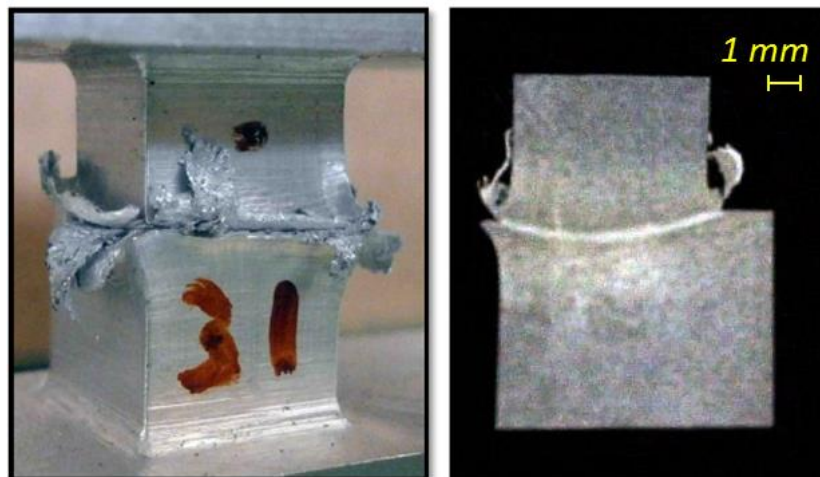


Figure 71. Joint 57.85 Hz, 50 MPa

In Figure 71 a joint produced using operating parameters 57.85 Hz and 50 MPa is shown. Abundant flash is present, also visible at naked-eye, while a not very thick welding line is found.

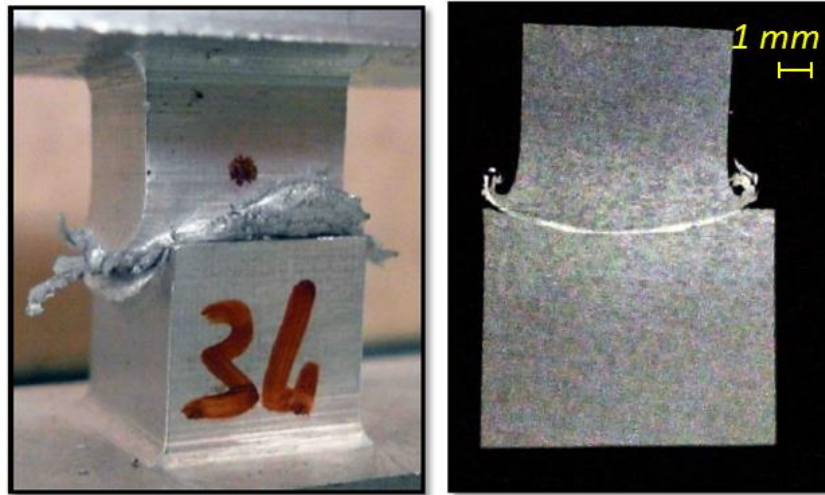


Figure 72. Joint 57.85 Hz, 40 MPa

In Figure 72 a welded joint, using an oscillation frequency of 57.85 Hz and an interface pressure of 40 MPa, is shown. On the left a plentiful flash is shown, visible in the cross section where the deformation of the two samples separated by a thin weld line is observed.

The welds obtained by using an oscillation frequency equal to 45.64 Hz are analyzed in Figure 73-Figure 75.



Figure 73. Joint 45.64 Hz, 60 MPa

In Figure 73 a joint welded using $f=45.64$ Hz and $p=60$ MPa is shown. On the left picture, depicting the outside of the joint, a flake-shaped flash is observed, while in the cross section are not observed significant deformation of the specimens. An important aspect concerns the bond failure occurring in the weld areas.

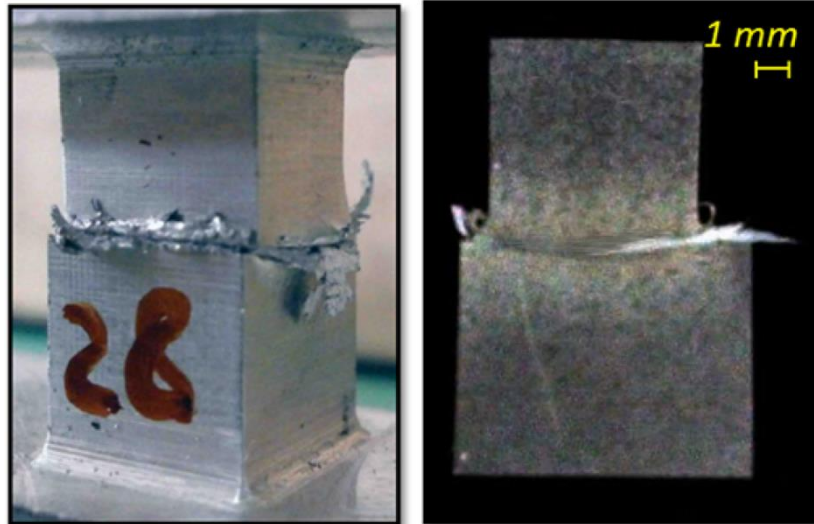


Figure 74. Joint 45.64 Hz, 50 MPa

The joint welded using oscillation frequency of 45.64 Hz and interface pressure of 50 MPa is shown in Figure 74. Small amount of flash in the form of “chip” is observed. In this test, the specimens did not undergo large deformations and the welding line is very thin and not continuous. As it can be observed from the process window, this condition is close to the insufficient heat condition.

Further decreasing the interface pressure down to 40 MPa, the generated heat turns out to be insufficient for the weld. A not welded joint because of insufficient amount of heat during the process is shown in Figure 75; the operating parameters used are 45.64 Hz and 40 MPa.

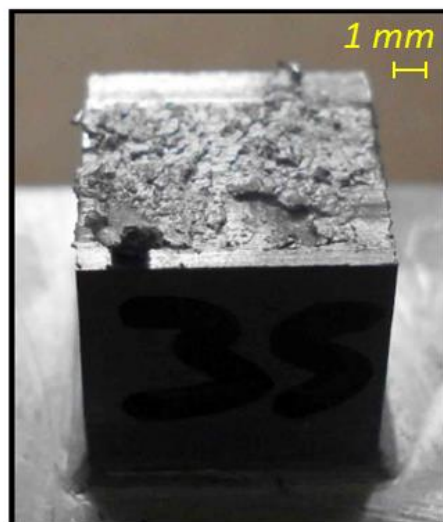


Figure 75. Insufficient heat effect 45,64 Hz, 40 MPa

AA6082

A joint welded using the oscillation frequency of 57.85 Hz and the interface pressure of 50 MPa is shown In Figure 76. An abundant formation of flash is observed in the joint picture and micrograph of the transverse section. Due to the etching it is possible to see the thin line in the weld area.

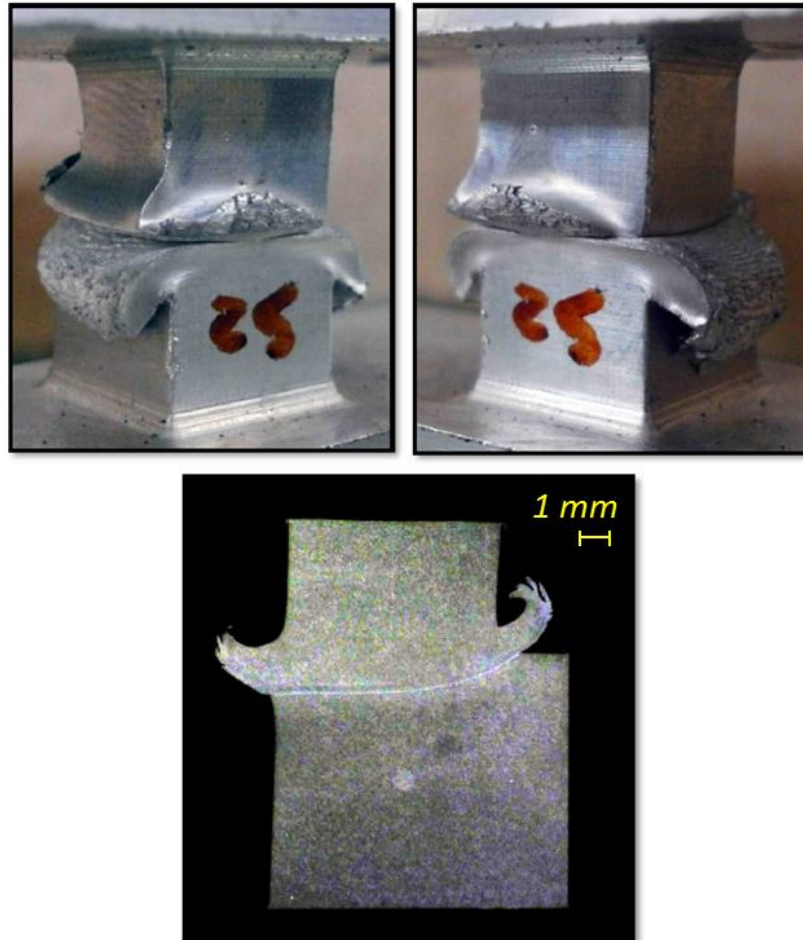


Figure 76. Joint 57,85 Hz, 50 MPa

As shown in the process window of the alloy AA6082 (Figure 65), when oscillation frequency remains constant and the interface pressure increases, instability occurs. An instable weld is shown in Figure 77; the operating parameters used are 57,85 Hz and 60 MPa. It is observed that the top specimen has collapsed preventing the formation of a weld.

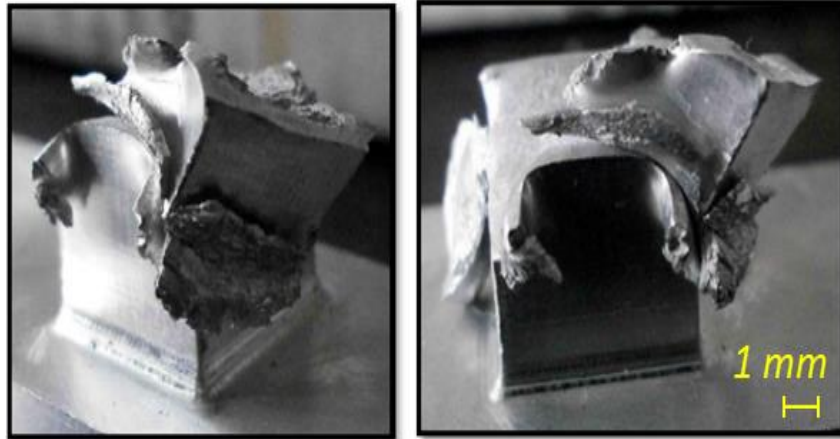


Figure 77. Instability effect, 57,85 Hz, 60 MPa

Maintaining the same oscillation frequency and decreasing the interface pressure welded joints can be obtained (Figure 78 and Figure 79).

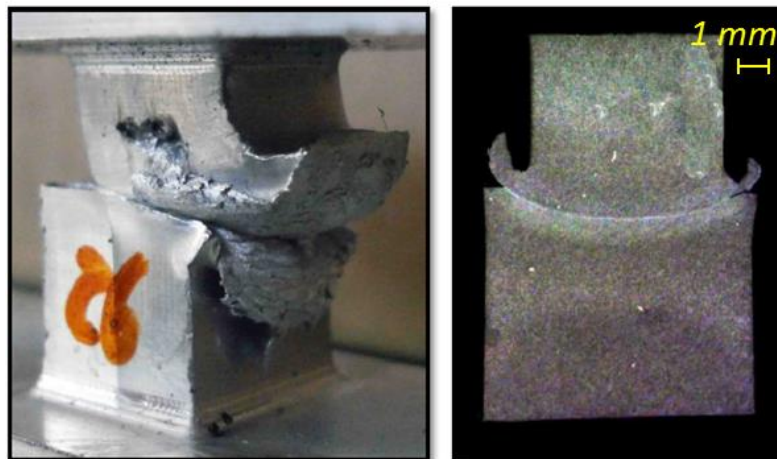


Figure 78. Joint 57,85 Hz, 40 MPa

In Figure 78 is shown a joint achieved with process parameters equal to 57,85 Hz and 40 MPa. On the left picture it is possible to see a flash plentiful, also visible in the macrography in which the deformation of the two samples separated by a thin line of welding is observed.

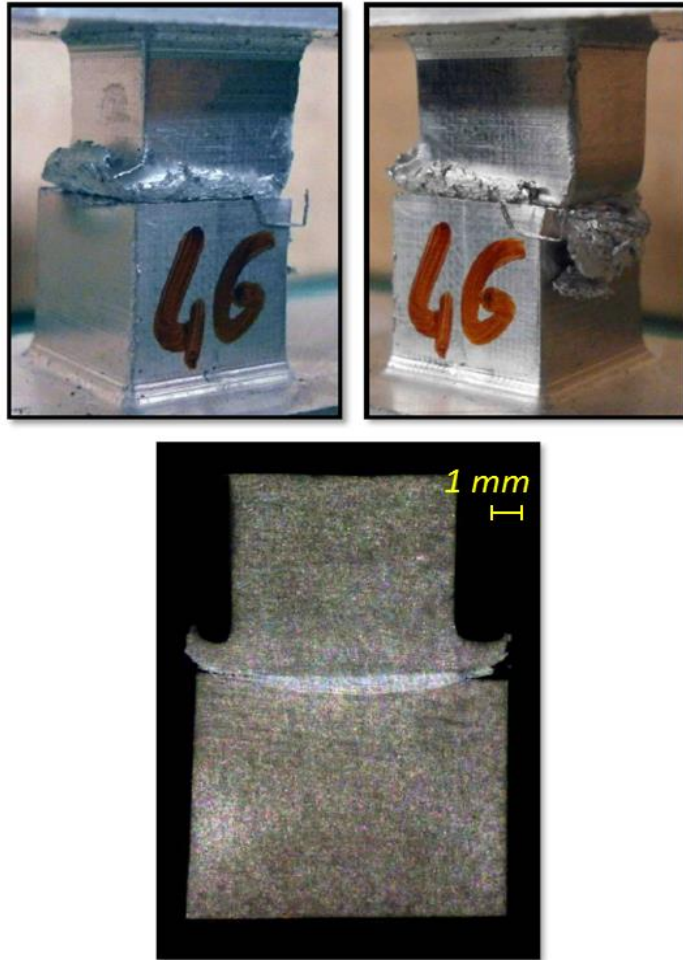


Figure 79. Joint 57,85 Hz, 30 MPa

The joint produced using an oscillation frequency of 57.85 Hz and an interface pressure of 30 MPa is shown in Figure 79. A correct formation of flash, as well as a thick weld line, that separates the two specimens, are observed.

The joints welded using oscillation frequency equal to 45.64 Hz show less flash with respect to the ones obtained with $f=57.85$ Hz because of the reduced heat input and consequent softening of material.

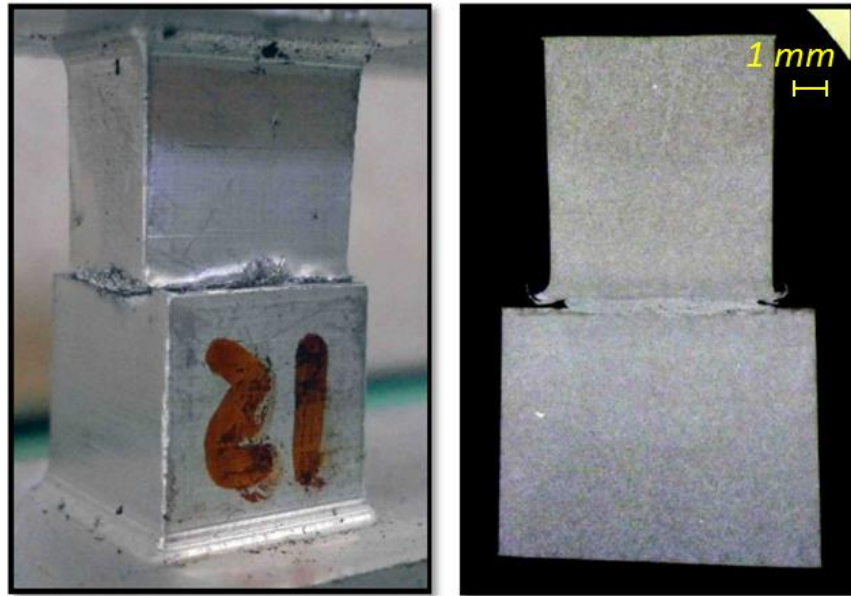


Figure 80. Joint 45.64 Hz, 50 MPa

The joint obtained using the oscillation frequency of 45.64 Hz and interface pressure of 50 MPa is shown in Figure 80. In the picture only a small flash is visible. Looking at the macrograph showing the central section of the joint it is clear that a very thin welding line is found resulting in limit conditions for complete bonding.

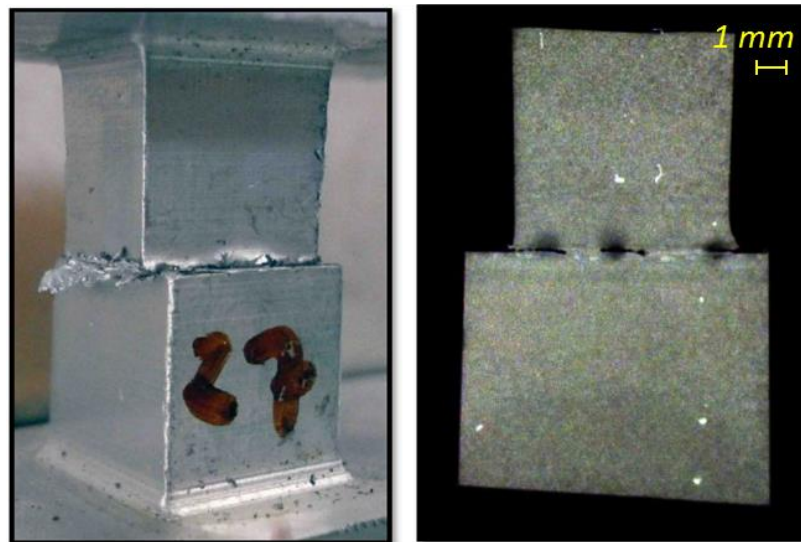


Figure 81. Joint 45.64 Hz, 40 Mpa

The joint obtained using as the operational parameters 45.64 Hz and 40 MPa is shown in Figure 81. Almost no flash is produced and no continuous bonding is obtained in the cross section indicating that, although it seems that bonding occurred, insufficient heat input was given to the joint. This condition was named "incipient bonding": the specimen showed all the visual characteristics of a good joint but metallurgical analysis has showed the lack of weld "seam" continuity at

the interface. This condition was observed also with pressure equal to 30MPa (Figure 82).

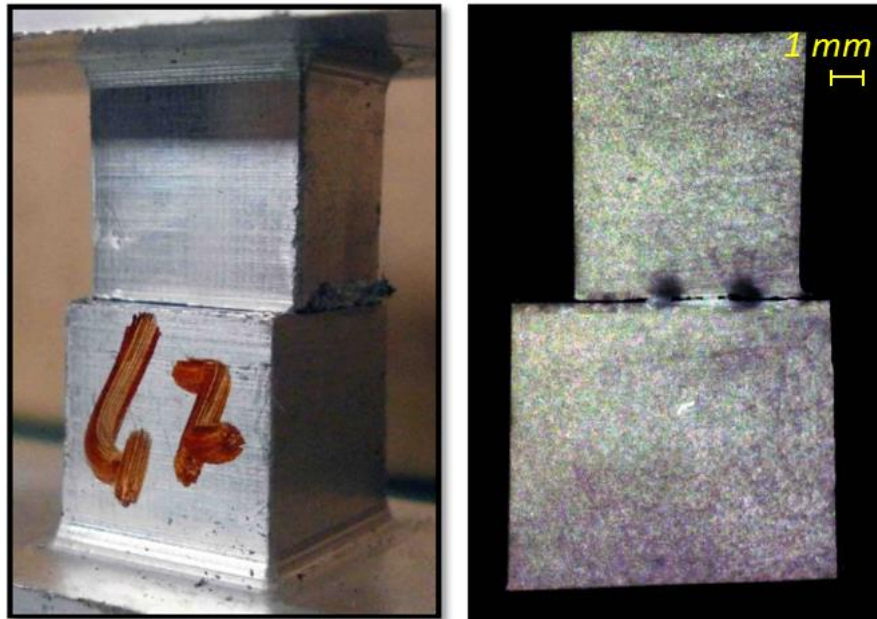


Figure 82. Joint 45.64 Hz, 30 MPa

When decreasing the oscillation frequency down to 36 Hz, the generated heat is insufficient to obtain the weld. In Figure 83 the top surface of the bottom specimen after the process is shown. The operating parameters used are 36 Hz and 60 MPa. A partially welded area can be observed in the center of the specimen surface. This indicates the onset of the bonding phenomenon that could not be completed because of the insufficient softening and pressure.

It is worth noting that the insufficient amount of generated heat during the process can cause defects in the weld area difficult to detect by non-destructive analysis methods, as is visible in Figure 81 and Figure 82.

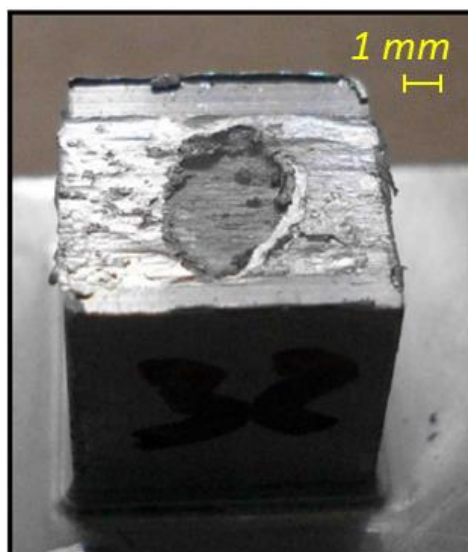


Figure 83. Insufficient heat effect, 36 Hz, 60 MPa

4.2.4. Micrographic analyses

The micrographic examination was carried out to investigate the material microstructural modifications after the process. In particular, the grain size was investigated and compared to that of the base material. For this analysis, an optical microscope and a dedicated imaging analysis software were used to acquire the images and for the measurements, respectively.

Four characteristic areas of the joints can be identified: the parent material (PM), the heat affected zone (HAZ), thermo-mechanically affected zone (TMAZ) and the weld zone (WZ). Figure 84 shows the typical material zones in a AA2011 joint.

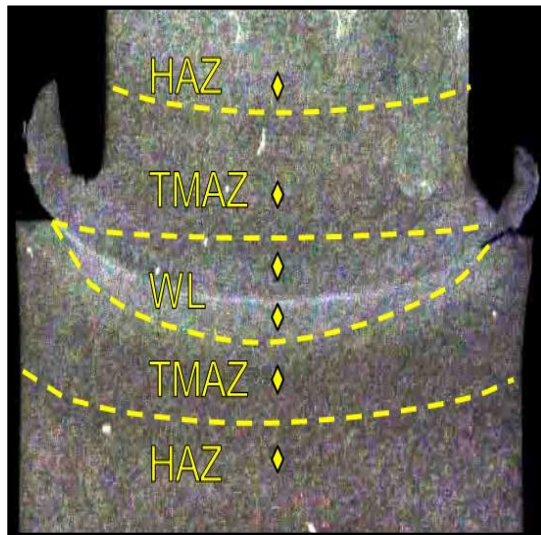


Figure 84. Typical material zones

A commercial material is never made of a single large crystal, but by numerous small crystals, called grains. During the solidification of a casted metal several solidification nuclei randomly oriented begin to form, more or less simultaneously. Once these grains are accruing until the complete solidification of the metal, the different formations of the crystallographic orientation are created thus hindering one another. Physically, the presence of the different grains is justified by the existence of the grain boundaries. The grain size, their mutual orientation and therefore the structure of the separation surfaces between the contiguous grains determine the mechanical properties of the material.

AA2011

Figure 85 shows the parent material area, the most distant from the weld line: in this area no microstructural mechanical properties or other properties change is found.

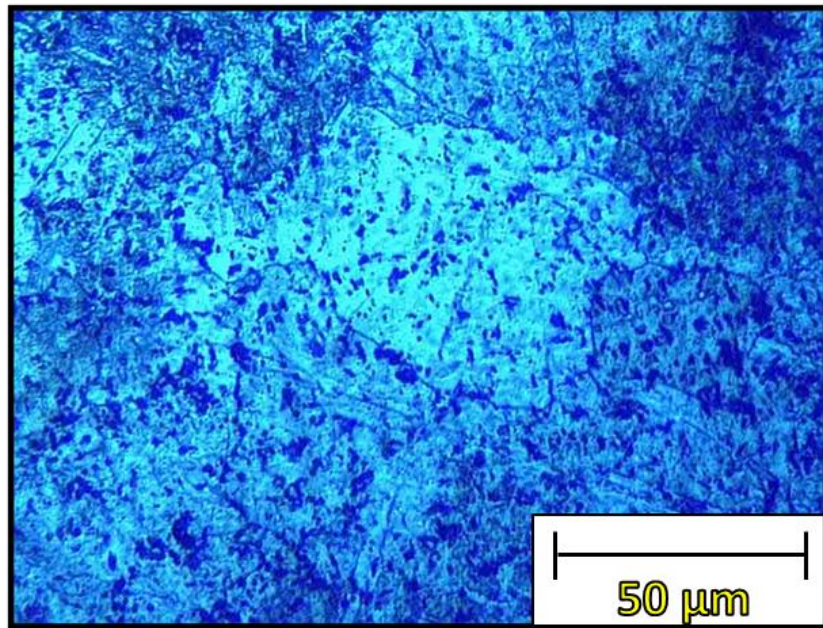


Figure 85. Micrograph of the base material (magnification 250x)

In the heat affected zone (HAZ) the microstructure has been changed by the temperature gradient generated during the welding. However in this zone, no plastic deformation is optically visible. In turn, the average grain size changes due to the heat effects (Figure 86).

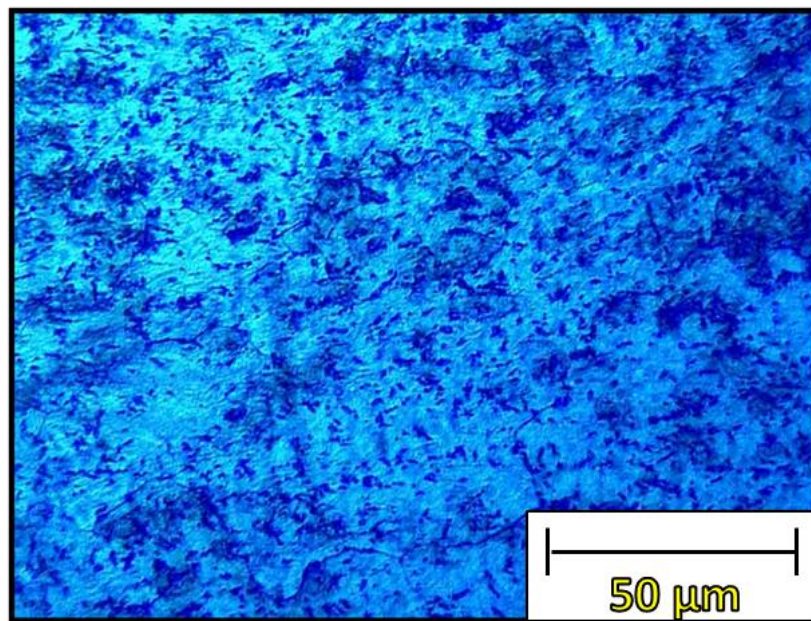


Figure 86. Micrograph of the heat affected zone (HAZ) (magnification 250x)

In the thermo-mechanically affected zone (TMAZ), the material was subjected to more heat than in the HAZ due to the proximity to the interface. In this zone, also a clear plastic deformation is observed. A further refinement of the average grain size is observed (Figure 87).

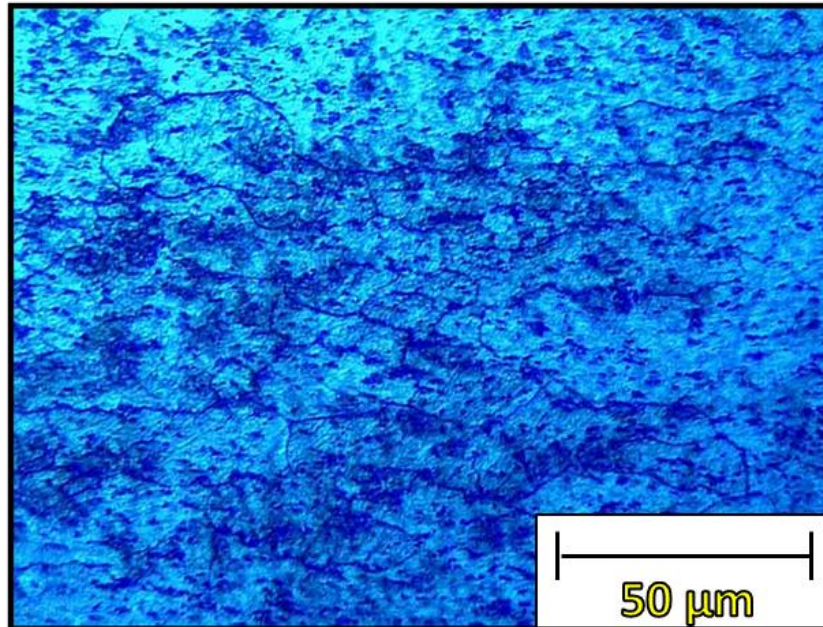
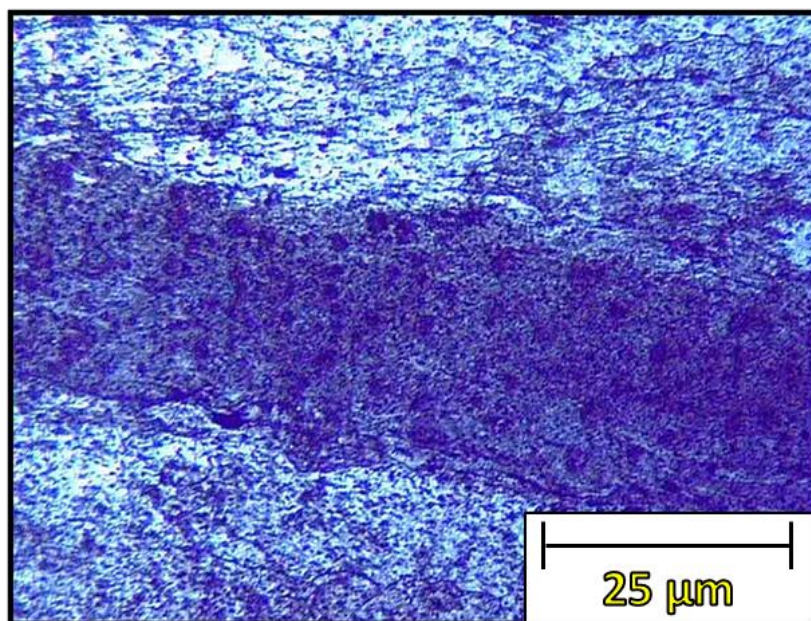


Figure 87. Micrograph of the thermo-mechanically affected zone (TMAZ), (magnification 250x)

Finally, in the weld zone (WZ), the microstructure is very different from the other parts of the welded joint. This is due to dynamic recrystallization (DRX), producing a region with very fine equiaxed grains. It should be noted that DRX occurs when proper temperature gradient and plastic flow are generated (Figure 88).



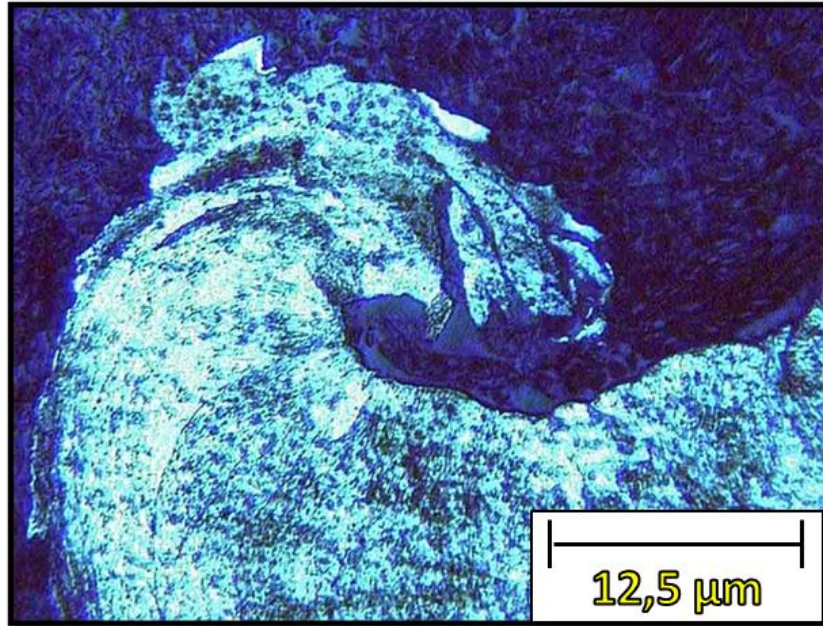


Figure 88. Micrograph of the the welding zone (magnification 125x) and flash (ingrandimento 62.5x)

For the determination of grain size, five different measurements have been taken into consideration for each micrograph: in the acquired image, a polygon is constructed point by point tracing the edge of the grain. A dedicated software was utilized providing the value of the grain area from which the equivalent diameter of the grain is easily determinable. The average value of the equivalent diameters measured for each zone was calculated and these data have been reported in a diagram, showing the evolution of the average grain size as a function of the weld region (Figure 89).

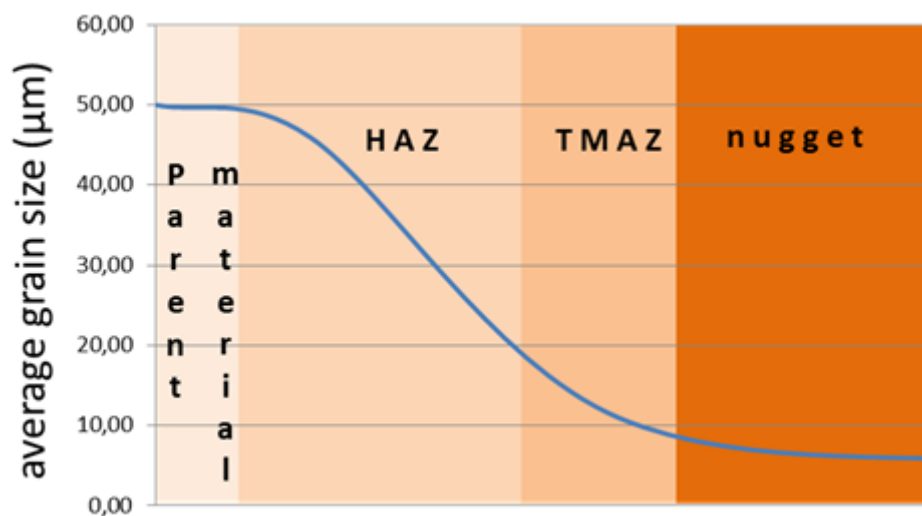


Figure 89. Graph on the average grain size

AA6082

As far as AA6082 tests are regarded, it was not possible to determine the average grain size. Due to its chemical composition, resulting in an elevated corrosion resistance, it is extremely difficult to observe its crystalline structure by acid etching. The microstructure of the four typical zones of the process are shown in Figure 90 and Figure 93.

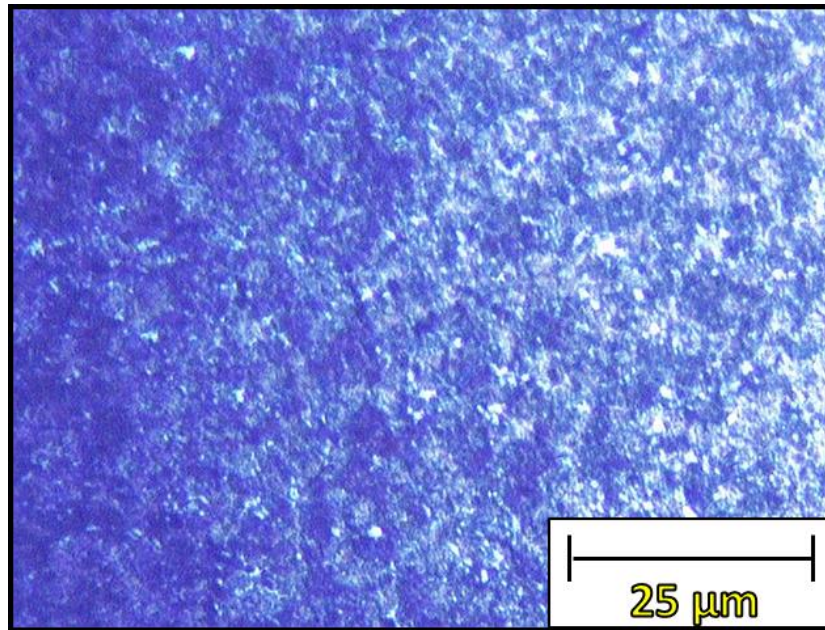


Figure 90. Micrograph of the parent material (magnification 125x)

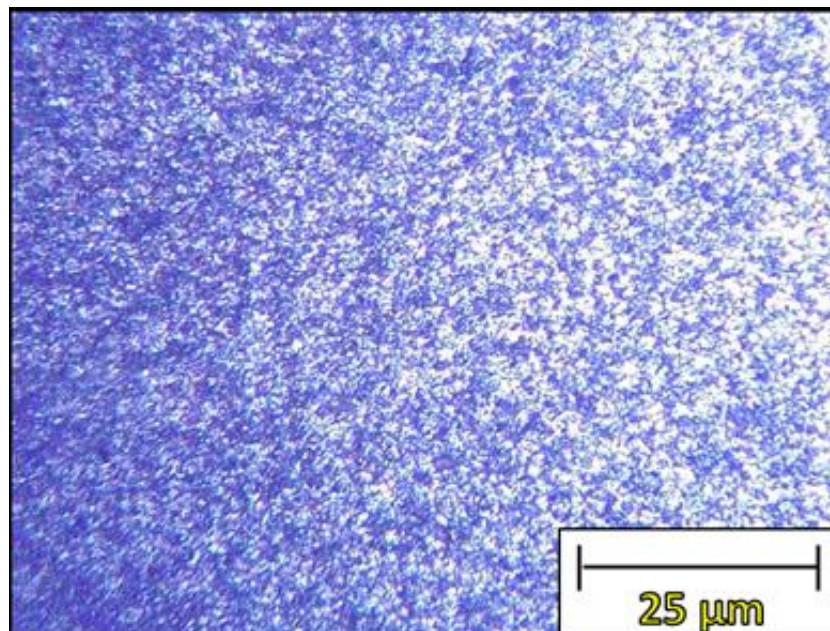


Figure 91. Micrograph of the HAZ (magnification 125x)

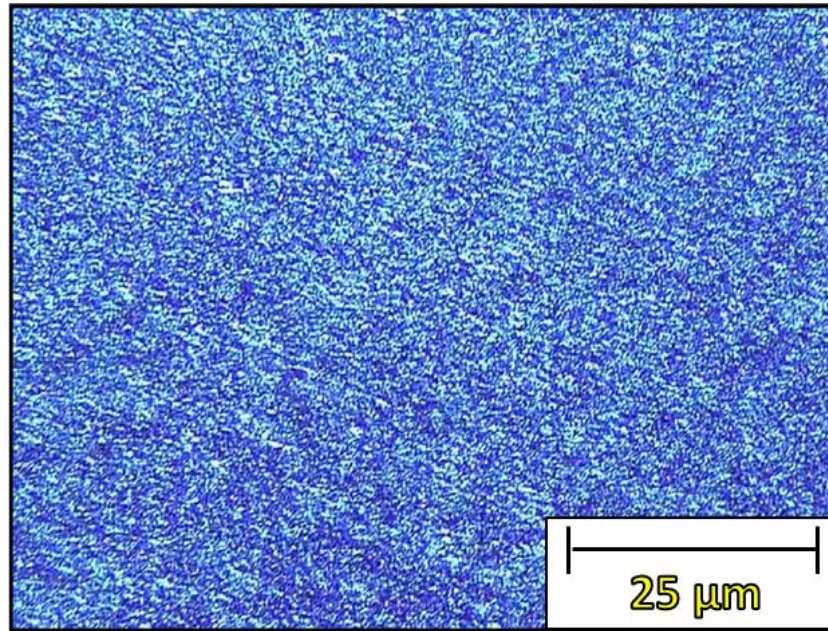


Figure 92. Micrograph of the TMAZ (magnification 125x)

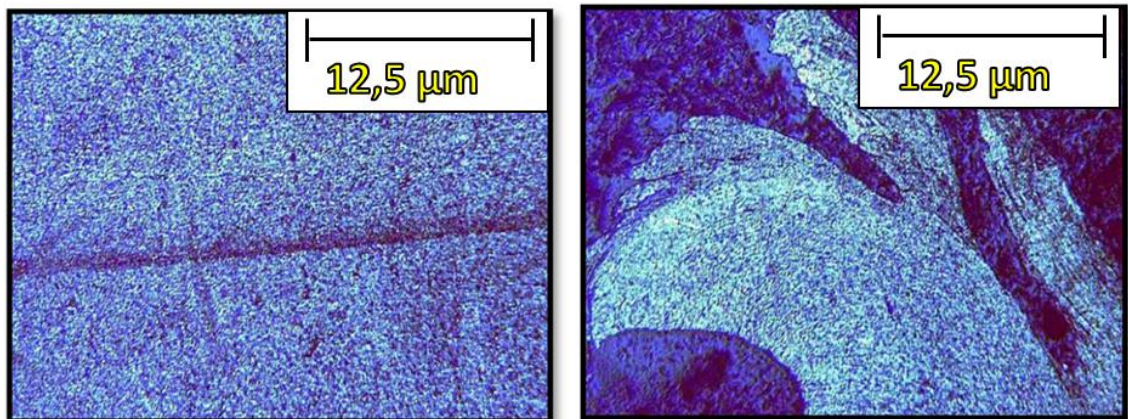


Figure 93. Micrograph of the WZ and flash (magnification 62.5x)

4.2.5. Microhardness analyses

Finally, microhardness measurements of the welded joints were carried out. In particular, for the Vickers microhardness a straight pyramid diamond indenter with a square base with a vertex angle of 136° is used [59] (Figure 94). The test was chosen due to the dimension of the specimens. The small size imprint obtained on the piece is measured by a microscope-indenter combined apparatus (Figure 94).

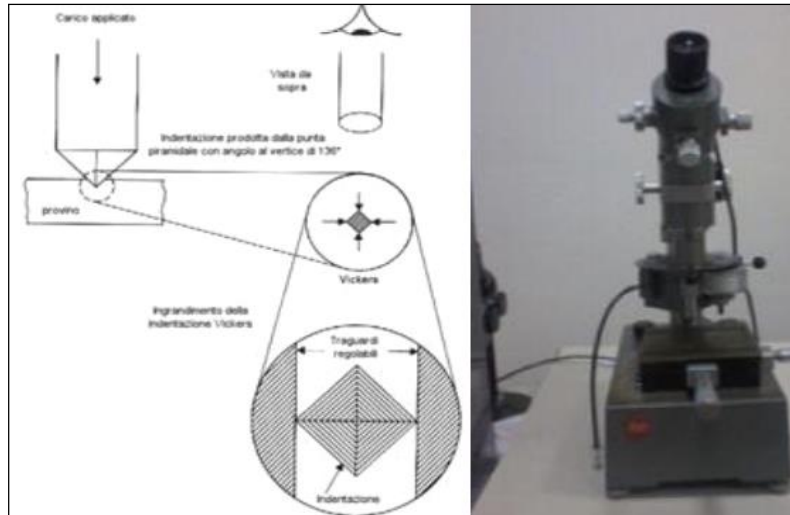


Figure 94. Imprint obtained on the piece and Microscope-indenter

The Vickers hardness value through the following formula is calculated:

$$HV = \frac{2P \sin\left(\frac{136}{2}\right)}{d_m^2}$$

where P is the applied load, measured in kg and d_m is the average value of the diagonals. It was chosen to apply a load of 0.5 kg in relation to the material of the specimens, for a holding time of about 30 s. Microhardness was measured along the central axis of the joint transverse section, with a distance between the measurements points equal to 0.5 mm (Figure 95).

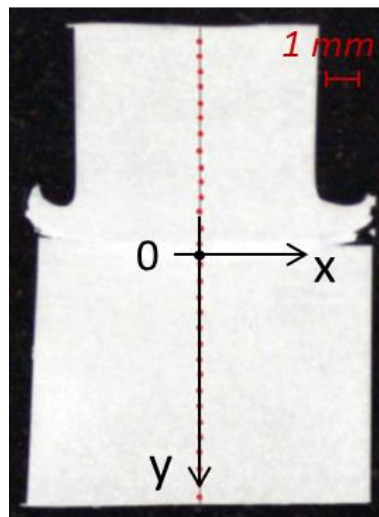


Figure 95. Relative points to microhardness test

The calculated hardness values were plotted versus the distance of the measurement points from the interface between the two welded specimens.

AA2011

For all the specimens analyzed, a hardness decrease is observed as approaching the welding zone. The graph in Figure 96 shows a decrease of the hardness in the welding area of approximately 22% compared to the parental material. A symmetry between the corresponding hardness values of the two welded parts is shown.

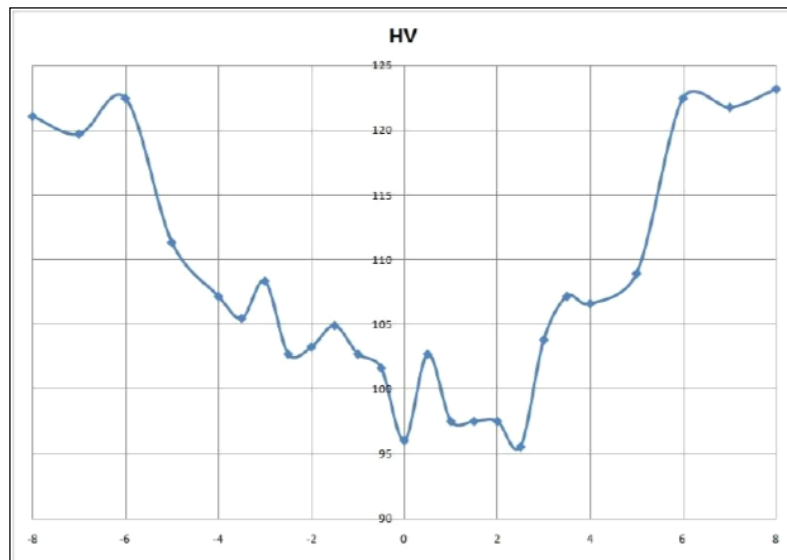


Figure 96. Hardness joint 57.85 Hz, 50 MPa

AA6082

As AA6082 is regarded, hardness decrease in the welding area of approximately 37.5% compared to the parental material is shown in Figure 97. The combined effect of the severe plastic deformation and recrystallization plays a very important role in the microhardness distribution.

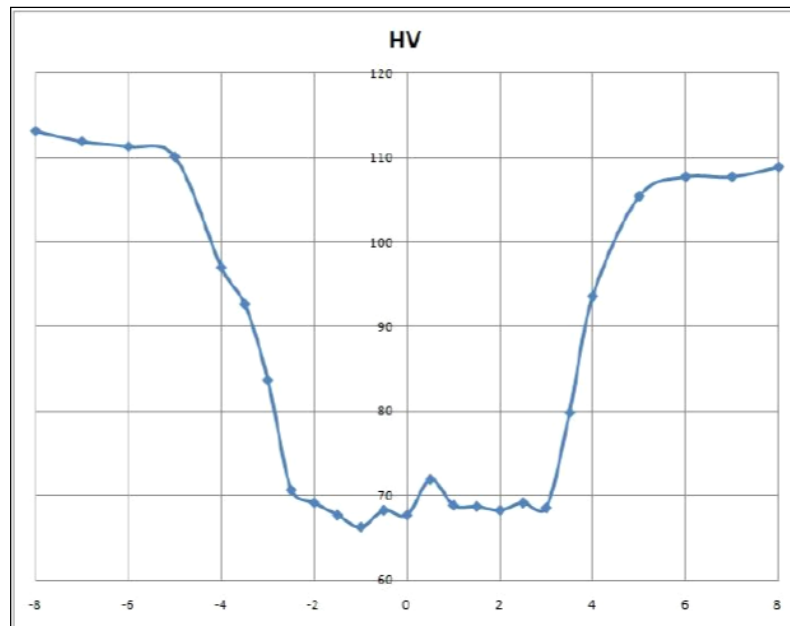


Figure 97. Hardness joint 57.85 Hz, 30 MPa

As reported by Genevois for FSW [63] and by Rotundo for LFW [46], a hardness decrease in both HAZ and TMAZ is observed. In turn, the high temperature in the welding line involves the combined recrystallization effect with the grain refinement. The presence of this effect explains the increased hardness in the weld center.

4.3. Mixed joint

In the last ten years, mixed joints have been attracting both industry and academia due to the advantages they provide in the design of high performing parts that have to respect very restricted weight limits. In literature, very few information is found on LFW of mixed joints. The researches published are focused exclusively on mixed welding in the electric connectors field [65-67]. In turn, a few researches can be found concerning the Friction Stir Welding process [59-60].

Besides the analysis of the effect that the main process variables, namely frequency of oscillation and pressure at the interface, have on the welding itself and on the metallurgical evolutions of each single alloy, the mutual position of the two alloys during the welding must be also taken into account for mixed joints.

A microstructural characterization of the obtained joints was carried out in order to investigate the interactions created in the welding. Possible weaknesses during the process were highlighted.

4.3.1. Process windows

For convenience, the term "top" was used to indicate the top specimen

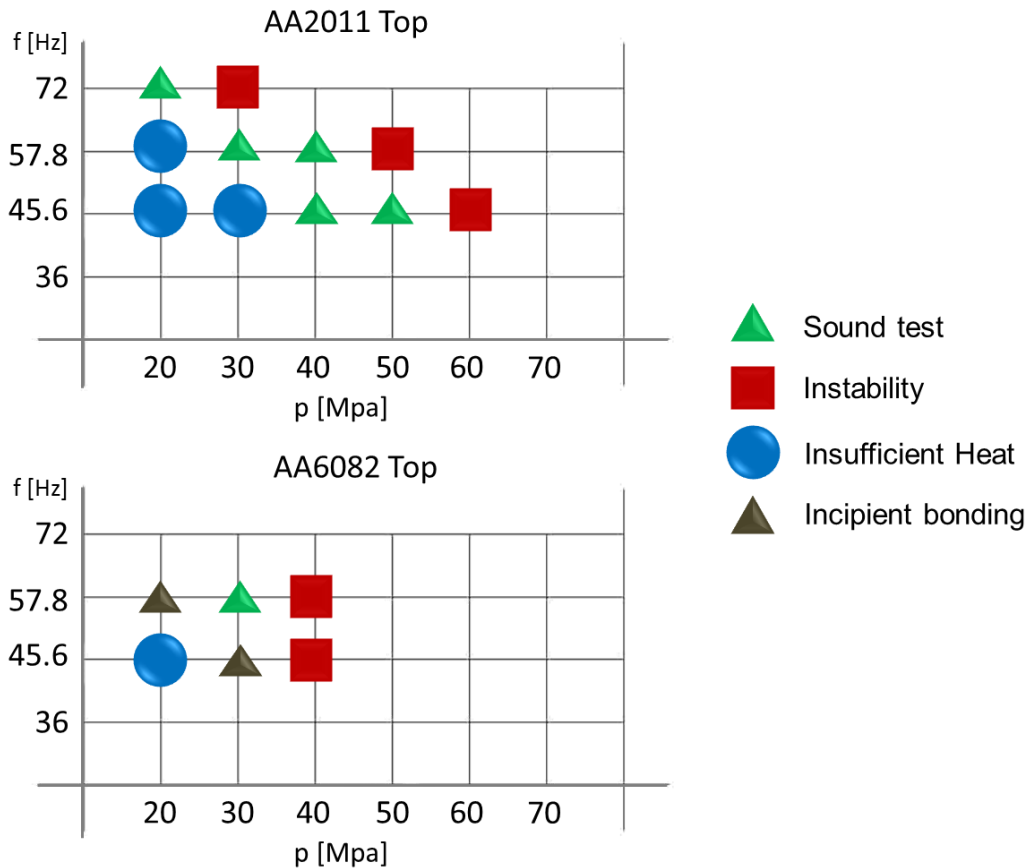


Figure 98. Process window

A first observation regards the process window reduction, justified by the different thermo-mechanical characteristics of two alloys. Another peculiarity of this kind of junction is that, for a given oscillation frequency, a translation to the left of the "sound" tests with respect to the ones obtained with homologue materials is observed. This implies that lower pressures are needed in order to obtain sound dissimilar joints with the considered alloys.

Finally, as in the case of AA6082, "incipient bonding" was observed for all the welds obtained when the AA6082 is the top specimen material.

4.3.2. Macroscopic analysis

Once the machine has stopped, the specimen is not immediately disconnected from it but a preliminary tensile test is carried out using the pressure of the

hydraulic system. Although the applied load is modest, yet it is sufficient to identify the “incipient bonding” conditions.

After this examination, the visual analysis of the joint was carried out observing the junction characteristics such as the presence of the plasticized material expelled at the interface in the flash form. In literature, the presence of abundant flash is reported to be a condition for sound welding [18]. However, this has been proved only for similar welds and does not apply to dissimilar ones.

AA2011 top – AA6082 bottom

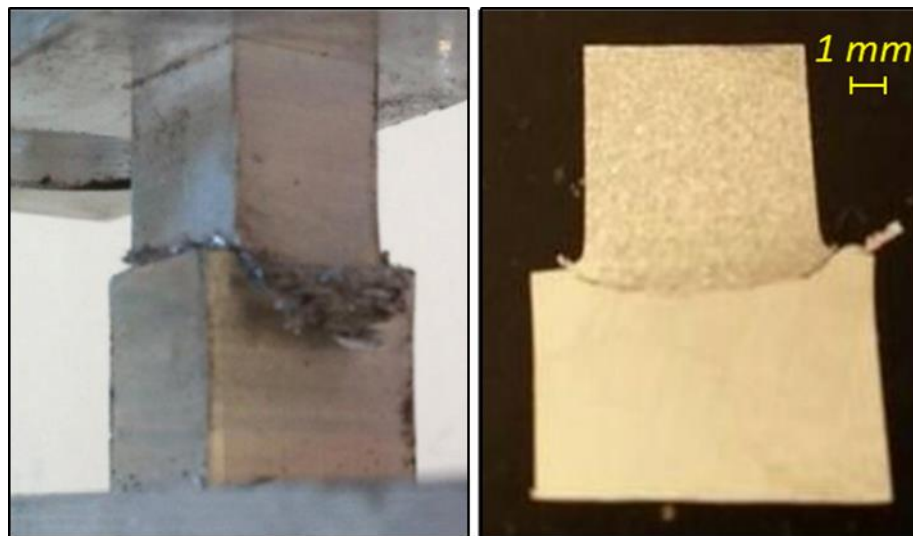


Figure 99. Joint 45,6 Hz, 40 MPa

Figure 99 shows on the left the welding made with oscillation frequency of 45.6 Hz and interface pressure of 40 MPa, while on the right the etched cross section is shown. Despite a low production of flash, especially in the direction perpendicular to oscillation, a sound weld is obtained due to the higher flow stress of the AA2011. The bottom AA6082 specimen "embraces" the AA2011 thus allowing to participate to the welding. In fact, the interaction of the two alloys during the test is observed, even if the AA2011 with modest extent.

Figure 100 shows the joint welded using $f= 57.8$ Hz and $p=40$ MPa.

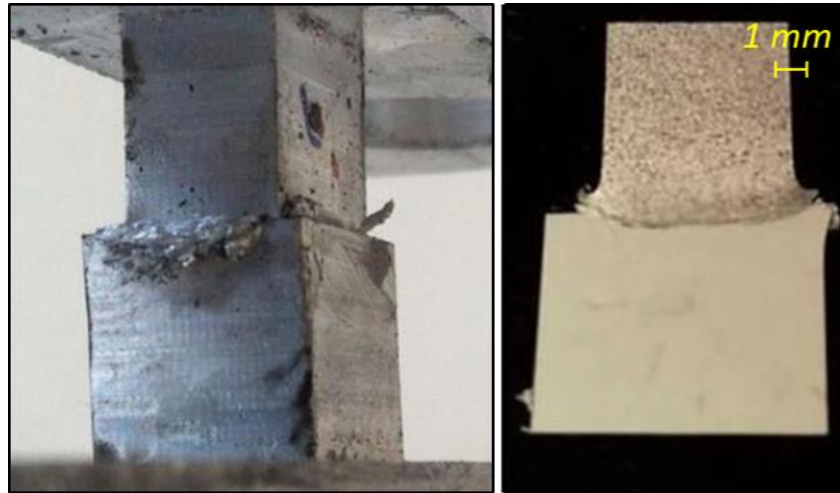


Figure 100. joint 57,8 Hz, 40 MPa

Small amount of flash is observed also for this process conditions, however, the heat input is higher than the previous case study and the transverse section shows a wider thermo-mechanically affected zone.

The joint in Figure 101 is made using an oscillation frequency of 57.8 Hz and an interface pressure of 30 MPa. Larger amount of flake-shaped flash is observed. This feature is typical of the AA2011 alloy that sets it apart, making it particularly suitable for machining.



Figure 101. Joint 57,8 Hz, 30 Mpa

A good participation of both alloys is observed, although the pressure is lower with respect to the previous case studies. Additionally, a greater penetration of the AA2011 in AA6082 is observed.

The specimen in Figure 102, produced with a frequency of 45.6 Hz and an interface pressure of 30 MPa, is characterized by insufficient heat. Although at the end of the process the specimens seemed joined, a small tensile force separated the specimens indicating the “incipiend bonding” conditions.

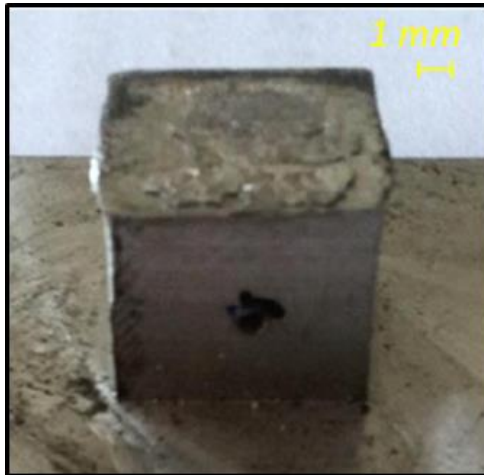


Figure 102. Insufficient heat effect, 45.6 Hz, 30 MPa

The specimen obtained with a frequency of 72 Hz and interface pressure of 20 MPa (Figure 103) shows a very large amount of flash.

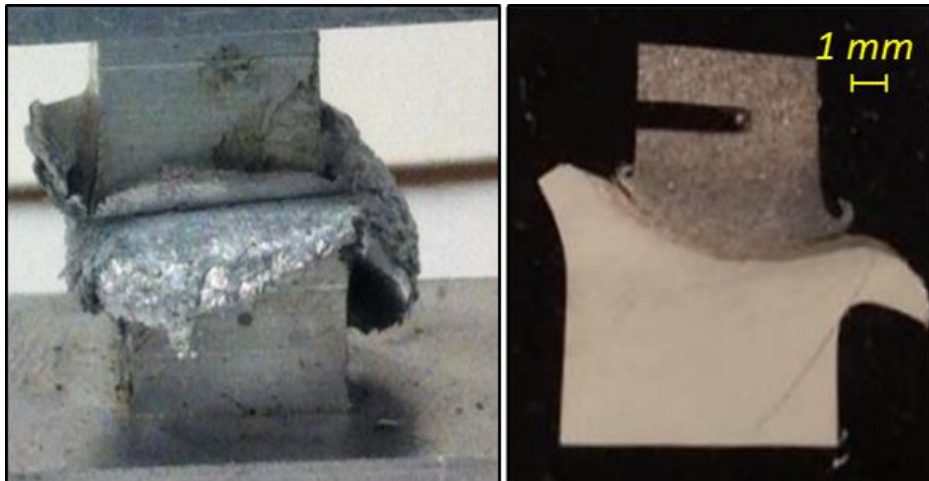


Figure 103. Joint 72 Hz, 20 MPa

The welded specimen shows the participation of both alloys. Two types of flash are distinguished. In particular, the typical flake-shaped flash is present in the top specimen, in agreement with the characteristics of the AA2011 alloy, while the flash appears more fluid in the bottom specimen, due to the lower flow stress of the AA6082 at high temperatures.

Figure 104 reports the weld obtained using $f=45.6$ Hz and $p=50$ MPa. A good production of flash is observed. Although not perfectly aligned, both the two specimen shows good flash production.



Figure 104. Joint 45,6 Hz, 50 MPa

AA6082 top – AA2011 bottom

Figure 105 shows a weld obtained with $f=45.6\text{Hz}$ and $p=30\text{MPa}$. As anticipated, differently from similar joints, in dissimilar joints the presence of a significant amount of flash is not an indicator of sound/poor weld. In particular, the flash is very abundant, especially in the oscillation direction. Although the top specimen has undergone a significant deformation, almost no deformation is observed in the bottom joint and a continuous weld is not obtained, i.e. the weld bead does not cover the entire interaction surface showing only a few points of junction.

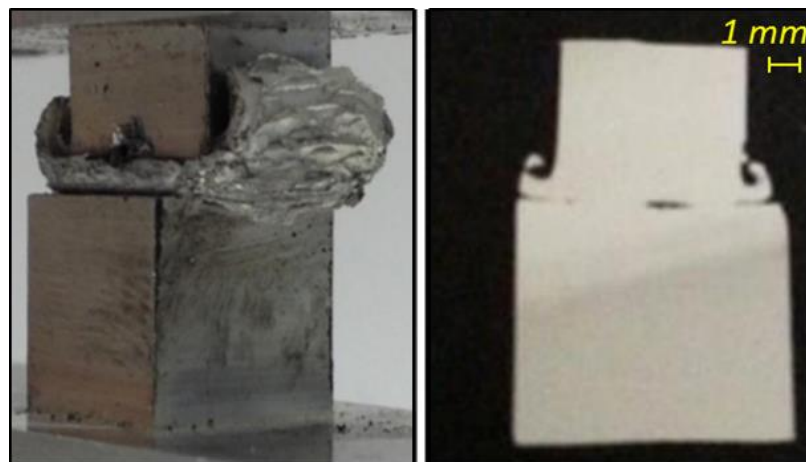


Figure 105. Joint 45,6 Hz, 30 MPa

It should also be noted that, although the junction surface of the welded joint is small, proper bonding conditions are reached in the areas actually welded. In fact, before removing the specimen from the machine, a tensile force equal to 2000N was applied observing no joint separation.

Figure 106 shows the specimen welded with an oscillation frequency equal to 57.8 Hz and an interface pressure of 30 MPa. As in the previous case, the

participation is almost exclusively of the AA6082 alloy, while, for the AA2011, no deformation is shown.

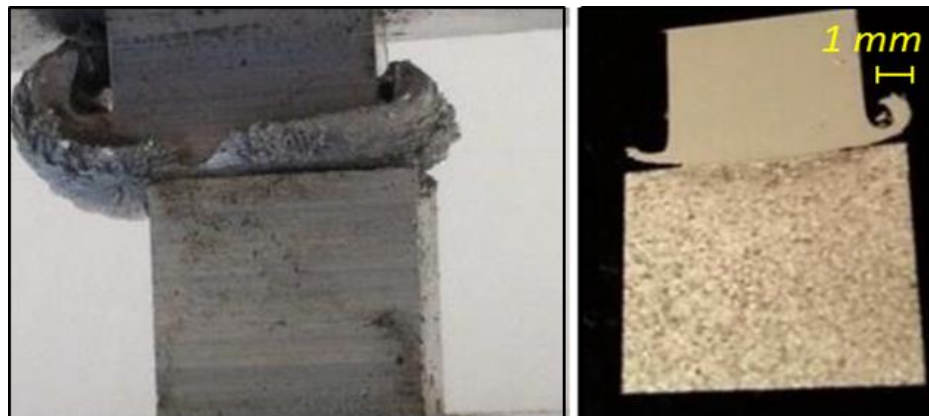


Figure 106. Joint 57,8 Hz, 30 MPa

The flash is still abundant and the weld line appears to be continuous, as can be seen by observing on the left image showing the specimen after etching by Keller's reagent.

Figure 107 shows the specimen produced with an oscillation frequency equal to 57.8 Hz and an interface pressure of 20 MPa. From the micrograph of the cross section it is visible that a sound weld could not be obtained. In turn, the “incipient bonding” conditions are observed as the welding line exhibits more than one interruption.



Figure 107. Joint 57,8 Hz, 20 MPa

The joint obtained by providing an oscillation frequency of 45.6 Hz and an interface pressure of 40 MPa is shown in Figure 108. In this test the generated heat was not sufficient to soften the materials and activate the different phases of the LFW process. Separation of the two alloys occurred when the joint was subjected to minimum tensile stress.



Figure 108. Joint 45,6 Hz, 40 MPa

On the other hand, using $f=57.8$ Hz and $p=40$ MPa resulted in excessive heat production thus obtaining instability.



Figure 109. Instability effect, 57.8 Hz, 40 MPa

4.3.3. Micrographic analysis

Due to the presence of two different alloys, it was not possible to carry out the micrographic analysis in a single step. A two steps analysis was conducted: first, the specimen was immersed in Keller's reagent for a time equal to 10 seconds, and then it was decided to rinse under water and proceed with the micrographic examination of AA2011. After that, the specimens are again immersed for additional 80 seconds, and rinsed again thus proceeding with the AA6082 analysis.

The parent material area (Figure 110) of AA2011 is the area where no microstructural change occurred due the thermo-mechanical effects of the process.

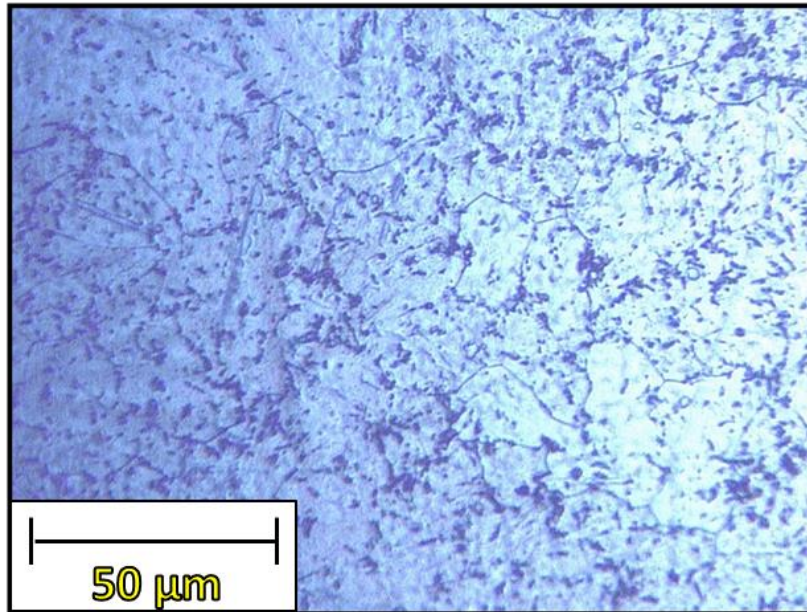


Figure 110. Micrograph of the base material (magnification 250x)
Joint 45,6 Hz-30 MPa

In the heat affected zone (HAZ) the microstructure, e.g. average grain size, and/or the other properties have been changed by the temperature gradient generated during the welding (Figure 111).

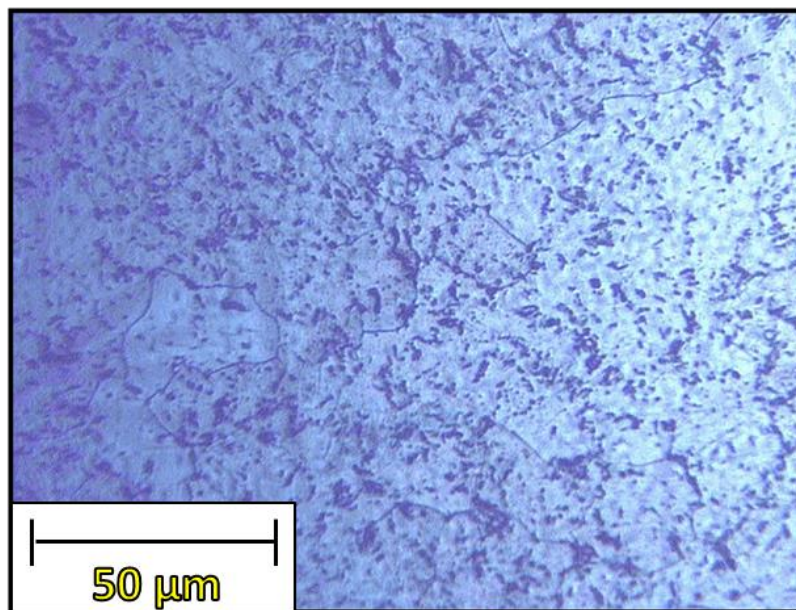


Figure 111. Micrograph of the heat affected zone (HAZ) (magnification 250x)
Joint 45,6 Hz-30 MPa

In the thermo-mechanically affected zone (TMAZ), the material was subjected to more heat than in the HAZ due to the proximity to the interface. In this zone, not only the temperature gradient is visible but also a clear plastic deformation is observed: a further refinement of the average grain size is shown (Figure 112).

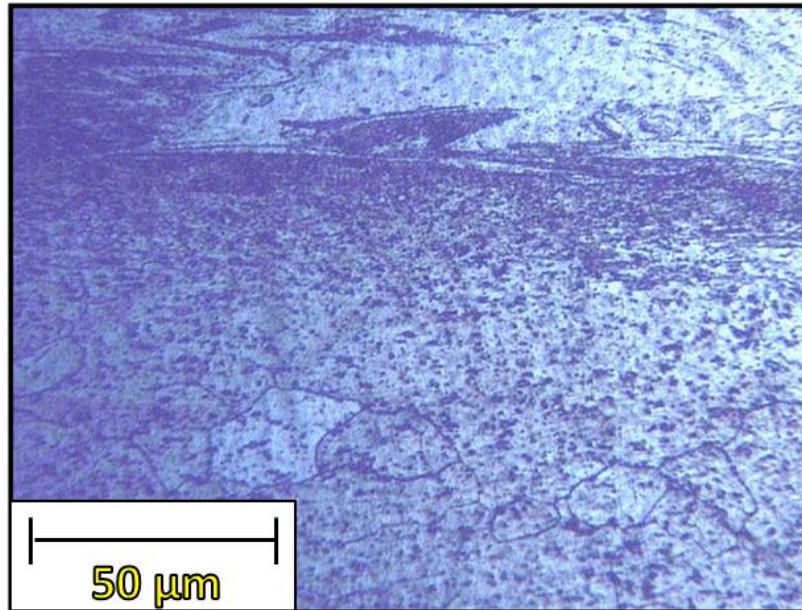


Figure 112. Micrograph of the thermo-mechanically affected zone (TMAZ), (magnification 250x)
Joint 45,6 Hz-30 Mpa

As for the analysis of homologous joints, for AA6082, due to its anti-corrosive properties of this aluminum alloy, it was not possible to detect the average grains size. Some special areas and features of this alloy are shown below.

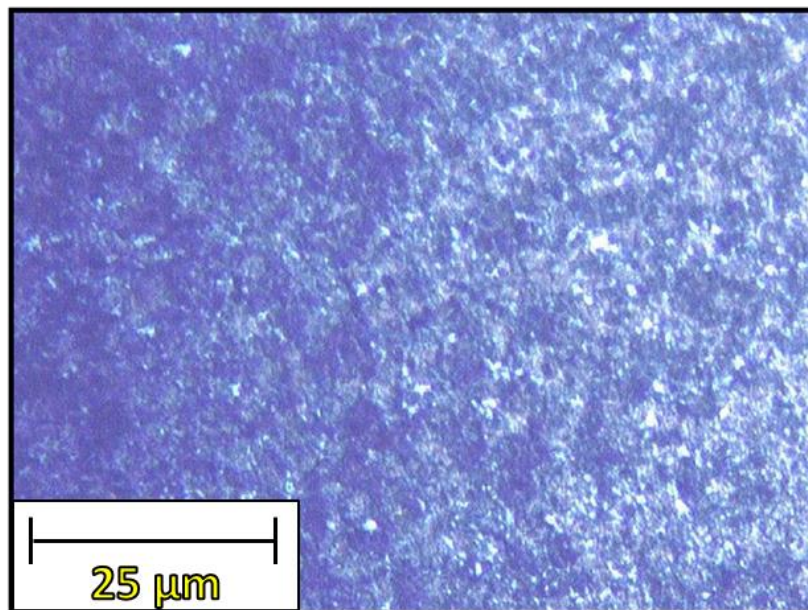


Figure 113. Micrograph of the parent material (PM) (magnification 125x)
Joint 57,8 Hz-40 MPa

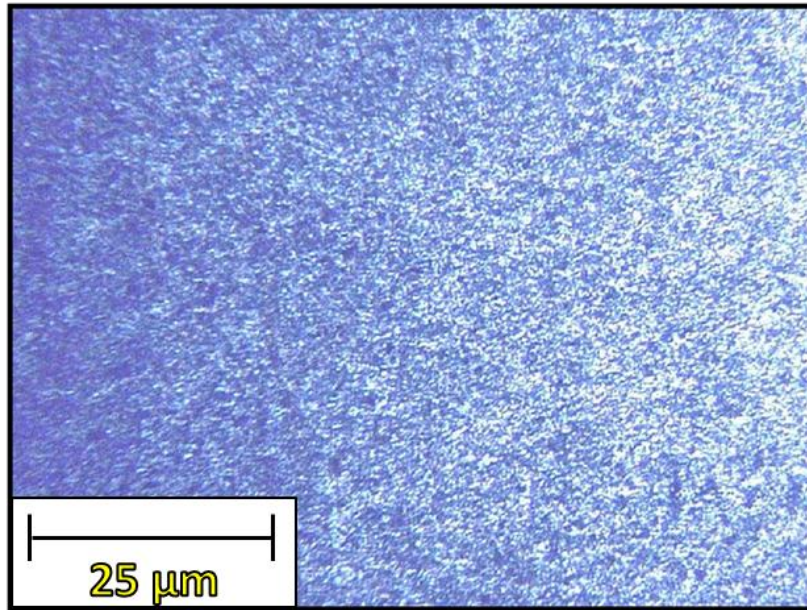


Figure 114. Micrograph of the Heat affected zone (HAZ) (magnification 125x)
Joint 57,8 Hz-40 MPa

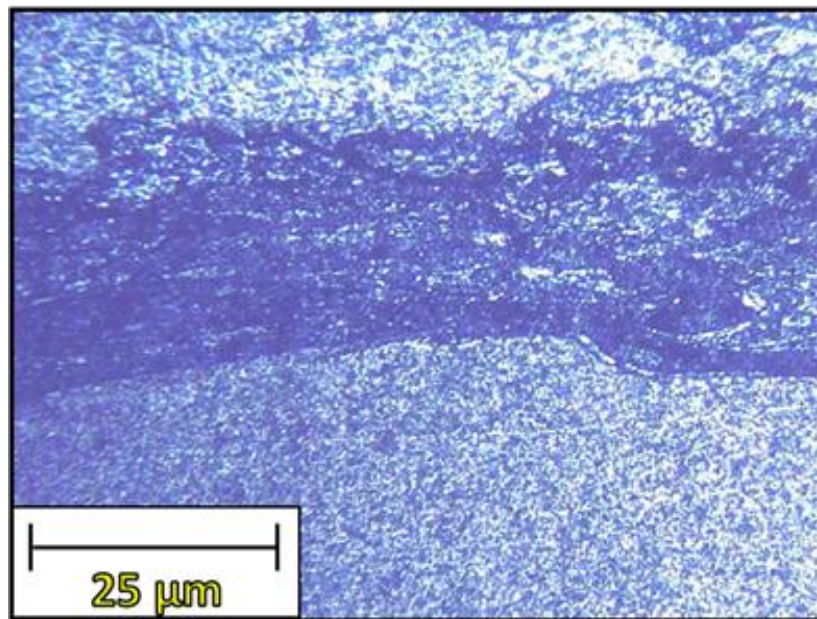


Figure 115. Micrograph of the Thermo-mechanical zone (TMAZ) (magnification 125x)
Joint 57,8 Hz-40 MPa

Grain size measurements were performed on the transverse sections of welds in order to highlight the metallurgical evolutions the material underwent during the process. HAZ; TMAZ and welding zone were taken into account. First, the joints with AA2011 as top specimen were investigated. In particular, two tests having the same pressure of 40 MPa and frequencies of 45.6 Hz and 57.8 Hz, were considered. These tests are referred to two sound welds as reported in Figure 98.

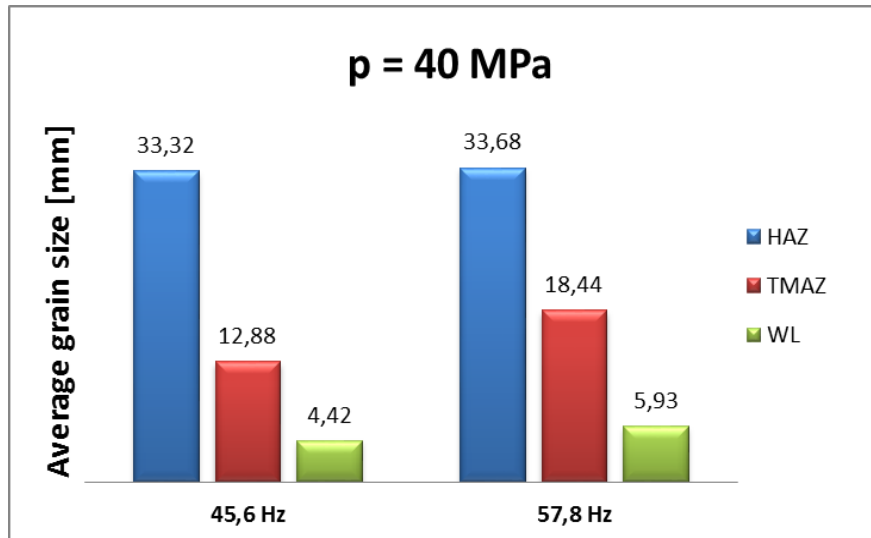


Figure 116. 2011 top - Average grain size with fixed pressure

Figure 116 shows that, although the tests are characterized by different frequencies, similar grain size values are noted in all the three zones. However, larger average grain size is observed for the joint characterized by $f=57.8\text{Hz}$, in the TMAZ and welding line area. The increase of grain size is due to grain growth phenomena enhance by the larger heat produced during the higher frequency. A second comparison was carried out with varying pressure and maintaining the frequency constant at 57.8Hz . In particular, two sound tests and one insufficient heat test were taken into account. Figure 117 shows how the pressure affects the recrystallization and consequently the bonding quality

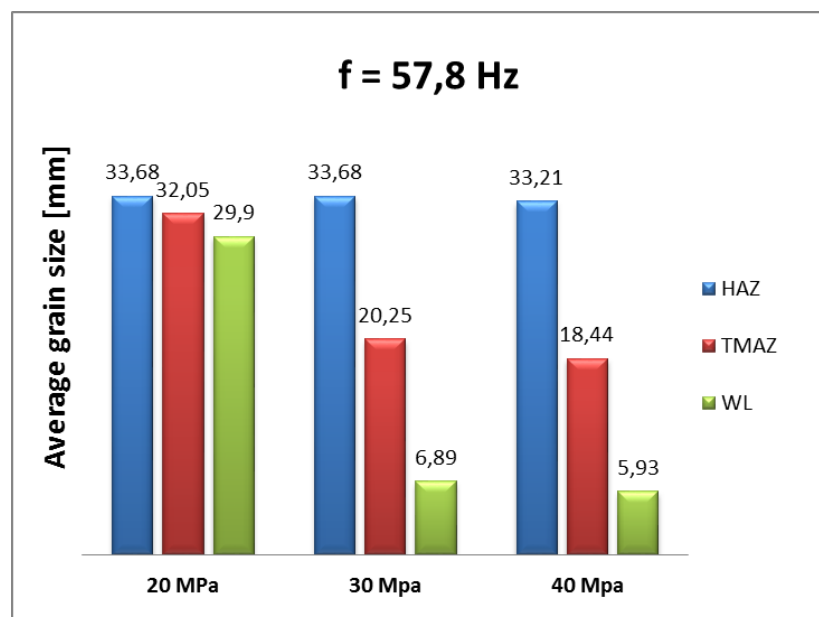


Figure 117. 2011 top - Average grain size with fixed frequency

With pressure equal to 20 MPa, no recrystallization is observed, indicating that both temperature and strain are below the required thresholds in order to activate DRX. As a consequence, similar average grain size values in the three different zones are observed. When pressure increases from 20 MPa up to 30 MPa, a sound joint is produced. This is confirmed by the average grain size trend, showing a decrease of about one order of magnitude in the welding line area. No significant difference is observed with further increasing pressure. As it will be shown in the numerical analysis paragraph, with increasing pressure the heat produced increases. However the flash produced increases as well thus enhancing thermal exchange with environment. In this way the actual temperature of the specimens does not significantly increase as it could be expected.

Finally, the average grain size was measured for the two different joints configurations, namely the mutual position of the two alloys. For the comparison, the joints characterized by $f=57.8$ Hz and $p=30$ MPa, corresponding to sound welds, were considered (Figure 98).

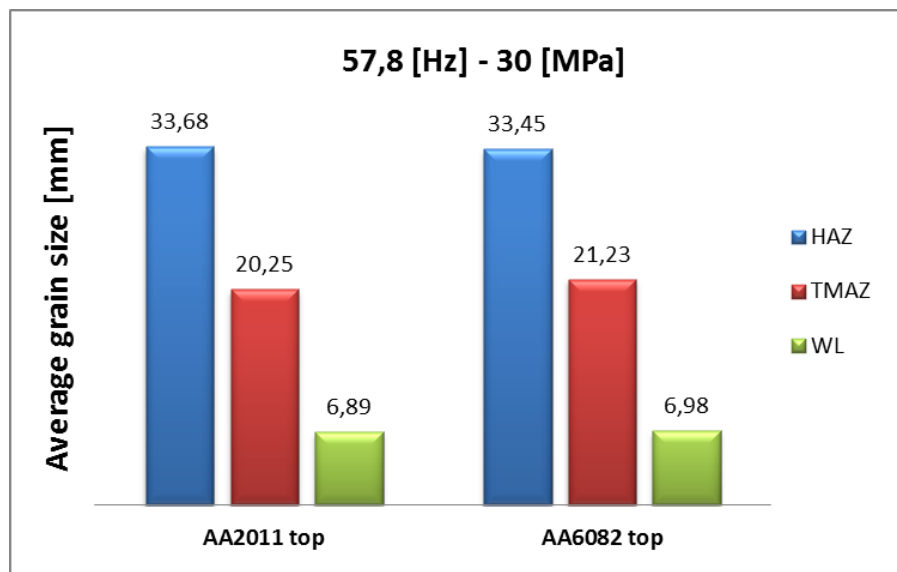


Figure 118. Average grain size with different configuration

Figure 118 shows that very similar values are found in the different zones. Further investigation is therefore needed. In the following, microhardness and EDAX analyses results will be presented.

4.3.1. Temperature trends analysis

In the following, just the AA2011 top – AA6082 bottom configuration is considered based on the micrographic analysis showing ineffective bonding for all the welds obtained with AA6082 as top specimen material.

AA2011 top – AA6082 bottom

Linear Friction Welding is a multistage process in which the thermal flow plays a fundamental role. In order to obtain a more detailed analysis of the process and to understand the influence of the two different materials, the temperature trend during the test was recorded. Figure 119 shows the acquired temperatures for each case study.

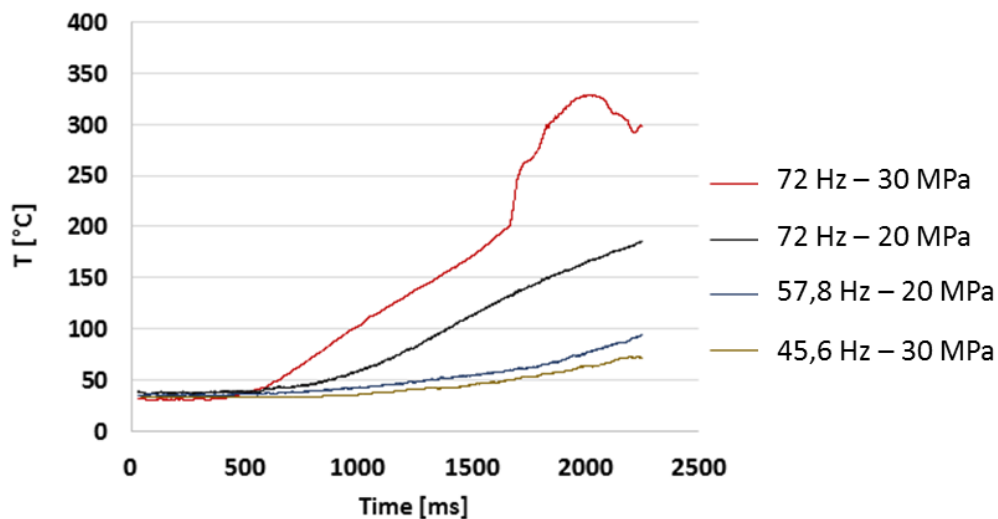


Figure 119. Temperature trend

Observing the temperature trends, it is possible to notice the substantial differences between the various joints in terms of generated heat. The joint obtained with $f=72\text{Hz}$ and $p=30\text{MPa}$ shows "instability" conditions. The measured temperature shows a sudden change of slope at about 1600ms. Due to the sudden shortening of the welding specimen, the thermocouple reached the welding interface before the complete collapse of the specimen itself. A maximum temperature of 350°C is measured. When $f=72\text{ Hz}$ and $p=20\text{MPa}$ are selected, a "sound" joint is produced. The trend curve of this test shows a constant increase till the end of the oscillation with maximum temperature of 200 °C. The interface temperature, which can be estimated through the developed numerical model around 350°C (see the next paragraph), is lower than the previous case thus not causing instability. It is noted that the curves shown were taken at a distance of

6 mm from the interface. The measured temperatures, except for the instability case, are lower due to not only of the distance between thermocouple at the junction surface, but also as the temperature is influenced by the conduction and radiation phenomena occurring. The other two trends are related to tests conducted with frequency of 45.6 Hz and 57.8 Hz, with pressure equal to 30 MPa and 20 MPa, respectively. These parameters result in insufficient heat conferred to the joints. Similar temperatures are observed for the two welding conditions with maximum value below 100°C.

4.3.2. Microhardness analysis

HV Microhardness tests were carried out, for the mixed joints, considering the same measurement points used for similar joints (see Figure 95). In particular, a load of 0.5 kg applied for 30 s and a distance between the measurement points of 0.5 mm were selected. The HV profile shown in Figure 120 was obtained for a sound joint welded with $f=57.8\text{Hz}$ and $p=30\text{MPa}$ having the AA2011 as top specimen material.

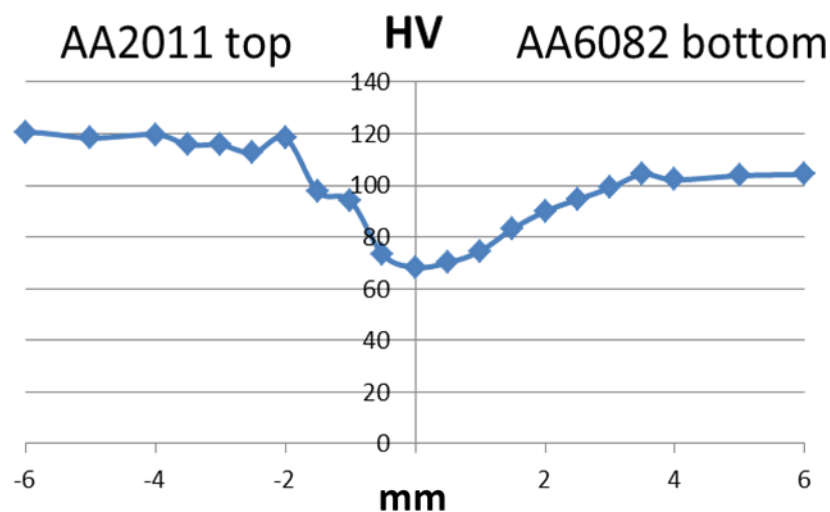


Figure 120. AA2011 top: $f=57,8\text{ Hz}$, $p=30\text{ Mpa}$

As it can be observed, the hardness of the base material is found at a distance of about 3.5 mm from the interface, i.e. 120HV for AA2011 and 100HV for AA6082. In the central part of the joint, which is about 7 mm in height, a smooth transition is observed with a minimum value found at the welding centerline. This trend indicates that proper mixing occurred.

Figure 121 shows the HV profile for the only sound joint obtained when AA6082 is the top specimen material. A similar trend is found, with a smaller extension of the central area where actual mixing between the two materials occurs. This indicates that lower mechanical properties are expected for this joint. The minimum value, equal to about 75HV and observed in correspondence of the interface, is comparable to the one found for the previous case study.

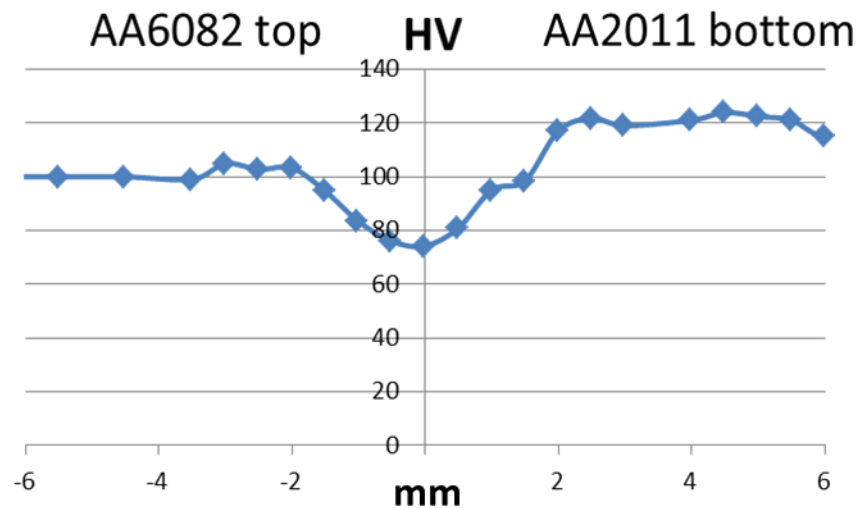


Figure 121. AA6082 top: $f=57.8$ Hz, $p=30$ Mpa

Finally, Figure 122 shows the microhardness profile obtained for joint characterized by incipient bonding, i.e. $f=57.8$ Hz and $p=20$ MPa, AA6082 top. A completely different behavior can be observed. The bottom specimen, i.e. shows no variation till the interface, indicating that the specimen did not participate to the bonding process and that material mixing was largely insufficient. As far as the top specimen is regarded, some softening is observed at a distance of about 2mm from the weld interface. Although AA6082 is somewhat involved by material flow and deformation, the extension of the area is small and only incipient bonding conditions are reached.

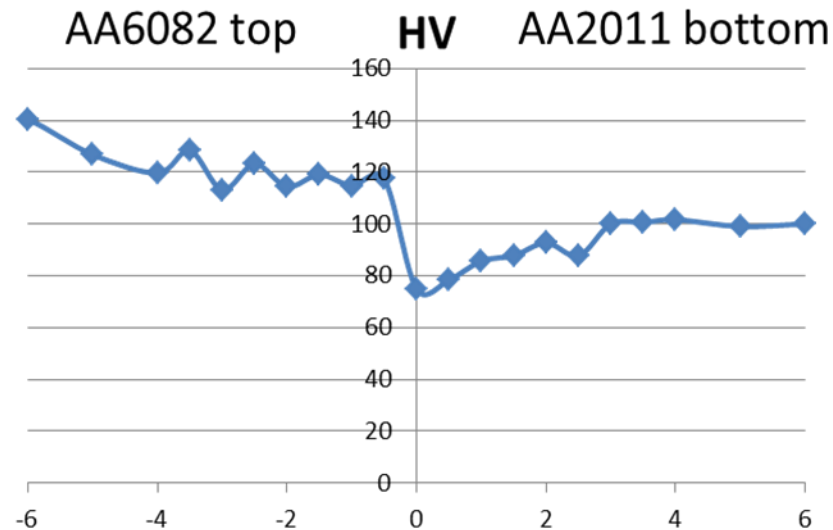


Figure 122. Incipient bonding, 57,8 Hz, 20 Mpa

4.3.3. EDAX analysis

A scanning electron microscope was used for the EDAX analysis to investigate in detail the possible atomic transmission between the two alloys.

In order to observe the atomic transmigration, copper (Cu) was selected as “spy-element”. This element, as shown in the chemical composition of the two alloys, is present in AA2011 only.

The following Figure 123 shows the concentration close to the welding line for the joint obtained with $f = 57.8$ Hz and $p = 30$ MPa.

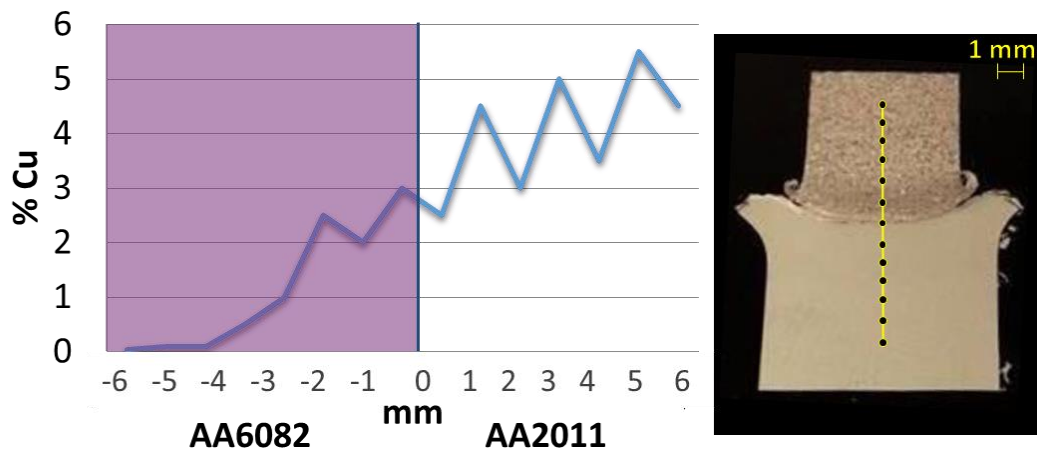


Figure 123. Joint 57,8 Hz, 30 Mpa

It is noted that a percentage of Cu in the range of 2%-3% is found in the bottom specimen, i.e. in the AA6082. This indicates that during the welding operation the thermo-mechanical action exerted on the two materials created a transition zone within which intermediate properties are found with respect to the two base materials.

In turn, the analysis results for the joint welded with $f=57.8$ Hz and $p=20$ MPa show a sharp separation between the two specimen, as no Cu is found in the bottom specimen. This confirms the hypothesis done based on the micrographic analysis (see again Figure 124) according to which only “incipient bonding” occurs and no sound weld is produced.

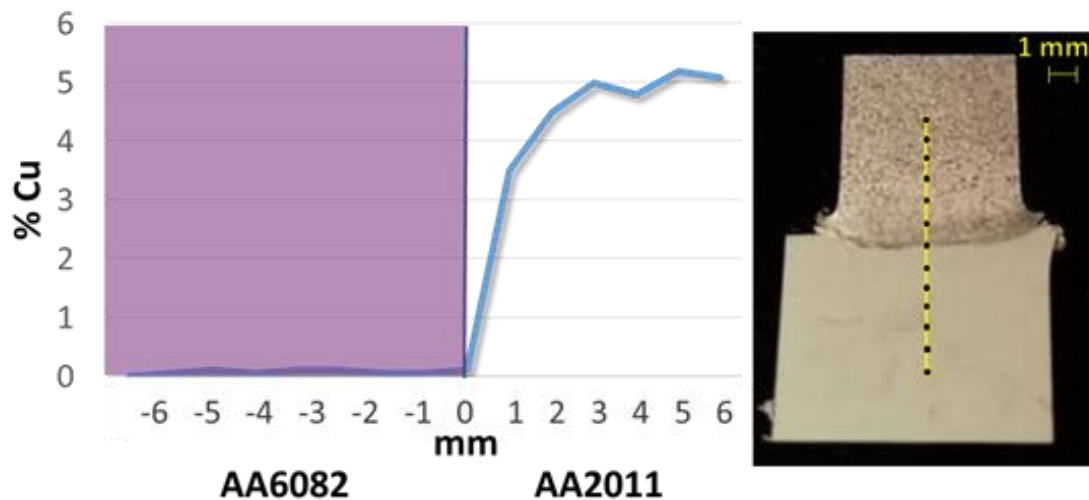


Figure 124. Joint 57,8 Hz, 20 Mpa

4.4. Numerical Analysis

With the development of computer technology and numerical analysis, the finite element simulation has become a reliable technique for the prediction of field variable distribution due to a manufacturing process.

Linear Friction Welding is characterized by a complex process mechanics. A reliable numerical model of the process can represent an essential tool for effective process design as well as a challenge for the researcher. In order to simulate the Linear Friction Welding process DEFORM3D has been used. In particular, the effects of the oscillation frequency and pressure on the temperature, strain and strain rate distribution has been studied.

In order to properly model the LFW process, the developed numerical tool must possess a number of specific features:

- *Thermo-mechanical coupling*: the process can be separated into a thermal and mechanical problem to be solved with a staggered approach (DEFORM 3D) during each step of the analysis. The work done by the

friction forces in the mechanical analysis affects the temperature field which, in turn, influences the mechanical properties of the material and the behavior of the parts to be welded. A Lagrangian implicit approach was selected in order to properly address the above-described needs.

- *Non-linear material model*: the first papers regarding numerical modeling of LFW used simple analytical models [49]. These researches have shown that the materials properties significantly affect the field variable distribution.
- *Complex thermal boundary conditions*: includes the heat exchange at the interface between the specimens, the heat losses to the environment by convection and conduction within the specimen. The "Heat transfer" option activates the calculation of heat transfer between the objects and the environment and the heat generation due to deformation and friction.
- *Complex mechanical boundary conditions*: includes the variation of the contact surface between the specimen, due to the sinusoidal movement of the specimens, and the variation of the friction coefficient as a function of time and/or temperature.

The two parts to be welded were modeled as two different objects, namely, a plastic specimen on which acts the compression force and a rigid one possessing the oscillatory movement. This choice was made in order to simplify the contact condition avoiding numerical instabilities due to the deformable-deformable object contact.

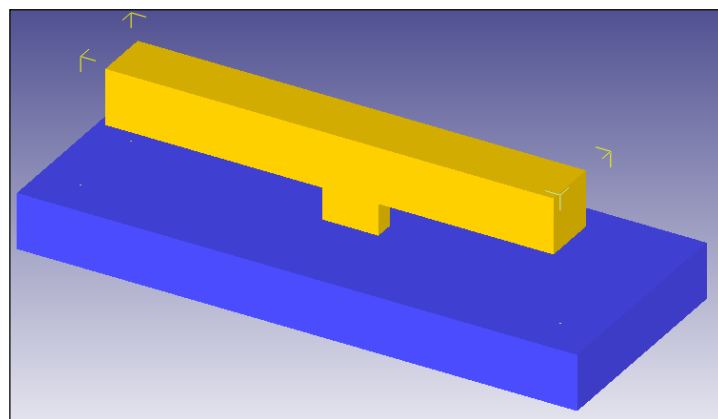


Figure 125. Rigid (down) and plastic (up) elements

As far as the plastic object is regarded, a tetrahedral elements discretization was used, with three refining mesh windows placed close to the contact surface in

order to obtain good accuracy without excessively increasing the CPU time. An average length of 0.25 mm was selected for the elements near to the sliding surface.

The specimen is constrained against x and y translation for 7/8 of its height for increased stability (Figure 126), while an axial load was imposed on the top surface of the workpiece along the z axis.

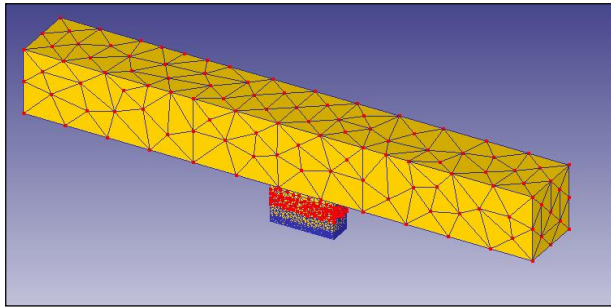


Figure 126. The mesh and the nodes blocked (red dots) on the plastic element

A symmetry plane parallel to the oscillation direction (y-axis) was used in order to reduce CPU time. Finally, heat exchange with environment was imposed on the lateral surfaces of the object.

The rigid object oscillates along y-axis. The motion equation is the one calculated for the experimental machine as shown in Figure 48. Table data were used to reproduce the experimental motion curve.

For all simulations, the aluminum alloy AA6082 was used. The thermo-mechanical characteristics were taken from literature [62].

The following constant values were used:

- *Thermal conductivity* equal to $180 \text{ W}\cdot\text{m}^{-1}\cdot\text{K}^{-1}$.
- *Heat capacity* equal to $2,43 \text{ J}\cdot\text{K}^{-1}$
- *Young' modulus* equal to $68947 \text{ N}\cdot\text{mm}^{-2}$;
- *Poisson's number* equal to 0,3;
- *Coefficient of thermal expansion* equal to $2,2\cdot 10^{-5}$

Regarding the contact between the two objects, a shear model was considered:

$$\tau = m * \tau_0$$

where τ is the shear stress, τ_0 is the shear yield stress and m is the friction factor. In other words, the friction is a function of shear yield stress of the deformed body at given temperature, strain and strain rate conditions.

As far as the contact between the two objects is regarded, the considered shear friction model was a function of temperature, with the m factor of the friction shear model reaching a steady value of 0.95 for temperature values larger than 400°C. Finally it suddenly drops in the proximity of the melting temperature, i.e. above 550°C [49].

The time step was set to 0.001 sec. An automatic remesh was imposed each 25 steps in order to avoid convergence issues due to the high strain rate at the contact surface.

The same tests conducted during the experimental campaign on this alloy (reported in Figure 65) were considered for the numerical analysis. Two different values of oscillation frequency and three of interface pressures, resulting in six different case studies, were selected. In particular, the axial pressures on the top surface of the top specimen assumed values of 30MPa, 40MPa and 50MPa. While for the oscillation frequency 45Hz, 58Hz were used. Additionally, the test characterized by $f= 36\text{Hz}$ and $p= 30\text{MPa}$, reported as “insufficient heat” during the experimental campaign, was simulated. No instability condition was considered as convergence problems arise due to self-contact and folding occurring in the deformable object. Figure 127 shows the experimental and numerical campaigns conducted on AA6082.

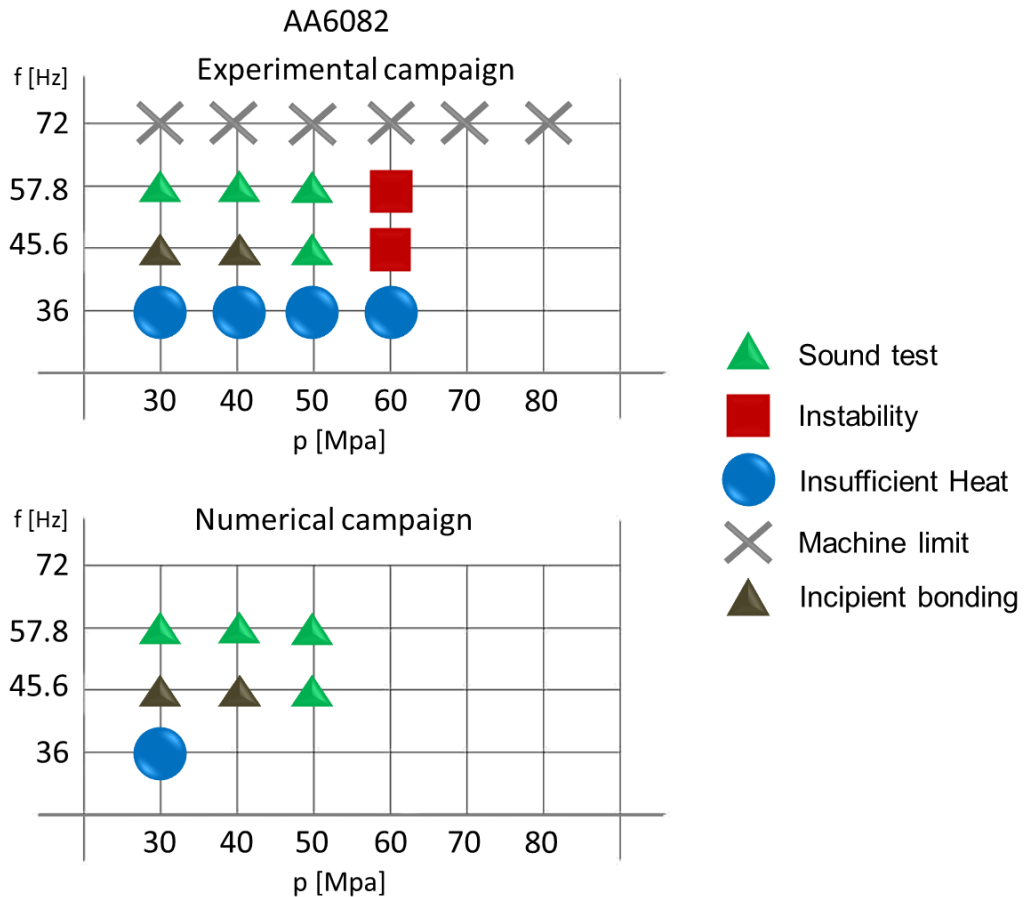


Figure 127. Experimental and numerical campaigns

In the following, the results and discussion and the comparison with the experimental evidence are reported.

The maximum axial shortening measured, after the welding process, has been used to study the effect of the process parameters. During the process a certain amount of axial shortening occurs, due to the extrusion of the plasticized material expelled from the welding surface as flash form. Figure 128 shows a typical plot of axial shortening during the process.

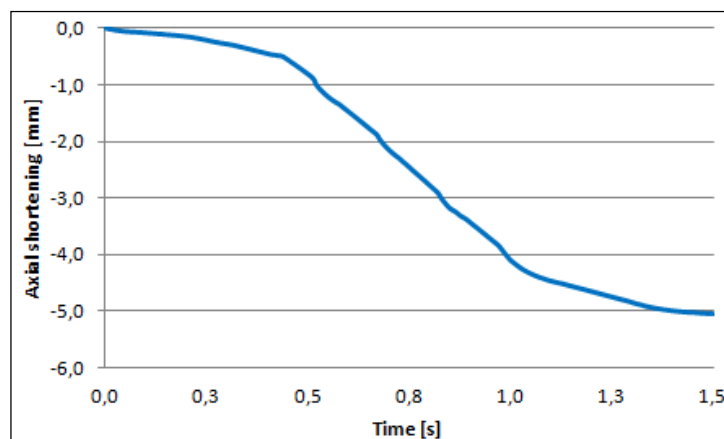


Figure 128. Typical axial shortening, 58 Hz and 50 MPa

After about 0.5 seconds, the material reaches a soft state and collapses under the pressure applied.

Figure 129 shows the axial shortening trend obtained with fixed pressure ($p=30$ MPa) and variable axial shortening. An almost negligible axial shortening is observed for the “insufficient heat” test, i.e. $f=36$ Hz, being the curve almost flat. This indicates that the equilibrium phase of the process was not reached. In turn, a change in the slope of axial shortening for the other case studies indicating that softening of the material occurred and flash is expelled. Finally, it is observed that axial shortening significantly increases with the largest frequency value, i.e. $f=58$ Hz.

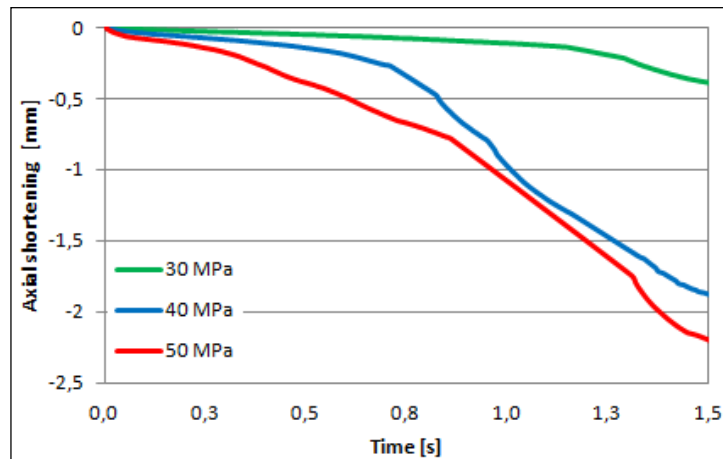


Figure 129. Axial shortening, 30 MPa

Figure 130 shows the increasing of axial shortening with increasing pressure and fixed oscillation frequency equal to 45Hz.

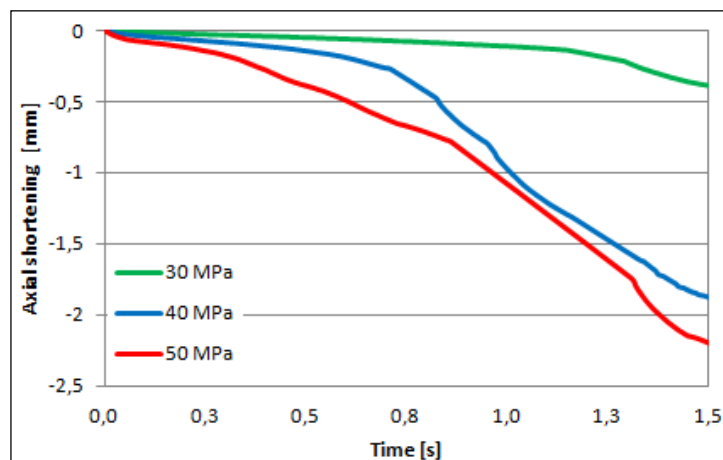


Figure 130. Axial shortening, 45 Hz

Comparing the previous results with the ones obtained when frequency is equal to 58Hz (Figure 131), a significant increase in axial shortening is observed. In

particular, with $f=58$ Hz the final height of the specimen is reduced by half, i.e. 5mm. In this case, the selected process parameters leads to sort of “threshold” between sound and instability conditions.

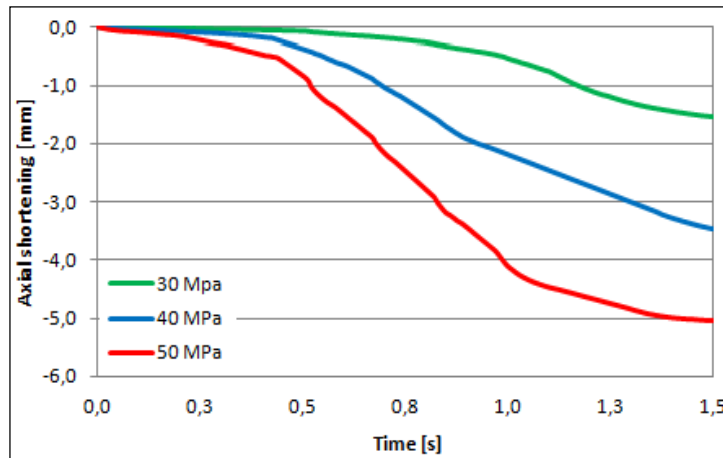


Figure 131. Axial shortening, 58 Hz

Figure 132 shows a comparison of the final axial shortening as function of pressure and frequency.

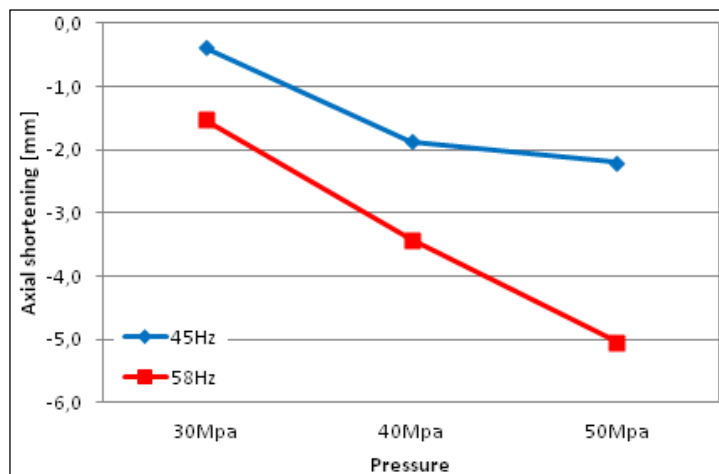


Figure 132. Axial Shortening at the welding end

Form the above figure, it can be concluded that the axial shortening increases with increasing pressure and the frequency of oscillation.

In the following a comparison of the flash (shape and length) obtained by experimental analysis and numerical simulation is carried out.

The weld quality has been studied through the parallel observation of the temperature reached after 1.5 seconds, namely when the oscillation of the rigid element is stop, and flash morphology.

First, the “insufficient heat” case study is examined. When $p=30$ MPa and $f=36$ Hz maximum temperature does not exceed 250 °C (on the welding surface). Additionally, no flash is extruded form the lateral surface of the specimen. As

expected, the joint is not welded, and this hypothesis was confirmed by the experimental test.

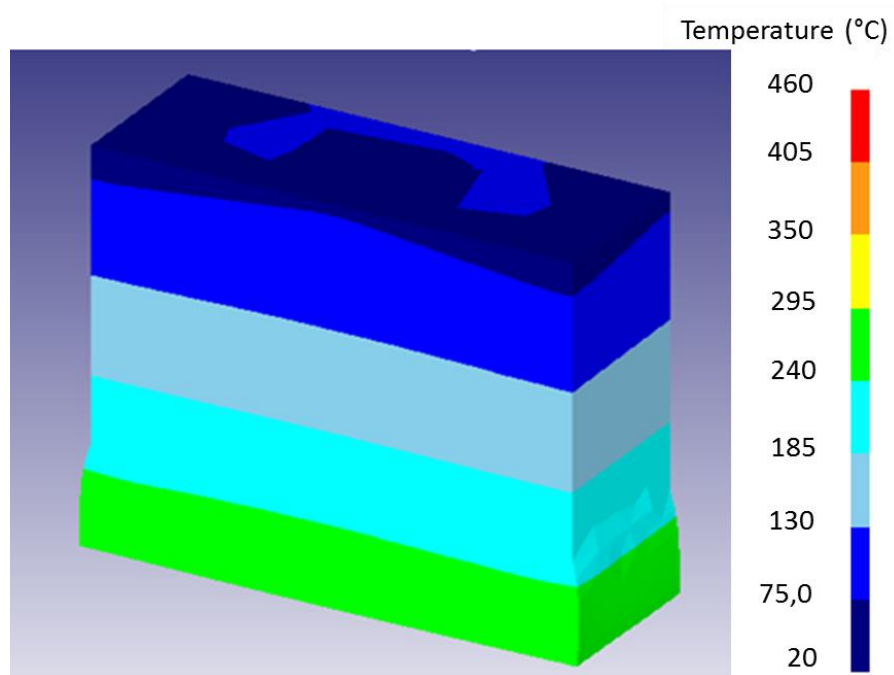


Figure 133. Temperature distribution, 36 Hz and 30 MPa

Looking at the strain distribution at the interface, almost zero deformation is calculated all over the surface indicating that just a “rubbing” of the surfaces occurred (Figure 134).

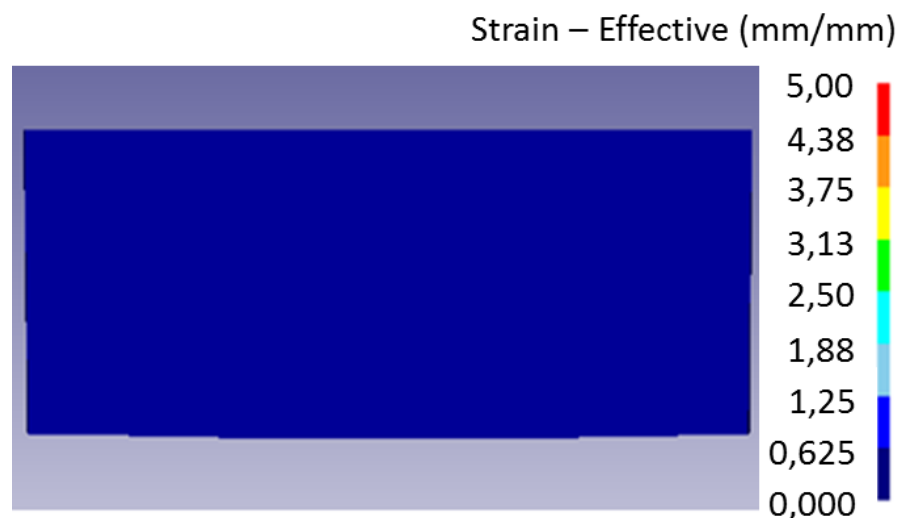


Figure 134. Strain distribution at the interface, 36 Hz and 30 MPa

As sound welds are taken into account, a comparison between experimental results and numerical simulation is reported in Figure 127. In particular, the specimen geometry after the process was considered for the case study characterized by pressure equal to 30 MPa and frequency of 45Hz.

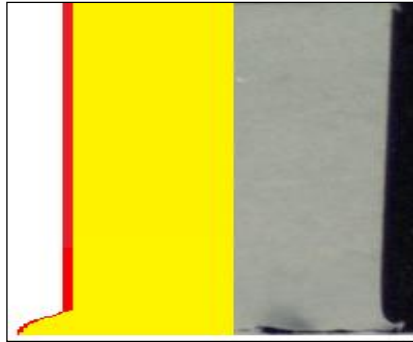


Figure 135. Experimental-numerical comparison of specimen geometry, 45 Hz and 30 MPa

The maximum temperature reached is about 310 °C, allowing a sufficient a certain material softening. However, due to the relatively low pressure, only a small amount of flash is visible both in the experimental profile and in the calculated one. The welding line is not continuous in the transverse section and “incipient bonding” conditions are reached.

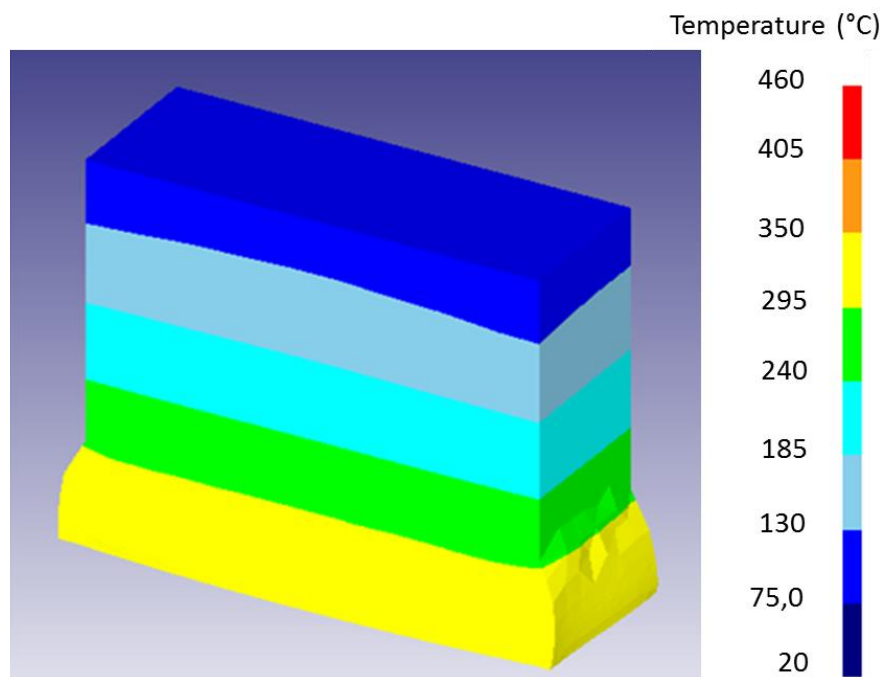


Figure 136. Temperature distribution, 45 Hz and 30 MPa

Once again, the strain distribution shows extremely low values indicating unsatisfying bonding conditions.

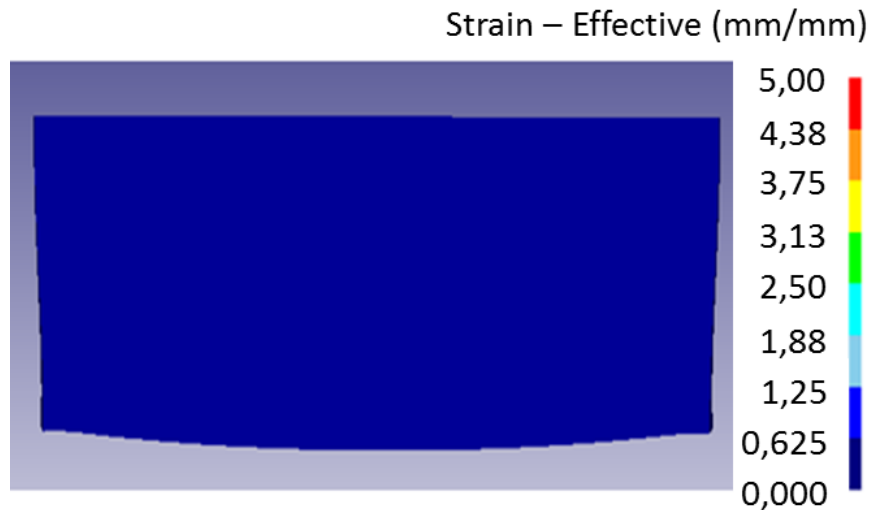


Figure 137. Strain distribution at the interface, 45 Hz and 30 MPa

Figure 138 shows the joint obtained with the same oscillation frequency, namely 45 Hz, but with higher pressure, equal to 40 MPa. Greater flash formation is observed. Although joint strength and weld quality increase with increasing interface pressure, still a poor weld is produced.

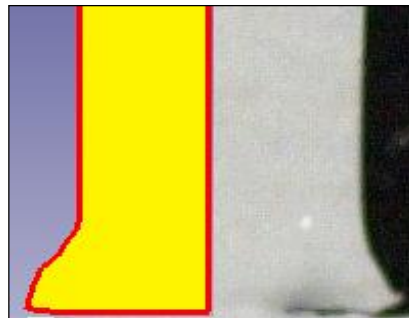


Figure 138. Experimental-numerical comparison, 45 Hz and 40 MPa

In Figure 139 the temperature distribution is shown. The maximum temperature is about 330°C, i.e. about 30°C more than the previous case study. However the obtained conditions are still not sufficient to obtain full welding of the cross section.

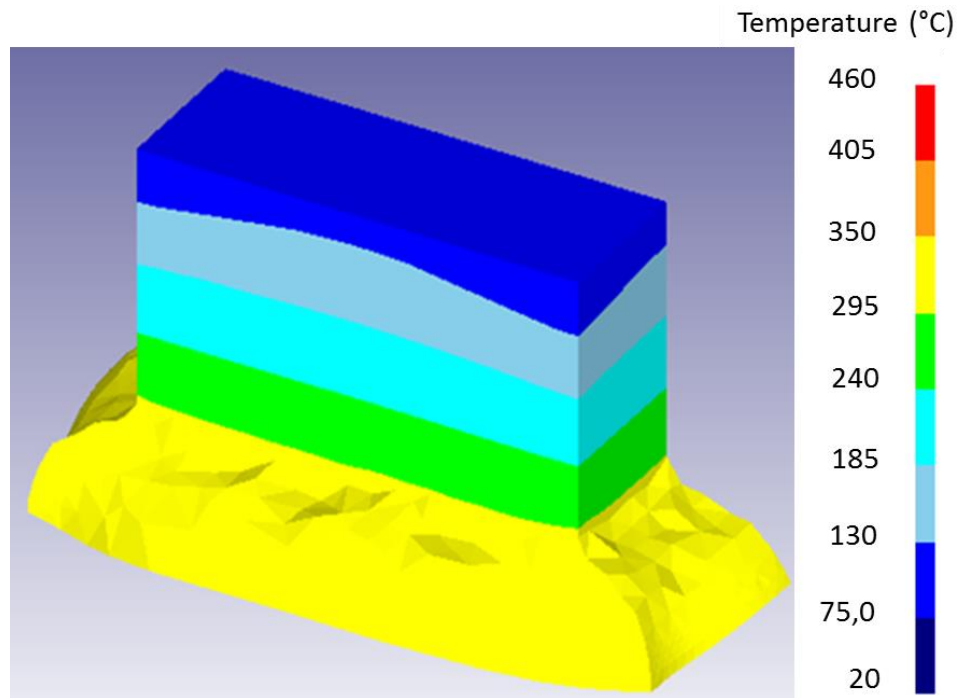


Figure 139. Temperature distribution, 45 Hz and 40 MPa

Looking at the effective strain distribution (Figure 140) a significant increase is observed.

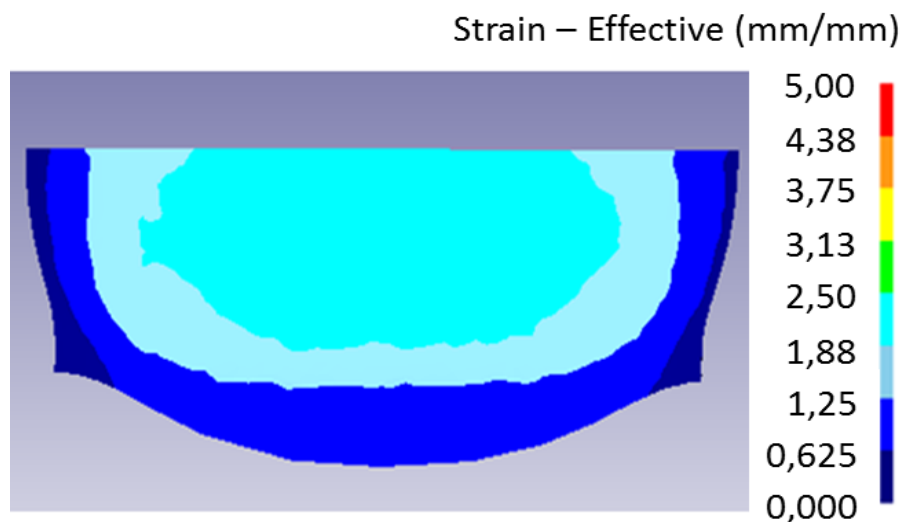


Figure 140. Strain distribution at the interface, 45 Hz and 40 MPa

Even if the specimen reaches temperatures only slightly higher with respect to the previous case, the greater pressure applied not only favors the greater flash formation, but also a better welding quality. This means that the welded joint is stronger than the previous. The weld obtained with these parameters can be considered as a limit between poor joint and complete welding.

As pressure is increased to 50 MPa, good flash formation is obtained (Figure 141). Similarly to the previous case studies, the numerical model matched the experimental one with acceptable precision.

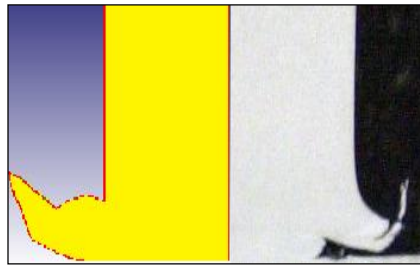


Figure 141. Experimental-numerical comparison, 45 Hz and 50 MPa

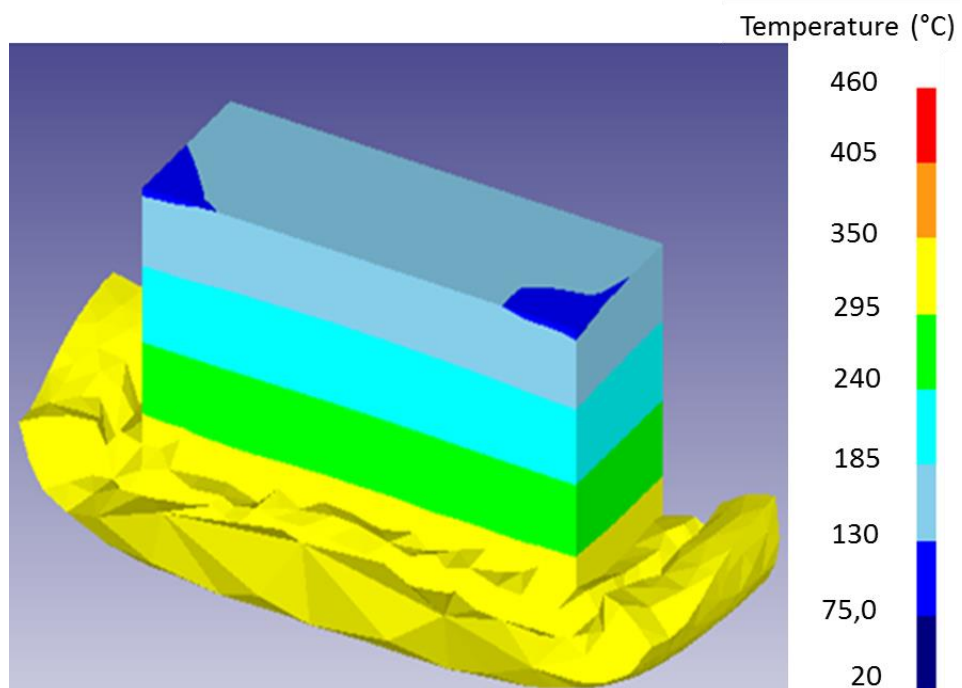


Figure 142. Temperature distribution, 45 Hz and 50 MPa

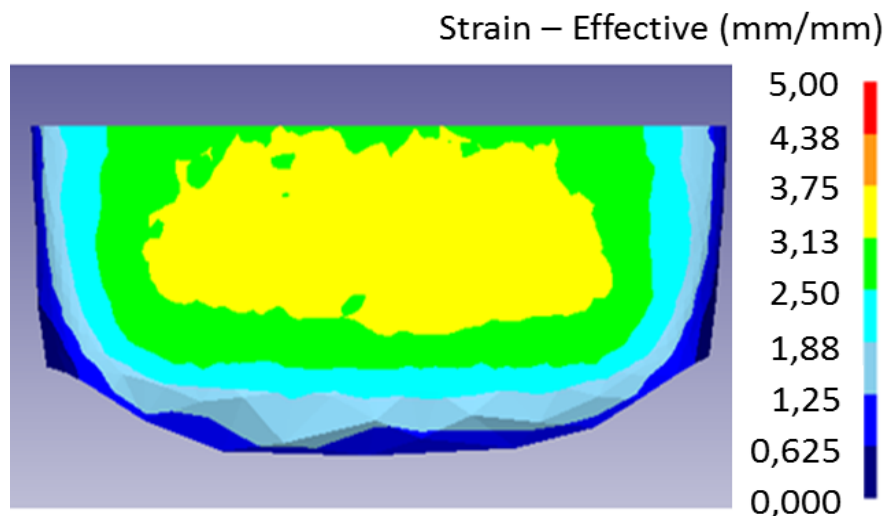


Figure 143. Strain distribution at the interface, 45 Hz and 50 MPa

Figure 142 and Figure 143 show temperature and effective strain distributions, respectively. Compared to the previous case study, although temperature does not increase significantly, the pressure increase favors the flash formation and the strain at the interface.

When oscillation frequency is set to 58Hz, flash formation is conspicuous even at low pressures. Figure 144, Figure 145 and Figure 146 show the obtained profile, the temperature distribution and strain distribution, respectively.

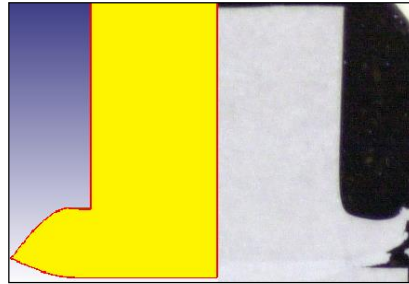


Figure 144. Experimental-numerical comparison, 58 Hz and 30 MPa

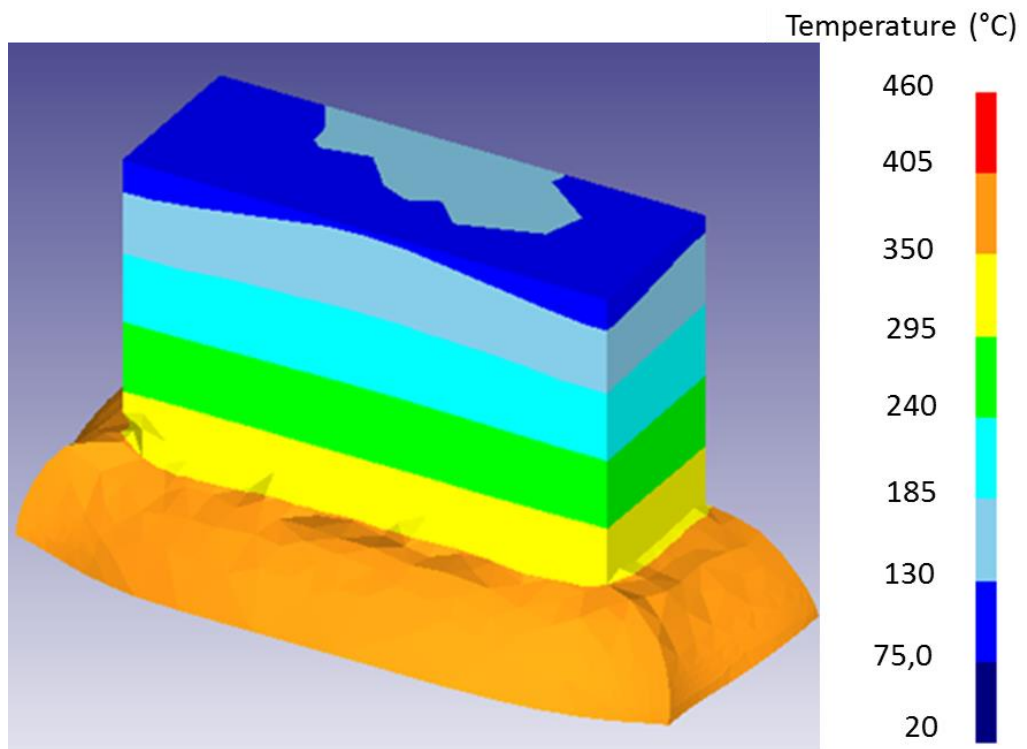


Figure 145. Temperature distribution, 58 Hz and 30 MPa

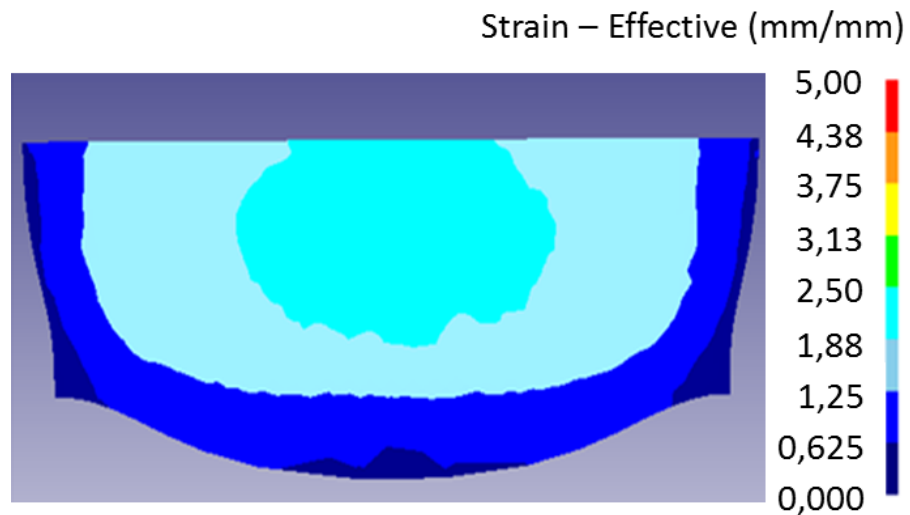


Figure 146. Strain distribution at the interface, 58 Hz and 30 Mpa

In spite of the low pressure applied, resulting in a maximum strain equal to 2, the joint shows a considerable temperature increase, which promotes the material softening and the consequent increase of flash formation. As shown in through the experimental micrographic analysis, this weld presents a good quality welding area with good integrity.

When pressure further increases, flash formation is enhanced and a significant amount of flash is produced (Figure 147).

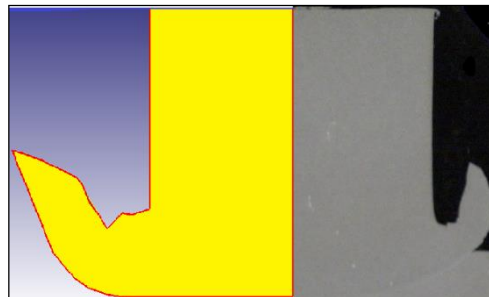


Figure 147. Experimental-numerical comparison, 58 Hz and 40 MPa

It is worth noticing that in the 3D isometric view showed in Figure 147, the external part of the flash is visible. Although a larger amount of heat is produced, when the material is extruded as flash, the latter is quickly cooled down by the surrounding environment. However, the undeformed part of the specimen is characterized by larger temperatures with respect to the previous case study.

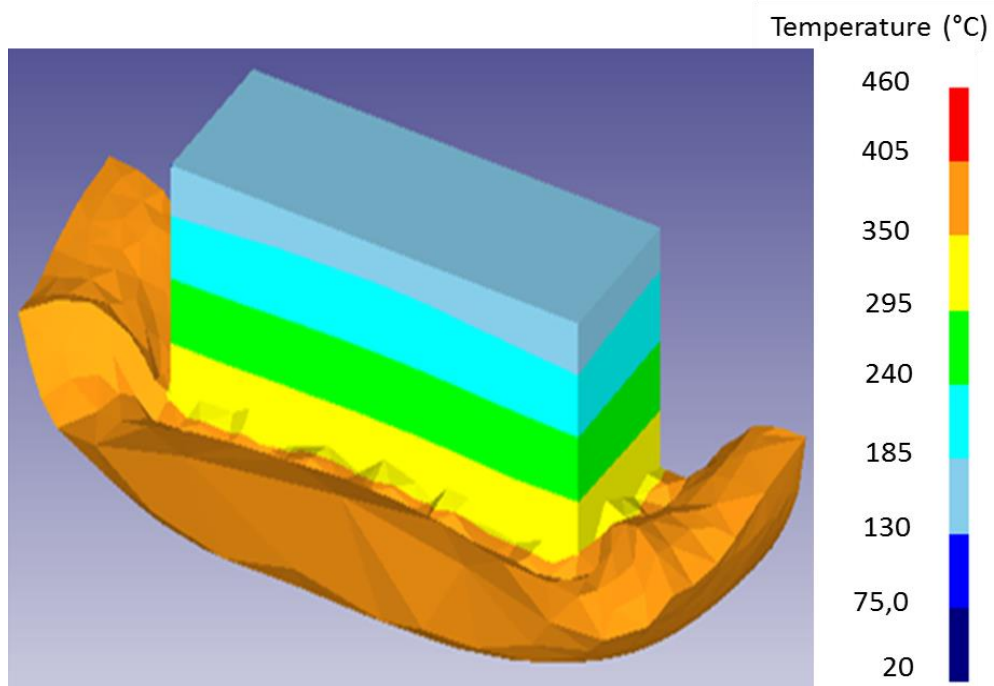


Figure 148. Temperature distribution, 58 Hz and 40 MPa

A significantly different effective strain distribution is observed. Two main zones can be identified: the zone still in contact with the bottom specimen experience very high strain values; on the other hand, the zones of the material belonging to the flash, which have been in contact with the bottom specimen for a smaller time, show lower values.

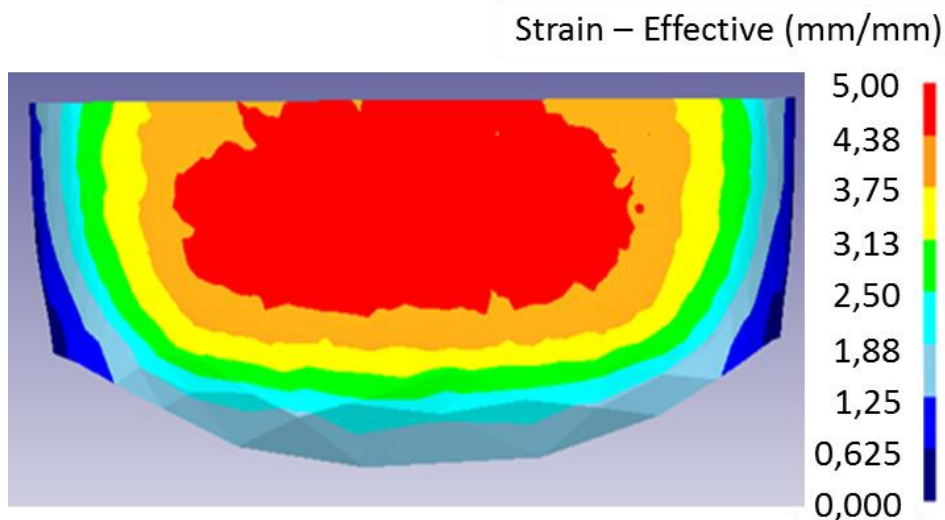


Figure 149. Strain distribution at the interface, 58 Hz and 40 MPa

A huge amount of flash, corresponding to a significant axial shortening equal to about 5 mm, is found when pressure further increases to 50 MPa (Figure 150).

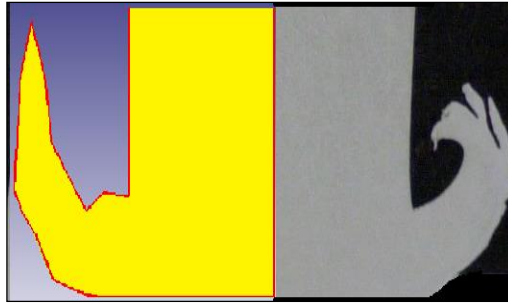


Figure 150. Experimental-numerical comparison, 58 Hz and 50 MPa

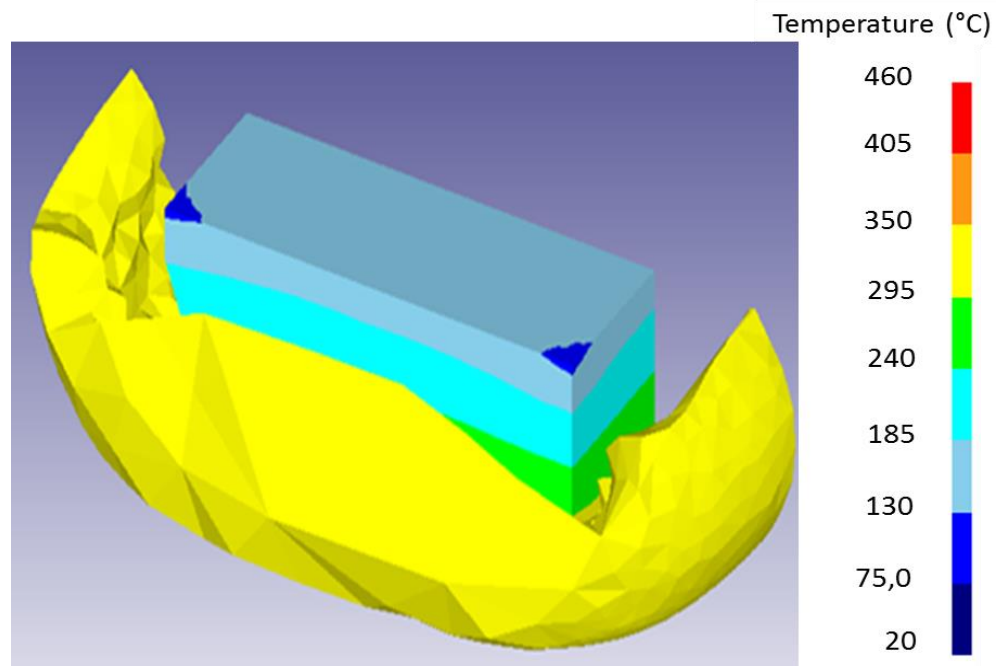


Figure 151. Temperature distribution, 58 Hz and 50 MPa

As already observed, in spite of the increased heat input, the 3D view shows a flash characterized by a lower temperature. Because of the high pressure and frequency, flashing begins soon after the test start. In this way the flash is cooled by the surrounding air for a longer time. Thus, the heat exchange with environment is enhanced by both larger surface and longer time. Consequently, temperature in the specimen is not higher than the one calculated for the previous case study.

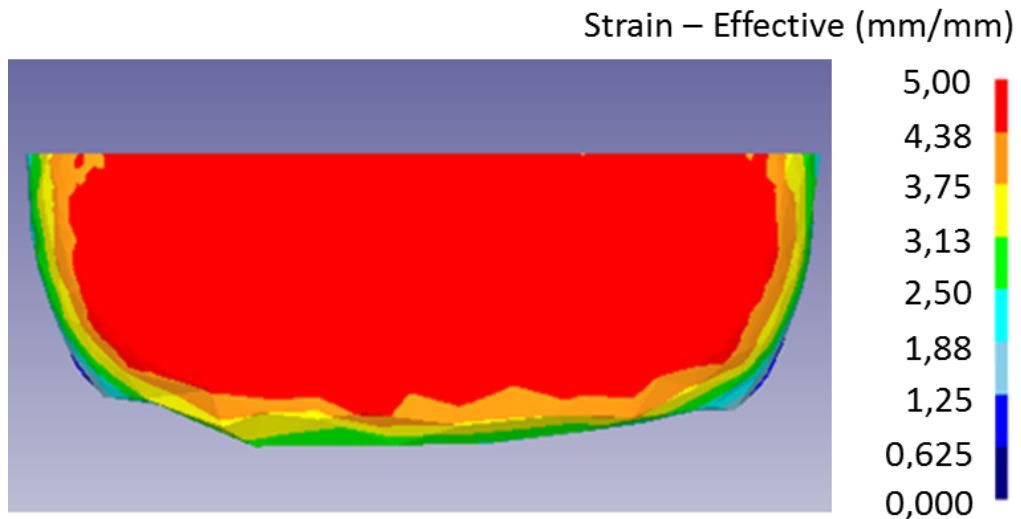


Figure 152. Strain distribution at the interface, 58 Hz and 50 MPa

Finally, the obtained results are summed up in a general overview of the temperature and effective strain at the welding interface at the end of the oscillation phase. Figure 153 and Figure 154 show the variation of the analyzed field variables as function of the process variables, namely applied pressure and oscillation frequency. It is known that the heat input increases with increasing both pressure and frequency. However, temperature increases only with increasing frequency. As previously explained, when larger pressure values are utilized, the flash amount increases thus enhancing heat exchange with environment.

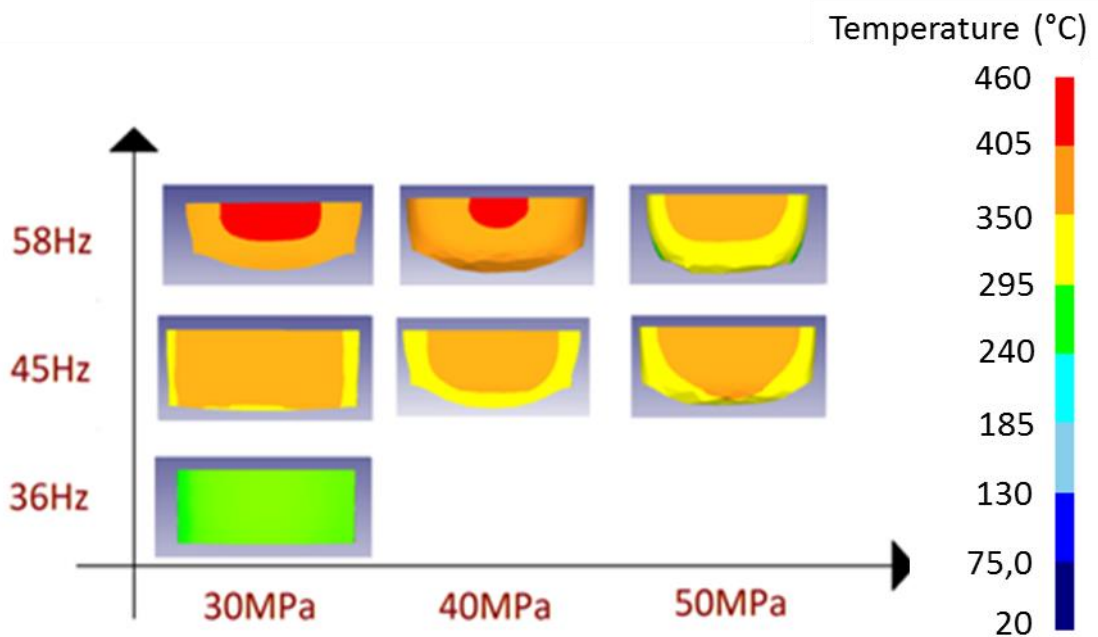


Figure 153. Temperature overview

In turn, effective strain increases with increasing heat input to the weld, i.e. with increasing pressure and frequency. In this way it can be stated that effective strain can be used as a valid indicator of the flash produced. Only proper combination of both strain and temperature are needed in order to obtain a sound joint.

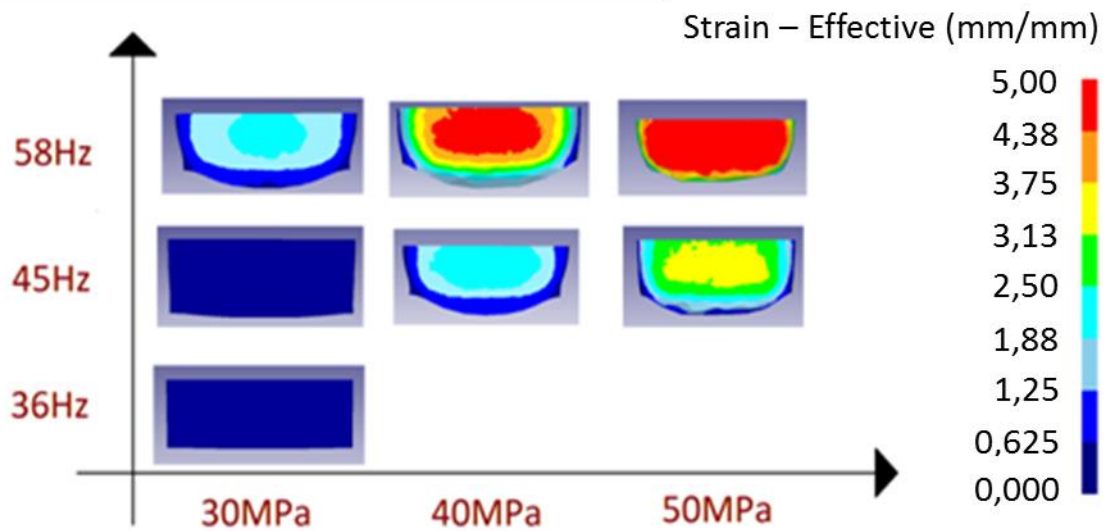


Figure 154. Strain effective overview

5. Accumulative Roll Bonding

5.1. Process description

Severe Plastic Deformation (SPD) is a promising technique for the production of bulk metallic material with an ultrafine grain (UFG) structure because it introduces a very large plastic strain, while maintaining the original geometry. The most important strengthening mechanisms, which lead to the high strength of materials processed by any SPD technique, are work hardening induced grain refinement. The innovative potential of UFG materials for advanced applications in engineering and medicine is high, and the production of these materials is becoming more and more economically feasible [78]. By increasing the production rate, UFG materials can be widely used for industrial applications.

Accumulative Roll-Bonding is a relatively new severe plastic deformation (SPD) process, which was originally introduced and developed by Saito in 1998 [74]. The ARB process shown is schematically represented in Figure 8. The process is cyclical; the main phases of the process are:

- *Wire brushing* of sheet surfaces in order to remove the oxide layer;
- *Stacking of two sheets* on top of each other;
- *Rolling*
- *Sheet cutting*

A strip is neatly placed on top of another strip. The adjoining surfaces of the two sheets are pre-treated in order to enhance bond strength. The two layers of material are joined together by rolling, as in a conventional roll-bonding process. Then, the rolled sheet is cut along the direction perpendicular to the rolling one in order to obtain two identical sheets. The cut strips are again surface-treated, stacked and roll-bonded. The whole process is repeated for a fixed number of times. In most cases, the process is repeated up to 10 times.

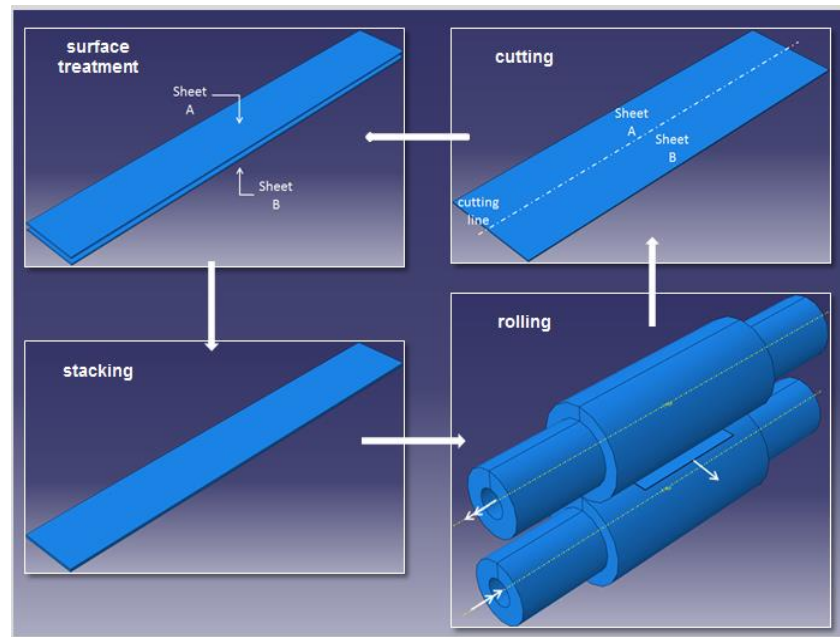


Figure 155. Schematic illustration of the ARB process

The process should be conducted at an elevated temperature below the re-crystallization temperature because the latter eliminates the effects of accumulated strain [80]. Too low temperature would result in insufficient ductility and bond strength. Furthermore, there is a critical rolling reduction in one pass roll-bonding, below which it is difficult to achieve sufficient bonding. The critical reduction depends on the materials and processing temperatures. Usually, more than 35% reduction for each pass is necessary, so that the rolling-force becomes bigger when compared with the conventional rolling.

Sheet deformation mainly occurs in the rolling direction. There is no need for an increase in the sheet width since the sheets are wide enough and the broadening is prevented by high frictional resistance. It should be pointed that if the sheets metal are relatively wide, it can be assumed that there is only an increase in length and no increase in the width of a sheet during rolling. The increase in width [81] can therefore be considered as negligible when the width is much bigger than the length of deformation zone.

The following expression must be verified: $b/l \geq 10$.

During roll bonding the number of single layers increases according to the following power law equation:

$$n = 2^N$$

In the equation, n indicates the number of sheet layers while N is the number of ARB cycles.

The thickness of each layer can be calculated from:

$$t = \frac{t_0}{2^N}$$

Where t_0 indicates the initial sheet thickness and t the final thickness of the individual layer.

Therefore, the total reduction r_{tot} after N cycles can be calculated as:

$$r_{tot} = 1 - \frac{t}{t_0} = 1 - \frac{1}{2^N}$$

After 10 ARB cycles with 50% thickness reduction per cycle, a 1 mm thick sheet is formed by 1024 individual layers, each having a theoretical thickness of 1 μm , while the total reduction approaches 100%. Assuming von Mises yield criterion and plane strain condition, the total equivalent strain after N cycles can be calculated according to equation.

$$\varepsilon = \left\{ \frac{2}{\sqrt{3}} \ln\left(\frac{1}{2}\right) \right\} \times n = 0.80n.$$

Table 6 includes the relevant geometrical changes that take place during accumulative roll bonding of two 1 mm thick sheets, with a thickness reduction of 50% reduction per cycle [74].

No. of cycles	1	2	3	4	5	6	7	8	9	10	n
No. of layers	2	4	8	16	32	64	128	256	512	1024	2^n
No of bonded boundaries	1	3	7	15	31	63	127	255	511	1023	$2^n - 1$
Layer interval (μm)	500	250	125	62.5	31.2	15.6	7.8	3.9	1.9	0.96	$1000/2^n$
Total reduction (%)	50	75	87.5	93.8	96.9	98.4	99.2	99.6	99.8	99.9	$(1 - 1/2^n) \times 100$
Equivalent strain	0.8	1.6	2.4	3.2	4.0	4.8	5.6	6.4	7.2	8.0	$\left(\frac{2}{\sqrt{3}} \ln 2\right) n = 0.8 n$

Table 6 Geometrical change of the materials during the ARB where two piece of the sheets 1mm thick are roll-bonded by 50% reduction per cycle [74]

The most serious problem in ARB processes is the fracture of the sheets. Because a large amount of total plastic strain is accumulated in the materials and the rolling is not a hydrostatic process, edge-cracks sometimes occur in the

sheets especially with large number of cycles. In some materials, as Aluminum-Mg alloy, the edge cracks propagate into the center of the sheets. In this case, it becomes impossible to proceed to subsequent cycles. However, there are several techniques to avoid such cracking, and sound bulky sheets can be fabricated by ARB with most of the metallic materials.

5.2. Process parameters

Different parameters influence the effectiveness of the ARB process. The latter can be quantitatively evaluated through the analysis of microstructure and mechanical properties. The most important ARB process parameters include: process temperature, percentage reduction per cycle, number of ARB cycles, roll diameter and roll speed, initial material condition before rolling, surface roughness of the sheets as well as oxide layer.

5.2.1. Temperature

Process temperature is a key variable influencing the microstructure, thermal stability, mechanical properties as well as the quality of the metal sheet bonding. An optimal process temperature usually has to be determined for every material. It is trade-off between good bonding and a good thermal stability. The highest hardness is reached when the rolling is performed at the lowest possible temperature, although, for aluminum alloys, better bonding is obtained at temperatures higher than 200° C. The reasons for softening include dynamic recovery and/or partial re-crystallization during pre-heating and rolling. Higher temperatures enhance grain growth thus decreasing the potential for a rapid grain refinement. The sheet temperature affects bonding by influencing the adhesion of the oxide layer of the parent metal. In particular the strength of the bond between the oxide and the strip decreases with temperature with beneficial effects for the bonding quality.

5.2.2. Reduction per rolling cycle

Generally, 50% reduction per cycle is necessary for a good quality bond of aluminum alloy sheets, as well as other material such as titanium, interstitial free steel, or even aluminum-magnesium composites. Roll bonding below 50% thickness reduction results in low bonding strength or unsuccessful bonding between the sheets while values above 50% lead to edge cracking. Thus, the

optimal thickness reduction seems to be a compromise between good quality of the bond material and the minimal crack development at the edges.

5.2.3. Rolling cycles number

The increment in the number of ARB cycles results in hardness, yield and tensile strength increase. The strengthening mechanisms active in aluminum alloys include: solid solution strengthening, precipitation strengthening, grain boundary strengthening. During the first few cycles, the dominating strengthening mechanism is the work hardening. Later, the contribution of grain boundary strengthening becomes more a dominating strengthening mechanism due to the formation UFG microstructure. Usually, values in the range of 4-8 are used for aluminum alloys.

5.2.4. Roll diameter

Roll diameter directly influences the angular velocity of the rolls and the deformation area of the sheets. Smaller roll diameter leads to higher rolling speed, smaller deformation area and therefore higher roll pressures. The strength of bond decreases by increasing the rolling speed. This is due to the faster strain hardening of the surface asperities and shorter contact times between the asperities of the two surfaces to be joined. Initially, it was expected that the higher strain rate would result in a more effective grain subdivision process due to the higher dislocation density. However, irrespective of the deformation mode used, the grain size increased with an increment in strain rate. This was a consequence of the large amount of heat generated during the process. Some researchers believe that the grain size increased due to a mechanism of short-range grain boundary migration, which was attributed to heat generation during plastic deformation. On the other hand, it was also suggested that the high speed plastic deformation would be potentially a more effective grain subdivision process if the effect of heat could be minimized [75].

Higher roll pressures generally lead to better inter-lamellar bonding between the sheets. It has been hypothesized that the shear strength of the bond approaches that of the parent metal when the sufficient amount of energy (the activation Energy to initiate the bonding process) is provided to the two components that must be joined. This Energy may be provided by heating and/or by mechanical means.

5.2.5. Oxide layer removal

The removal of the oxide layer before roll bonding is important for good inter-lamellar bond strength between the sheets and the oxide particles may act as obstacles to grain growth. Early work showed that aluminum oxide breaks up into small particles due to the elongation process, during conventional cold rolling and leaves behind a newly generated metal surface. They are aligned to the rolling direction and form stringers outlining the original position of the foil surfaces. During ARB, the oxide layer is generally removed mechanically using a rough wire brush, leaving behind only a very thin oxide layer which will be broken up during ARB processing. The removal of an oxide layer is difficult especially for aluminum alloys because of the high aluminum affinity to oxygen and the extremely high rate of new oxide layers formation when aluminum is exposed to air. The oxide layer thickness also varies with the environmental temperature and the thin oxide layer which is still present after wire brushing.

5.2.6. Friction

The success of accumulative rolling strongly depends on the friction between the rolls and the sheet metal as the sheet has to be taken in by the rolls and pulled through the rolls. The influence of the friction with respect of the ARB process has not been investigated yet.

5.3. *Current state of the art*

SEVERE PLASTIC DEFORMATION

Severe plastic deformation (SPD) indicates to the class of fabrication techniques that produce nanocrystalline materials by means of plastic deformation often under high pressure and relatively low temperatures [70] [86]. The most common severe plastic deformation techniques are: Equal Channel Angular Extrusion (ECAE) [89–92], High Pressure Torsion (HPT), Repetitive Corrugation And Straightening (RCS) [99], Cyclic Extrusion Compression (CEC) [100], Torsion Extrusion [101], Severe Torsion Straining (STS) [102], Cyclic Closed-Die Forging (CCDF) [103], Super Short Multi-Pass Rolling (SSMR) [104] and Accumulative Roll Bonding (ARB) [104–106]. It is worth pointing out that SVP can be used only with materials with certain potential to plastic deformation.

The basic mechanisms behind these techniques are aimed to increase the dislocation density within the original material through intense plastic deformation. In order to reduce the strain field associated with dislocation structure, they recover into cell wall structures and deformation shear bands. Through room temperature recovery-recrystallization, these microstructures can further transform into low-angle and high-angle grain boundaries [88]. A number of elemental and alloy systems (nickel, copper, aluminum, and magnesium) have been produced by severe plastic deformation methods. It has been shown that the grain sizes of these bulk systems are in the order of 100 nm. Additionally, the mechanical properties of the processed alloys significantly increase. As an example, ARBed aluminum alloys with ultra-fine grains showed large strength at room temperature, up to 3.7 times larger than that of the parent materials [104-105].

In spite of the variety of different SPD processes, three processes have attracted the industrial and academic researches more than the others, namely ECAE, HPT and ARB. Table 7 presents a schematic configurations of the three processes and the attainable plastic strain [70]

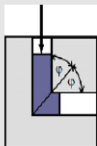
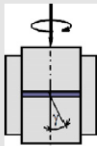
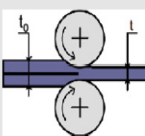
Process name	Schematic representation	Equivalent plastic strain
Equal channel angular extrusion (ECAE) (Segal, 1977)		$\varepsilon = n \frac{2}{\sqrt{3}} \cot(\varphi)$
High-pressure torsion (HPT) (Valiev et al., 1989)		$\varepsilon = \frac{\gamma(r)}{\sqrt{3}}, \gamma(r) = n \frac{2\pi r}{l}$
Accumulative roll-bonding (ARB) (Saito, Tsuji, Utsunomiya, Sakai, 1998)		$\varepsilon = n \frac{2}{\sqrt{3}} \ln\left(\frac{l_0}{l}\right)$

Table 7 Summary of major SPD processes [70]

ACCUMULATIVE ROLL BONDING

Only a limited number of papers is found in literature on ARB. Ultra-fine grained bulk aluminum (1100 alloy) with the mean grain size of 670nm was successfully produced by accumulative roll-bonding (ARB) process by Saito, Tsuji, Utsunomiya, Sakai and Hong [93] as a novel intense straining process using

rolling deformation. The ARB process was carried out with reduction in thickness per cycle equal to 50% and rolling temperature of 473K (Figure 156).

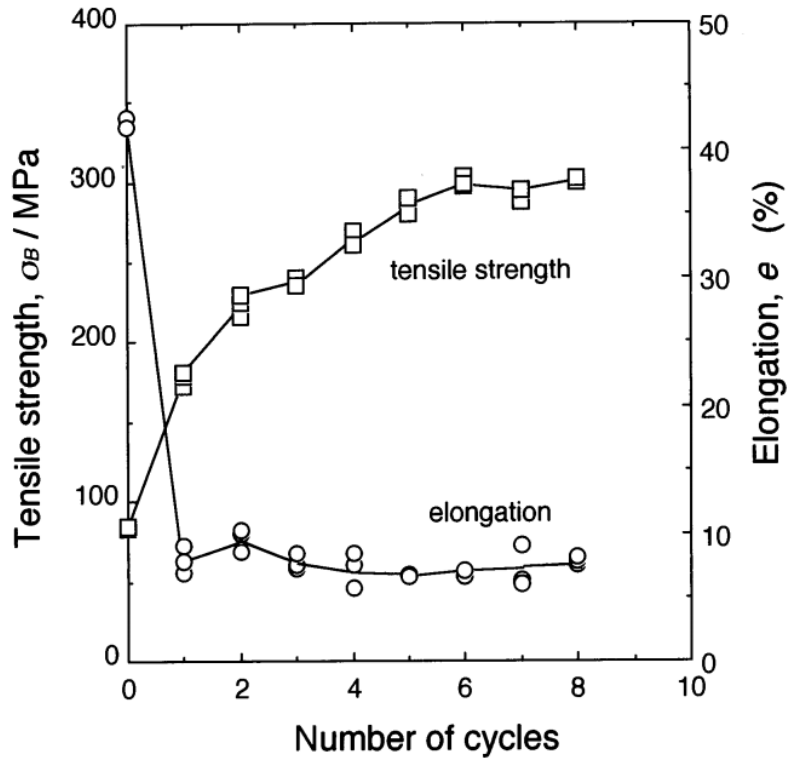


Figure 156. Mechanical properties at ambient temperature of the 1100 aluminum after ARB at 473K [93]

The obtained results showed how the tensile strength of the ARBed aluminum sheets increased with increasing the number of cycles, i.e., strain, and reached up to 300MPa after 6 cycles of ARB. Although the elongation dropped down after 1 cycle, no further reduction was observed during the subsequent cycles. Ultra-fine grains with diameter smaller than $1\mu\text{m}$ partially formed after 3 cycles of ARB, and the volume fraction of the ultra-fine grains involving large misorientations in the sheet increased with increasing strain. After 6 cycles of ARB, the microstructure was entirely made of ultra-fine grains. The microstructural evolution corresponded with change in strength, indicating that the significant strengthening obtained by intense plastic deformation strongly relates to the evolution of ultra-fine grained polycrystals. The results obtained show the possibility to produce the bulk aluminum with ultra-fine grained structure and unusual strength by the ARB process.

The possibility to produce the bulk steel sheets with ultra-fine grains by ARB process was investigated by Tsuji, Saito, Utsunomiya and Tanigawa [94]. As known, steel is the most used structural material, hence, the ultra-grain refining

of steel is greatly desired in many fields. The ultra-grain refining and strengthening produced on steels could largely reduce the weight of any constructions, and the strengthening without alloying elements would be preferable for recycling.

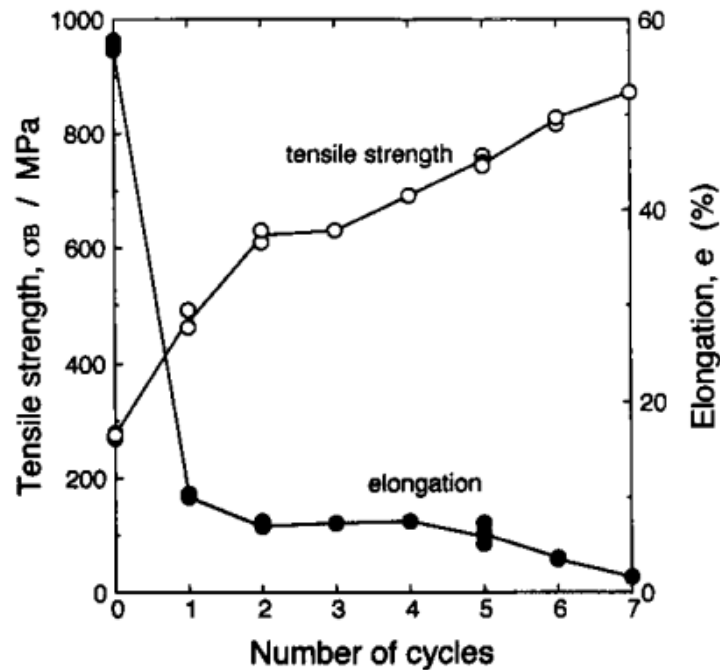


Figure 157. Mechanical properties at ambient temperature of the IF steel after various cycles of ARB [94]

The change in mechanical properties and the microstructural evolution during the ARB process were shown (Figure 157). It is interesting noticing that the found trends of tensile strength and elongation are quite similar to those of the aluminum alloys previously studied. The authors concluded that ARB is very useful process for high straining and ultra-grain refining, and most of structural metallic materials with ultra-fine grains could be easily achieved by ARB.

Mechanical properties of UFG steels were shown based on Tsuji's experimental data [95]. UFG steels are usually characterized by very high strength but limited uniform tensile ductility when they have single phase structure. The limited uniform elongation was understood in terms of early plastic instability, which is an inevitable feature of the UFG single-phased materials. It was also indicated at the same time that dispersing nano-carbides within the UFG ferrite matrix is an effective way to improve the uniform elongation of the UFG steels. Steels have various options of multi-phased structure, such as, ferrite + cementite, ferrite + martensite, ferrite + bainite, and so on (Figure 158).

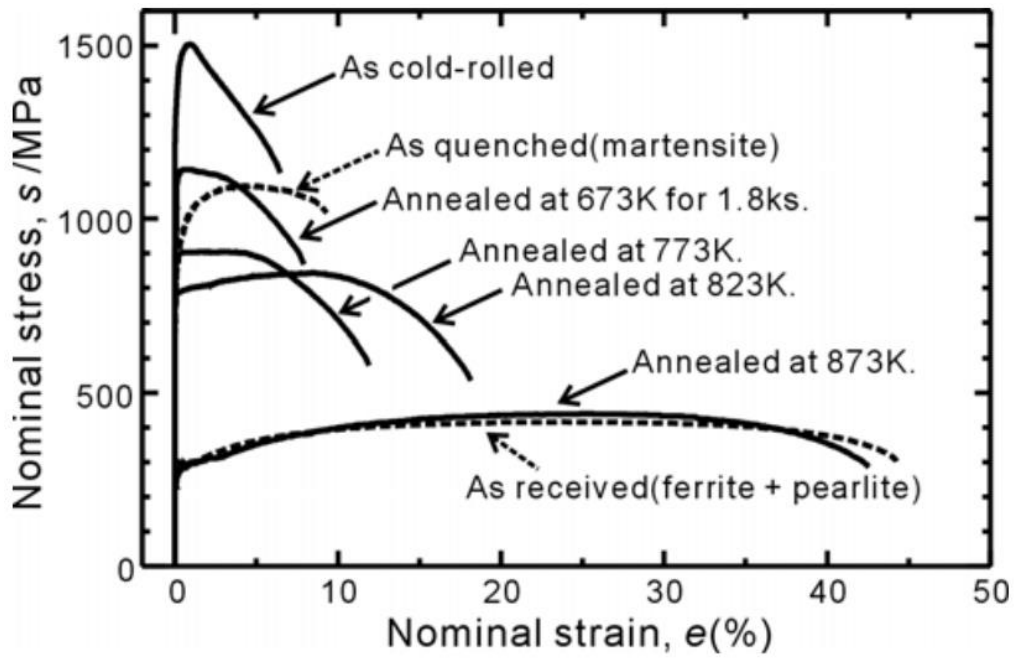


Figure 158. Nominal stress-strain curves of the SS400 steel 50% cold-rolled and annealed at various temperatures for 1.8ks. Starting microstructure was martensitic [95].

The paper conclusions clearly indicated that the studies of the UFG steels should be focused on “multi-phase” in future.

Saito, Utsunomiya, Tsuji and Sakai [74] investigated the application of ARB to commercial aluminum (1100), Al–Mg alloy (5083) and interstitial free (IF) steel. Well-bonded bulk materials were successfully obtained. After several cycles of ARB, ultra-fine (sub-micron) grain structure with large misorientations, i.e. polycrystal, was formed and the materials were strengthened dramatically.

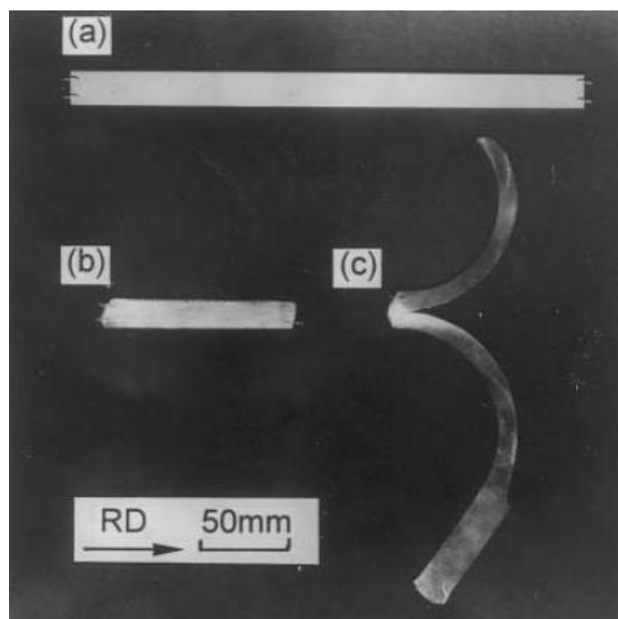


Figure 159. Appearance of initial and ARB processed 5083 strips at 473 K: (a) initial; (b) and (c) after three cycles [74]

Lee, Saito, Tsuji, H Utsunomiya and Sakai [80] studied the role of shear strain in grain refinement of aluminum during ARB. The through thickness distribution of redundant shear strain of the ARB processed aluminum sheets was quantitatively evaluated. With increasing the number of ARB cycles, the amount of shear strain and the number of shear strain peaks increase and the distribution of shear strain becomes more complicated (Figure 160). It was clearly demonstrated that shear strain greatly affects the ultragrain refinement by ARB. The grain size distribution through thickness synchronized well with the shear strain distributions. The role of shear strain in grain refinement was considered from the viewpoints of equivalent strain, strain gradient and strain path.

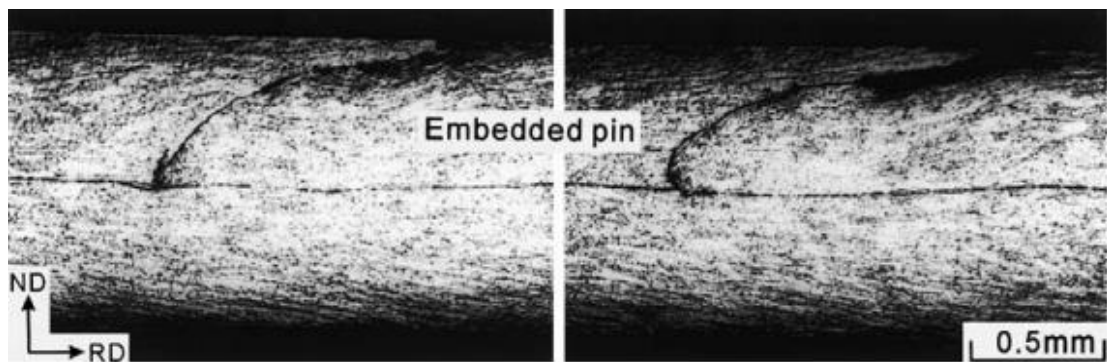


Figure 160. Optical microstructures showing the flexion of the embedded pin in the 1100 aluminum sheet ARB processed by one cycle at ambient temperature without lubricant. Observed on a longitudinal section [80]

6. Accumulative Roll Bonding Experiments

One of the objectives of this thesis was to develop an effective and efficient tool to realistically model the mechanical behavior of the sheets in the Accumulative Roll Bonding process. In the next step, the performances of this model were evaluated to assure its robustness and quickness, in order to achieve and prove its sustainability in the industrial field.

The experimental analysis was carried out to obtain the material behavior using different numbers of cycles, and to validate the numerical results in comparison with the data measured during the experimental tests (such as the pressure on the lateral arms of the roll and velocity of the roll themselves). It has to be noticed that the results from these experiments and the related simulations agree very well.

For the study of the process two software are used, such as Abaqus CAE 6.9 2D/3D modes and DEFORM 3D mode. The two software programs use two different algorithms making them better suited to different tasks. In fact, has been used to study the acting forces on the rolls during the process, Abaqus software while Deform software was used to study the tensions and deformations on the sheets.

6.1. *Experimental set up*

6.1.1. **Used material**

It is well known that the reduction of grain size increases the material strength. The need of nanocrystalline and ultrafine-grained materials has drastically increased over the last 20 years. Ultrafine-grained materials have enhanced strength in comparison to the conventionally grain sized materials, as confirmed by many researchers [74] [80]. In some cases both the ductility and the strength can be increased, e.g. nanocrystalline titanium and copper processed and reported as the “Paradox of strength and ductility” [86].

For this study, AA1050 aluminum alloy sheets, 1mm in thickness, 2000 mm in length and 450 mm in width, were used.

The flow stress curves at room temperature of the alloys AA1050 is reported in Figure 161. In the same figure, the flow stress of AA6082 is reported for

comparison. It should be observed that both the materials will be used for the numerical analysis of the process.

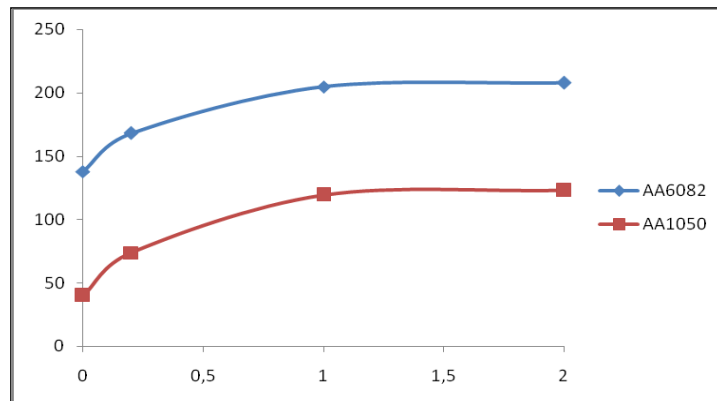


Figure 161. Material characteristics at room temperature

6.1.2. Fixture and parameters

A Gerd Wolff Maschinenfabrik rolling machine was used at the Fürth laboratory for the experiments. This machine has four high rolling machine and a roll diameter of 229 mm.



Figure 162. Gerd Wolff Maschinenfabrik

At the end of each cycle, the thickness of sheets was measured and a tru laser machine 3030 was used to reshaping of the sheets. The tests were carried out at room temperature, for N4 cycles and without lubricant.

A few process parameters were kept constant for all the tests: 50% of reduction, convexity of the rolls equal to 0.04 mm, in order to reduce the vertical oscillation,

and rotational speed equal to 50 RPM. Table 8 summarized the fixed process parameters.

Technical Parameters	Reduction	R%	50	%
	Convexity	c	0.04	mm
	Velocity	ω	50	rpm
	Tamb	temp	22	°C
Geometrical Parameters	Thick	T	1	mm
	Length	L	2000	mm
	Width	W	450	mm

Table 8 Fixed parameters

It is worth noticing that convexity is a very important parameters because, if this is chosen correctly, the vertical oscillation during the process will be significantly reduced by stiffening the rolls.

6.2. Experimental Tests

Thickness and width of the ARB-blanks were measured after each cycle in different locations. Figure 163 shows the measurement points and the information acquired.

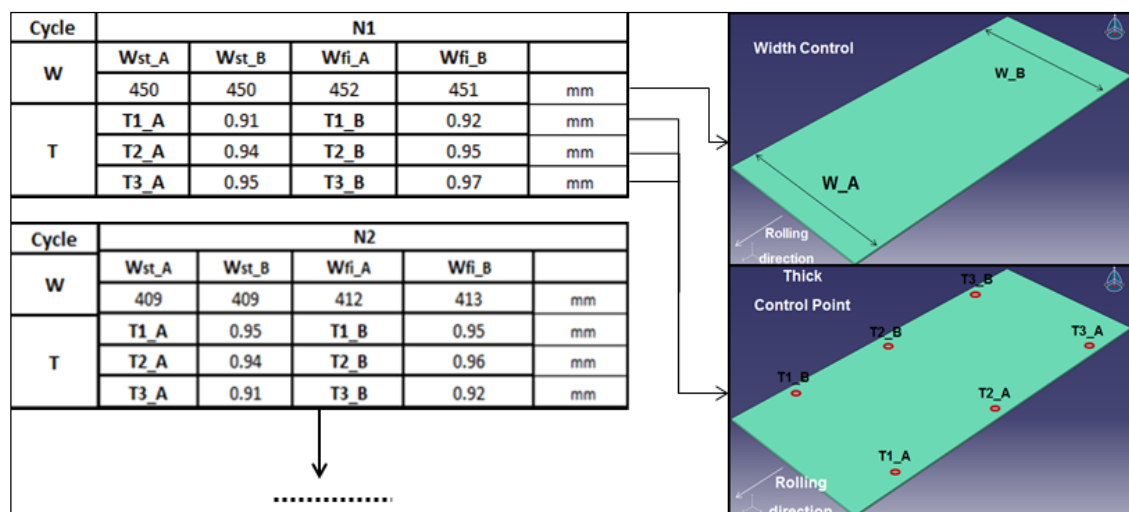



Figure 163. Thickness and width measurements

In particular, the thickness was measured in three different points in both sides in order to know the real reduction. During the tests, the sheets temperature was measured in order to assure cold conditions. The maximum temperature measured on all the experimental campaign was below 70°C.

Final obtained results include: Geometrical inputs and outputs, % of reduction, separating forces on the rolls, Number of layers and finally qualitative observation. Table 9 shows the obtained results for the N4 cycles.



hin [mm]	win [mm]	hout [mm]	wout [mm]	Reduction [%]	FA [kN]	FB [kN]	Layers	Comments
2	452	1	451	50	2710	2710	2	Good Bond
2	433	0.99	432	50.5	2760	2760	4	Good Bond
1.98	420	0.90	420	54	2710	2760	8	Good Bond
1.80	376	0.90	378	45	2460	2510	16	Good Bond

Table 9 Input and output data for N4 cycle

As it can be seen from the table, the forces acting on the arms of the rollers after the third cycle are no longer equal. Additionally, a change in the reduction is observed. The reason for this behavior is the deformation of the rollers, due to the mechanical characteristic of the material which increases with the number of cycles. This effect is very difficult to predict and it is function of the technological parameters chosen.

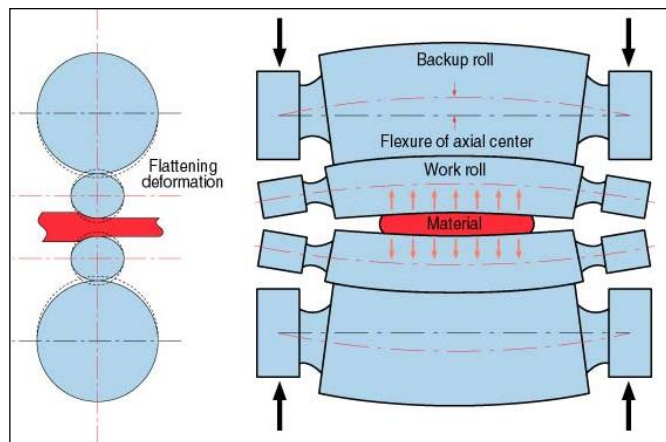


Figure 164. sketch of the elastic rolling deformation [107]

This "effect" transmitted on the sheet involves the undulation "defect", as highlighted in the following Figure 165.

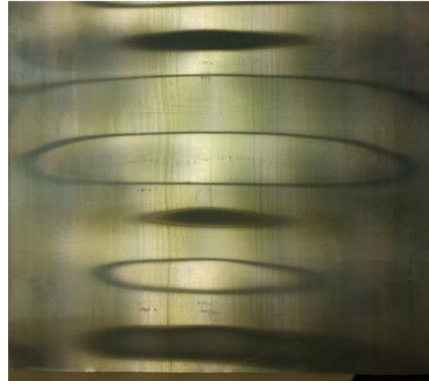
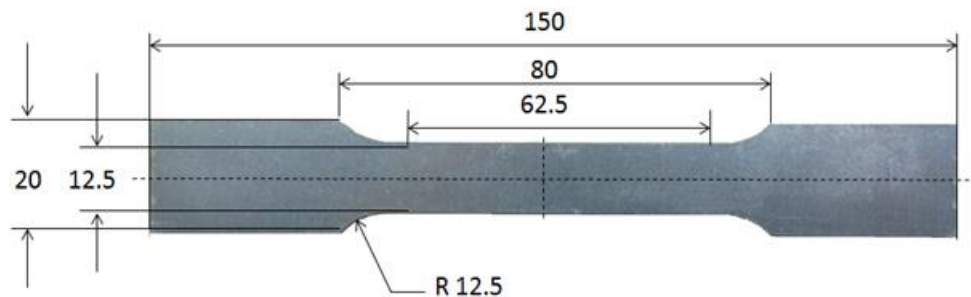


Figure 165. Undulation "defect" on the top sheet surface

Tensile tests were carried out on the ARB-blanks (Figure 166), in order to obtain the flow stress curves cycle by cycle. These curves were used to implement the material model in the numerical analysis. Representative tensile stress-strain curves of samples tested in the rolling direction can be seen in Figure 166. A general trend is that yield and tensile strength, as well as elongation to failure progressively increase with increasing number of ARB cycles. After only two ARB cycles, the yield strength can be increased by more than 100% but elongation to failure is compromised by up to 90% in comparison to the as-received state. However, further ARB rolling can considerably improve elongation to failure of both materials.

A growing divergence of yield and tensile strength curves after the first ARB cycle of AA1050 suggests a growing strain hardening potential. The saturation level is reached after 2 ARB cycles and it is attributed to a relatively fast dynamic recovery process during rolling.

Figure 166 shows the geometrical parameters of the specimen and the results of the tensile tests results.



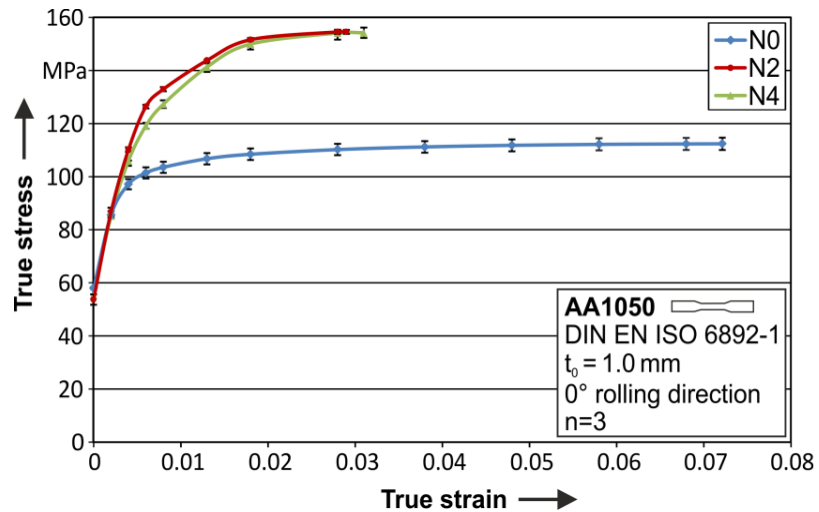


Figure 166. Geometrical parameters and Characteristic true stress vs strain curves in the rolling direction of commercial purity aluminum AA1050 processed at room temperature

The evolution of mechanical properties in the rolling direction (RD) and the normal direction (ND) with an increasing number of ARB cycles can be seen in Figure 167. As shown earlier, yield and tensile strength, as well as elongation to failure progressively increase with the growing number of ARB cycles. A growing divergence of yield and tensile strength curves after the first ARB cycle of AA1050 suggests a growing strain hardening potential. The saturation level reached after 2 ARB cycles and it is attributed to a relatively fast dynamic recovery process during rolling.

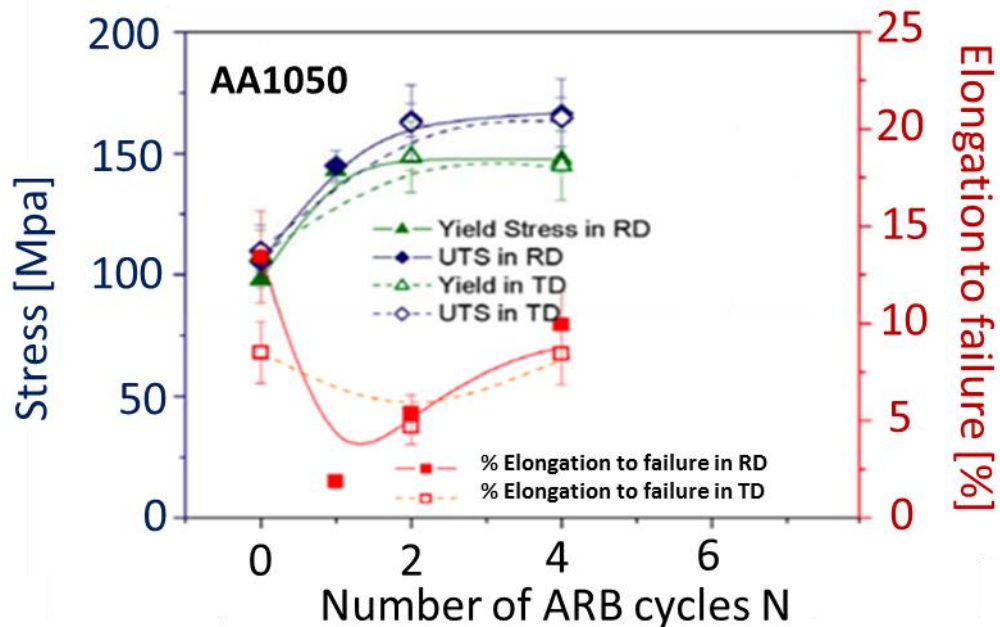


Figure 167. Yield strength and elongation to failure in the rolling direction and transverse direction vs. the number of ARB cycles for a commercial purity aluminum AA1050 processed at room temperature.

From Figure 167, it is evident that sample in the normal direction shows no significant deterioration of strength of elongation to failure in comparison to the samples in the rolling direction, even though a strongly elongated microstructure was observed for both materials.

6.3. Numerical Analyses

The Finite Element Method (FEM) is one of the most used technique for manufacturing process simulation as it can reproduce a great variety of real processes [84]. The F.E.M. is used to solve problems based on linear and nonlinear constitutive laws. There are different sources of nonlinearity that may be present in the simulations, these include:

- Material Non-Linearity: *this is a very common source of nonlinearity and it shows when the tensions of the materials that exceed the field of linear elasticity. This model uses an elastic-plastic formulation;*
- Geometric Non-Linearity: *this type of non-linearity is present when a change in the geometry or in the orientation of the structure changes its response. This geometric nonlinearity occurs when the large deformations change the shape of the structure. This type of non-linearity is certainly present in this analysis;*
- Boundary Non-Linearity: *this appears when the boundary conditions change during the analysis process. During the simulation of ARB process, the most important source of non-linearity comes from the contact between rolls and sheets, and between the two sheets.*

Two main approaches are used in order to solve these problems:

- Explicit: *when using this type of formulation, the solution at the end of each increment is based only on initial conditions. The explicit*

scheme is easy to implement and requires a shorter time to find a solution, compared to the implicit model;

- *Implicit: this approach assembles and solves the system matrix for each increment and it finds an equilibrium for each. This needs a higher CPU time to converge to a solution than the Explicit method. In addition, it can handle strong non-linearity as in the ARB process. This is the most common method used in the FEM analysis of bulk processes.*

In the first phase of this study a model using explicit integration was used. In the explicit integration the CPU time is very low compared to implicit analysis. The goal of this phase was to obtain the deformation on the rolls and compare them with experimental results in order to have a design tool for the determination of optimal technological parameters to be used in the experimental campaign. Moreover a numerical model using implicit integration was implemented in order to simulate the thermo-mechanical process thus studying the stress distribution in the sheet due to the high pressure during the tests.

6.3.1. Explicit model

The ARB process was simulated by the software SIMULIA Abaqus/CAE 6.9. The simulation of each cycle was divided in two steps [82]:

- *Closing*: the distance of rolls decrease obtaining the desired reduction;
- *Rolling*: the rolls rotate for the pulling out the two plates.

The equivalent deformation, registered in the Rolling step (y-axis direction ϵ_{22}), was used to compare the result of the simulated ARB process to the real process result.

3D approach

The first analysis was conducted using a 3D approach, due to the necessity to investigate on the rolls behavior during the test, influencing the change of the reduction with increasing number of cycles.

DIN 86CrMoV7, which is a material typical for steel rolls, was selected for the roll. The mechanical properties were taken from online database (Table 10). For the sheet material the characteristics obtained through the tensile tests on the real ARB-blanks were used.

Density [g/cm ³]	7.85
Modulus of elasticity [10 ³ x N/mm ²]	210
Poisson coefficient	0.3
Tensile strength [Mpa]	880
Elongation [%]	25
Yield strength [Mpa]	550

Table 10 Roll characteristic (DIN 86CrMoV7)

The geometrical parameters adopted for roll and sheet are reported in the following Figure 168.

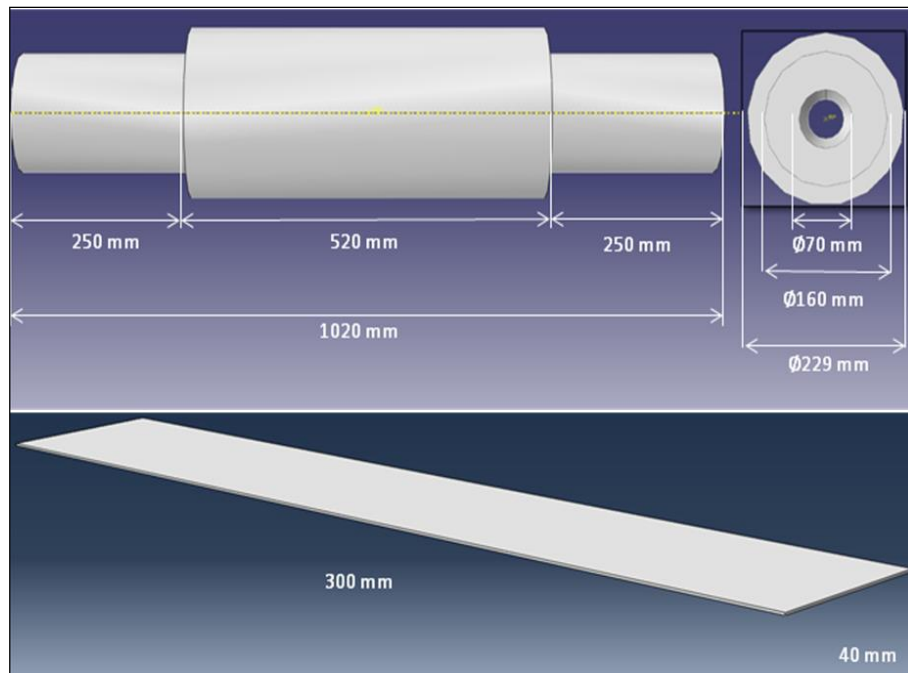


Figure 168. Geometrical parameters

A symmetry plane between the sheets, parallel to the xz plane, was used. No additional symmetry plane was adopted in order to calculate the longitudinal forces. It was important that the roll geometry was the same of the real case, in order to calculate the actual effect of the moment generated or other causes which can lead to elastic deformation phenomena on the roll during the test. It was necessary to establish five reference points to apply the boundary conditions. Coupling constraints type was used. This constraint requires one point and one surface, i.e. the transverse surfaces on the roll axis.

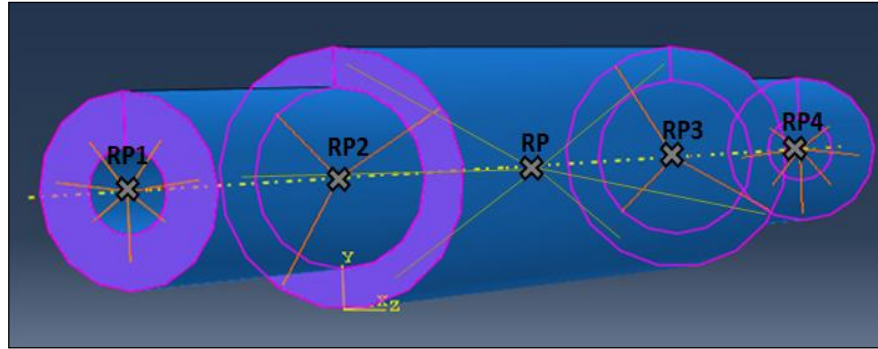


Figure 169. Reference point

On the external reference points, namely RP-1 and RP-4, all movements were imposed equal to zero except the rotational movement along x. While, in all reference points, the rotational speed was imposed, equal to 3.14 radians per second. The analysis was carried out with an explicit dynamic step. As already specified, the process was divided in two different phases, called Initial and Rolling. In the first step, it was necessary to establish the contact between bodies, while the second step, namely Rolling, it was used for the ARB process.

The Coulomb coefficient between roll and sheet was set 0.35.

The variation of the reduction was one of the main output of the simulation due to the roll deformation. This defect is visible on the top side of the sheet.

First, the undulation effect was analysed. Figure 170 shows how the numerical simulation faithfully follows the real deformation. In particular, it was chosen to compare the pressure effect in the experimental analysis and the pressure distribution in the numerical analysis.

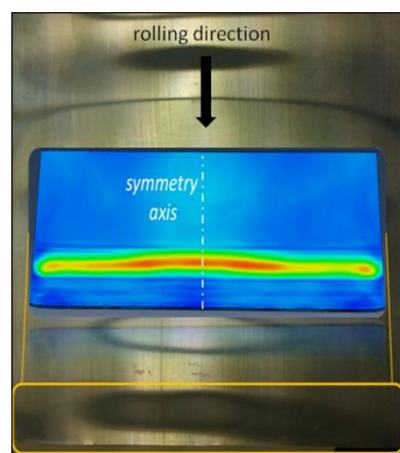


Figure 170. Comparison between the pressure effect in experimental and the pressure distribution in numerical results

The variation of the reduction with increasing number of cycles was analyzed. Figure 171 show the change in the forces on the roll after N2 cycles. For the study

of this process, the separating forces on the top roll, measured during the experimental tests, were compared with the reaction forces on the Reference points, i.e. in RP2 and RP3 in the numerical simulation.

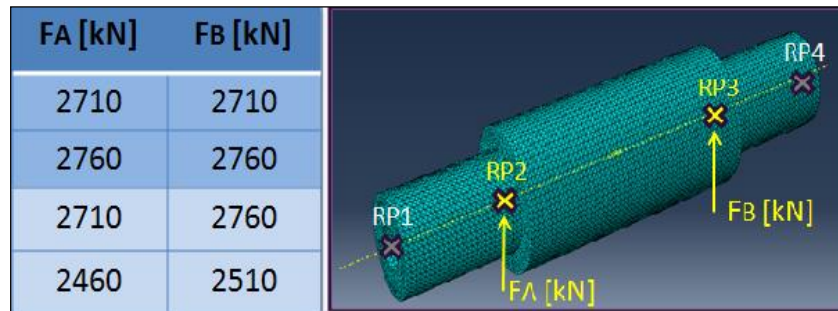


Figure 171. Forces acting on the roller

In Figure 172, it is possible to see as from $t=0$ s up to $t=0.4$ s, the numerical simulation curves have a different trend compared to the experimental analysis. After 0.4 seconds, the curves trend (Figure 172) of the numerical simulation follow the curves of the experimental analysis. The difference is due to the different approach used to establish the contact. In the experimental tests, the sheets were placed between the rolls and then crushed while, in the numerical analysis, the contact is similar to the typical rolling process.

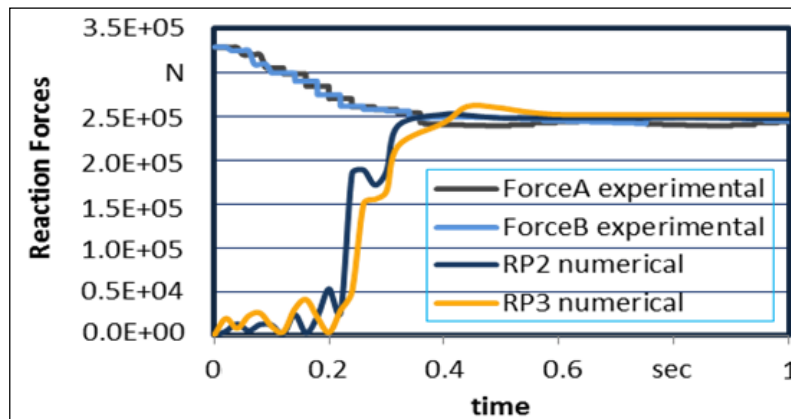


Figure 172. Curves comparison between the experimental and numerical analysis

One drawback of the proposed approach is the high CPU time. For this reason, the model parameters were optimized pursuing CPU time minimization. Different solution were tested, as the variation of the mass scaling parameter. The main goal was to model the process with the shortest CPU time and the highest mass scaling, until the inertial forces are still insignificant. It was noticed that the stress on the rolls was considerably influenced by the choice of the mass scaling value. High mass scaling values results in excessive stress concentration as highlighted in Figure 173.

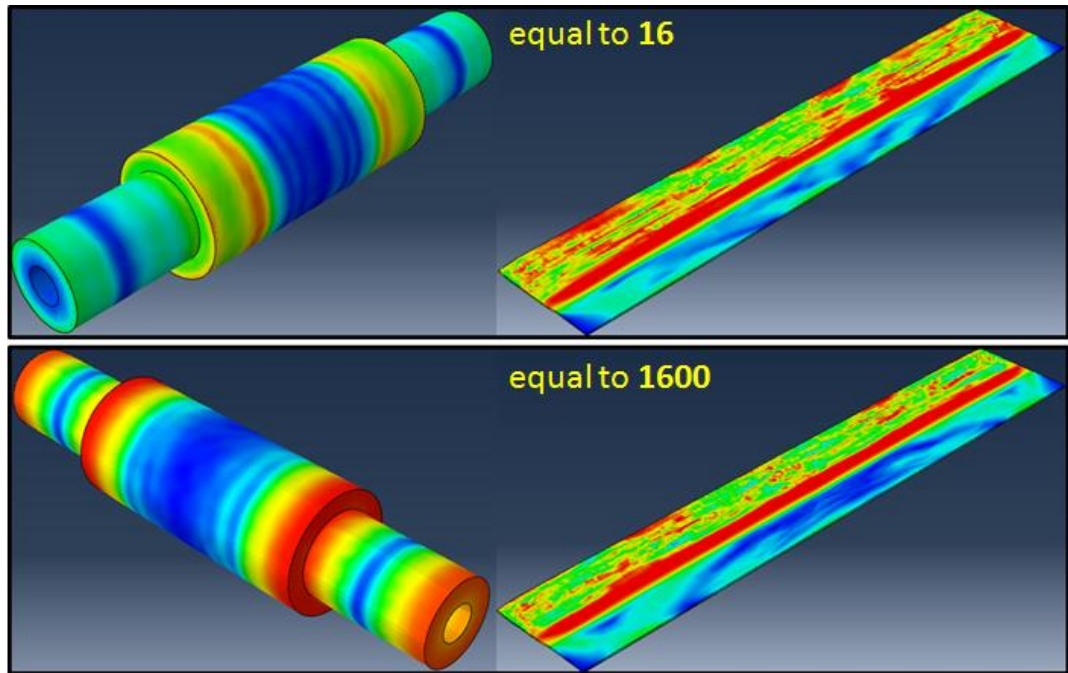


Figure 173. Different mass scaling parameters
(Up equal to 16, down equal to 1600)

The optimum mass scaling parameter was found equal to 16. With this parameter the CPU time decreased from 15 hours down to 11 hours without relevant changes of the results accuracy. In order to further reduce the CPU-time, a 2D model was created.

2D approach

First, a dramatic reduction of the CPU time, equal to 30min, was observed.

As already mentioned the sheet reveals the typical defect of the undulating surface, due to the uneven pressure distribution during the process. As a matter of fact, a cyclical pressure distribution is obtained instead of a uniform one.

For this reason two different zone were studied, namely Lateral Side where the rotational center coincides with the center of the roll and Central Side, where the rotational center was moved by a distance equal to the roll convexity (0.04 mm).

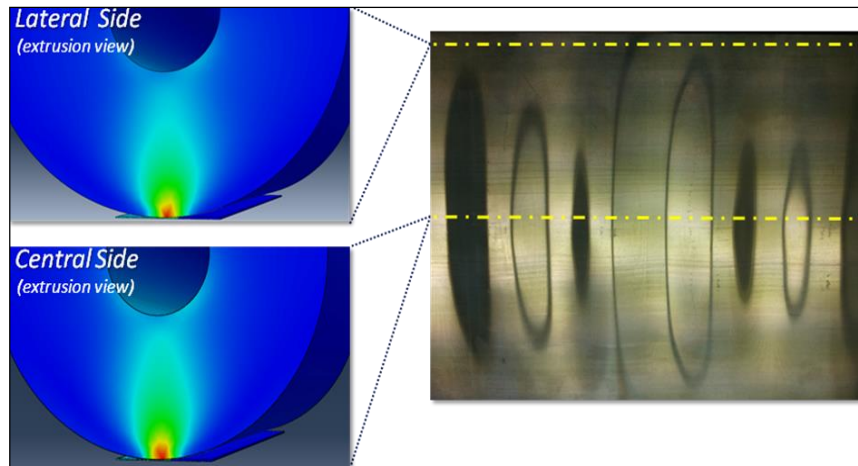


Figure 174. The different zones: Lateral Side and Central Side

From the comparison between the 2D model results (Lateral and Central Sides), it arises (Figure 175):

- ✓ Pressure is higher in the Central Side by 8.65% with respect to the Lateral Side.
- ✓ Equivalent plastic strain is larger in the Central Side by 7.2% with respect to the Lateral Side.

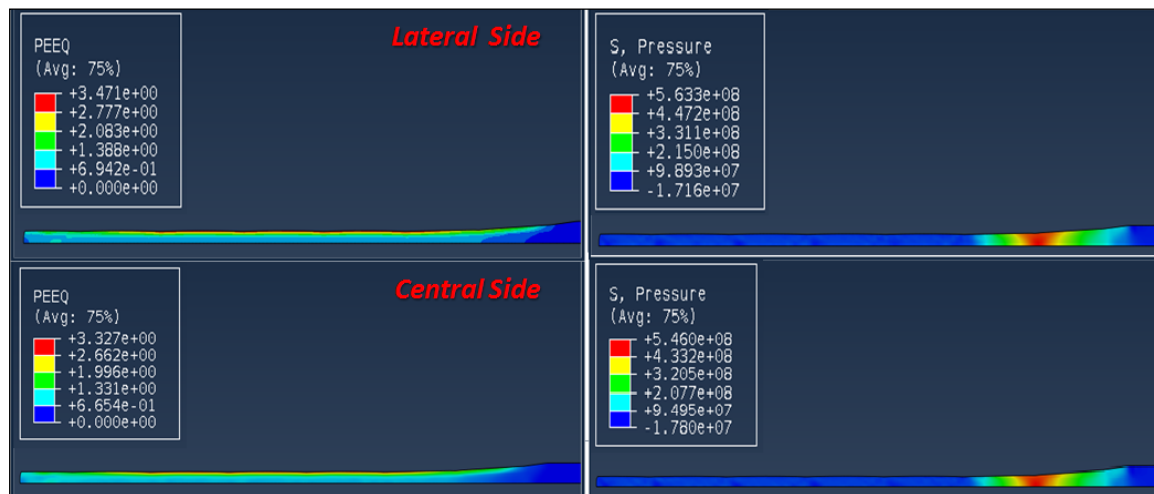


Figure 175. Pressure distribution on the right and equivalent plastic strain distribution on the left for lateral (up) and central (down) sides

The 3D model and the central side of 2D model were compared against Von Mises stress (Figure 176). The 3D model calculates a Von Mises stress 8.45% larger than the 2D model. On the other hand, pressure values are 3.78% larger in the 2D model.

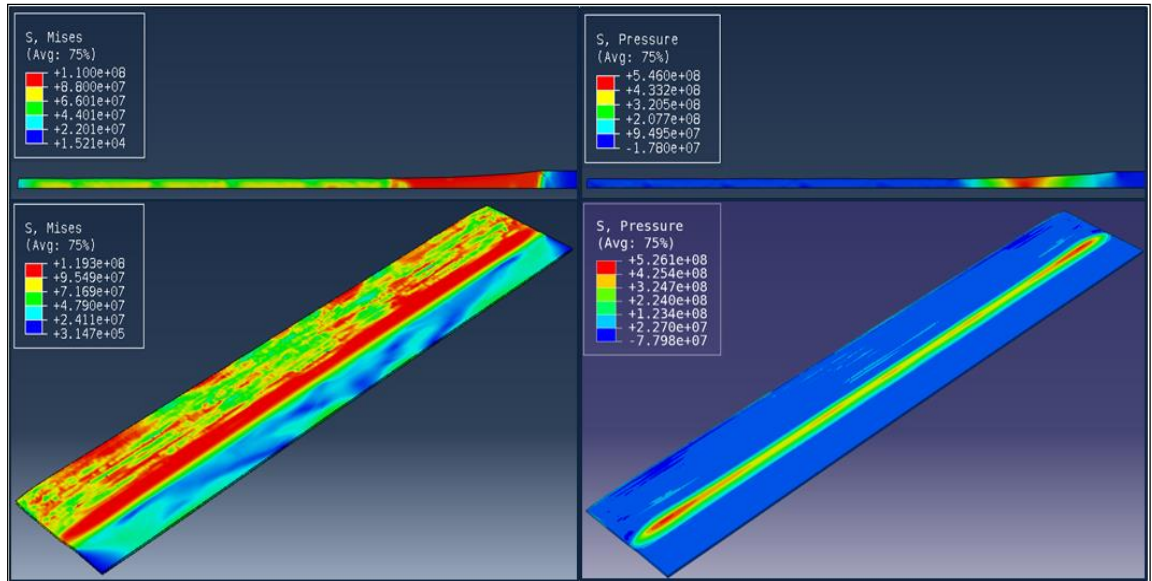


Figure 176. Comparison between the 2D (up) and 3D (down) modes, for von Mises stress (left) and pressure distribution (right)

Symmetrical distributions of von Mises stress and pressure were found out, at least at a micro level due to numerical instabilities. Another comparison of the von Mises stress was conducted in the two different parts of the roll involved in the contacts with the sheet. These data were compared with the ones obtained from the 2D simulation. A difference of less than 4%, between the lateral side and lateral cut was found (Figure 177) while, between central side and central cut, this difference was of about 8% (Figure 178).

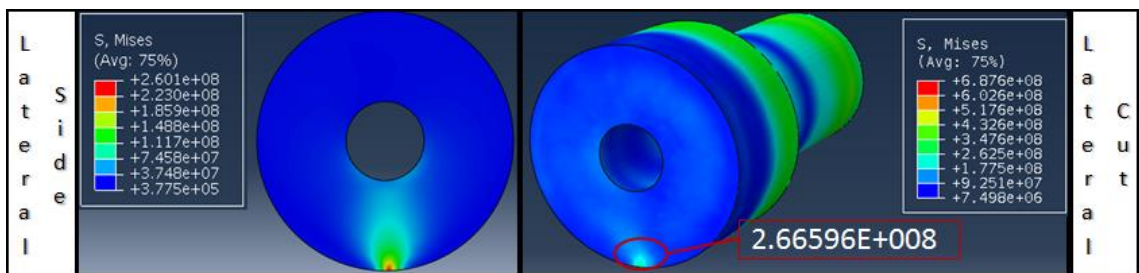


Figure 177. Comparison between Lateral Side and lateral cut

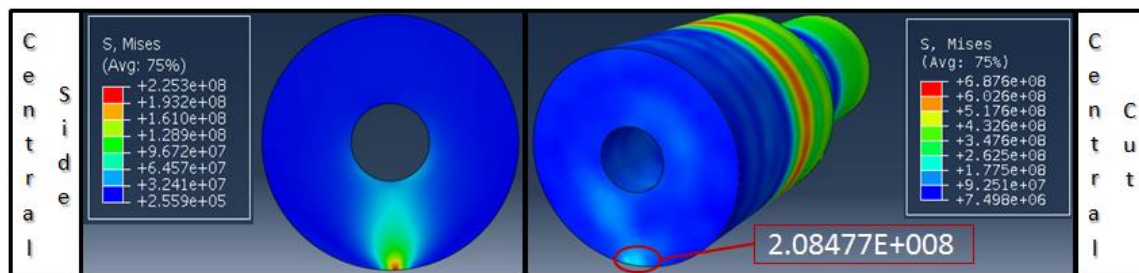


Figure 178. Comparison between Central Side and central cut

Hence it can be stated that the 2D model can be successfully used to predict the deformation and stress distribution both in the sheet and the roll.

Finally, it is possible to compare the Von Mises stress in lateral side of the 2D simulation with the central cut of the 3D simulation. In this case, a difference of about 25% indicating that the effect of roll bending cannot be neglected.

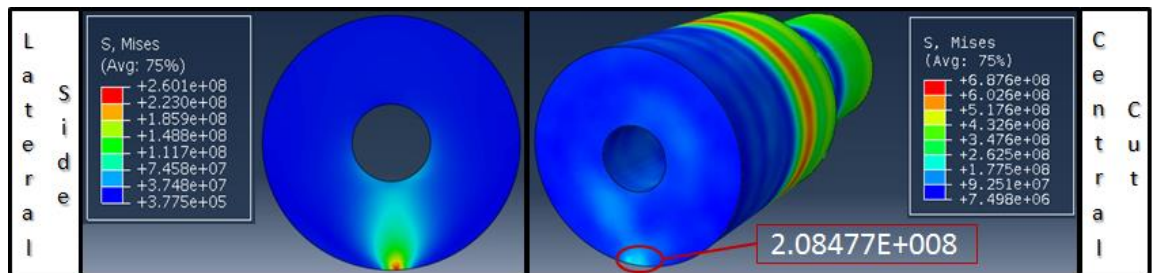


Figure 179. Comparison between Lateral Side and central cut

6.3.2. Implicit model

When the analysis on the explicit model was completed, a simulation with implicit method was developed. This allows to model the ARB process in a more accurate and complete way. Although the model structure remains the same, the introduction of the thermal analysis permitted to analyze more in detail the process.

Thermo-mechanical analysis

For the thermo-mechanical analysis, the software DEFORM 3D was used. The implicit model, already described in the chapter of the Linear Friction Welding, was created with the aim to acquire pressure, temperature and strain rate distributions in the sheet. Two symmetry planes were used, in the longitudinal and transverse direction, respectively. In order to save computational time, the roller was made by two objects: the part in contact with the sheet was modeled as deformable body while the remaining part as a rigid body (Figure 180). A "sticking condition" contact between the two parts was set in order to eliminate the relative motion between them, while the sheet was created as a fully deformable body.

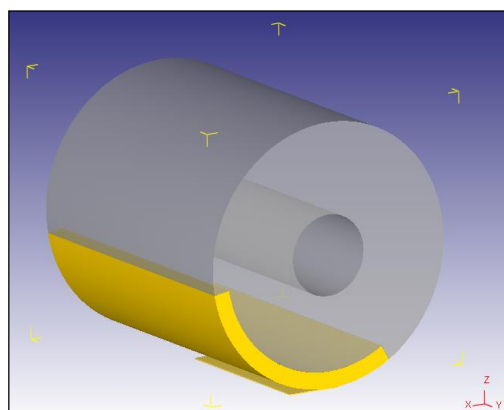


Figure 180. Rigid/deformable roll parts

The ratio between the thickness of the deformable part of the roll and the sheet was 10/1 in order to ensure the contact between deformable bodies thus excluding the influence of the rigid body.

The material used was the AA1050 and the test was conducted at room temperature but with addition of the heat exchanges with the environment.

The process was divided into two steps. The first step was used to establish the contact between the bodies by assigning a tangential speed to the sheet till the process reached a steady state. Once the contact occurred, before moving on to the second step, it was assessed that the sheet position was such as to allow the roller to drag it during the rolling. The Coulomb model was used and the friction coefficient was set equal to 0,35.

A time increment equal to 0.0005 sec/step was imposed in order to improve the convergence. Two points were selected on the sheet having the same coordinates except for the z. Point 1 was taken on the lower surface, i.e. at middle thickness of the real sheet, while point 2 at the opposite extreme on the top surface. Figure 181 shows the temperature evolution for the two observation points. The points do not move with the sheet but remain in a fixed position, in order to know the temperature at a fixed point in the space (eulerian approach).

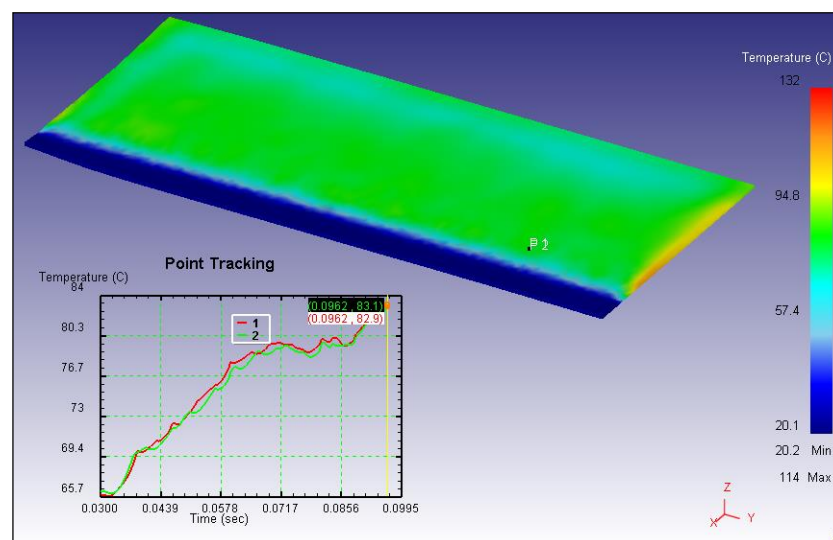


Figure 181. Point tracking of temperatures distribution (fixed points)

As it can be seen from the figure no noticeable difference is found between the two points. Maximum temperature is equal to 83°C.

A further investigation was conducted changing the characteristics of the selected points, namely moving with the sheet so as to know the velocity of heat exchange to the environment.

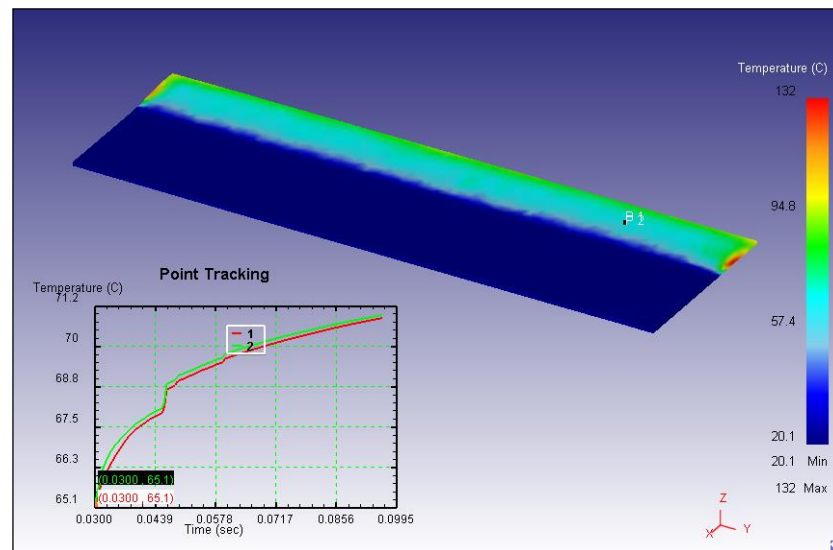


Figure 182. Point tracking of temperatures distribution (moving points)

The results faithfully follow those obtained by pyrometer measurement during the experimental campaign, as discussed in the previous paragraph. The temperature measured in the experimental analysis was about 70°C while the calculated analysis is 71°C.

A further investigation was carried out to know the strain rate distribution (Figure 183). In particular, examining the strain rate along x-axis (rolling direction), it can be noted that the strain rate is greater for the point located at the interface between the sheets. It should be noted that fixed points were used for the analysis in order to know the strain rate in the rollers zone.

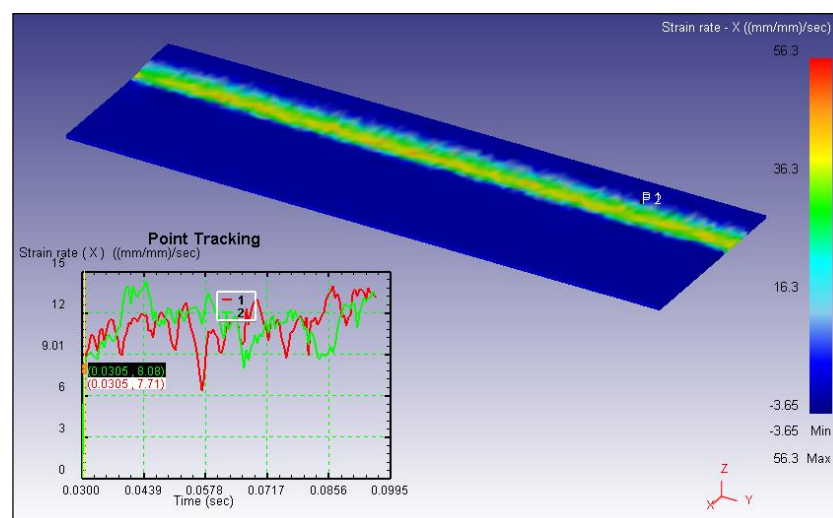


Figure 183. Point tracking of strain rate distribution along x-axis (fixed points)

The strain distribution is shown in following Figure 184. It is observed that strain is larger at the bottom surface with respect to top surface. In this way favorable conditions are created for the bonding process to occur. As already observed for the LFW, high strain is one of the needed conditions for sound bonding.

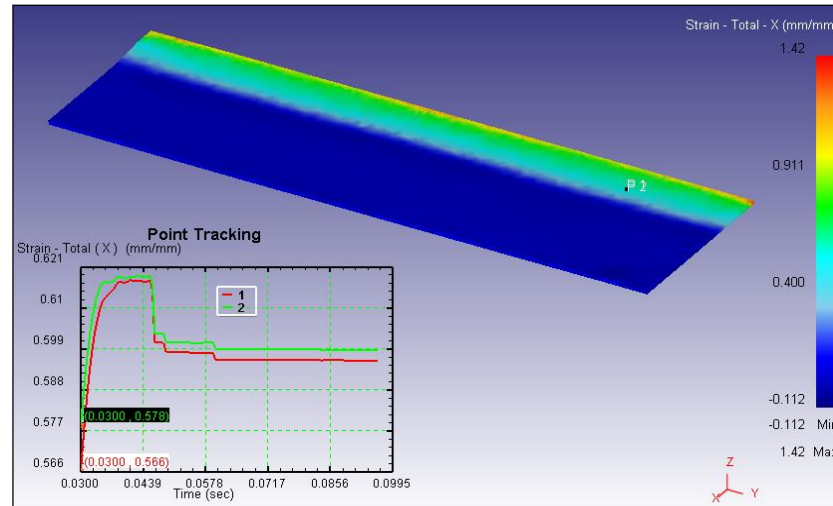


Figure 184. Point tracking of strain distribution along x-axis (fixed points)

Pressure is the second key variable for successful solid bonding. Figure 185 shows the pressure distribution in the sheet.

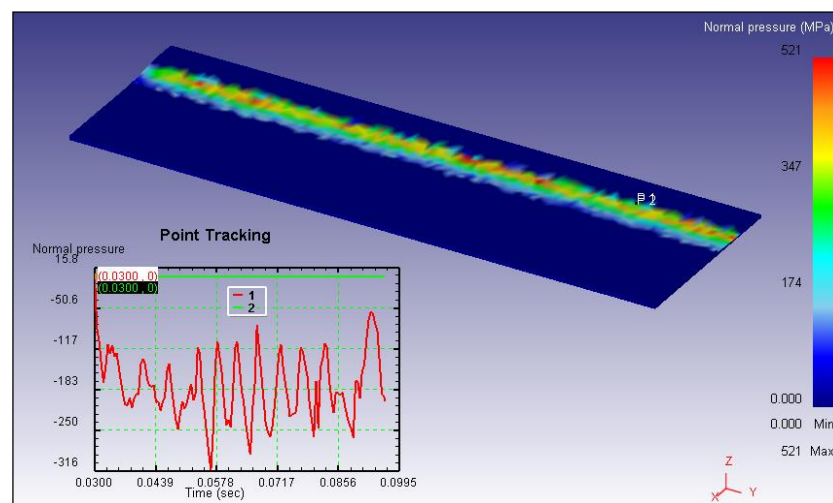


Figure 185. Point tracking of pressure distribution (fixed points)

It has to be noted that the pressure variable is intended, for the utilized software, only between two objects in contact. A parameter that can provide the trend of the interface pressure between the plates is the sigma along z-axis as shown in Figure 186. Values very close to the ones obtained with the explicit model are found. This confirms the validity of the two models.

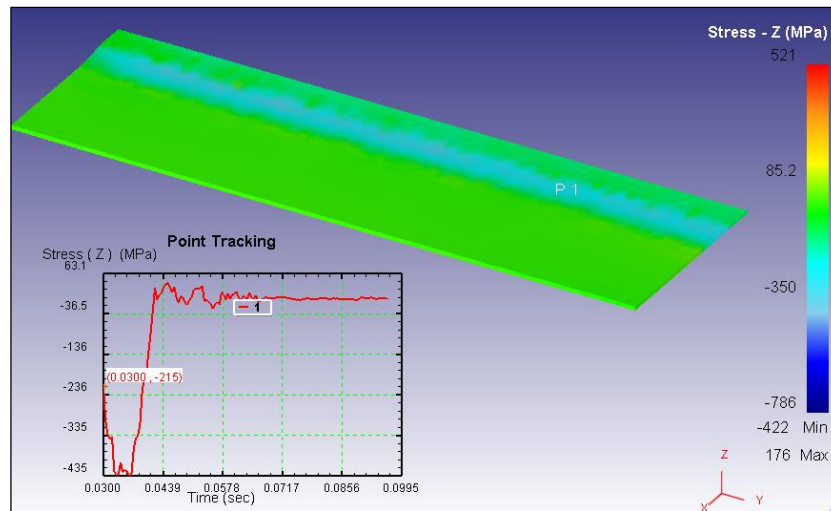


Figure 186. Point tracking of stress along z-axis

As far as cold ARB is performed using the implicit or the explicit approach leads to equivalent results. The higher potential of the explicit approach can be deployed when warm or hot ARB is considered as it will be better highlighted in the next chapter.

7. Comparison of Thermo-mechanical Implicit models

In this chapter, the comparison between the ARB thermo-mechanical models with two different materials, namely AA1050 and AA6082 [85] will be carried out. Then, the main field variable distributions influencing solid bonding in LFW and ARB will be compared with using AA6082. In order to compare the solid bonding phenomenon in the two processes belonging to the different families, the implicit thermo-mechanical simulation models will be used.

7.1. Comparison between ARB thermo-mechanical models

As known, the mechanical characteristics of the alloy AA6082 are higher than the AA1050 alloy. In order to reduce the resistance of the material, the ARB of AA6082 was carried out in warm conditions. In Figure 187, the mechanical properties at $T = 20\text{ °C}$ and $T = 250\text{ °C}$ for alloy AA6082 are shown.

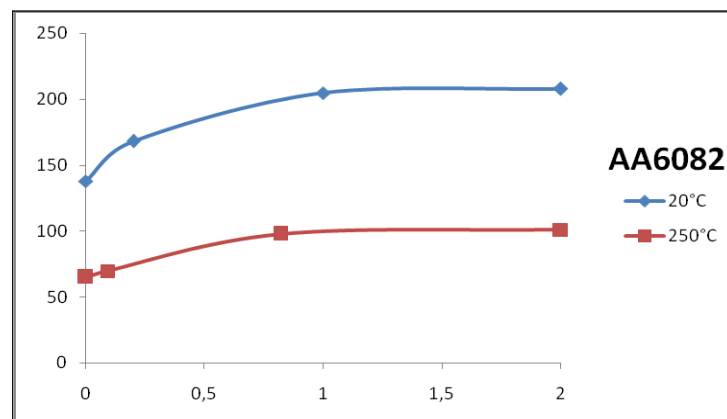


Figure 187. Material characteristics AA6082

As already mentioned, one of the most serious process issues regards the rolls deformation occurring after N2 cycles. As the flow stress of AA6082 at 250°C is similar to the flow stress of AA1050 at room temperature, it arises that warm conditions are needed in order to carry out the experiments with AA6082. For this reason, the roll external surface was heated up to 230°C. However, the sheet temperature will always be lower than the roll temperature.

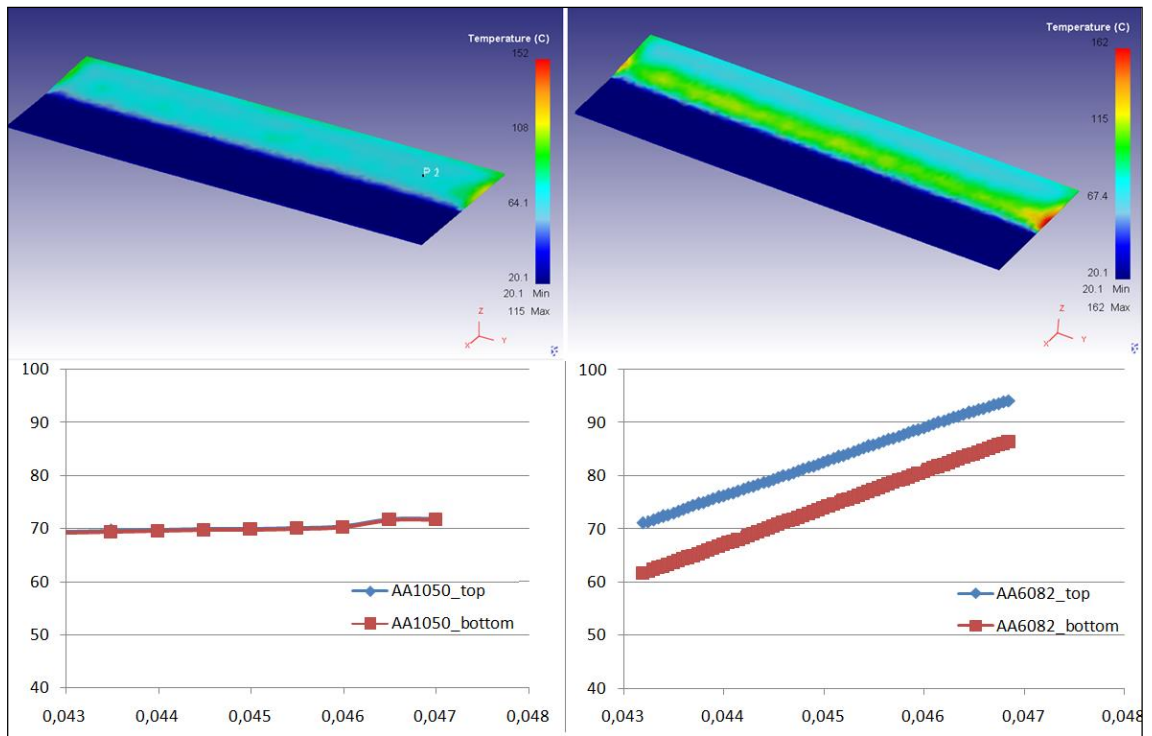


Figure 188. Comparison of the temperature distributions.

Figure 188 shows that, an increasing temperature is observed while the sheet is in contact with the rolls. Additionally, in the case of hot process, two distinct temperatures curves are obtained for the two observation points located on the top and bottom surface of the sheet, respectively. In turn, in the cold process, the temperature curves tend to coincide.

The effective strain distribution is shown in Figure 189.

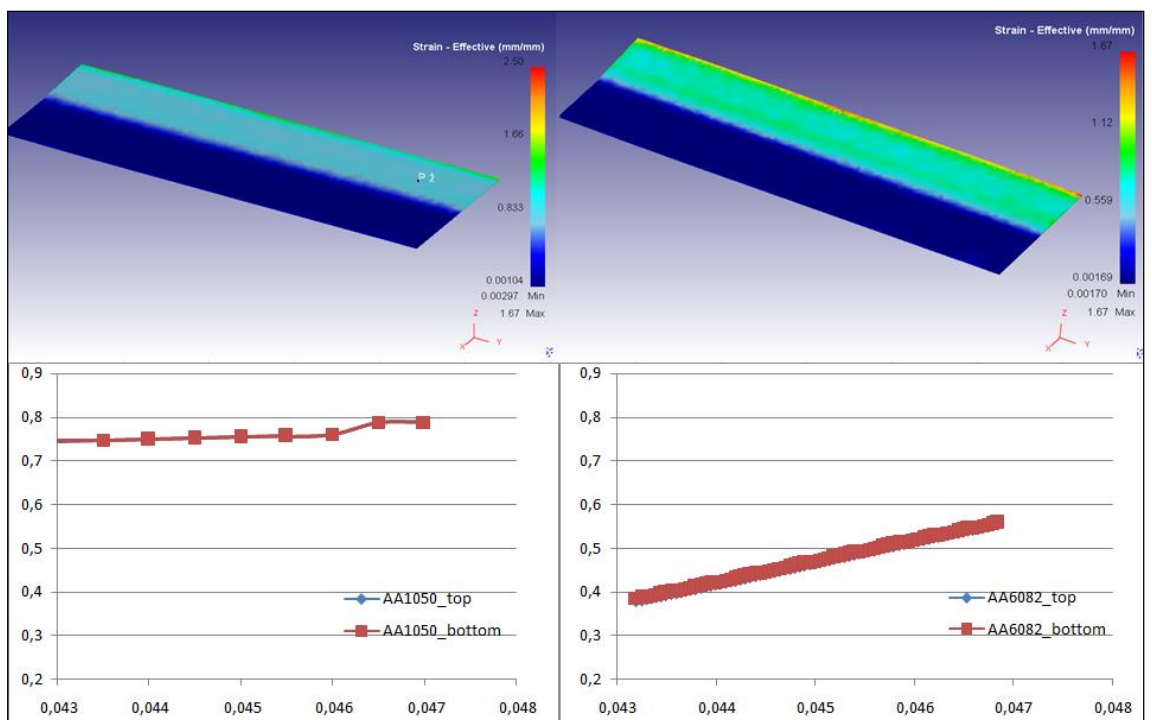


Figure 189. Comparison of the strain distributions.

The heated rolls produce beneficial effects as they allow sheet softening, avoiding stretching phenomena which combined with sheet springback, generates defects such as undulated sheet or snatched sheet.

Also a comparison between the pressure distributions was carried out. As already mentioned, this variables refers exclusively to the contact between the sheet and the roll.

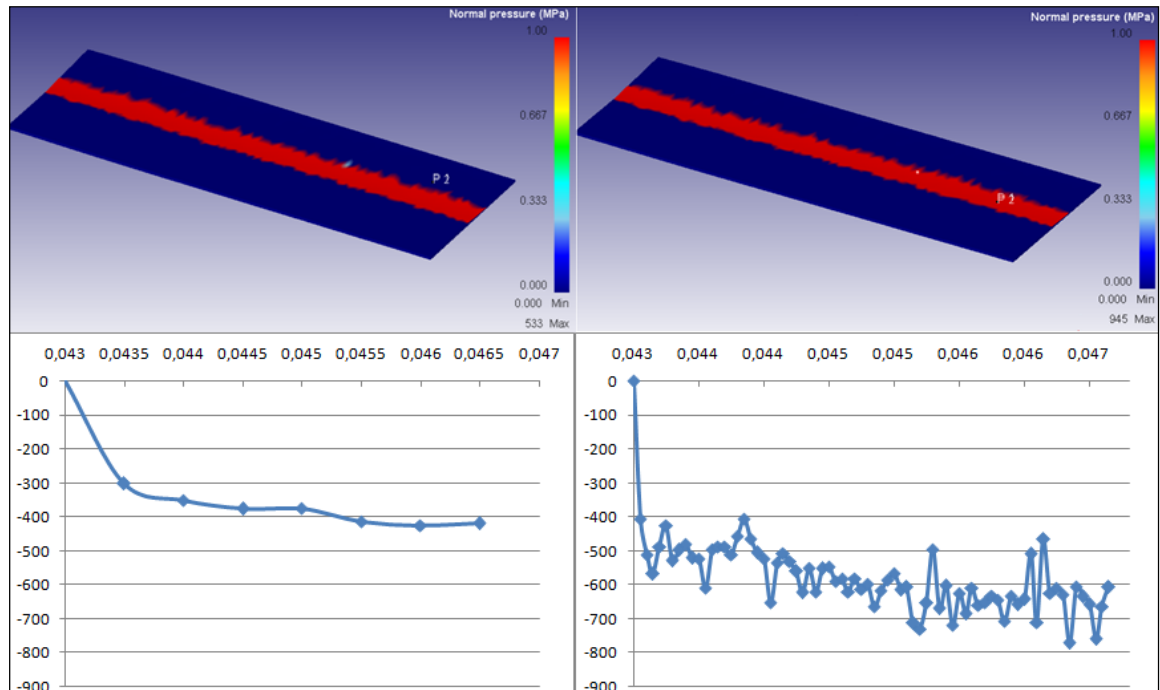


Figure 190. Comparison of the normal pressure distributions.

7.2. Comparison between LFW and ARB models

As already mentioned in chapter 1, the solid bonding phenomenon is governed by three parameters such as time, temperature and pressure which, in turn, depend on the technological parameters of the considered process.

As LFW is considered, pressure at the interface, oscillation frequency and friction coefficient mainly influence the interface temperature reached; on the other hand, amplitude oscillation, oscillation frequency and pressure mainly influence strain rate. As ARB is considered, roll speed greatly affects the strain rate, while roll diameter and distance between the rolls greatly affect the strain.

As LFW of a sound joint is considered, looking at the evolution of the strain during the process for a point located at the interface, a change in the slope can be observe (Figure 191). In particular, from this instant onward, i.e. at $t=1.26s$ for

this simulation, chemical-physical material characteristics were reached in order to obtain the solid bonding phenomenon. In this point the effective strain value is equal to 0.186 (mm/mm).

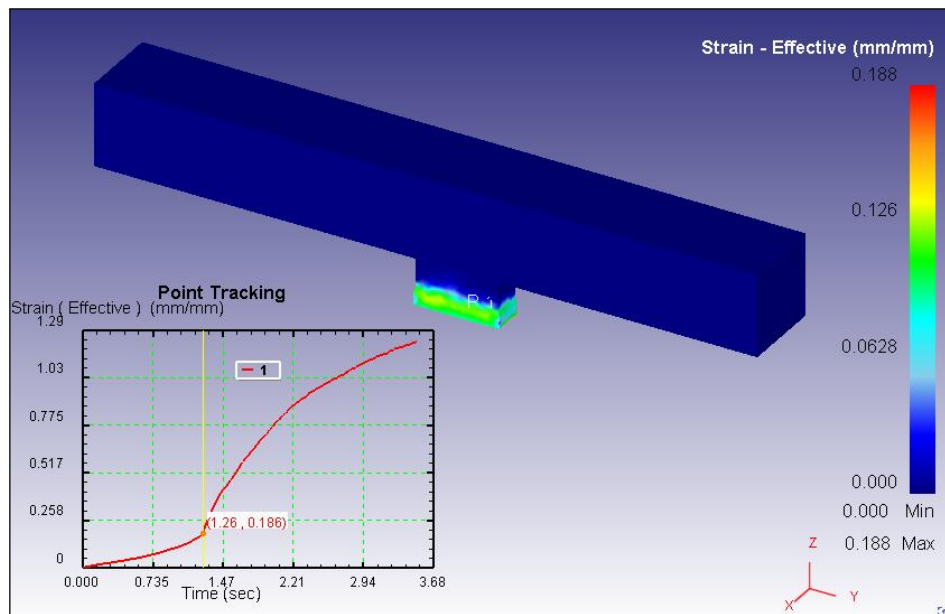


Figure 191. AA6082 - Effective strain in LFW process.

Another important parameter for the purposes of the study of solid bonding, is the strain rate. At the considered time the effective strain rate value is equal to 1.23 ((mm/mm)/sec).

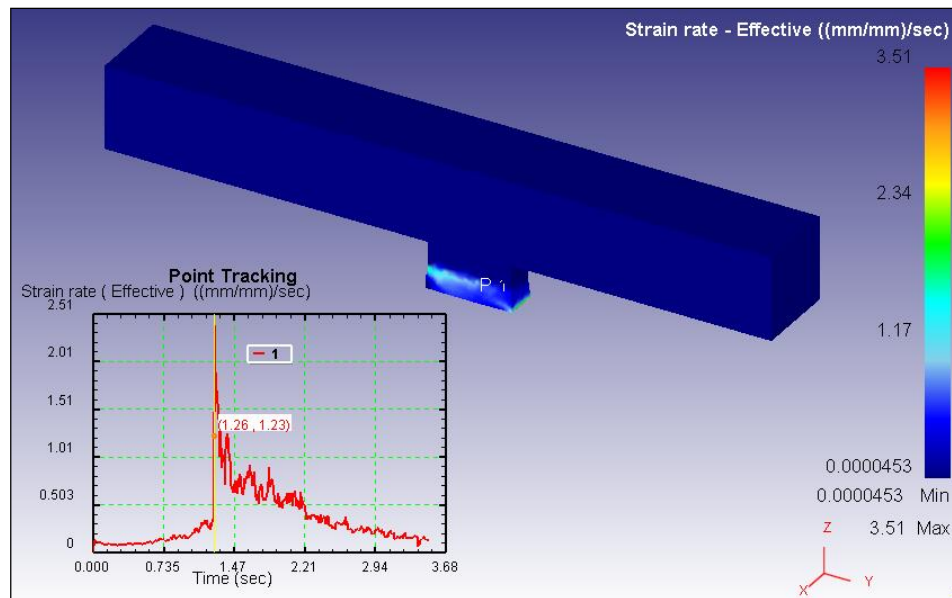


Figure 192. AA6082 - Effective strain rate in LFW process.

Finally, pressure and temperature are shown in Figure 193 and Figure 194

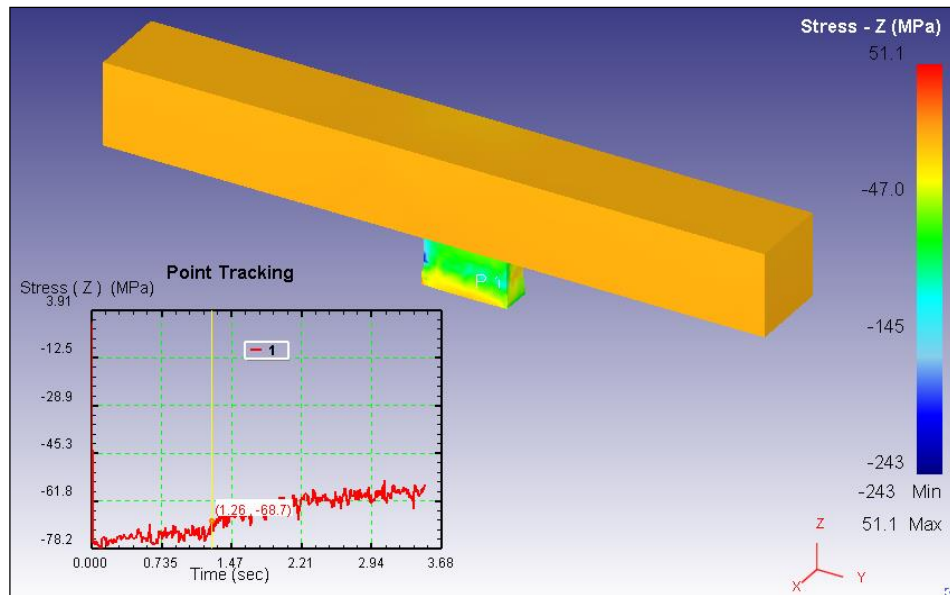


Figure 193. AA6082 - Pressure in LFW process.

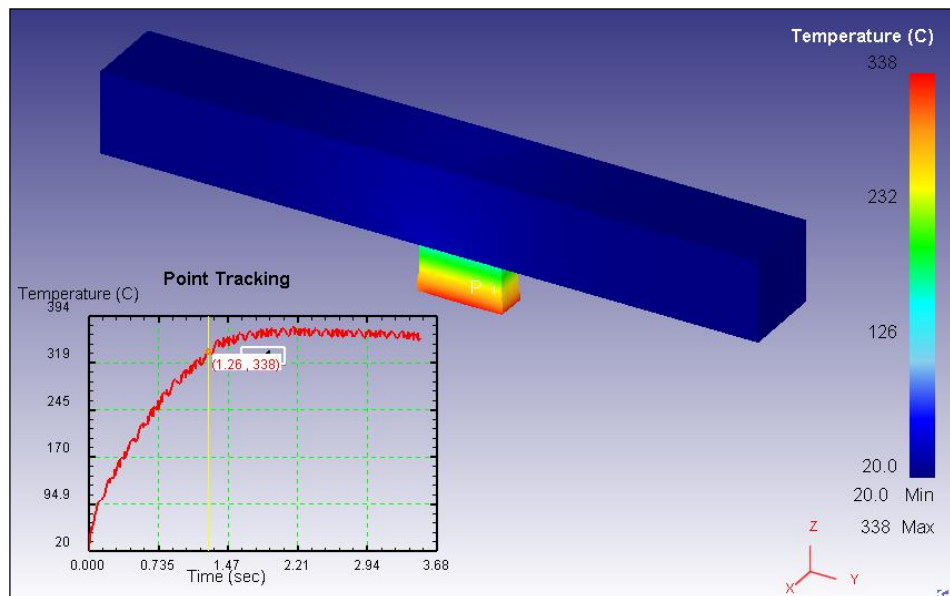


Figure 194. AA6082 - Temperature in LFW process.

Pressure and temperature values obtained are: -68,7 MPa and 338 °C. As it can be seen, almost the highest temperature value is reached at the considered time. In turn, pressure and strain continue increasing till the stop of the oscillation. The same analysis was carried out for the ARB process. In order to make the same considerations, a point having the same characteristics, was selected. For this reason, the bottom surface of the sheet, i.e. the interface surface between the two sheets to be joined, was observed. An effective strain value equal to 0.771 was calculated (Figure 195).

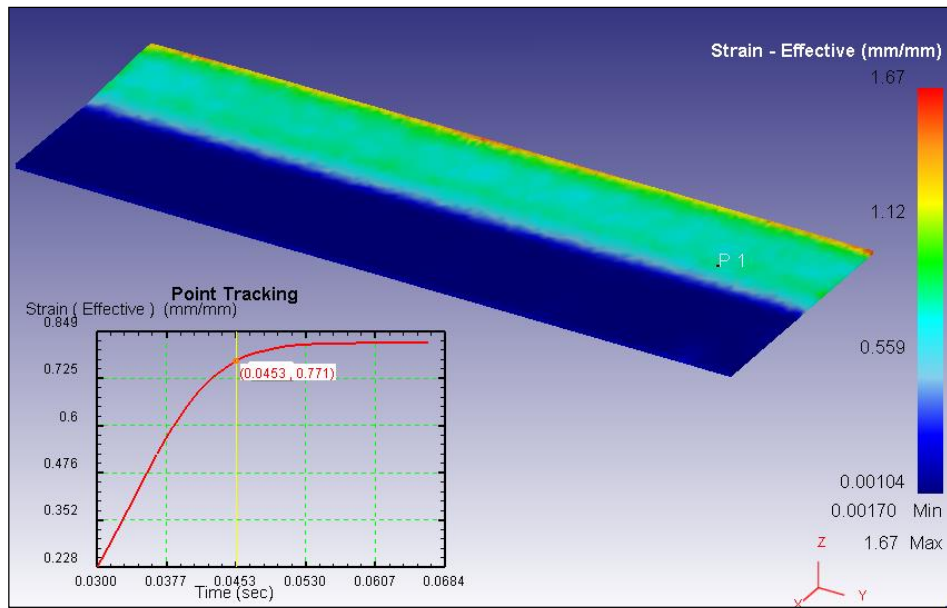


Figure 195. Effective strain in LFW process.

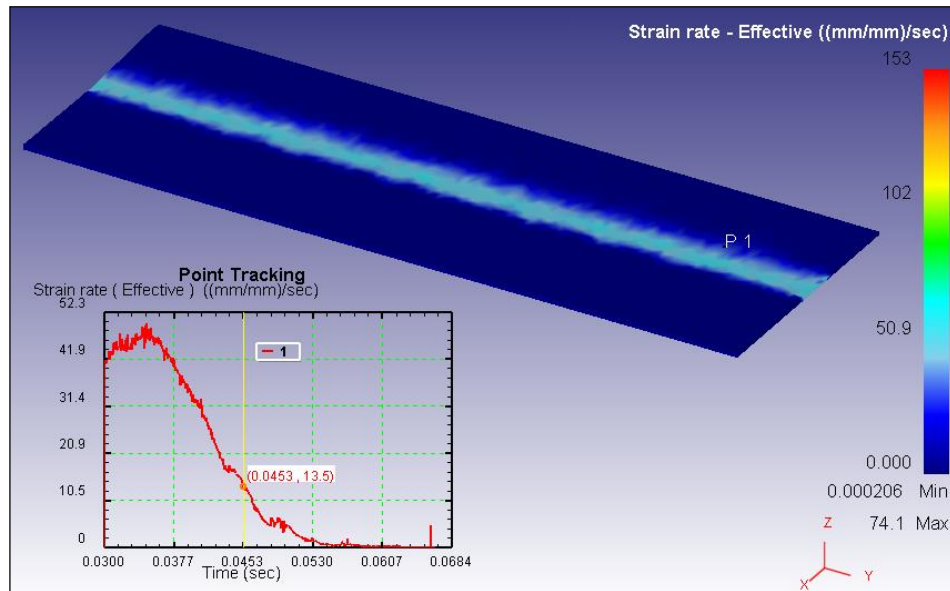


Figure 196. Effective strain rate in LFW process.

Figure 196 shows the effective strain rate distribution and the obtained value equal to 13.5 ((mm/mm)/sec). Finally, pressure and temperature distributions are reported in Figure 197 and Figure 198.

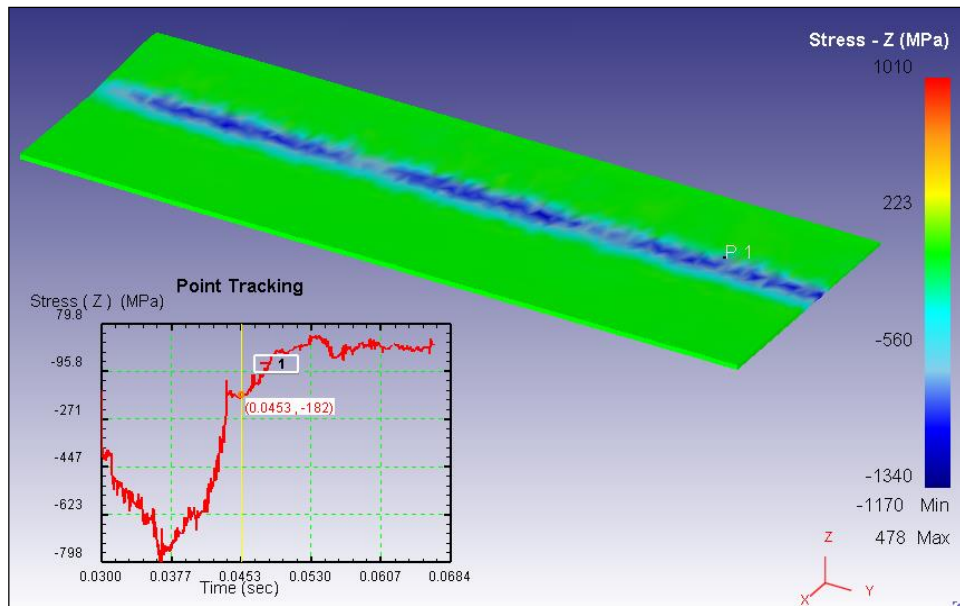


Figure 197. Pressure in LFW process.

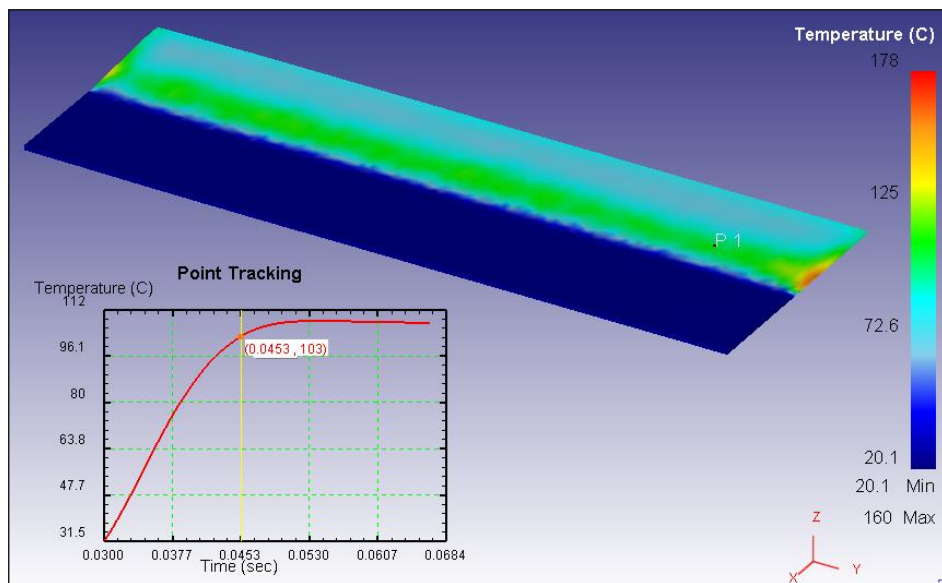


Figure 198. Temperature in LFW process.

The pressure and temperature values obtained, are: -182 MPa and 103 °C.

All the calculated values are summarized in the following Table 11.

processes parameters	Linear Friction Welding	Accumulative Roll Bonding
ϵ [mm/mm]	0.186	0.771
$\dot{\epsilon}$ [mm/mm/sec]	1.23	13.5
σ_z [MPA]	-68.7	-182
T [°C]	338	103

Table 11 Comparison simulation data

Concerning the obtained data, it can be observed that in ARB process high pressure and strain rate are reached, while for LFW high temperature values are reached. Concerning the strain, it is noted that the calculated value in LFW process is not very high; As a matter of fact the reference time is related to the beginning of bonding, i.e. when the axial shortening has not occurred yet. From the reported data it can be concluded that pressure and temperature seems to be as the two most influencing variables for effective bonding. Considering a given process condition, when pressure is one third for one process, temperature is about three times. In this way a sort of balance must be reached between pressure and temperature for solid bonding to occur.

8. Conclusion

The main aim of the present work was to investigate the bonding phenomenon occurring in two different manufacturing processes, namely the solid state welding process Linear Friction Welding and the Severe Plastic Deformation based process ARB used for obtaining Ultra Fined Grain materials.

In order to develop the LFW experimental campaign, a dedicated machine was designed and developed at the University of Palermo, Dept. of Chemical, Management, Computer Science and Mechanical Engineering. The experimental campaign was carried out during my third doctoral year.

As LFW is regarded, process maps were drawn for **aluminum AA2011 and AA6082** with varying oscillation frequency and interface pressure between the specimens, keeping constant process time, equal to 1.5 s, and oscillation amplitude.

Micrographic analyses and microhardness tests were used for the verification of the welded joints.

Based on the obtained results, the following conclusions can be draw:

- The process parameters have a significant influence on the welding temperature. The heat input increases with increasing oscillation frequency and applied pressure. However, during the experimental campaign it was found that the welding temperature decreases when pressure increases over a certain threshold value. This is due to the increased quantity of flash resulting in enhanced heat exchange with environment.
- The peak temperature at the interface during the LFW process is very high, even if it does not exceed the melting temperature of the materials to be welded. The combined effect of the high temperatures that are reached near the weld line, the compression force and the severe plastic deformation suffered by the material, entails significant microstructural changes.
- From a careful examination of the crystal structure of the joint has been detected a decrease of the average grain size. The microstructure of a joint obtained by Linear Friction Welding is usually characterized by four regions: the weld zone (WZ) , the thermo-mechanically affected zone

(TMAZ) in the vicinity of the welding line , the heat affected zone (HAZ) farther away from the weld line and the microstructure of the parent material unaltered.

In the weld zone the microstructure is very different from the one found in other parts of the joint. This is due to the dynamic recrystallization resulting in very fine and equiaxed grains. In the thermo-mechanically affected zone the material was subjected heat and plastic deformation but dynamic recrystallization does not occur. In the heat affected zone the microstructure and / or the other properties have been changed by the heat input to welding (temperature gradient), but there is no plastic deformation effect.

- Microhardness decreases in the HAZ and TMAZ and WZ with respect to the base material. Moreover, the combined effect of recrystallization and grain refinement in the WZ results in greater hardness of the material in this area with respect to the TMAZ. The local hardening of the severely deformed material, however, explains the presence of fluctuations in the hardness values measured on the joint, especially in the TMAZ.

As **mixed joints** of AA2011 and AA6082 are regarded, again oscillation frequency and interface pressure were chosen as process variables, keeping constant the process time, equal to 2.25 s, and oscillation frequency.

Based on the obtained results, the following conclusions can be draw:

- The best mixed joint configuration is given by the aluminum AA2011 as top specimen and the aluminum AA6082 as bottom specimen. Due to the higher mechanical properties of the AA2011, in this configuration the AA6082 alloy "hugs" the AA2011 alloy thus ensuring a lower heat dissipation.
- For both the configurations carried out, it was observed a translation of the process window to the left, i.e. sound joints are obtained at low interface pressures, keeping constant the oscillation frequencies.
- Copper was selected as spy-element (element present only in the AA2011 alloy) for the EDAX analysis. The tests showed that the presence of copper in the AA6082 alloy occurred only in the sound joints obtained with AA2011 as top specimen and AA6082 as bottom one.

- The atomic transmigration in the opposite configuration did not occur. In this configuration, the incipient bonding was verified having moderate mechanical characteristics.
- Finally, high pressures result in detrimental effects for the joint, while the increase of the oscillation frequency gave a beneficial effect to the bonding quality.

The study carried out through the use of thermo-mechanical model showed excellent results compared with the results experimentally obtained. The model is able to predict the effects of process variables, namely pressure and oscillation frequency, on the main field variables distributions a temperature, strain and strain rate. In this way a complete CAE of the process can be achieved.

The experimental campaign and the numerical analysis of Accumulative Roll Bonding (ARB) process were carried out at the Furth laboratory, during the second doctoral year. Numerical calculation and experiments were performed to analyze the cold Accumulative Roll Bonding process, a severe plastic deformation process. Aluminum AA1050 was used for the experiments, while AA6082 and AA1050 were used for the numerical campaign, developed using both a dynamic explicit finite element model and an implicit one.

Von Mises stress distribution, plastic strain and pressure have been numerically calculated for roll and sheet. The 2D model was proved effective to predict roll deformation, maximum reduction to be applied and maximum pressure on the roll with significant CPU time savings with respect to the 3D analysis.

On the other hand, the 3D model can be used in order to have the correct pressure distribution (so as to ensure a correct bonding, for example to calculate the suitable roll convexity). The comparison between the 2D and 3D models has given good results. It is possible to assert that the 2D model is able to provide useful results in very short times, such as the Von Mises stress, pressure on the sheet or the rolling velocity.

The thermo-mechanical analysis was used to investigate the temperature distribution occurring both in cold conditions, due to the deformation work decaying into heat, and in hot conditions when stronger materials, i.e. AA6082, are used. The comparison between the ARB thermo-mechanical models with

different materials, namely AA1050 and AA6082, led to the following conclusion:

- Temperature is not constant along the sheet thickness due to the contact with the pre-heated rolls. In this way larger temperatures are found at the external surface of the sheets.
- Hot rolls results in lower accumulated strain thus reducing the risk of fracture during the process.

LFW and ARB, carried out on with the same material (AA6082), were compared. Field variables distributions were observed at the onset of the bonding phenomenon. The main conclusions are:

- ARB is characterized by higher pressures and strain rates.
- LFW is characterized by higher temperatures. Effective strain is quite low. However, it increases during the rest of the process due to the axial shortening.
- A general “balance” is noted between pressure and temperature: if one of the two is low, the other must be high in order to create solid bonding conditions.

9. Future developments

This thesis aims to give a know-how on the raised issues. In fact, it must be considered as a step of a broader search. In this regard, a few points may give rise to new research:

- Regarding the LFW machine, studies for the redesign of vertical load application are already in place, in order to make it feasible for harder materials such as titanium.

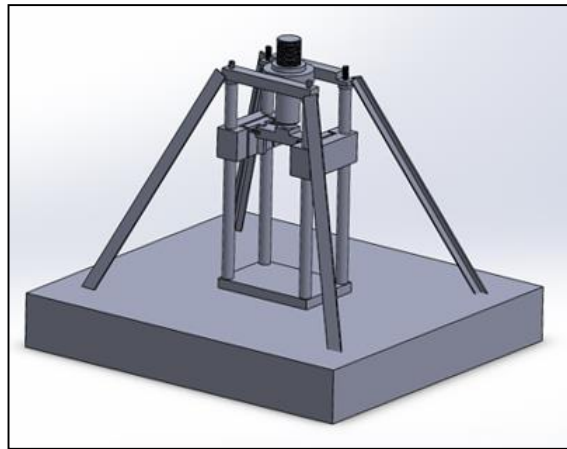


Figure 199. Critical machine part

- The possibility to consider a bonding criterion in order to study the field variables as a function of time will be evaluated. The developed criterion should be tested on multiple solid bonding dominated processes such as Porthole Die Extrusion, Accumulative Roll Bonding or Friction Stir Welding.

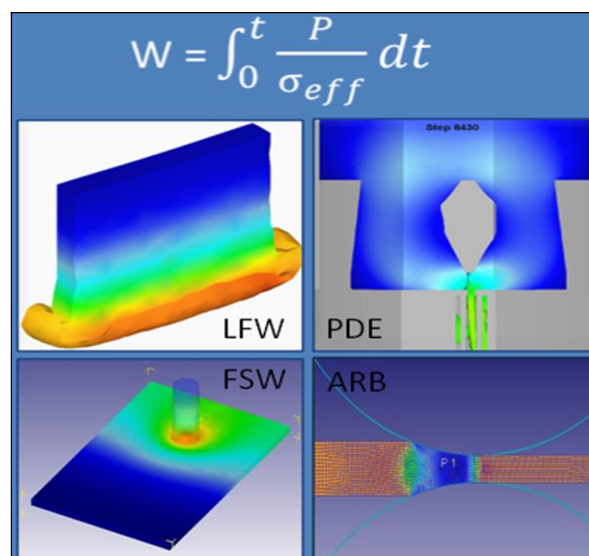


Figure 200. Multiple solid bonding dominated processes

10. Bibliography

1. K. Weman, *Welding processes handbook*. New York: CRC Press LLC, 2003. 0-8493-1773-8.
2. F. Gabrielli, R. Ippolito, F. Micari, *Processi di collegamento. Analisi e tecnologia delle lavorazioni meccaniche*. Milano: McGraw-Hill, 2008.
3. <http://www.twi-global.com/>
4. R. J. Heideman et al., 2000, Friction Stir Welding Tool. U.S. Patent 6,053,391
5. Carter, W. Robert, *Pin Tool Design* Proceedings of the NASA MSFC Friction Stir Welding Workshop and Showcase, Huntsville, Al, September 2003.
6. <http://www.frictionstirlink.com/>
7. C. T. Sims, N. S. Stoloff, and W. C. Hagel, editors. *Superalloys II*. John Wiley and Sons Inc., 1987.
8. C. A. Dandre, C. A. Walsh, R. W. Evans, R. C. Reed, S. M. Roberts. *Microstructural evolution of nickel-base superalloy forgings during ingot-to-billet conversion: process modelling and validation*. In T.M. Pollock et al, editor, *Superalloys 2000*, TMS, USA, pages 85–94, 2000.
9. <http://www.fpe.co.uk/processes/friction-welding>
10. <http://www.alunnatubes.com/porthole-extruded-tubes.html>
11. F. Wetscher, A. Vorhauer, R. Stock, R. Pippana, *Structural refinement of low alloyed steels during severe plastic deformation*,

Materials Science and Engineering: A Volumes 387–389, 15 December 2004, Pages 809–816.

12. A. Oosterkamp, L. Djapic Oosterkamp, A. Nordeide, '*Kissing Bond*' Phenomena in Solid-State Welds of Aluminum Alloys Discontinuities in extrusion welds are a model for friction stir welding defects. Supplement to the welding journal, august 2004 Sponsored by the American Welding Society and the Welding Research Council.
13. <http://www.compes.com/>
14. W. Richter, *Herbeifuehrung einer haftverbindung zwischen plaettchen aus werkzeugstahl und deren traegern nach art einer schweissung oder loetung*. 1929. Patent: DE477084.
15. *Untersuchungen zum linear-reibsscheissen von metallen*. Nentwig, A.W. E. Berlino Schweissen und Schneiden, 1995.
16. R. Maurya, J. Kauzlarich, *Bonding apparatus - friction welding by reciprocal motion*. 1969. Patent: Caterpillar Tractor Co, US3420428-A; DE1552871-A; CA844858-A.
17. P. Wanjara, M. Jahazi, *Linear friction welding of Ti-6Al-4V: Processing, microstructure, and mechanical-property inter-relationships*. sl :Metall. Mater. Trans. A, 2005.
18. A. Vairis, M. Frost, *High frequency linear friction welding of a titanium alloy*. sl: Wear, 1998.
19. B. Eng thesis, Garton, J.H.L., Investigation into Linear Friction Welding of Blisks, University of Bristol, 1987.
20. A. M. Korsunsky and K. E. James, (2004-January-September). *Residual stresses around welds in nickel-based superalloys*. Journal of Neutron Research, 12 (1-3), 153-158.

21. M. E. Nunn, *Aeroengine improvements through linear friction welding*. Queen's University Belfast: Proc. 1st Int. Conf. on 'Innovation and Integration in Aerospace Sciences', Paper no 2005-0040, 2005.
22. M. Frost, A. Vairis, *On the extrusion stage of linear friction welding of Ti6Al4V*. sl: Mater. Sci. Eng. A-Struct. Mater. Prop. Microstruct. Process. 1999.
23. Vairis, A. and Frost, *Modeling the linear friction welding of titanium blocks*, J. Mater. Sci. Eng. (2000), 292(1), p 8-17).
24. B. Crossland, *Friction Welding*. sl: Contemporary Physics, 1971.
25. Bhamji, Preuss, Threadgill, Addison. *Solid state joining of metals by linear friction welding: A literature review*. Manchester: Materials Science & Technology, 2011.
26. R. Ates, H. Bayindir, *Comparison of the constructed control methods for a friction-welding machine*, Materials and Manufacturing Processes 2005, 20 (2), 131–146.
27. Mumin Sahin, *Joining with friction welding of high-speed steel and medium-carbon steel*, Mechanical Engineering Department of Trakya University, Turkey, 2004.
28. M. Corzo, Y. Torres, M. Anglada, A. Mateo, *Fracture behaviour of linear friction welds in titanium alloys*, Anales de la Mecánica de Fractura, Vol 1, 2007.
29. Corzo M., Mendez J., Villechaise P., Rebours C., Ferte J.-P., Gach E., Roder O., Llanes L., Anglada M. y Mateo A., *High-cycle fatigue performance of dissimilar linear friction welds of titanium alloys*, Proceedings of the 9th International Fatigue Congress, Ed. Elsevier, Atlanta, USA, 2006.

30. B. Lang, T. C. Zhang, X. H. Li, D. L. Guo, *Microstructural evolution of a TC11 titanium alloy during linear friction welding*, J Mater Sci, 45:6218–6224, 2010.
31. Tiejun Ma, Wen Ya Li, Dr. Quanz hou Xu, Dr. Yong Z hang, Jinglong Li, Siqian Yang, Hanlin Liao, *Microstructure Evolution and Mechanical Properties of Linear Friction Welded 45 Steel Joint*, Advanced Engineering Materials, 2007.
32. Tiejun Ma, Wen Ya Li, Dr. Quanz hou Xu, Dr. Yong Z hang, Jinglong Li, Siqian Yang, Hanlin Liao, *Effect of friction time on flash shape and axial shortening of linear friction welded 45 steel*, Materials Letters 62, 293-296, 2008.
33. Romero, Attallah, Preuss, Karadge, Bray, *effect of the forging pressure on the microstructure and residual stress development in Ti–6Al–4V linear friction welds*, Acta Materialia 57, 5582–5592. 2009.
34. Chamanfar, Jahazi, Gholipour, Wanjara e Yue, *Suppressed Liquefaction and Microcracking in Linear Friction Welded WASPALOY*, Materials and Design, 2009.
35. Helm D. y Lutjering G., *Microstructure and properties of friction-welds in titanium alloys*, Titanium'99: Proceedings of the 9th World Conference on Titanium: Saint Petersburg, 1999, pp. 1726-1733.
36. C. Mary and M. Jahazi, *Multi- Scale Analysis of IN-718 Microstructure Evolution During Linear Friction Welding*, Dept. of Mechanical and Materials Engineering Nantes, France, Aerospace Manufacturing Technology Center, Institute for Aerospace Research National Research Council Canada Montreal, PQ, Canada, 2008.
37. Li e Ma, *Numerical simulation of linear friction welding of titanium alloy: Effects of processing parameters*, Materials and Design, 2009.
38. A. M. Yamileva, A. V. Yuldashev and I. Sh. Nasibullayev, *Comparison of the parallelization efficiency of a thermo-structural problem*

simulated in simulia abaqus and ansys mechanical, journal of engineering science and technology review 5 (3) (2012) 39-43.

39. Lang, Zhang, Li, Gua, *Microstructural evolution of a TC11 titanium alloy during linear friction welding*, J Mater Sci, 45:6218–6224, 2010.
40. Varis A. y Frost M., *Modelling the linear friction welding of titanium blocks*, Materials Science and Engineering A292, 8 – 17, 2000.
41. Varis A. y Frost M., *Design and Commissioning of a Friction Welding Machine*, Materials and Manufacturing Processes.
42. E. D. Nicholas, *Friction surfacing and linear friction welding*. 3rd International SAMPE Metals Conference, October PY92. pp. 450-463.
43. A. Vairis, Ear. J. Mech., *Investigation of frictional behavior of various materials under sliding conditions*, A/Solids 16 (1997) 929- 945.
44. P. Threadgill, *Linear Friction Weld*, TWI Knowledge Summary, The Welding Institute, UK, Available online at http://eurostir.co.uk/j32k/protected/band_3/ksplt001.html.
45. Jun, Rotundo, Song, Ceschini, Korsunsky, *Residual strains in AA2024/AlSiCp composite linear friction welds*, Materials and Design, 2009.
46. Rotundo, Ceschini, Morri, Jun, Korsunsky. *Mechanical and microstructural characterization of 2124Al/25 vol. %SiC joints obtained by linear friction welding (LFW)*. Bologna: Composites, 2010.
47. G.Buffa, M.Cammalleri, D.Campanella, L.Fratini, A.Pasta *Ingegnerizzazione di una macchina prototipale per processi di saldatura linear friction welding*
48. L. Fratini, G. Buffa, M. Cammalleri, D. Campanella, *On the linear friction welding process of aluminum alloys: Experimental insights through*

- process monitoring*, CIRP Annals - Manufacturing Technology 62 (2013) 295–298.
49. L. Fratini, G. Buffa, D. Campanella, D. La Spisa, *Investigations on the linear friction welding process through numerical simulations and experiments*, Materials and Design, 40 (2012) 285–291.
 50. V. I. Vill, *Friction welding of metals*. New York : American Welding Society, 1965.
 51. J. Sorina-Müller, M. Rettenmayr, D. Schneefeld, O. Roder, and W. Fried, FEM Simulation of the Linear Friction Welding of Titanium Alloys, *Comput. Mater. Sci.*, 2010, 48, p 749–758.
 52. A. Rivola, *Meccanismi con camme*.
 53. D. Moreno, E. Mucchiy, G. Dalpiazzy, A. Rivolaz, *multibody analysis of the desmodromic valve train of the ducati motogp engine, multibody dynamics 2007, eccomas*, Thematic Conference C.L. Bottasso, P. Masarati, L. Trainelli (eds.), Milano, Italy, 25–28 June 2007.
 54. R. Monastero, *Le cammes*
 55. <http://www.tecnicaindustriale.net>
 56. <http://www.oppo.it>
 57. E. Dalgard, M. Jahazi, and J.J. Jonas: *Friction Stir Welding and Processing—V*, TMS 2009 Annual Meeting & Exhibition, R.S. Mishra, M.W. Mahoney, and T.J. Lienert, eds., TMS, San Francisco, CA, 2009, pp. 55–64.

58. Romero, Attallah, Preuss, Karadge, Bray. *Effect of the forging pressure on the microstructure and residual stress development in Ti-6Al-4V linear friction welds*. sl: Acta Materialia, 2009.
59. S. K. Tiwari, Dinesh Kumar Shukla, R. Chandra, *Friction Stir Welding of Aluminum Alloys: A Review*, International Journal of Mechanical, Industrial Science and Engineering Vol: 7 No: 12, 2013.
60. Krishna, P. Murali; D. Simhachalam, N. Ramanaiah, *Effect of Ageing on Mechanical Properties of Dissimilar Friction Stir Welded Aluminum Alloy (AA2024 and AA6351) Joints*, Journal of Applied Sciences;2012, Vol. 12 Issue 10, p1053.
61. A. Cigada, M. Cabrini, D. Sinigaglia, *Comportamento alle sollecitazioni e prove meccaniche*. [boekaut.] A. Cigada, G. Re en D. Sinigaglia. *Struttura e proprietà dei materiali metallici*. Milano: Ambrosiana Editore, 1993.
62. G. E. Totten, D. S. MacKenzie, *Handbook of Aluminum: Vol. 1: Physical Metallurgy and Processes*
63. C. Genovois, D. Fabrègue, A. Deschamps, *On the coupling between precipitation and plastic deformation in relation with friction stir welding of AA2024 T3 aluminium alloy*. sl: Mater Sci Eng, 2006.
64. F. Gabrielli, R. Ippolito, F. Micari, *Processi di collegamento. Analisi e tecnologia delle lavorazioni meccaniche*. Milano: McGraw-Hill, 2008.
65. Nauman, D. *Forge welding*. Hammer's blow. 2004, 10.
66. Shirzadi, A. *Diffusion Bonding*. 2010.
67. Grujicic, G. Arakere, B. Pandurangan, C.-F. Yen, B. A. Cheeseman, *process modelling of Ti-6Al-4V Linear Friction Welding*.

68. N. Ahmed, *New Developments in Advanced Welding*. Boca Raton: CRC Press LLC, 2005. 0-8493-3469-1.
69. Society, American Welding. *Welding Handbook: Welding Science and Technology*. USA: American Welding Society, 2001. 0-87171-657-7.
70. A. Azushima, R. Kopp, A. Korhonen, D.Y. Yang, F. Micari, G.D. Lahoti, P. Groche, J. Yanagimoto, N. Tsuji, A. Rosochowski, A. Yanagida, *Severe plastic deformation (SPD) processes for metals*, CIRP Annals - Manufacturing Technology 57 (2008) 716–735
71. Y. Saito, N. Tsuji, H. Utsunomiya, T. Sakai and R.G. Hong, *Ultra-fine grained bulk aluminum produced by Accumulative Roll-Bonding (ARB) Process*, Department of Materials Science and Engineering, Osaka University, Japan;
72. M. Furukawa, Z. Horita, M. Nemoto, T. G. Langdon, *Processing of metals by equal-channel angular pressing*, Journal of Materials Science, 20010615, Volume 36, Issue 12, pp 2835-2843
73. Z. Horita, D. J. Smith, M. Furukawa, N. Nemoto, R. Z. Valiev, T. G. Langdon, *An Investigation of Grain Boundaries in Submicrometer-Grained Al-Mg Solid Solution Alloys Using High-Resolution Electron Microscopy*, J. Mater. Res. 11, 1880-1890 (1996).
74. Y. Saito, H. Utsunomiya, N. Tsuji, T. Sakai, *Novel ultra-high straining process for bulk materials development of the accumulative roll-bonding (ARB) process*, Volume 47, Issue 2, 15 January 1999, Pages 579–583.
75. R. Song, D. Ponge, D. Raabe, J.G. Speer and D.K. Matlock, *Overview of processing, microstructure and mechanical properties of ultrafine grained bcc steels*, Overview of ultrafine grained bcc steels.

76. S. H. Lee, T. Sakai, Y. Saito, H. Utsunomiya, N. Tsuji, *Strengthening of sheathe-rolled aluminum based MMC by the ARB process*, materials transactions, JIM, Vol. 40, No. 12 (1999), pp. 1422-1428.
77. Y. Ito, N. Tsuji, Y. Saito, H. Utsunomiya, T. J. Sakai, The Japan Institute of Metals and Materials, 2000, 64, 429.
78. N. Takata, S.-H. Lee, N. Tsuji, *Ultrafine grained copper alloy sheets having both high strength and high electric conductivity*, Materials Letters, Volume 63, Issue 21, 31 August 2009, Pages 1757–1760.
79. N. Tsuji, Y. Ito, Y. Saito, Y. Minamino, *Strength and ductility of ultrafine grained aluminum and iron produced by ARB and annealing*, Scripta Materialia, Volume 47, Issue 12, 9 December 2002, Pages 893–899.
80. N. Tsuji, Y. Saito, S.-H. Lee, Y. Minamino, ARB (Accumulative Roll-Bonding) and other new Techniques to Produce Bulk Ultrafine Grained Materials, Advanced Engineering Materials, Volume 5, Issue 5, pages 338–344, May, 2003.
81. I. Topic, H. W. Höppel, D. Staud, M. Merklein, M. Geiger, M. Göken, *Formability of Accumulative Roll Bonded Aluminum AA1050 and AA6016 investigated using Bulge Tests*.
82. L. Fratini, M. Merklein, W. Boehm, D. Campanella, *Modelling Aspects in Accumulative Roll Bonding process by Explicit Finite Element Analysis*.
83. G. Buffa, L. Fratini, S. Pellegrino, F. Micari, *On the Field Variables Influence on Bonding Phenomena during FSW Processes: Experimental and Numerical Study*, Key Engineering Materials, 2013, (Volume 549), 484-491.

84. Tadanobu Inoue, Nobuhiro Tsuji, *Quantification of strain in accumulative roll-bonding under unlubricated condition by finite element analysis*, Computational Materials Science, Volume 46, Issue 1, July 2009, Pages 261–266.
85. Juliane Scharnweber, Werner Skrotzki, Carl-Georg Oertel, Heinz-Günter Brokmeier, Heinz Werner Höppel, Irena Topic, Jörn Jaschinski, *Texture, Microstructure and Mechanical Properties of Ultrafine Grained Aluminum Produced by Accumulative Roll Bonding*, Advanced Engineering Materials, 2010, Volume 12, Issue 10, pages 989–994.
86. R.Z. Valiev, I.V. Alexandrov, Y.T. Zhu and T.C. Lowe, *Paradox of strength and ductility in metals processed by severe plastic deformation*, *J. Mater. Res.*, Vol. 17, No. 1, Jan 2002.
87. R.Z. Valiev, R.K. Islamgaliev, I.V. Alexandrov, *Progress in Materials Science* 45, pp. 103-189, 2000
88. D.G. Morris, *Mechanical Behaviour of Nanostructured Materials*, Trans Tech Publications, Enfield NH USA, 1998
89. V. M. Segal, *Severe Plastic Deformation: Simple Shear Versus Pure Shear*, *Materials Science and Engineering A* 338(1–2):331–344.
90. R. Z. Valiev, Y. Estrin, Z. Horita, T. G. Langdon, M. J. Zehetbauer, Y. T. Zhu, *Producing Bulk Ultrafine-grained Materials by Severe Plastic Deformation*. *JOM* 58(4):33–39.
91. R. Z. Valiev, T. G. Langdon, *Principles of Equal-channel Angular Pressing as a Processing Tool for Grain Refinement*. *Progress in Materials Science* 51(7):881–981.
92. Azushima A (2000) *Materials Development by Extrusion Process*. *Journal of the Japan Society for Technology of Plasticity* 47(544):456–459. (in Japanese).

93. Y.Saito, N.Tsuji, H.Utsunomiya, T.Sakai and R.G. Hong, *Ultra-Fine Grained Bulk Aluminum Produced by Accumulative Roll-Bonding (ARB) Process*, Scripta Mater., 39 (1998), pp.1221-1227.
94. N.Tsuji, Y.Saito, H.Utsunomiya and S.Tanigawa, *Ultra-fine grained bulk steel produced by accumulative roll-bonding (ARB) process*. Scripta Mater., 40 (1999), pp.795-800.
95. N Tsuji, *Ultrafine grained steels managing both high strength and ductility*, International Conference on Advanced Structural and Functional Materials Design 2008.
96. N. Tsuji (2005) *Formation of Ultrafine Grain of Structure Metals by Severe Plastic Deformation*, Journal of the Japan Welding Society 74(2):92–96. (in Japanese).
97. R. Z. Valiev, N. A. Krasilnikov, N. K. Tsenev, *Plastic Deformation of Alloys with Submicron-grained Structure*. Materials Science and Engineering A 197:35–40.
98. R. Z. Valiev, *Structure and Mechanical Properties of Ultrafine-grained Metals.*, Materials Science and Engineering A 234–236:59–66.
99. J. Y. Huang, Y. T. Zhu, H. Jiang, Lowe TC (2001), *Microstructures and Dislocation Configurations in Nanostructured Cu Processed by Repetitive Corrugation and Straightening*. Acta Materialia 49(9):1497–1505.
100. A. Korbel, M. Richert, J. Richert (1981), *The Effects of Very High Cumulative deformation on Structure and Mechanical Properties of Aluminium*. Proceedings of Second RISO International Symposium on Metallurgy and Material Science, Roskilde, September 14–18, 445–450.
101. S. Mizunuma (2005), *Large Straining Behavior and Microstructure Refinement of Several Metals by Torsion Extrusion Process*. Materials Science Forum 503–504:185–190.

102. K. Nakamura, K. Neishi, K. Kaneko, M. Nakagaki, Z. Horita (2004) *Development of Severe Torsion Straining Process for Rapid Continuous Grain Refinement*. *Materials Transactions* 45(12):3338–3342.
103. A. K. Ghosh, W. Huang (2000) in Lowe TC, Valiev RZ, (Eds.) *Investigations and Applications of Severe Plastic Deformation*. 29–36.
104. Y. Saito, N. Tsuj, H. Utsunomiya, T. Sakai, and R. G. Hong, in Proceedings of the 6th International Conference on “*Aluminum Alloys (ICAA-6)*”, Japan Institute of Light Metals, p. 1967 (1998).
105. Y. Saito, N. Tsuji, H. Utsunomiya, T. Sakai, and R. G. Hong, *Scripta Mater.* 39, 1221 (1998).
106. N. Tsuji, K. Shiotsuki, H. Utsunomiya, and Y. Saito, in Proceedings of the International Symposium on “*Towards Innovation in Superplasticity-II*,” Trans Tech Publications
107. www.leonghuat.com